Fadhel M. Ghannouchi • Abbas Mohammadi

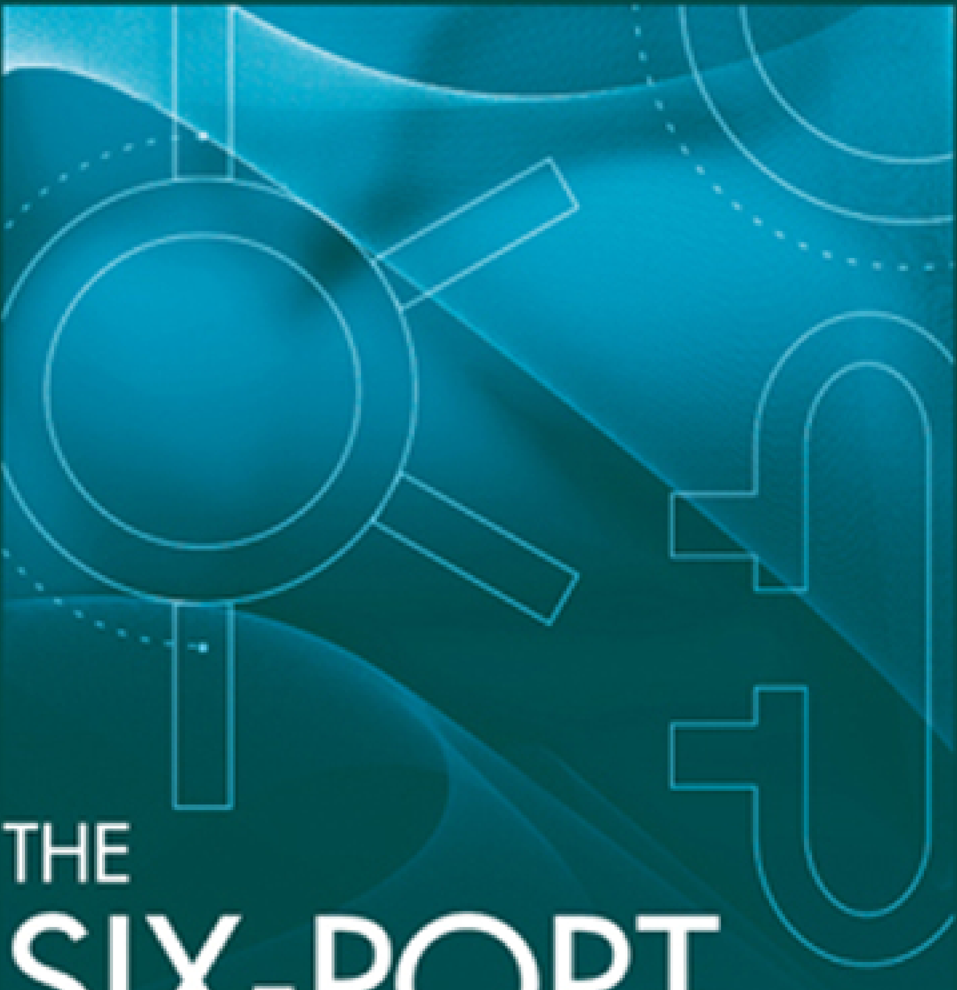

THE SIX-PORT TECHNIQUE

WITH MICROWAVE AND WIRELESS APPLICATIONS

The Six-Port Technique with Microwave and Wireless Applications

For a listing of recent titles in the
Artech House Microwave Library,
turn to the back of this book.

The Six-Port Technique with Microwave and Wireless Applications

Fadhel M. Ghannouchi
Abbas Mohammadi

ARTECH
HOUSE

BOSTON | LONDON
artechhouse.com

Library of Congress Cataloging-in-Publication Data
A catalog record for this book is available from the U.S. Library of Congress.

British Library Cataloguing in Publication Data
A catalogue record for this book is available from the British Library.

ISBN-13: 978-1-60807-033-6

Cover design by Yekaterina Ratner

685 Canton Street
Norwood, MA 02062

10 9 8 7 6 5 4 3 2 1

Contents

Chapter 1 Introduction to the Six-Port Technique

Chapter 2 Six-Port Fundamentals

Chapter 3 The Design of Six Port Junctions

Chapter 4 Calibration Techniques

Chapter 5 Six-Port Network Analyzers

Chapter 6 Source Pull and Load-Pull Measurements Using the Six-Port Technique

Chapter 7 Six-Port Wireless Applications

Chapter 8 Six-Port Microwave Applications

Chapter 1

Introduction to the Six-Port Technique

This chapter is an introductory chapter to the book and it briefly reports the basic concepts and principles related to transmissions lines, modeling of linear networks, defining S parameters, and some elements relevant to microwave metrology and the design of network analyzers.

1.1 MICROWAVE NETWORK THEORY

The definition of voltages and currents for non-TEM lines is not straightforward [1]. Moreover, there are some practical limitations when one tries to measure voltages and currents in microwave frequencies. To solve these problems, the incident and reflected powers and their parameters are measured in microwave frequencies. The scattering parameters, which indeed are the parameters that can be directly related to power measurements, are used to characterize microwave circuits and networks.

1.1.1 Power and Reflection

Figure 1.1 shows a one-port network with input impedance Z that is connected to the generator V_g with generator impedance Z_g. Power is transmitted from the generator to the one-port network. The current and voltage at terminal are

$$i = \frac{V_g}{Z_g + Z} \tag{1.1}$$

and

$$v = \frac{ZV_g}{Z_g + Z} \tag{1.2}$$

In order to receive the maximum available power from generator in the load, the conjugate matched, $Z = Z_g^*$, conditions must be realized. Let $Z_g = R_g + jX_g$; then, under this condition, the incident current and voltage are defined as [2]

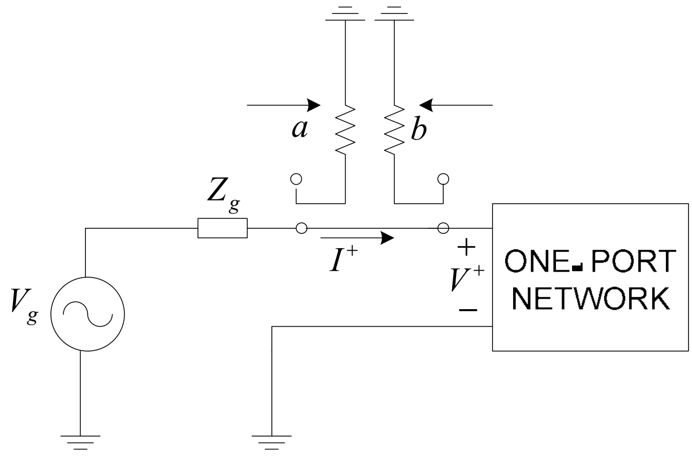

Figure 1.1 One-port network and extraction of incident and reflected waves using a directional coupler.

$$I^+ = \frac{V_g}{Z_g^* + Z_g} = \frac{V_g}{2R_g} \tag{1.3}$$

and

$$V^+ = \frac{Z_g^* V_g}{Z_g^* + Z_g} = \frac{Z_g^* V_g}{2R_g} \tag{1.4}$$

The relationship between incident voltage and incident current is given by

$$V^+ = Z_g^* I^+ \tag{1.5}$$

The maximum available power is

$$P_A = \mathrm{Re}(VI^*) = \frac{|V_g|^2}{4R_g} \tag{1.6}$$

where current and voltage are RMS values. As may be seen from (1.4) and (1.5), incident voltage and incident current are independent of the impedance of the one-port network. The terminal voltage and current according to Figure 1.1 are obtained as

$$V = V^+ + V^- \tag{1.7a}$$

$$I = I^+ - I^- \tag{1.7b}$$

From (1.6), the incident power is defined as the maximum available power from a given generator as

$$P_{inc} = \mathrm{Re}\left[V^+ (I^+)^*\right] = \frac{|V_g|^2}{4R_g} \tag{1.8}$$

By using (1.4), the incident power (1.8) can be written as

$$P_{inc} = \frac{|V^+|^2 R_g}{|Z_g^*|^2} \tag{1.9}$$

The magnitude of the normalized incident wave, *a,* and reflected wave, *b,* are defined as the square root of the incident and reflected powers as

$$|a| = \sqrt{P_{inc}} = \frac{V^+ \sqrt{R_g}}{Z_g^*} = I^+ \sqrt{R_g} \tag{1.10a}$$

$$|b| = \sqrt{P_r} = \frac{V^- \sqrt{R_g}}{Z_g^*} = I^- \sqrt{R_g} \tag{1.10b}$$

The dimensions of *a* and *b* are the square root of power. They are directly related to power flow. The ratio of the normalized reflection wave to normalized incident wave is called reflection coefficient

$$\Gamma = \frac{b}{a} \tag{1.11}$$

1.1.2 Scattering Parameters

The normalized incident and reflected waves are related by scattering matrix. The scattering matrix characterizes a microwave network at a given frequency and operating conditions. Let the characteristics impedance of the transmission lines in Figure 1.2 be equal to Z0; then the scattering matrix of a two-port network can be represented as

$$\begin{bmatrix} b_1 \\ b_2 \end{bmatrix} = \begin{bmatrix} s_{11} & s_{12} \\ s_{21} & s_{22} \end{bmatrix} \begin{bmatrix} a_1 \\ a_2 \end{bmatrix} \tag{1.12}$$

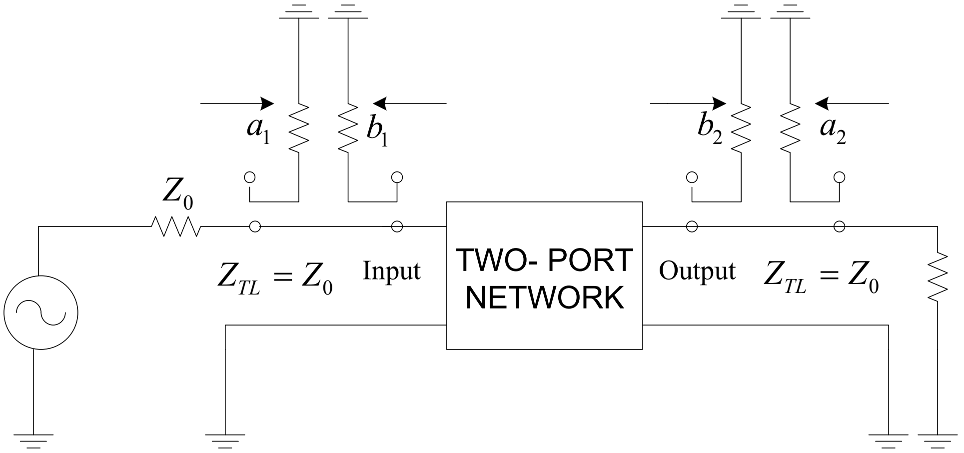

Figure 1.2 Two-port network and extraction of incident and reflected waves using directional coupler.

where $s_{11} = b_1 / a_1 \big|_{a_2=0}$ is the input reflection coefficient while the output is terminated with Z_0,

$s_{21} = b_2 / a_1 \big|_{a_2=0}$ is the forward transmission coefficient between Z_0 terminations,

$s_{12} = b_1 / a_2 \big|_{a_1=0}$ is the reverse transmission coefficient between Z_0 terminations,

and $s_{22} = b_2 / a_2 \big|_{a_1=0}$ is the output reflection coefficient while the input is terminated with Z_0.

If we have a lossless passive two-port, the power applied to the input port is either reflected or transmitted. Accordingly,

$$|s_{11}|^2 + |s_{21}|^2 = 1 \tag{1.13}$$

The advantage of scattering parameters is that they can be evaluated by attaching direction couplers to all of the network ports. The directional couplers separate incident and reflected power waves directly, simplifying the measurement procedure. The fact to remember is that the conditions required for determining the individual s-parameter value need properly terminated transmission lines at the various ports [3].

The scattering matrix may be expanded to define any N-port network, where N is any positive integers. The characteristic impedance of the different port can be the same. This is the case in the many practical applications. However, the scattering matrix can be generalized to include the different characteristic impedances in various ports [1]. An N-port network is shown in Figure 1.3, where a_n is the incident wave in port n and b_n is the reflected wave in port n.

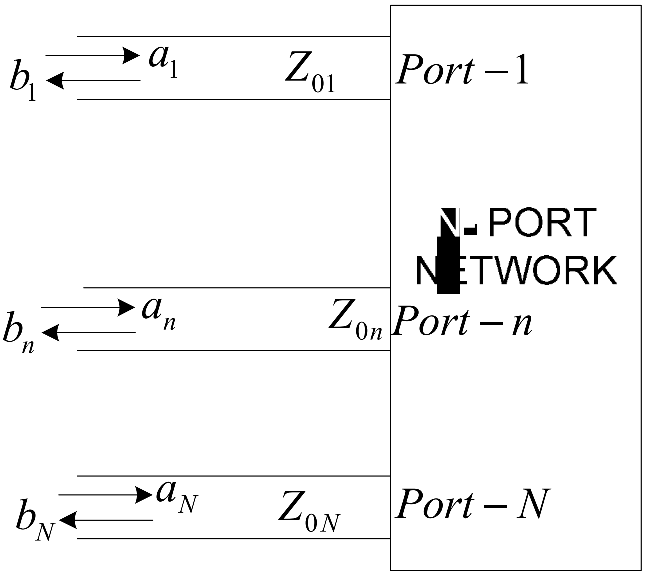

Figure 1.3 An arbitrary N-port microwave network.

The scattering matrix, or [S] matrix, is defined in relation to these incident and reflected waves as

$$\begin{bmatrix} b_1 \\ b_2 \\ \vdots \\ b_N \end{bmatrix} = \begin{bmatrix} s_{11} & s_{12} & \cdots & s_{1N} \\ s_{21} & & & \vdots \\ \vdots & & & \\ s_{N1} & \cdots & & s_{NN} \end{bmatrix} \begin{bmatrix} a_1 \\ a_2 \\ \\ a_N \end{bmatrix} \tag{1.14}$$

A specific element of [S] matrix is defined as

$$s_{i,j} = b_i / a_j \Big|_{a_k = 0 \, for \quad k \neq j} \tag{1.15}$$

A vector network analyzer is mostly used to measure the scattering parameters. A vector network analyzer is basically a four-channel microwave receiver that processes the amplitude and phase of the transmitted and reflected waves from a microwave network.

A vector network analyzer generally includes three sections: RF source and test set, IF processing, and digital processing. To measure the scattering parameters of a DUT, RF source sweep over a specific bandwidth, the four-port reflectometer samples the incident, reflected and transmitted RF waves, and a switch allows the network to be driven from either ports of DUT.

1.2 MICROWAVE CIRCUITS DESIGN TECHNOLOGIES

1.2.1 Microwave Transmission Lines

Transmission lines are the main passive elements in microwave circuit design. They are used to transmit the signals and to realize the passive microwave circuits such as directional couplers, quadrature hybrids, and filters. A transmission line is defined with characteristics impedance, Z_0, and electrical length $\theta = \beta_g l$, where $\beta_g = 2\pi\sqrt{\varepsilon_{eff}}/\lambda$ is the propagation constant through the transmission line, ε_{eff} is the effective dielectric constant of the line, λ is the free space wavelength, and l is the physical length of the transmission line.

The common transmission lines in integrated microwave circuits are stripline microstrip lines, slot lines, and coplanar lines [3]. Figure 1.4 shows some types of transmission lines.

The two-port scattering parameter of a matched lossless transmission line with electrical length θ is obtained as

$$\begin{bmatrix} b_1 \\ b_2 \end{bmatrix} = \begin{bmatrix} 0 & e^{-j\theta} \\ e^{-j\theta} & 0 \end{bmatrix} \begin{bmatrix} a_1 \\ a_2 \end{bmatrix} \tag{1.16}$$

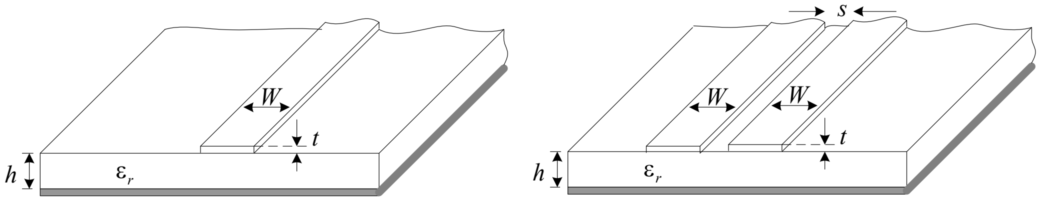

Microstrip

Microstrip – coupled lines

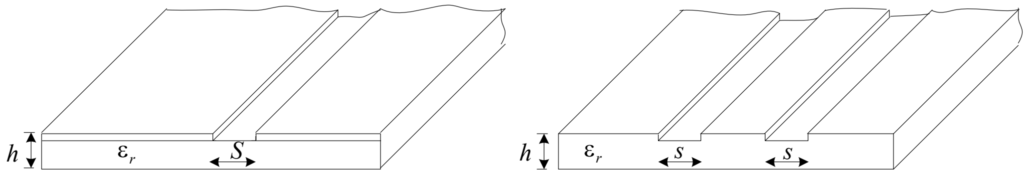

Slotline

Coplanar – Waveguide

Figure 1.4 Different microwave transmission lines.

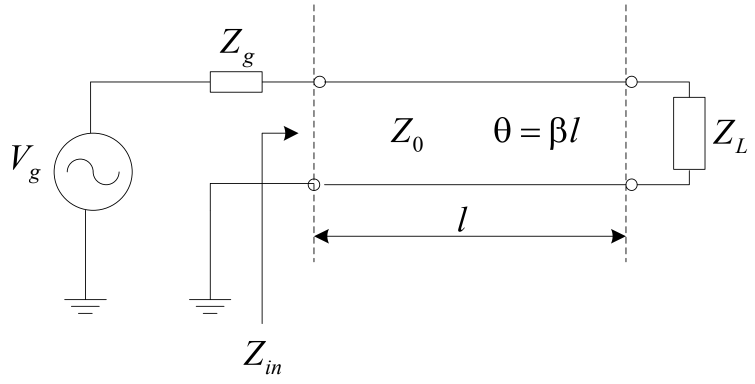

Figure 1.5 A terminated transmission line.

In practice, a transmission line is terminated to a load. A terminated transmission line is shown in Figure 1.5. Let us assume that the load impedance is Z_L, the physical length and the characteristic impedance of the transmission line l, Z_0, respectively. By use of the classic transmission lines theory, it can be shown that the input impedance of a lossless terminated transmission line is obtained as [1]

$$Z_{in} = Z_0 \frac{Z_L + jZ_0 \tan(\beta l)}{Z_0 + jZ_L \tan(\beta l)} \tag{1.17}$$

1.2.2 Microwave Passive Circuits

A microwave subsytem includes transmission lines, passive circuits, and active devices. The passive circuits are the key sections in microwave signal processing. These circuits are usually realized using transmission lines and lump elements. In this section, some microwave passive circuits, which are commonly used in microwave signal processing and multiport architectures, are explained.

Wilkinson Power Divider A Wilkinson power divider is shown in Figure 1.6. This divider is used to in-phase split the power. Although this circuit can be used for arbitary power division, the equal split power divider (3 dB) is more common. This divider is often made in microstrip or stripline. The scattering parameter of an ideal Wilkinson power divider can be shown as

$$[S] = \begin{bmatrix} 0 & -j/\sqrt{2} & -j/\sqrt{2} \\ -j/\sqrt{2} & 0 & 0 \\ -j/\sqrt{2} & 0 & 0 \end{bmatrix} \tag{1.18}$$

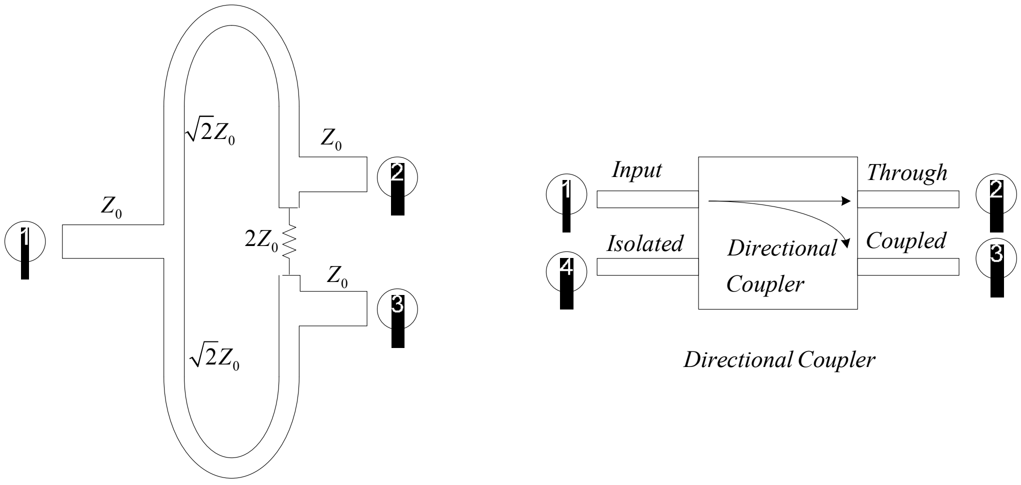

Directional Coupler

Wilkinson Power Divider

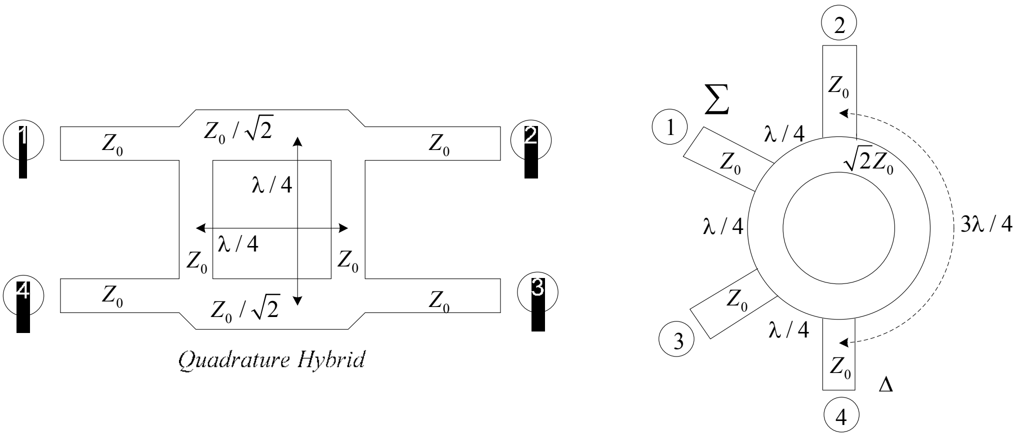

Quadrature Hybrid

Rat-Race Coupler

Figure 1.6 Some microwave passive circuits.

Directional Coupler A directional coupler is a four-port circuit matched at all ports. The scattering matrix of a symmetrical direction coupler is as

$$[S]=\begin{bmatrix} 0 & \alpha & j\beta & 0 \\ \alpha & 0 & 0 & j\beta \\ j\beta & 0 & 0 & \alpha \\ 0 & j\beta & \alpha & 0 \end{bmatrix} \tag{1.19}$$

where the amplitudes α and β are related as

$$\alpha^2+\beta^2=1 \tag{1.20}$$

According to (1.18), power supplied to port 1 is coupled to port 3 (the coupled port) with the coupling factor $|s_{13}|^2 = \beta^2$, while the reminder of the input power is delivered to port 2 (the through port) with the coefficient $|s_{12}|^2 = \alpha^2 = 1 - \beta^2$. In an ideal directional coupler, no power is delivered to port 4 (the isolated port). The following relations are generally used to characterize a directional coupler [1]:

$$Coupling = C = 10\log\frac{P_1}{P_3} = -20\log\beta \quad \text{dB} \tag{1.21a}$$

$$Directivity = D = 10\log\frac{P_3}{P_4} = 20\log\frac{\beta}{|s_{14}|^2} \quad \text{dB} \tag{1.21b}$$

$$Isolation = I = 10\log\frac{P_1}{P_4} = -20\log|s_{14}|^2 \quad \text{dB} \tag{1.21c}$$

Quadrature Hybrid Couplers Hybrid couplers are special cases of direction couplers, where the coupling factor is 3 dB. A hybrid coupler is shown in Figure 1.6. The qudrature hybrid has a 90 degree phase shift between ports 2 and 3 when fed at port 1. The scattering matrix for a quadrature coupler is as

$$[S] = \frac{1}{\sqrt{2}}\begin{bmatrix} 0 & 1 & j & 0 \\ 1 & 0 & 0 & j \\ j & 0 & 0 & 1 \\ 0 & j & 1 & 0 \end{bmatrix} \tag{1.22}$$

Rat-Race Couplers A rat-race coupler, shown in Figure 1.6, has a 180 degree phase difference between port 2 and 3 when fed at port 4. The scattering matrix of a rat-race coupler is

$$[S] = \frac{1}{\sqrt{2}}\begin{bmatrix} 0 & 1 & 1 & 0 \\ 1 & 0 & 0 & -1 \\ 1 & 0 & 0 & 1 \\ 0 & -1 & 1 & 0 \end{bmatrix} \tag{1.23}$$

The microwave circuits commonly use the passive circuits including transmission lines, couplers, lumped elements, and resonators. Table 1.1 shows the different uses of microwave passive technologies.

Table 1.1
Passive Circuit Technologies

Application Versus Devices	*Matching Circuits*	*Signal Filtering*	*Signal/ Dividing/ Combining*	*Device Biasing*	*Impedance Transformer*	*Phase Transformer*
Transmission Lines	High	High	High	High	High	High
Coupled Lines	Low	Moderate	High	Low	Low	High
Lumped Elements	Yes (Low freq.)	Moderate (Low freq.)	Low	High	Low	No
Hybrid Couplers	No	Low	High	No	Low	Yes
Discontinuities	High	High	Low	Yes	Low	No
Resonators	Moderate	High	No	No	No	No

1.2.3 Fabrication Technologies

Microwave and RF passive and active circuits are realized by use of transmission lines, microwave passive circuits, and solid state devices. Moreover, the wireless and microwave systems demand smaller size, lighter weight, and lower cost. Microwave solid state devices are an integral part of technology advancement using different fabrication technologies. The modern microwave circuits are usually fabricated by the use of microwave integrated circuits (MIC) monolithic hybrid microwave integrated circuits (MHMIC), and monolithic microwave integrated circuits (MMIC)

1.2.3.1 Microwave Solid State Devices

The microwave solid state devices are generally categorized into two main groups: microwave diodes and microwave transistors. The microwave diodes have different applications in microwave systems including detecting, mixing, switching, and oscillating. A Schottky diode is usually used for mixing and detection applications, while for attenuation and switching applications, a PIN diode usually is recommended.

In varactor diode, the nonlinear behavior of the PN junction capacitance is used. Varactor diodes are commonly used for resonance phase shifting applications. A Gunn diode is a negative resistance device and its power properties depend on the behavior of bulk semiconductor rather than junction. The main application of this device is in designing oscillators.

On the other hand, the microwave transistors are the key devices to realize microwave active circuits. The various types of transistors that find their use in microwave applications are bipolar junction transistors (BJT) field effect transistors (FET), metal-semiconductor field effect transistors (MESFET), heterojunction bipolar transistor (HBT), and high electron mobility transistors (HEMT). Table 1.2 summarizes the different applications of microwave diodes and transistors.

Table 1.2

Active Device Technologies

Application Versus Devices	*Signal Amplification*	*Signal Generation*	*Frequency Multiplication*	*Frequency Conversion*	*Modulation and RF Signal Processing*	*Signal Detection*
Transistors	High	Moderate	Moderate	High	Low	Low
Schottky Diodes	No	No	Low	Low	Low	High
Varactor Diodes	No	Moderate	Moderate	No	High	No
PIN Diodes	No	No	No	No	High	No
SRD Diodes	No	No	High	No	No	No
IMMPATT and GUNN Diodes	No	High (millimeter wave)	No	No	No	No

1.2.3.2 MIC Technology

In this technology, the discrete solid-state devices and passive components are mounted on a dielectric substrate. Then, they are connected to the passive circuits using transmission lines on the same substrate. The matching circuits are generally realized using distributed design. The substrate is commonly selected from plastic lossless materials such as RT-Duroid. The circuit size is large in this technology, but it is realized in low cost. This technology is useful to implement the circuits with operating frequency less than 20 GHz. A power amplifier, which is realized in MIC technology, is shown in Figure 1.7.

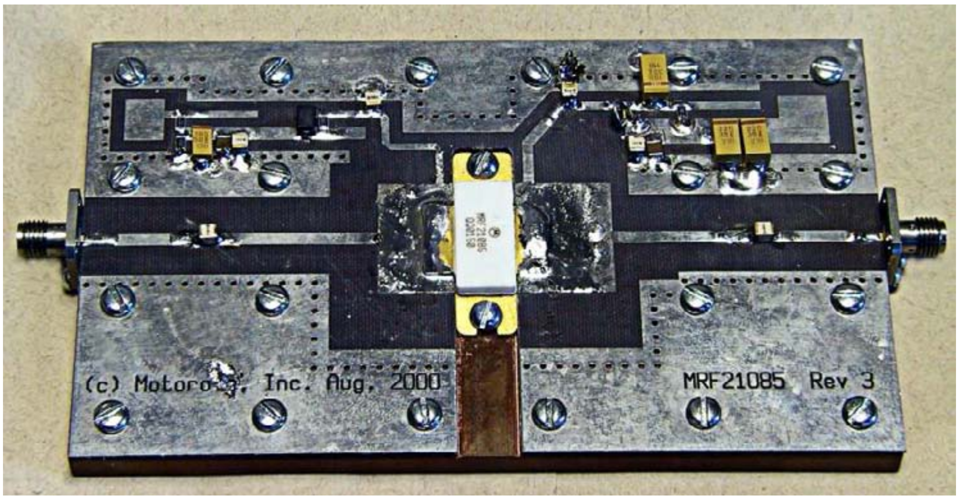

Figure 1.7 A power amplifier in MIC technology.

1.2.3.3 MHMIC Technology

In MHMIC technology, the substrate is usually alumina due to its high permittivity (about 10) and very low loss. The chip devices and circuits are used in this technology and the matching is realized using both distributed and lumped designs. The circuit size in this technology is small and its cost is moderate. This technology can be used to realize microwave circuits up to 50 GHz. A typical circuit fabricated using MHMIC technology is shown in Figure 1.8.

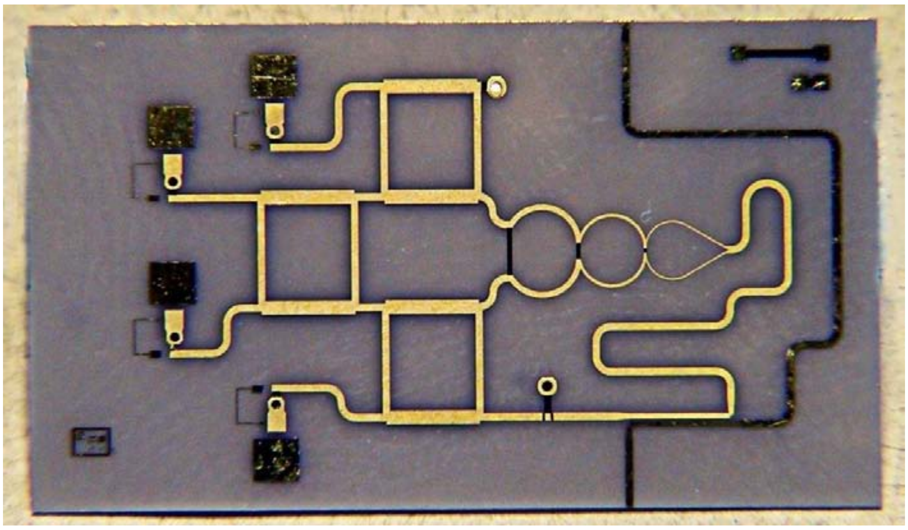

Figure 1.8 A six-port junction with integrated power detectors in MHMIC technology.

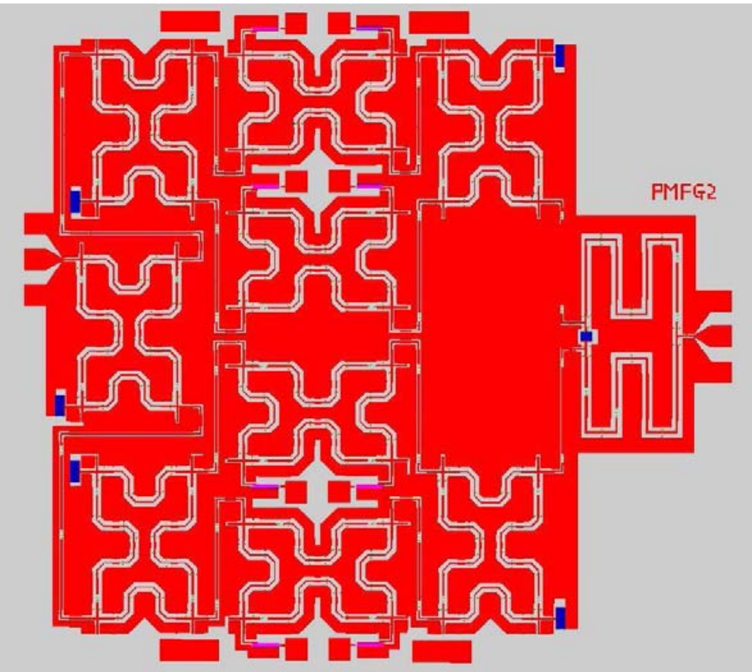

Figure 1.9 A Ku band I-Q vector modulator using CPW transmission line in MMIC.

1.2.3.4 MMIC Technology

In MMIC, by use of silicon, GaAs, or SiGe fabrication processes, the active devices are fabricated on substrate and passive devices are printed on substrate. The matching circuits are on-chip lumped or distributed. The circuit size is very small and the cost for high volume is low. The power handling in this technology is medium. The technology can efficiently be used in microwave and millimeter-wave circuits up to 100 GHz. A six-port junction designed with an MMIC technology and using coplanar waveguide transmission line is shown in Figure 1.9.

1.3 SIX-PORT CIRCUITS

1.3.1 Microwave Network Measurements

The microwave and wireless technology are founded based on microwave network measurements. A microwave network analyzer consists of a computer controlled automated measurement setup including a synthesizer source, a test-set, a receiver, and processing and display units. The network analyzer contains the required directional couplers and switches to measure one- or two-port networks. The main block of a vector network analyzer is shown in Figure 1.10. The full [S] parameters matrix measurement of a two-port requires two different setups [4]. The basic network analyzer has a synthesized RF source with Z_0 output impedance (characteristic and line impedance) and three RF input ports.

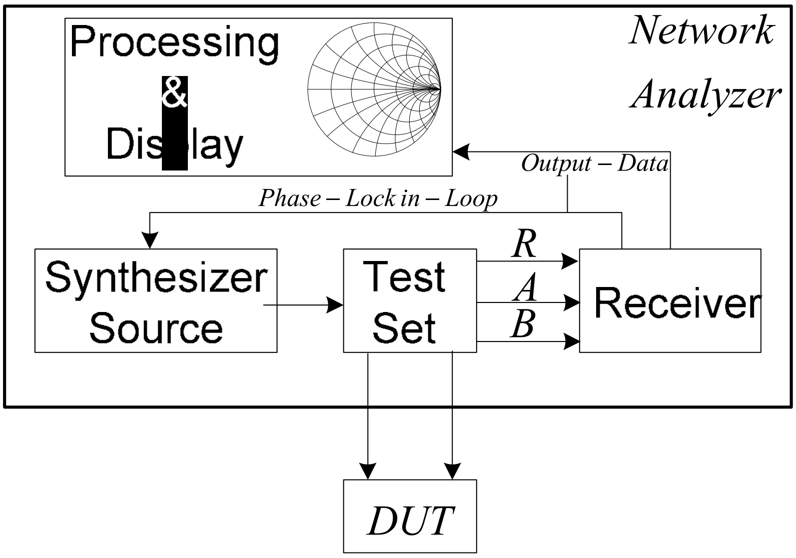

Figure 1.10 Block diagram of a vector network analyzer.

From these three ports, port R (reference) is used to measure the incident voltage of the applied RF signal, and the other two measure incident and reflected waves. The reflection in port 1 , s11, and the forward scattering parameters of a two-port, s21, are determined by using the setup of Figure 1.11(a).The direction couplers have Z_0 characteristic impedances. Accordingly, they present Z_0 terminations to the two-port that includes the device under test (DUT). The reflection in port 1 is computed from the complex ratio of b_1 / a_1. The forward transmission from the source to the load is computed using b_2 / a_1.

The reflection in port 2, s22, and the reverse transmission parameter, s12, are measured using Figure 1.11(b). In this setup the signal is applied to the output port while terminating the input port of the DUT with Z_0 through coupler 1. The reflection of the output port is obtained by the ratio of b_2 / a_2. The reverse transmission is computed from b_1 / a_2. The computerized storage and use of calibration data permit one to realize accurate and de-embedded measurements up to the device access ports.

A key element in the implementation of vector network analyzer (VNA) is a detection system that provides both amplitude and phase responses. The detection section is conventionally realized using heterodyne architecture involving multiple frequency conversion and the associated local oscillators. These components make the measurement system relatively complex and costly. However, a heterodyne VNA generally provides a better dynamic range compared to a homodyne VNA six-port network analyzer, which is described in Chapter 5. The source-pull and load-pull measurement techniques using six-port VNA are discussed in Chapter 6.

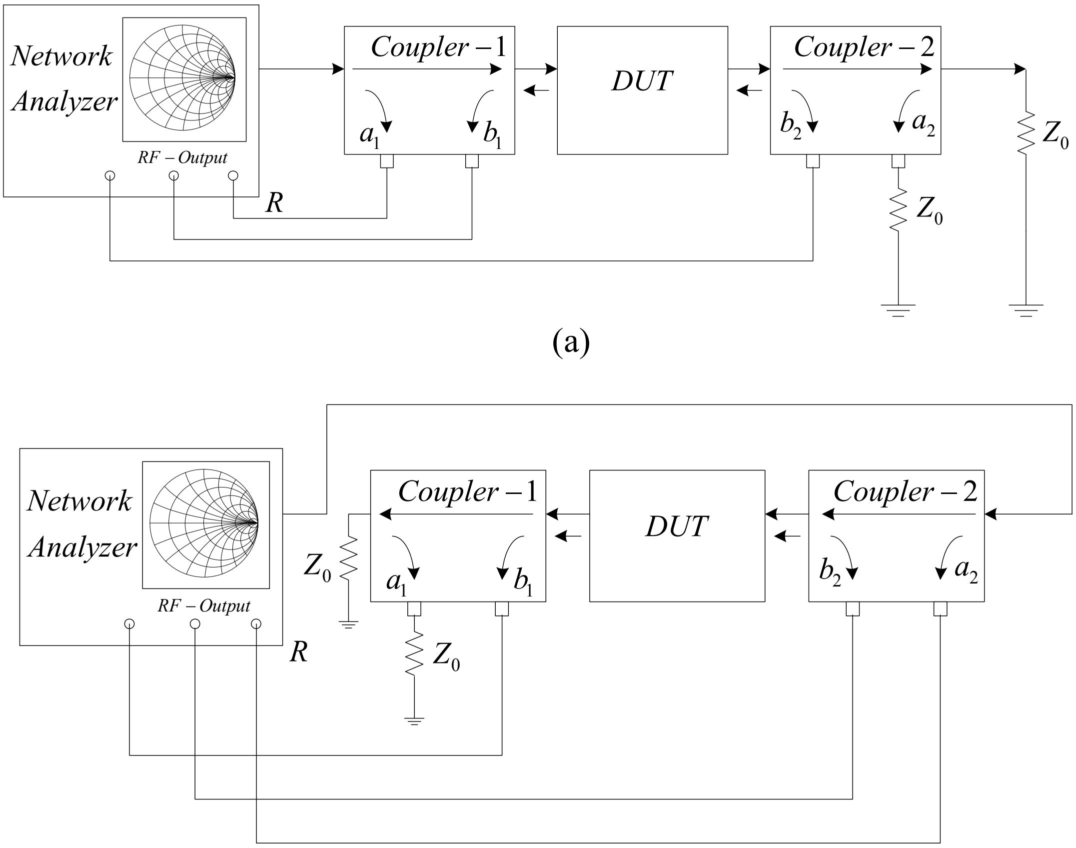

(a)

(b)

Figure 1.11 (a) The forward scattering parameters measurement using a network analyzer $s_{11} = b_1 / a_1|_{a_2=0}$ and $s_{21} = b_1 / a_1|_{a_2=0}$. (b) The reverse scattering parameters measurement using a network analyzer $s_{22} = b_2 / a_2|_{a_1=0}$ and $s_{12} = b_2 / a_2|_{a_1=0}$.

The six-port technique, on the other hand, provides a low-cost measurement of both amplitude and phase by the use of additional detectors. Moreover, the six-port, in addition to network parameters, has potential to perform power measurements. The name six-port is originally extracted from the associated network where four of the ports are terminated by these power detectors, while the remaining two ports provide a connection to the signal source and testport [5].

By use of the six-port, it is possible to make simultaneous power flow and impedance measurements using only amplitude measurements while no phase measurements are required. The use of one or two six-ports in conjunction with an appropriate test-set and calibration procedure can lead to the determination of the four scattering parameters of any two-port DUT [6]. The general block diagram of an automated network analyzer is shown in Figure 1.12.

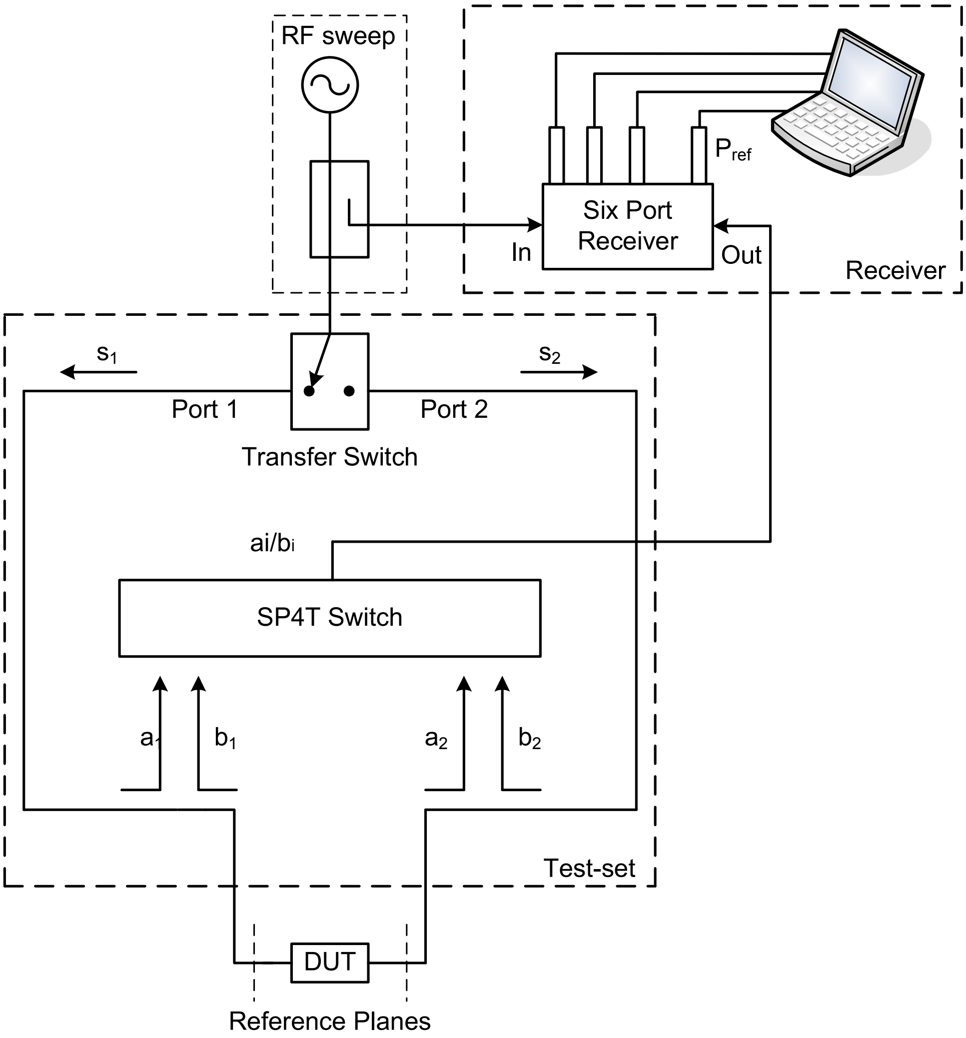

Figure 1.12 A six-port automated network analyzer.

1.3.2 Wireless Applications

There is an increasing demand to have the lower complexity and less power consumption in the design of the wireless terminals. Further, wideband, compact size, and low-cost digital transceivers are required to expand the mobile and wireless communications. Recently, some direct-conversion transceivers based on six-port technology were proposed and studied [7, 8]. Using a six-port homodyne technique is interesting due to the use of power detectors instead of mixers, which provided simpler circuits in comparison to six-port heterodyne technique. The advantages of such an approach are manifold. First of all, the broadband specifications can be easily obtained by passive elements. Moreover, they have very low power consumption. In addition, six-port homodyne hardware architecture is proposed as a means to avoid more costly transceivers [9]. The block diagram of a six-port receiver is shown in Figure 1.13.

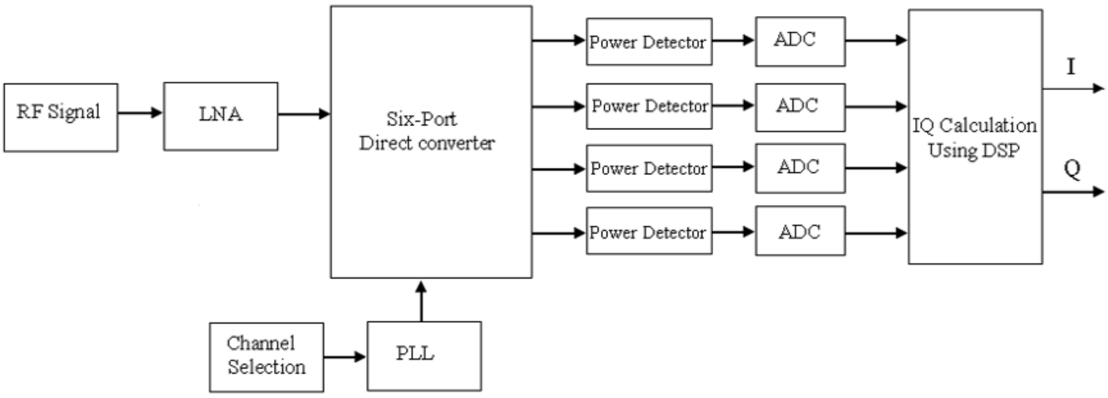

Figure 1.13 Direct conversion receiver based on six-port.

The main advantage of the six-port is the extremely large frequency bandwidth of the RF circuit. The other advantage of the six-port system is similar to that of the zero-intermediate frequency (IF) mixer based receiver (i.e., one local oscillator and no image rejection filter). The six-port transceiver architectures introduce various applications including software defined radio (SDR), ultra wideband system (UWB), and millimeter-wave [10–12].

Six-port has attracted much attention as a low-cost transceiver in new wireless standards. Recently, a six-port transceiver was implemented using CMOS technology in 60 GHz [13]. The target is to provide a very low-cost, miniaturized, and low DC power consumption transceiver for IEEE 802.15 applications. It is shown that the total DC power consumption of the transceiver is less than 100 mW. The wireless applications of six-port technology are extensively discussed in Chapter 7.

1.3.3 Microwave Applications

The six-port technique has great potential in microwave applications where measuring the phase and amplitude of a microwave signal is required. A common application is the reflectometer where the reflection coefficient of device under test (DUT) is measured [5]. The directional finding of the received waveform is the other application where a six-port may be used as a wave correlated [14].

The six-port application in radar is shown in Figure 1.14. This technology has attracted attention to realize low-cost and high performance radar, especially in the automobile industry [15]. Moreover, antenna measurement, including the near-field and polarization measurement, can be achieved using six-port technology.

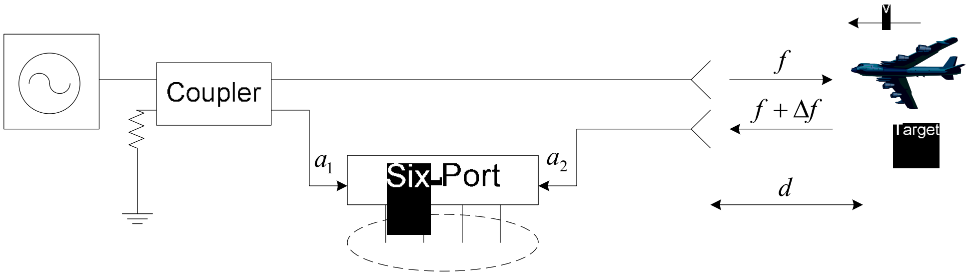

Figure 1.14 Block diagram of a six-port radar system.

The material characterization, especially in high power applications, is a very interesting use of this technology [16]. Moreover, there are recently some applications to use the six-port architecture in optical systems [17]. The microwave applications of six-port systems are presented in Chapter 8.

References

[1] Pozar, D. M., *Microwave Engineering*, Third Edition, New York: John Wiley & Sons, 2005.

[2] Vendelin, G. D., A. M. Pavio, and U. L. Rohde, *Microwave Circuit Design Using Linear and Nonlinear Techniques,* Second Edition, New York: Wiley-Interscience, 2005.

[3] Maloratsky, L. G., *Passive RF & Microwave Integrated Circuits*, New York: Elsevier, 2004.

[4] Besser, L., and R. Gilmore, *Practical RF Circuit Design for Modern Wireless Systems*, Volume 1, Norwood, MA: Artech House, 2003.

[5] Engen, G. F., *Microwave Circuit Theory and Foundation of Microwave Metrology*, IEE Electrical Measurement Series 9, London: Peter Peregrinus Ltd., 1992.

[6] Ghannouchi, F. M., Y. Xu, and R. G. Bosisio, "A One-Step Connection Method for the Measurement of N-Port Microwave Networks Using Six Port Techniques," *IEE Proceedings Part-H. Microwave, Antenna & Propagation,* Vol. 141, No. 4, pp. 285–289, August 1994.

[7] Bosisio, R.G., Y. Y. Zhao, X. Y. Xu, S. Abielmona, E. Moldovan, Y. S. Xu, M. Bozzi, S. O. Tatu, J. F. Frigon, C. Caloz, and K. Wu, "New-Wave Radio," *IEEE Microwave Magazine,* pp. 89–100, February 2008.

[8] Luo, B., and M. Y. W. Chia, "Performance Analysis of Serial and Parallel Six-Port Modulators," *IEEE Trans. Microwave Theory & Tech.,* Vol. 56, No. 9, September 2008.

[9] Boulejfen, N., F. M. Ghannouchi, and A. B. Kouki, "A Homodyne Multiport Network Analyzer for S-Parameter Measurements of Microwave N-Port Circuits/Systems," *Microwave & Optical Technology Letters*, Vol. 24, No.1, pp. 63–67, January 2000.

[10] Mohajer, M., A. Mohammadi, and A. Abdipour, "Direct Conversion Receivers Using Multi-Port Structures for Software Defined Radio Systems," *IET Microwaves, Antennas & Propagation*, Vol. 1, No. 2, pp. 363–372, April 2007.

[11] Zhao, Y., J. F. Frigon, K.Wu, and R. G. Bosisio, "Multi(Six)-Port Impulse Radio for Ultra-Wideband," *IEEE Trans. Microwave Theory & Tech.*, Vol. 54, No. 4, pp. 1707–712, June 2006.

[12] Mirzavand, R., A. Mohammadi, and A. Abdipour, "Low-Cost Implementation of Broadband Microwave Receivers in Ka Band Using Multi-Port Structures," *IET Microwaves, Antennas & Propagation*, Vol. 3, No. 3, pp. 483–491, 2009.

[13] Wang, H., K. Lin, Z. Tsai, L. Lu, H. Lu, C. Wang, J. Tsai, T. Huang, and Y. Lin, "MMICs in the Millimeter-Wave Regime," *IEEE Microwave Magazine,* pp. 99–117, February 2009.

[14] Yakabe, T., F. Xiao, K. Iwamoto, F. M. Ghannouchi, K. Fujii, and H. Yabe, "Six-Port Based Wave-Correlator with Application to Beam Direction Finding," *IEEE Trans. on Instrumentation and Measurements*, Vol. 50, No. 2, pp. 377–380, April 2001.

[15] Miguelez, C. G., B. Huyart, E. Bergeault, and L. P. Jallet, "A New Automobile Radar Based on the Six-Port Phase/Frequency Discriminator," *IEEE Trans. Vehicular Tech.*, Vol. 49, No. 4, pp. 1416–1423, July 2000.

[16] Caron, M., A. Akyel, and F. M. Ghannouchi, "A Versatile Easy to Do Six-Port Based High Power Reflectometer," *Journal of Microwave Power and Electromagnetic Energy,* Vol. 30, No. 4, pp. 23–239, 1995.

[17] Fernandez, I. M., J. G. Wanguemert-Pérez, A. O. Monux, R. G. Bosisio, and K. Wu, "Planar Lightwave Circuit Six-Port Technique for Optical Measurements and Characterizations," *Journal of Lightwave Technology,* Vol. 23, No. 6, pp. 2148–2157, June 2005.

Chapter 2

Six-Port Fundamentals

The basic work related to the six-port technique was carried out in the 1970s primarily by Engen and Hoer [1–4]. Since that time, many researchers have been involved in six-port measurement techniques from the theoretical side as well as the experimental side [5–14]. The main advantage of this technique is its capability to make impedance measurement and network analysis using only scalar measurements such as power or voltage measurement. No phase measurements are required; hence, no frequency downconversion is needed for the measurements. This simplifies a lot the hardware requirements and reduces the cost of the equipment. In addition, the six-port technique can be used to make multiport measurements and can also be used for power measurements. In this chapter, the fundamentals of the six-port technique and the analysis and the modeling of the six-port reflectometer are presented. Some practical considerations are also discussed.

2.1 ANALYSIS OF SIX-PORT REFLECTOMETERS

A six-port reflectometer is generally composed of an arbitrary, time-stationary, linear, and passive microwave six-port junction, where four ports are fitted with power detectors, D3, D4, D5 and D6, with port 1 connected to a microwave source and port 2 to the device under test (DUT), as shown in Figure 2.1. a_i and $\boldsymbol{b}_i$, i = 1, 2, ..., and 6, are the incident and reflected normalized voltages at the sixth terminal of the six-port junction. The a_i and $\boldsymbol{b}_i$ are related through the scattering parameters of the six-port junction as follows:

$$\underline{\mathbf{b}} = \mathbf{S}\underline{\mathbf{a}} \tag{2.1}$$

where S is a (6×6) complex matrix, $\underline{\mathbf{b}} = (b_1, b_2, ..., b_6)$ and $\underline{\mathbf{a}} = (a_1, a_2, ..., a_6)$. Let's designate the reflection coefficient of the power detector D$_i$ by Γ_i , such as:

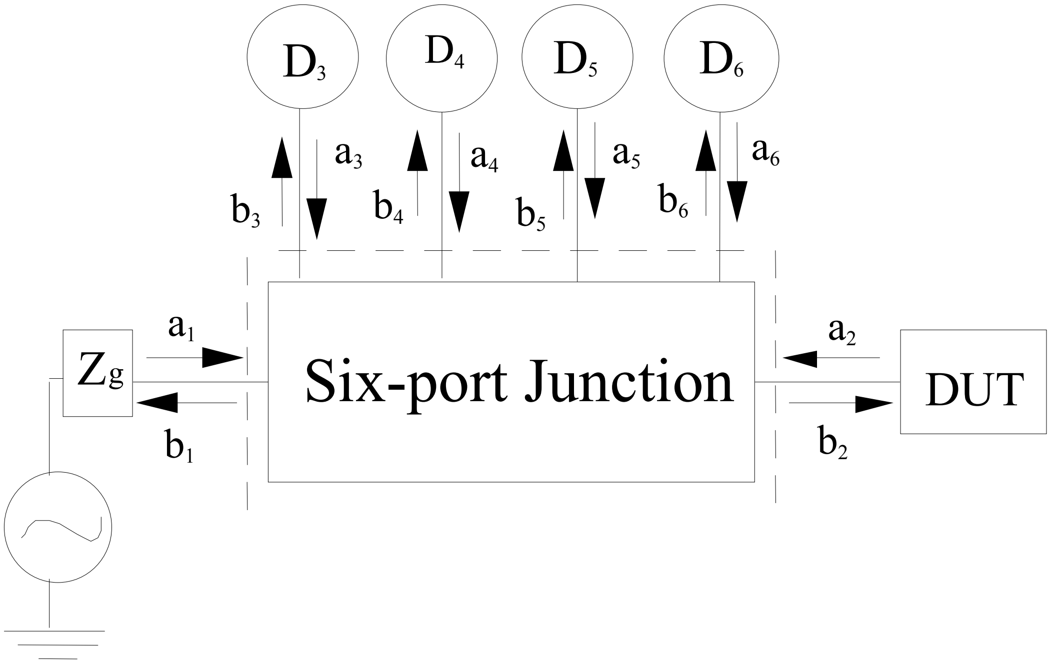

Figure 2.1 A six-port reflectometer.

$$\Gamma_i = \frac{a_i}{b_i}, \ i = 3, 4, 5, \text{and } 6 \tag{2.2}$$

by substituting (2.2) into (2.1) and after algebraic manipulations, one can obtain

$$\begin{bmatrix} b_1 \\ b_2 \\ 0 \\ 0 \\ 0 \\ 0 \end{bmatrix} = \begin{bmatrix} s_{11} & s_{12} & s_{13}\Gamma_3 & s_{14}\Gamma_4 & s_{15}\Gamma_5 & s_{16}\Gamma_6 \\ s_{21} & s_{22} & s_{23}\Gamma_3 & s_{24}\Gamma_4 & s_{25}\Gamma_5 & s_{26}\Gamma_6 \\ s_{31} & s_{32} & (s_{33}\Gamma_3 - 1) & s_{34}\Gamma_4 & s_{35}\Gamma_5 & s_{36}\Gamma_6 \\ s_{41} & s_{42} & s_{43}\Gamma_3 & (s_{44}\Gamma_4 - 1) & s_{45}\Gamma_5 & s_{46}\Gamma_6 \\ s_{51} & s_{52} & s_{53}\Gamma_3 & s_{54}\Gamma_4 & (s_{55}\Gamma_5 - 1) & s_{56}\Gamma_6 \\ s_{61} & s_{62} & s_{63}\Gamma_3 & s_{64}\Gamma_4 & s_{65}\Gamma_5 & (s_{66}\Gamma_6 - 1) \end{bmatrix} \begin{bmatrix} a_1 \\ a_2 \\ b_3 \\ b_4 \\ b_5 \\ b_6 \end{bmatrix} \tag{2.3}$$

the solution of the last matrix equation given the following:

$$a_1 = m_{11}b_1 + m_{12}b_2 \tag{2.4a}$$

$$a_2 = m_{21}b_1 + m_{22}b_2 \tag{2.4b}$$

and

$$b_i = m_{i1}b_1 + m_{i2}b_2,\ i = 3, 4, 5, \text{ and } 6 \tag{2.5}$$

where m_{ij} are the entries of the inverse of the (6×6) matrix introduced in (2.3). The reflection coefficient of the DUT connected to port 2 of the six-port junction is:

$$\Gamma = \frac{a_2}{b_2} \tag{2.6}$$

By substituting (2.6) into (2.5) and by using (2.4), one can obtain

$$b_i = h_i\left(\Gamma + \frac{k_i}{h_i}\right)b_2 = h_i\left(\Gamma - q_i\right)b_2,\ i = 3, 4, 5, \text{ and } 6 \tag{2.7}$$

where

$$h_i = \frac{m_{i1}}{m_{21}}\ ,\ k_i = m_{i2} - \frac{m_{22}m_{i1}}{m_{21}}, \text{ and } q_i = -\frac{k_i}{h_i} \tag{2.8}$$

The net absorbed power by the power detector D$_i$ can be calculated as follows:

$$\begin{aligned} P_i &= \nu_i\left(\left|b_i\right|^2 - \left|a_i\right|^2\right) \\ P_i &= \nu_i\left(1 - \left|\Gamma_i\right|^2\right)\left|h_i\right|^2\left|\Gamma - q_i\right|^2\left|b_2\right|^2 = \alpha_i^2\left|\Gamma - q_i\right|^2\left|b_2\right|^2 \end{aligned} \tag{2.9}$$

where ν_i is a scalar parameter that characterizes the detector and

$$\alpha_i = \left|h_i\right|\sqrt{\nu_i\left(1 - \left|\Gamma_\text{i}\right|^2\right)},\ \text{with } i = 3, 4, 5, \text{ and } 6 \tag{2.10}$$

Equation (2.9) is a quadratic equation that relates each power reading to the reflection coefficient Γ of the DUT. This equation constitutes the starting point of any calibration technique. It is important to remember that this equation is obtained for a time-stationary, passive, and linear six-port junction and no constraints are stated for the generator's internal impedance and the input impedance of the power detectors.

In the case where the power detectors are perfectly matched to the output ports of the six-port junction $(\Gamma_i = 0)$, q_i point values can be directly calculated using the S parameters of the six-port junction. In such situations, one can write:

$$b_2 = s_{21}a_1 + s_{22}a_2 \tag{2.11}$$

and

$$b_i = s_{i1}a_1 + s_{i2}a_2\,; \quad i = 3, 4, 5, \text{and } 6 \tag{2.12}$$

Knowing that $a_2 = \Gamma b_2$ and eliminating a_1 from (2.12) by using (2.11), and after identification with (2.7), one can deduce that

$$h_i = \frac{s_{i2}s_{21} - s_{22}s_{i1}}{s_{21}} \text{ and } q_i = \frac{s_{i1}}{s_{22}s_{i1} - s_{i2}s_{21}} \tag{2.13}$$

2.2 LINEAR MODEL

Equation (2.9) can be expanded in a linear manner and grouped in matrix format as follows:

$$\underline{\mathbf{P}} = \begin{bmatrix} P_3 \\ P_4 \\ P_5 \\ P_6 \end{bmatrix} = |b_2|^2 \begin{bmatrix} \alpha_3^2|q_3|^2 & \alpha_3^2 & -\alpha_3^2 q_3^* & -\alpha_3^2 q_3 \\ \alpha_4^2|q_4|^2 & \alpha_4^2 & -\alpha_4^2 q_4^* & -\alpha_4^2 q_4 \\ \alpha_5^2|q_5|^2 & \alpha_5^2 & -\alpha_5^2 q_5^* & -\alpha_5^2 q_5 \\ \alpha_6^2|q_6|^2 & \alpha_6^2 & -\alpha_6^2 q_6^* & -\alpha_6^2 q_6 \end{bmatrix} \begin{bmatrix} 1 \\ |\Gamma|^2 \\ \Gamma \\ \Gamma^* \end{bmatrix} \tag{2.14}$$

Knowing that $\text{Re}(\Gamma) = 1/2\left(\Gamma + \Gamma^*\right)$ and $\text{Im}(\Gamma) = j/2\left(\Gamma - \Gamma^*\right)$, one can write:

$$\underline{\mathbf{\Gamma}} = \begin{bmatrix} 1 \\ |\Gamma|^2 \\ \text{Re}(\Gamma) \\ \text{Im}(\Gamma) \end{bmatrix} = \begin{bmatrix} 1 & 0 & 0 & 0 \\ 0 & 1 & 0 & 0 \\ 0 & 0 & 1/2 & 1/2 \\ 0 & 0 & -j/2 & j/2 \end{bmatrix} \begin{bmatrix} 1 \\ |\Gamma|^2 \\ \Gamma \\ \Gamma^* \end{bmatrix} \tag{2.15}$$

By introducing (2.15) into (2.14), one can obtain the following equation [5]:

$$\underline{\mathbf{P}} = |b_2|^2 \begin{bmatrix} \alpha_3^2|q_3|^2 & \alpha_3^2 & -2\alpha_3^2\mathrm{Re}(q_3) & -2\alpha_3^2\mathrm{Im}(q_3) \\ \alpha_4^2|q_4|^2 & \alpha_4^2 & -2\alpha_4^2\mathrm{Re}(q_4) & -2\alpha_4^2\mathrm{Im}(q_4) \\ \alpha_5^2|q_5|^2 & \alpha_5^2 & -2\alpha_5^2\mathrm{Re}(q_5) & -2\alpha_5^2\mathrm{Im}(q_5) \\ \alpha_6^2|q_6|^2 & \alpha_6^2 & -2\alpha_6^2\mathrm{Re}(q_6) & -2\alpha_6^2\mathrm{Im}(q_6) \end{bmatrix} \underline{\mathbf{\Gamma}} = \rho \mathbf{C} \underline{\mathbf{\Gamma}} \qquad (2.16)$$

Where $\rho = |b_2|^2$ and **C** is a (4×4) real matrix which characterize the six-port reflectometer.

Using (2.16), one can easily deduce that

$$\underline{\mathbf{\Gamma}} = \frac{1}{\rho}\mathbf{C}^{-1}\underline{\mathbf{P}} = \frac{1}{\rho}\mathbf{X}\underline{\mathbf{P}} \qquad (2.17)$$

The q_i point values can be directly calculated using the entries of matrix **C** as follows:

$$q_i = \frac{c_{i3} + jc_{i4}}{-2c_{i2}} \qquad (2.18)$$

We can assume that the six-port junction has q_i point position values in such a way that the determinant of **C** is not equal to zero. Therefore, the real and imaginary parts of the complex reflection coefficient can be deduced as follows:

$$\mathrm{Re}(\Gamma) = \frac{\sum_{j=1}^{4} x_{3j} P_{j+2}}{\sum_{j=1}^{4} x_{1j} P_{j+2}} \qquad (2.19a)$$

$$\mathrm{Im}(\Gamma) = \frac{\sum_{j=1}^{4} x_{4j} P_{j+2}}{\sum_{j=1}^{4} x_{1j} P_{j+2}} \qquad (2.19b)$$

where x_{ij} are the entries of the matrix **X**. Equation (2.19) automatically accounts for the fact that the measurement of the reflection coefficient of a linear DUT is power independent. The power flow exciting the DUT is:

$$\rho = \sum_{j=1}^{4} x_{1j} P_{j+2} \tag{2.20}$$

The normalization of all entries of matrix **X** by x_{11} does not affect the above formalism; thus, (2.17) is still valid for the calculation of Γ. In the above formalism, eleven linearly independent real parameters are sufficient to model the six-port reflectometer. These parameters have to be determined in advance using an appropriate calibration technique.

2.3 QUADRATIC MODEL

It was shown for an arbitrary six-port reflectometer so that the power readings at the four detection ports of the six-port junction are:

$$P_i = \alpha_i^2 \left|\Gamma - q_i\right|^2 \left|b_2\right|^2,\ i = 3,\ 4,\ 5,\ \text{and } 6 \tag{2.21}$$

By normalizing P_4, P_5 and P_6 by P_3, one can obtain three power independent equations

$$P_i = \frac{P_i}{P_3} = \mu_\mathrm{i}^2 \left|\frac{\Gamma - q_i}{\Gamma - q_3}\right|^2,\ i = 4,\ 5,\ \text{and } 6 \tag{2.22}$$

where

$$\mu_i = \frac{\alpha_i}{\alpha_3} \tag{2.23}$$

From (2.22), it can be deduced that 11 real and independent parameters are needed to completely model the six-port reflectometer. In addition, it can be seen that Γ is the solution of a set of three quadratic equations.

Equation (2.22) is a circle equation that can alternatively be written in the following format [15]:

$$R_i^2 = \left|\Gamma - Q_i\right|^2 \qquad i = 4, 5, \text{ and } 6 \tag{2.24}$$

where the center and the radius of the circles in the Γ plane are, respectively:

$$Q_i = \frac{\dfrac{p_i}{q_3^*} - \dfrac{\mu_i^2}{\left|q_3\right|^2} q_i}{\dfrac{p_i}{\left|q_3\right|^2} - \dfrac{\mu_i^2}{\left|q_3\right|^2}} \tag{2.25a}$$

$$R_i^2 = \frac{p_i \left| -\dfrac{\mu_i}{q_3} + \dfrac{q_i \mu_i}{\left|q_3\right|^2} \right|^2}{\left(\dfrac{\mu_i^2}{\left|q_3\right|^2} - \dfrac{p_i}{\left|q_3\right|^2} \right)^2} \tag{2.25b}$$

Figure 2.2 shows a graphical interpretation of the set of (2.22). The reflection coefficient Γ is the intersection of three circles having Q_i and R_i as the centers and radius, respectively.

From (2.25), one can see that for an arbitrary six-port reflectometer, the three Q_i points that characterize the six-port junction are functions of the power readings in the Γ plane. These power readings are directly related to the load connected to the measuring port (port 2). In other words, they are not only relying on the six-port junction but also depending on power readings. This makes the solution of the nonlinear set of equations in (2.24) difficult in practical situations. For this reason, a bilinear mapping will be applied to (2.24) to eliminate the dependence of the Q_i points on the power readings.

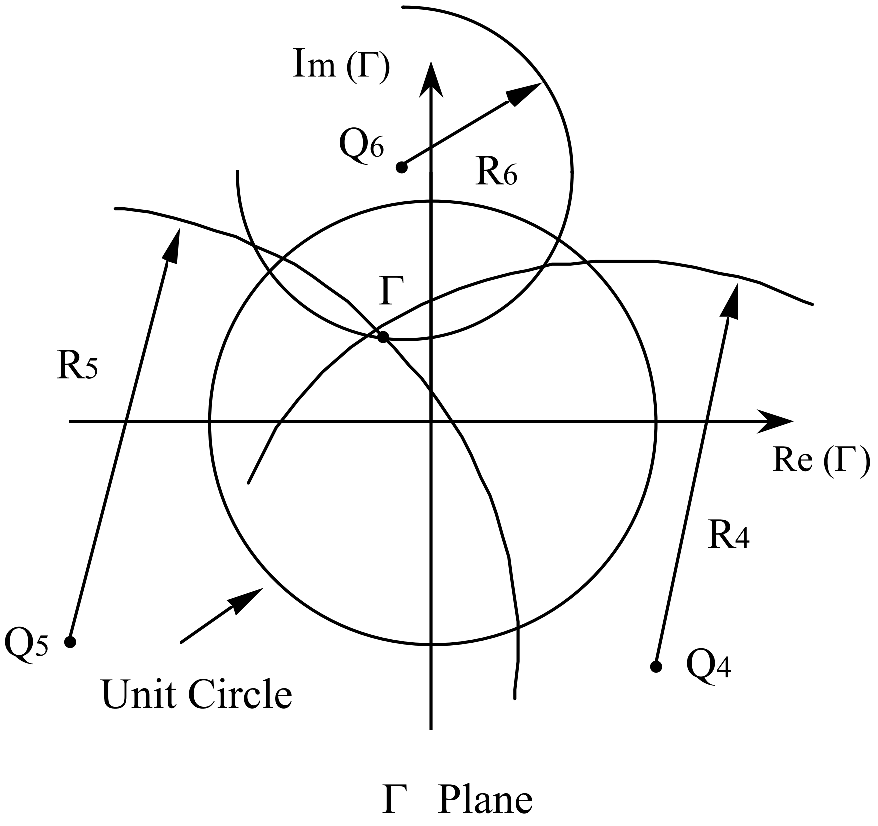

Figure 2.2 A graphical solution of the six-port state equations in the Γ plane.

2.4 SIX- TO FOUR-PORT REDUCTION

It was mentioned earlier that the direct calculation of Γ using (2.24) is difficult due to the dependence of the Q_i points on the power readings and consequently on the reflection coefficient of the DUT connected to port 2 of the six-port junction. To avoid this cross-dependence on power reading, a mapping of the state (2.22) using a bilinear transformation is required. This will transform the actual six-port reflectometer model to a more convenient and easily calibrated system constituted by an ideal reflectometer followed by a two-port network, called the error box network. Consequently, the measurements and the calibration procedures will be subdivided into different steps: the calibration step and the error-box procedure. Equation (2.22) can be rewritten in the following manner:

$$p_i = |w_i|^2 = \left|\frac{d_i\Gamma + e_i}{c_3\Gamma + 1}\right|^2, \ i = 4, 5, \text{and } 6 \tag{2.26}$$

where $d_i = -\frac{\mu_i}{q_3}$, $e_i = \frac{q_i\mu_i}{q_3}$, and $c_3 = -\frac{1}{q_3}$.

Using (2.26), one can deduce the reflection coefficient Γ as of function w_i as follows:

$$\Gamma = \frac{e_4 - w_4}{c_3 w_4 - d_4} = \frac{e_5 - w_5}{c_3 w_5 - d_5} = \frac{e_6 - w_6}{c_3 w_6 - d_6} \tag{2.27}$$

Using (2.27), one can derive that

$$w_i = \frac{e_i c_3 - d_i}{e_j c_3 - d_j} w_j + \frac{d_i e_j - d_j e_i}{e_j c_3 - d_j} \tag{2.28}$$

with $i = 4$, 5, and 6; $j = 4$, 5, and 6 with $i \neq j$.

Using (2.28) to calculate w_5 and w_6 as functions of w_4 and after the substitution of their corresponding expressions (2.26), one can obtain

$$p_4 = |w_4|^2 \tag{2.29a}$$

$$p_5 = \frac{1}{A_5^2} |w_4 - m|^2 \tag{2.29b}$$

and

$$p_6 = \frac{1}{A_6^2} |w_4 - n|^2 \tag{2.29c}$$

where

$$A_5 = \left| \frac{e_4 c_3 - d_4}{e_5 c_3 - d_5} \right| \quad \text{and} \quad A_6 = \left| \frac{e_4 c_3 - d_4}{e_6 c_3 - d_6} \right| \tag{2.30a}$$

and

$$m = |m| e^{j\varphi_m} = \frac{d_5 e_4 - d_4 e_5}{e_5 c_3 - d_5} \tag{2.30b}$$

and

$$n = |n| e^{j\varphi_n} = \frac{d_6 e_4 - d_4 e_6}{e_6 c_3 - d_6} \qquad (2.30c)$$

Equation (2.29) shows that the expressions of the Q_i points, *o*, *m*, and *n* in the w_4 plane are power independent and rely only on the six-port junction. This is opposite of the expressions of Q_i points in the Γ plan; see (2.25).

Equation (2.29) is circle’s equations. The intersection of these three circles in the W_4 plane provides the solution shown in Figure 2.3.

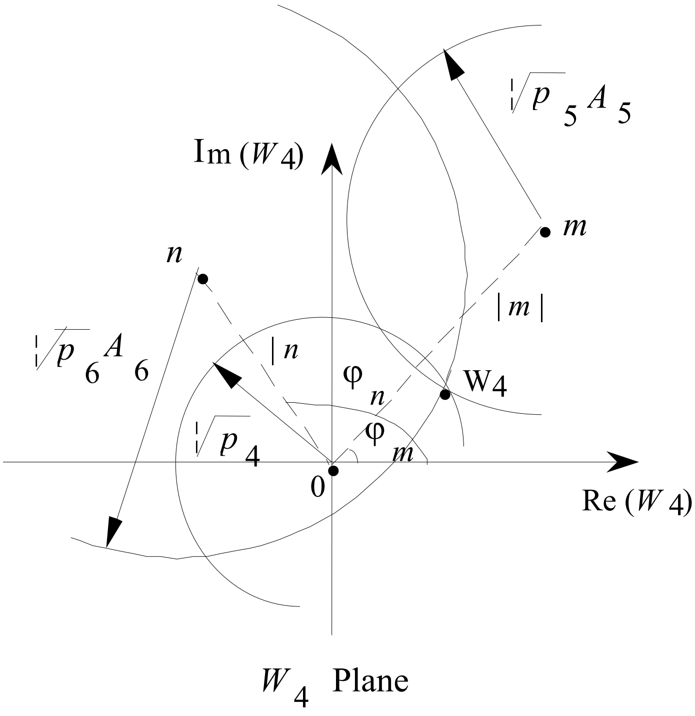

Figure 2.3 A graphical solution of the six-port state equations in the W_4 plane.

Equation (2.29) can be expanded in a linear manner and grouped in a matrix format as follows:

$$\begin{bmatrix} p_4 \\ A_5^2 p_5 \\ A_6^2 p_6 \end{bmatrix} = \begin{bmatrix} 0 \\ |m|^2 \\ |n|^2 \end{bmatrix} + \begin{bmatrix} 1 & 0 & 0 \\ 1 & -m & -m^* \\ & -n & -n^* \end{bmatrix} \begin{bmatrix} |w_4|^2 \\ w_4^* \\ w_4 \end{bmatrix} \qquad (2.31)$$

After several matrix manipulations and one matrix inversion, one can obtain an explicit expression to calculate w_4 as function of the three normalized power readings and the six-port calibration parameters A_5^2 , A_6^2 , m and n . Knowing that $\mathrm{Re}(w_4) = 1/2\left(w_4 + w_4^*\right)$ and $\mathrm{Im}(w_4) = j/2\left(w_4 - w_4^*\right)$, one can deduce [1,15]:

$$\mathrm{Re}\left(w_4\right) = \frac{\sin\varphi_m\left(p_4 - A_6^2 p_6 + |n|^2\right)}{2|n|\sin\left(\varphi_n - \varphi_m\right)} + \frac{\sin\varphi_n\left(p_4 - A_5^2 p_5 + |m|^2\right)}{2|m|\sin\left(\varphi_n - \varphi_m\right)} \tag{2.32}$$

$$\mathrm{Im}\left(w_4\right) = \frac{\cos\varphi_m\left(p_4 - A_6^2 p_6 + |n|^2\right)}{2|n|\sin\left(\varphi_n - \varphi_m\right)} + \frac{\cos\varphi_n\left(p_4 - A_5^2 p_5 + |m|^2\right)}{2|m|\sin\left(\varphi_n - \varphi_m\right)} \tag{2.33}$$

The calibration parameters have to be calculated in advance using an appropriate calibration technique. Chapter 3 is devoted to this matter.

It is important to notice that there are several choices for the definition of the embedded reflection coefficient w_4. These choices depend on the selection of the normalizing power reading, P_3 or P_4 or P_5 or P_6, and on the choice of the independent embedded reflection coefficient, w_4 or w_5 or w_6.

2.5 ERROR BOX PROCEDURE CALCULATION

An actual reflectometer can be modeled as an ideal reflectometer connected to an error box network as shown in Figure 2.4. The embedded reflection coefficient, w , is related to the de-embedded reflection coefficient, Γ , by

$$w = \frac{d\Gamma + e}{c\Gamma + 1} \tag{2.34}$$

where $d = -\left(s_{11}s_{22} - s_{21}s_{12}\right)$, $e = s_{11}$, and $\mathrm{c} = -\mathrm{s}_{22}$ and *d, e,* and *c* are three complex parameters of the two-port network that models the transition between the measuring plane of an ideal six-port reflectometer and the measuring plane of an actual six-port reflectometer as shown in Figure 2.4. s_{ij} are the scattering parameters of the two-port error box network.

These parameters, d, e, and c, have to be known in advance. The use of three well-known standards, Γ_1^s, Γ_2^s, and Γ_3^s, allows the straightforward calculation of the three unknown parameters by solving a set of three linear complex equations.

$$w_i^s \Gamma_i^s c - \Gamma_i^s d - e = w_i^s \quad \text{and} \quad i = 1, 2, \text{and } 3 \tag{2.35}$$

In practice, the short-open-load technique (SOLT) is often used in case the measuring plane terminal of the six-port reflectometer is coaxial. The expression of the de-embedded reflection coefficient Γ as a function of the three error box parameters is:

$$\Gamma = \frac{e - w}{cw - d} \tag{2.36}$$

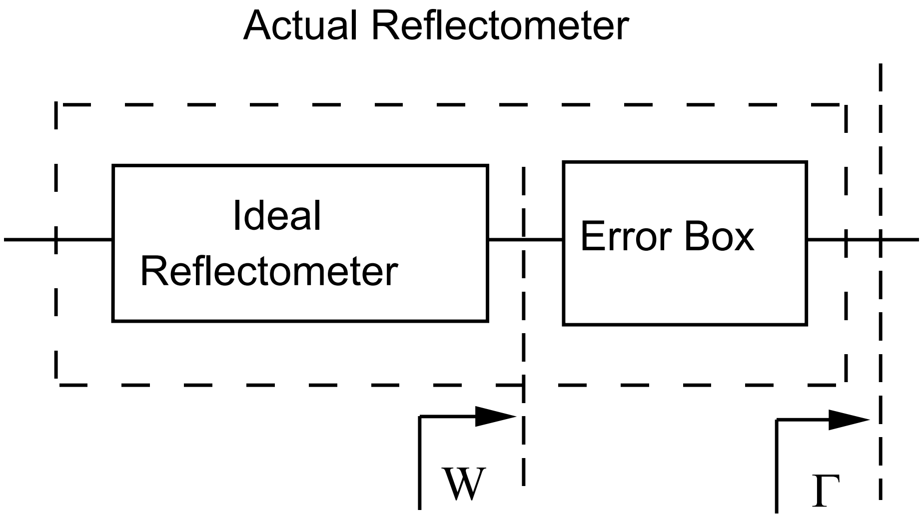

Figure 2.4 Modeling of an actual reflectometer as an ideal reflectometer connected to an error box network.

2.6 POWER FLOW MEASUREMENTS

The six-port reflectometer has the capability to measure the power absorbed by any DUT without the need to use an extra power meter and without the need to insert any coupler between the measuring port and the DUT. Using (2.9) and (2.26), one can write:

$$P_3 = \alpha_3^2 \left|\Gamma_{DUT} - q_3\right|^2 \left|b_2\right|^2 = \frac{\alpha_3^2}{\left|c_3\right|^2} \left|c_3 \Gamma_{DUT} + 1\right|^2 \left|b_2\right|^2 \tag{2.37}$$

and

$$P_{DUT} = |b_2|^2 - |a_2|^2 = \left(1 - |\Gamma_{DUT}|^2\right)|b_2|^2 \tag{2.38}$$

By substituting the expression of $|b_2|^2$ extracted from (2.37) into (2.38), one can obtain:

$$P_{DUT} = \frac{|c_3|^2 \left(1 - |\Gamma_{DUT}|^2\right) P_3}{\alpha_3^2 \, |c_3 \Gamma_{DUT} + 1|^2} \tag{2.39}$$

The only coefficient left unknown in (2.39) is α_3^2. To determine this coefficient, a power calibration has to be carried out using a precise power meter. By connecting a power meter to the measuring port, we can calculate α_3^2 as follows

$$\alpha_3^2 = \frac{|c_3|^2 \left(1 - |\Gamma_{PM}|^2\right) P_3}{P_{PM} \, |c_3 \Gamma_{PM} + 1|^2} \tag{2.40}$$

where Γ_{PM} and P_3 are, respectively, the measured reflection coefficient by the six-port reflectometer and the measured power level at port 3 of the six-port junction. P_{PM} is the power measured by the standard power meter and $c_3 = c$ (this will be proved in Chapter 4) is a complex parameter obtained during the error-box de-embedding procedure.

2.7 SIX-PORT REFLECTOMETER WITH A REFERENCE PORT

In most practical situations, the six-port junction is designed in such a way that its third port is isolated from the measuring port $(s_{32} \approx 0)$ and thus does not respond significantly to the DUT. In such a case the six-port junction comprises a reference port, P_3, which monitors the power flow exciting the DUT. In addition, if the mismatch of the measuring port is not excessive $(s_{22} \approx 0)$, the module of q_3 becomes too large in comparison to Γ. Therefore, the set of (2.9) becomes:

$$P_3 = a_3^2 \left|q_3\right|^2 \left|b_2\right|^2 \tag{2.41a}$$

$$P_4 = a_4^2 \left|b_2\right|^2 \left|\Gamma - q_4\right|^2 \tag{2.41b}$$

$$P_5 = a_5^2 \left|b_2\right|^2 \left|\Gamma - q_5\right|^2 \tag{2.41c}$$

$$P_6 = a_6^2 \left|b_2\right|^2 \left|\Gamma - q_6\right|^2 \tag{2.41d}$$

The division of (2.41b), (2.41c), and (2.41d) by (2.41a) leads to a similar equation (2.24). In such a case, the Q_i point expressions become independent of the power and their expressions are the following

$$Q_i = q_i \text{ ; } i = 4, 5, \text{ and } 6 \tag{2.42}$$

2.8 MEASUREMENT ACCURACY ESTIMATION

It was mentioned that the graphical solution of the state quadrature equations of the six-port reflectometer is the common intersection of three circles. The centers of these three circles are primarily determined by the six-port characteristics and are nominally independent of the reflection coefficient of the DUT. Figure 2.3 shows that the radius of each circle is proportional to the square root of the normalized power readings p_i. In practice, due to measurement errors and detector noises, the three circles usually do not intersect at a common point. Their intersection will fall inside a triangle area as shown in Figure 2.5.

Assume that the four real calibration parameters, A_5, A_6, m, and n, are known after a suitable calibration. Generally speaking, power detectors readings P_3, P_4, P_5, and P_6 are different from their corresponding noiseless values P_{3t}, P_{4t}, P_{5t}, and P_{6t}. A maximum likelihood estimation of w via a least square procedure can be used to find a best estimation of the reflection coefficient Γ.

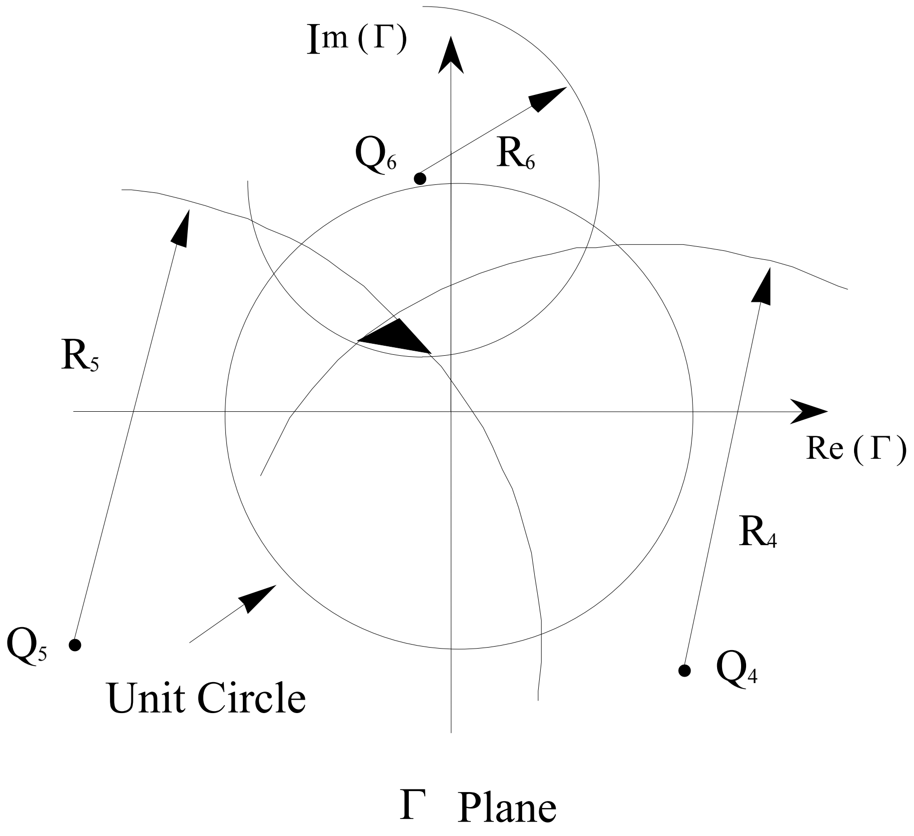

Figure 2.5 Confidence area of six-port reflectometer measurements.

If the power detector noise is assumed to be a Gaussian distribution, it can be shown that the maximum likelihood estimation of P_3, P_4, P_5, and P_6 is to minimize the error function as follows:

$$F = \sum_{i=3}^{6} \left(\frac{P_i - P_{it}}{\sigma_i} \right)^2 \tag{2.43}$$

where σ_i is the standard variance of the measured values P_i. In order to (2.43) for P_{it}, it is more convenient to substitute P_{it} as a function of P_{3t}.

By introducing a new parameter $\varepsilon_3 = P_3 - P_{3t}$ and using (2.29), it is easy to obtain :

$$\varepsilon_4 = P_4 - P_{3t} \left| w_4 \right|^2 \tag{2.44a}$$

$$\varepsilon_5 = P_5 - \frac{P_{3t}\left|w_4 - m\right|^2}{A_5^2} \tag{2.44b}$$

and

$$\varepsilon_6 = P_6 - \frac{P_{3t}\left|w_4 - n\right|^2}{A_6^2} \tag{2.44c}$$

The substitution of (2.43) into (2.42) gives:

$$F = \sum_{i=3}^{6}\left(\frac{\varepsilon_i}{\sigma_i}\right)^2 \tag{2.45}$$

The minimizing of F leads to the knowledge of P_{3t}, hence, P_{4t}, P_{5t}, P_{6t} via (2.43).

It is important to notice that the selection of the function to be minimized is only appropriate when the power detector noise is assumed to have a Gaussian distribution. In case of a strong departure from the Gaussian distribution, the maximum likelihood estimation will not give acceptable results, and a nonlinear minimization is required. Statistically based methods to construct estimators and to compare different six-port junction designs can also be found in the literature [9, 16].

References

[1] Engen, G. F., "The Six-Port Reflectometer: An Alternative Network Analyzer," *IEEE Trans. Microwave Theory and Tech.*, Vol. MTT-25, pp. 1075–1079, 1977.

[2] Engen, G. F., "The Six-Port Measurement Technique–A Status Report," *Microwave Journal*, Vol. 21, pp. 18–89, 1978.

[3] Hoer, C. A., "The Six-Port Coupler: A New Approach to Measuring Voltage, Current, Power, Impedance and Phase," *IEEE Trans. IM*, Vol. IM-21, 1972, pp. 466–470.

[4] Hoer, C. A., "Using Six-Port and Eight-Port Junctions to Measure Active and Passive Circuit Parameters," *NBS Tech. Note 673*, 1975.

[5] Oishi, T., and W. W. Kahn, "Stokes Vector Representation of the Six-Port Network Analyzer: Calibration and Measurement," *MTT International Microwave Symposium*, June 1985, St.Louis, MO, pp. 503–506.

[6] Woods, D., "Analysis and Calibration Theory of the General 6-Port Reflectometer Employing Four Amplitude Detectors," *IEE, Part H*, Vol. 126, No. 2, pp. 221–228, February 1979.

[7] Somlo, P. I., and Hunter, J. D., "A Six-Port Reflectometer and Its Complete Characterization by Convenient Calibration Procedures," *IEEE Trans. Microwave Theory Tech.*, Vol. MTT-30, No. 2, pp. 186–192, February 1982.

[8] Ghannouchi, F. M., *Mesures Micro-Ondes Assistants par Ordinateur Utilisant un Nouveau Corrtlateur Six-Port*, Ph.D. Thesis, Ecole Polytechnique de Montreal, 1987.

[9] Chang, K., *Encyclopedia of RF and Microwave Engineering*, New York: Wiley, 2005.

[10] Yakabe, T., F. M., Ghannouchi, E. Eid, K. Fujii, and H. Yabe, "Six-Port Based Wave Correlator with Application to Beam Direction Finding." *IEEE Transactions on Instrumentation and Measurement,* Vol. 50, No. 2, pp. 377–380, 2001.

[11] Bosisio, R. G. , Y. Y. Zhao, X. Y. Xu, S. Abielmona, E. Moldovan, Y. S. Xu, M. Bozzi, S. O. Tatu, J. F. Frigon, C. Caloz, and K. Wu, "'New-Wave Radio," *IEEE Microwave Magazine,* pp. 89–100, February 2008.

[12] Mohajer, M., A. Mohammadi, and A. Abdipour, "Direct Conversion Receivers Using Multi-Port Structures for Software Defined Radio Systems," *IET Microwaves, Antennas & Propagation*, 2007, Vol. 1, No. 2, pp.363–372*,* April 2007.

[13] Tatu, S. O., E. Moldovan, S. Affes, B. Boukari, K. Wu, and R. G. Bosisio, "Six-Port Interferometric Technique for Accurate W-Band Phase-Noise Measurements, *IEEE Trans. Microwave Theory & -Tech.*, Vol. 56, No. 6, pp.1372–1379, June 2008.

[14] Bensmida, S., P. Poiré, R. Negra, F. M. Ghannouchi, and G. Brassard , "New Time-Domain Voltage and Current Waveform Measurement Setup for Power Amplifier Characterization and Optimization," *IEEE Trans. Microwave Theory & Tech.*, Vol. 56, No. 1, pp. 224–231, January 2008.

[15] Engen, G. F., "A Least Square Solution for Use in Six-Port Measurement Technique," *IEEE Trans. Theory and Tech.*, Vol. MTT-28, pp. 1437–1477, 1980.

[16] Engen, G. F., *Microwave Circuit Theory and Foundation of Microwave Metrology*, IEE Electrical Measurement Series 9, London, U.K.: Peter Peregrinus Ltd., 1992.

Chapter 3

The Design of Six-Port Junctions

The most important characteristic of any microwave six-port reflectometer that directly influences the functionality of the reflectometer and determines the measurement accuracy, is the relative positions in the Γ plane of the four complex parameters, q_i; [1–6]. In most practical cases, the six-port junction comprises a reference port to monitor the incident power level; in such a case, only three invariant Q_i points remain pertinent in designing six-port junctions. Various proposed microwave six-port configurations are based on the interconnection of several four- and/or three-port networks such as hybrid junctions or power dividers [7–18]. In this chapter, analysis and design consideration for six-port junctions are discussed and several practical junctions designed in different transmission technologies are described.

3.1 DESIGN CONSIDERATION FOR SIX-PORT JUNCTIONS

It was mentioned in Chapter 2 that each six-port reflectometer comprises a microwave source, a six-port junction, and four power detectors. In cases where the six-port junction incorporates a reference port, the basic relationship that governs the operation of the reflectometer is as follows:

$$p_i = \frac{P_i}{P_3} = \mu_i^2 \left|\Gamma - q_i\right|^2 \text{, } i = 4, 5, \text{ and } 6 \qquad (3.1)$$

where

p_i is the normalized power reading value, μ_i^2 and q_i are the parameters which characterize the six-port reflectometer and are related to the calibration parameters, and Γ is the complex reflection coefficient of the DUT.

The first step to design a six-port junction is to choose the values of μ_i^2 and the positions of the q_i in the Γ plane. It is obvious from the inspection of (3.1) that μ_i^2 are proportionality factors that determine the power levels at the input of the power detectors. Usually, these parameters are chosen such that the measured power levels are within the power dynamic range of power detectors fitted to the four measuring ports of the six-port junctions. Therefore, the major task in designing six-port junctions is to select the positions of the q_i in the Γ plane [1].

Based on symmetric configurations, the optimal position of the q_i points of a preferred six-port junction, which offer uniform measurement accuracy, should be located at the vertices of an equilateral triangle, having its center at the origin of the Γ plane. In such a case, we obtain:

$$|q_4| = |q_5| = |q_6| \tag{3.2}$$

and the relative phase separations between q_i are equal to 120°. The only degree of freedom left is to fix the magnitude of the q_i points. Since the reflection coefficient, Γ, is determined from the intersection of three circles (see Chapter 2), it is evident that an ill-conditioned numerical situation will result when the centers of these circles become too large $\left(n \approx m \approx \infty\right)$ or too small $\left(n \approx m \approx 0\right)$, or when the q_i points are collinear ($\varphi_n - \varphi_m = 0$ or $\varphi_n - \varphi_m = \pi$). In addition, the selection of q_i inside the Smith chart will result in a singularity and measurement problem when $\Gamma = q_i$. Therefore the optimal design of the six-port junction results in:

$$q_4 \approx 1.5\angle\theta_o^{\circ} \tag{3.3a}$$

$$q_5 \approx 1.5\angle\left(\theta_o + 120^{\circ}\right) \tag{3.3b}$$

and

$$q_6 \approx 1.5\angle\left(\theta_o - 120^{\circ}\right) \tag{3.3c}$$

Where θ_0 is an arbitrary phase reference value.

3.2 WAVEGUIDE SIX-PORT JUNCTIONS

The simplest six-port junction to design is to connect three identical probes in an upside wall of a waveguide section [2]. Each probe is separated from its adjacent probe by an electrical length equal to L_g. A directional coupler to monitor the power level should be inserted between the source and the input port of the waveguide section. The DUT is connected to output port of the waveguide section. The block diagram of the waveguide six-port junction is shown in Figure 3.1. c_c and t_c are the coupling and the transmission factors of the lossless input directional coupler, respectively; c_g and t_g are the coupling and the transmission factors of the three waveguide probe directional couplers; and θ_c, θ_g, and θ_l are the phases associated with the electrical lengths, L_c, L_g, and L_l of the input directional coupler, the waveguide section between two adjacent probes and the waveguide section between the third waveguide probe coupler and the measuring reference plane of the six-port junction.

The following expression, which relates the DUT's excitation signal, b_2, to the six-port input signal, a_1, can be easily obtained:

$$b_2 = a_1 t_c t_g^3 e^{-j(\theta_c + \theta_l + 2\theta_g)} \tag{3.4}$$

The reflected signal by the DUT, a_2, is related to b_2 by the following equation:

$$a_2 = b_2 \Gamma \tag{3.5}$$

where Γ is the reflection coefficient of the DUT.

The straightforward analysis of the wave's propagation of the incident signal exciting port 1, a_1, and the reflected signal by the device under test (DUT), a_2, having a reflection coefficient of Γ, through the waveguide six-port junction allows for the calculation of the expressions of the four signals emerging at the four detection ports of the six-port junction as follows:

$$b_3 = \frac{b_2 c_c}{t_c t_g^3} e^{+j(\theta_l + 2\theta_g)} \tag{3.6}$$

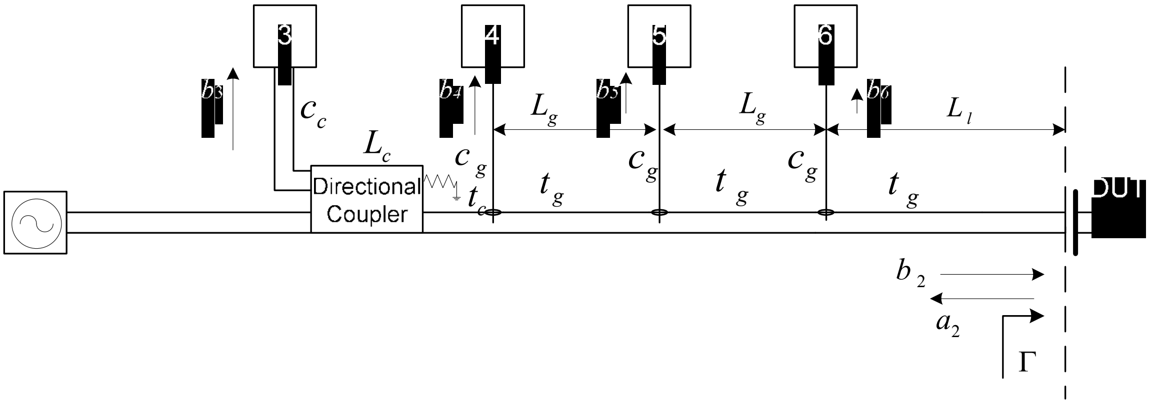

Figure 3.1 Block diagram of a waveguide six-port junction.

$$b_4 = b_2 t_g^2 c_g e^{-j(\theta_l + 2\theta_g)} \left(\Gamma + \frac{1}{t_g^5} e^{+j(4\theta_g + 2\theta_l)} \right) \tag{3.7}$$

$$b_5 = b_2 t_g c_g e^{-j(\theta_l + \theta_g)} \left(\Gamma + \frac{1}{t_g^3} e^{+j(2\theta_g + 2\theta_l)} \right) \tag{3.8}$$

and

$$b_6 = b_2 c_g e^{-j(\theta_l)} \left(\Gamma + \frac{1}{t_g} e^{+2j\theta_l} \right) \tag{3.9}$$

By identifying (3.8), (3.9), and (3.10) to basic equations of a six-port reflectometer, (2.7), one can easily deduce that the expression of the three q_i as functions of the characteristic of the components that constitute the six-port junction:

$$q_4 = \frac{-1}{t_g^5} e^{+j(4\theta_g + 2\theta_l)} \tag{3.10a}$$

$$q_5 = \frac{-1}{t_g^3} e^{+j(2\theta_g + 2\theta_l)} \tag{3.10b}$$

and

$$q_6 = \frac{-1}{t_g} e^{+j(2\theta_l)} \tag{3.10c}$$

From (3.10), it is clear that the positions of the q_i points in the Γ plane will rotate as the frequency changes, unless θ_l is equal to zero, which is difficult to obtain in practice. In addition to having a phase difference of $2\pi/3$ between each pair of $\left(q_i, q_j\right)$, θ_g must be equal to $\pi/3$, which corresponds to an L_g equal to $\lambda_g/6$. In practice, $t_g \approx 1$; in such a case, the q_i point positions become

$$q_4 \approx 1\angle\left(2\theta_l - 2\pi/3\right) \tag{3.11a}$$

$$q_5 \approx 1\angle\left(2\theta_l + 2\pi/3\right) \tag{3.11b}$$

and

$$q_6 \approx 1\angle 2\theta_l \tag{3.11c}$$

It is clear from the (3.11) that the q_i point positions will rotate as the frequency changes, and the phase separation of 120° between each pair of q_i points is obtained only for one frequency where $L_g = \lambda_g/6$. Therefore, this design is suitable only for narrow frequency band applications.

3.3 FREQUENCY COMPENSATED OPTIMAL SIX-PORT JUNCTIONS

A block diagram of a six-port junction incorporating three four-port directional couplers Q_1, Q_2 and Q_3, two two-way power dividers D_1 and D_2, and seven delay lines $L_1, \ldots L_7$ is shown in Figure 3.2. The purpose of the following analytical development is first to determine the values of the coupling factors of the directional couplers that permit one to obtain an optimal design [3]; and second, to calculate the electrical lengths of the delay lines that assure a frequency compensation of the six-port junction. The block diagram of the six-port junction is shown in Figure 3.2.

The following expression, which relates the DUT's excitation signal, b_2, to the six-port input signal, a_1, can be easily obtained:

$$b_2 = j a_1 c_1 e^{-j\left(\theta_q + \theta_1\right)} \tag{3.12}$$

The reflected signal by the DUT, $\boldsymbol{a}_2$, is related to $\boldsymbol{b}_2$ by the following equation:

$$a_2 = b_2 \Gamma \tag{3.13}$$

where Γ is the reflection coefficient of the DUT.

The straightforward analysis of the wave's propagation of the incident signal exciting port 1, a_1, and the reflected signal by the device under test (DUT), a_2, having a reflection coefficient of Γ, through the six-port junction allows the calculation of the expressions of the four signals emerging at the four detection ports of the six-port junction as follows:

$$b_3 = \frac{-jb_2t_1}{c_1\sqrt{2}} e^{-j\left(\theta_p + \theta_6 - \theta_1\right)} \tag{3.14}$$

$$b_4 = \frac{jb_2t_1c_2}{\sqrt{2}} e^{-j\left(2\theta_q + \theta_1 + \theta_2 + \theta_3 + \theta_p\right)} \left(\Gamma - \frac{t_2}{c_1c_2} e^{-j\left(-2\theta_1 - \theta_2 - \theta_3 - \theta_q + \theta_6 + \theta_7\right)} \right) \tag{3.15}$$

$$\begin{gathered} b_5 = \frac{t_1b_2}{\sqrt{2}} e^{-j\left(2\theta_q + \theta_1 + \theta_2 + \theta_5 + \theta_p\right)} \left(t_2t_3e^{-j\left(\theta_3 + \theta_4 + \theta_q - \theta_5\right)} + jc_3 \right) \\ .\left[\Gamma - \frac{-c_2t_3e^{-j\left(-2\theta_1 - \theta_2 - \theta_5 + \theta_4 + \theta_6 + \theta_7\right)}}{c_1\left(t_2t_3e^{-j\left(\theta_3 + \theta_4 + \theta_q - \theta_5\right)} + jc_3 \right)} \right] \end{gathered} \tag{3.16}$$

and

$$\begin{gathered} b_6 = \frac{t_1b_2}{\sqrt{2}} e^{-j\left(2\theta_q + \theta_1 + \theta_2 + \theta_5 + \theta_p\right)} \left(jt_2c_3e^{-j\left(\theta_3 + \theta_4 + \theta_q - \theta_5\right)} + t_3 \right) \\ .\left[\Gamma - \frac{-jc_2c_3e^{-j\left(-2\theta_1 - \theta_2 - \theta_5 + \theta_4 + \theta_6 + \theta_7\right)}}{c_1\left(jt_2c_3e^{-j\left(\theta_3 + \theta_4 + \theta_c - \theta_5\right)} + t_3 \right)} \right] \end{gathered} \tag{3.17}$$

Where θ_q, c_i, and t_i, are respectively, the electrical lengths, the coupling factors, and the transmission factors of the lossless quadrature hybrid directional couplers $(c_i^2 + t_i^2 = 1)$. θ_p is the electrical lengths of the 3 dB two-way power dividers and θ_i are the electrical lengths of the lossless transmissions lines connecting the different components of the six-port junction [4].

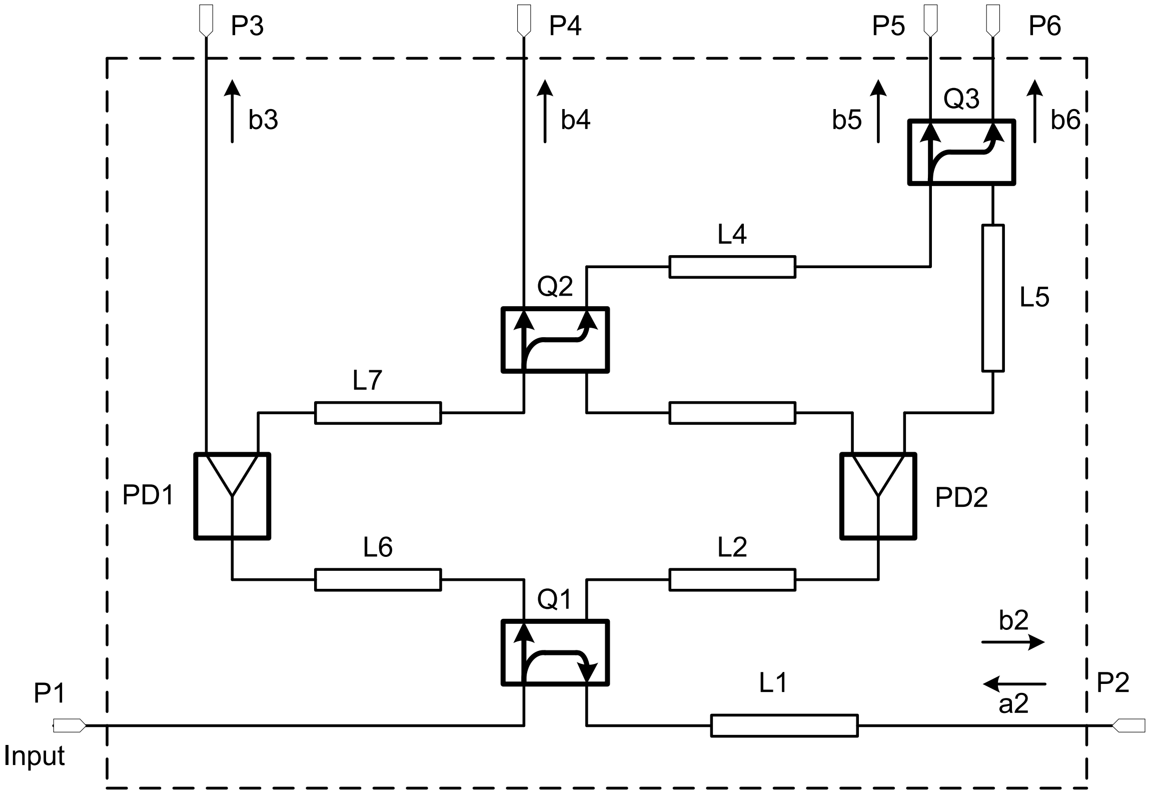

PDk: Power Divider
Qk: Directional Coupler
Lk: Transmission Line

Figure 3.2 Block diagram of an optimal six-port junction.

By identifying (3.15), (3.16) and (3.17) to the basic equation of a six-port reflectometer, (2.7), one can easily deduce that the expression of the three q_i as a function of the characteristics of the components which constitute the six-port junction:

$$q_4 = \frac{t_2}{c_1 c_2} e^{-j\left(-2\theta_1 - \theta_2 - \theta_3 - \theta_q + \theta_6 + \theta_7\right)} \tag{3.18a}$$

$$q_5 = \frac{-c_2 t_3 e^{-j\left(-2\theta_1 - \theta_2 - \theta_5 + \theta_4 + \theta_6 + \theta_7\right)}}{c_1 \left(t_2 t_3 e^{-j\left(\theta_3 + \theta_4 + \theta_q - \theta_5\right)} + j c_3 \right)} \tag{3.18b}$$

and

$$q_6 = \frac{-jc_2c_3e^{-j(-2\theta_1-\theta_2-\theta_5+\theta_4+\theta_6+\theta_7)}}{c_1\left(jt_2c_3e^{-j(\theta_3+\theta_4+\theta_q-\theta_5)}+t_3\right)} \tag{3.18c}$$

From the (3.18), it is clear that the positions of the q_i points in the Γ plane rotate as the frequency changes. To make the junction frequency compensated, the two following equations have to be satisfied:

$$2\theta_1+\theta_2+\theta_3+\theta_q=\theta_6+\theta_7 \tag{3.19a}$$

and

$$\theta_3+\theta_4+\theta_q=\theta_5 \tag{3.19b}$$

Substituting (3.19a) and (3.19b) into (3.18), we obtain:

$$q_4=\frac{t_2}{c_1c_2} \tag{3.20a}$$

$$q_5=\frac{-c_2}{c_1\left(t_2+j\,c_3/t_3\right)} \tag{3.20b}$$

and

$$q_6=\frac{-c_2}{c_1\left(t_2-j\,t_3/c_3\right)} \tag{3.20c}$$

To obtain an optimum design, the coupling factors of the directional couplers must be equal to

$$c_1=0.45\ (6.75\,\text{dB}) \tag{3.21a}$$

$$c_2=\sqrt{2}/\sqrt{3}\,(1.76\,\text{dB}) \tag{3.21b}$$

and

$$c_3 = 1/\sqrt{2}\,(3\,\mathrm{dB}) \tag{3.21c}$$

In such a case, the q_i point positions become

$$q_4 = 1.54\angle 0^\circ \tag{3.22a}$$

$$q_5 = 1.54\angle 120^\circ \tag{3.22b}$$

and

$$q_6 = 1.54\angle -120^\circ \tag{3.22c}$$

It is clear, from (3.22) that the magnitude of the q_i points can be adjusted by fixing the value of c_1. The values of μ_i can be calculated as follows:

$$|\mu_4| = \frac{t_2 c_2 c_1}{t_1} \approx 0.47 \tag{3.23a}$$

$$|\mu_5| = c_1 \left|t_2 t_3 + j c_3\right| \approx 0.47 \tag{3.23b}$$

$$|\mu_6| = c_1 \left|t_3 + j t_2 c_3\right| \approx 0.47 \tag{3.23c}$$

The equality of the three values of $\mu_i^2 \approx 0.22$ shows the advantage of frequency compensated six-port junction in minimizing the requirement of the dynamic range of the four power detectors. In such a case, the same quality power detectors, having a 50 dB dynamic range, can be sufficient for power reading purposes.

In case of frequency compensation of the six-port junction, only a slightly residual displacement of the q_i points in the Γ plane will result due to the non-ideal behaviors (mismatches, phase and amplitude variations, etc.) of the directional couplers and the power dividers over their operational frequency bandwidths [5,6].

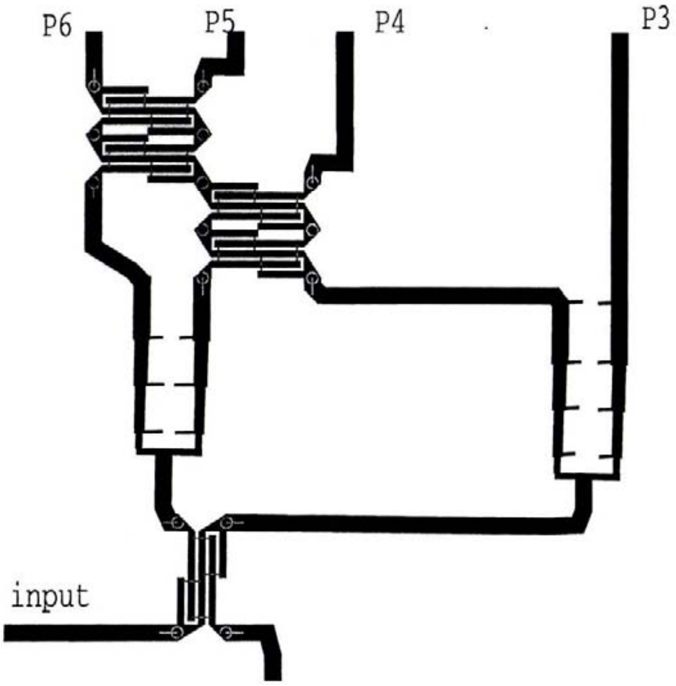

Figure 3.3 An optimal six-port junction in microstrip lines using Lange couplers and Wilkinson power dividers.

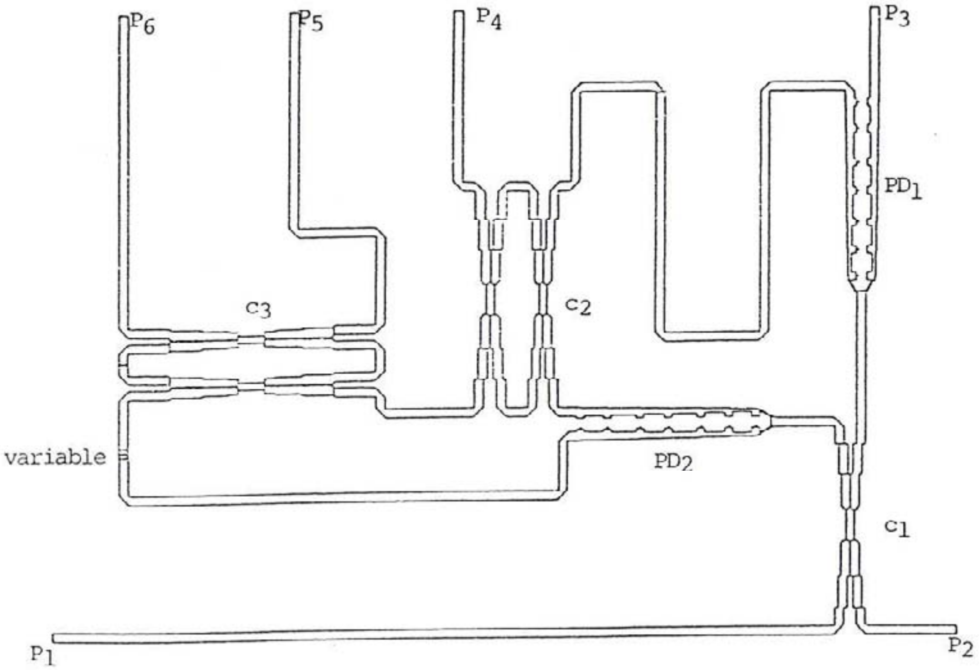

Figure 3.4 An optimal six-port junction in stripline using broadside multisection directional couplers and Wilkinson power dividers.

An optimal six-port junction in microstrip technology has been designed using Lange couplers and Wilkinson power dividers and reported in [8]. The layout of a six-port junction in microstrip is shown in Figure 3.3.

A wideband optimal six-port junction in stripline technology has been designed using broadside multisections directional couplers and stripline Wilkinson power dividers and reported in [19]. The layout of the six-port junction is shown in Figure 3.4.

3.4 FREQUENCY COMPENSATED QUASI-OPTIMAL SIX-PORT JUNCTIONS

It has been shown that an optimal six-port junction cannot be realized using only standard 3 dB hybrids and/or power dividers. A quasi-optimal design, shown in Figure 3.5, can be realized using 3 dB quadrature hybrid junctions and 3 dB power dividers. The relative positions of the q_i in the Γ plane are shown in the following:

$$q_4 = 1\angle\theta_o \tag{3.24a}$$

$$q_5 = \sqrt{2}\angle(\theta_o + 135^\circ) \tag{3.24b}$$

$$q_6 = \sqrt{2}\angle(\theta_o - 135^\circ) \tag{3.24c}$$

where θ_o is an arbitrary phase reference value.

A block diagram of a quasi-optimal six-port junction incorporating four-port 3 dB directional couplers Q_1, Q_2, Q_3, and Q_4, a two-way power divider D_1, and seven delay lines $L_1, \ldots L_7$ are shown in Figure 3.5. By repeating the same algebraic developments as for the frequency compensated optimum six-port junction, one can find the values of q_i point positions in the Γ plane as shown here:

$$q_4 = je^{-j\left(-2\theta_1+\theta_2+\theta_3-\theta_4+\theta_p-\theta_q\right)} \tag{3.25a}$$

$$q_5 = je^{-j\left(-2\theta_1+\theta_2+\theta_3-\theta_4+\theta_p-\theta_q\right)}\left(j - e^{-j\left(\theta_5+\theta_7-\theta_3-\theta_6\right)}\right) \tag{3.25b}$$

and

$$q_6 = -je^{-j\left(-2\theta_1+\theta_2+\theta_3-\theta_4+\theta_p-\theta_q\right)}\left(j+e^{-j\left(\theta_5+\theta_7-\theta_3-\theta_6\right)}\right) \tag{3.25c}$$

For the frequency compensated six-port junction, the electrical lengths L_i of the delay lines must satisfy the following equations:

$$\theta_q+\theta_4+2\theta_1=\theta_2+\theta_3+\theta_p \tag{3.26a}$$

$$\theta_5+\theta_7=\theta_3+\theta_6 \tag{3.26b}$$

In such a case, the q_i point positions in the Γ plane become frequency invariant.

$$q_4=1\angle 90^\circ \tag{3.27a}$$

$$q_5=\sqrt{2}\angle -135^\circ \tag{3.27b}$$

and

$$q_6=\sqrt{2}\angle -45^\circ \tag{3.27c}$$

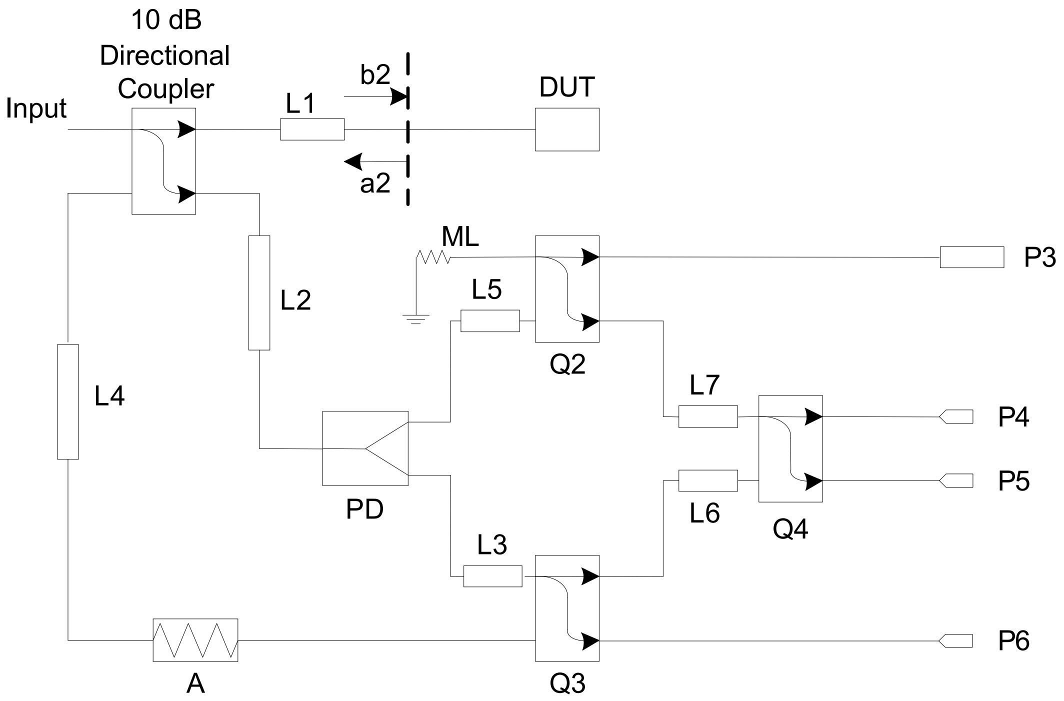

PD: Power Divider
Qk: 3 dB Hybrid Coupler
Pk: Power Detectors
A: 3 dB Attenuator
ML: Matched Load

Figure 3.5 Block diagram of a quasi-optimal six-port junction.

By adding a 3 dB attenuator in the delay line, L4, the q_i point positions in the Γ plane are pushed away by a factor of $\sqrt{2}$ from the center of the Smith chart and become

$$q_4 = \sqrt{2}\angle 90^\circ \tag{3.28a}$$

$$q_5 = 2\angle -135^\circ \tag{3.28b}$$

and

$$q_6 = 2\angle -45^\circ \tag{3.28c}$$

A frequency compensated quasi-optimal six-port junction designed using branch line couplers, a Wilkinson power divider, and a 3 dB attenuator has been manufactured in Miniature Hybrid Microwave Integrated Circuit technology (microstrip on 10 mil Alumina substrate). The layout of the six-port junction is shown in Figure 3.6 and the details are reported in [20].

A second frequency compensated coplanar waveguide quasi-optimal six-port junction, which incorporates four branch line couplers, a Wilkinson power divider, and a 3 dB attenuator, has been designed and manufactured in Monolithic Microwave Integrated Circuit technology on 500 μm GAs substrate. The four power detectors are integrated in the six-port junction. The dimension of the junction is 3×3.5 mm^2. The layout of the six-port junction is shown in Figure 3.7 and the details are reported in [21].

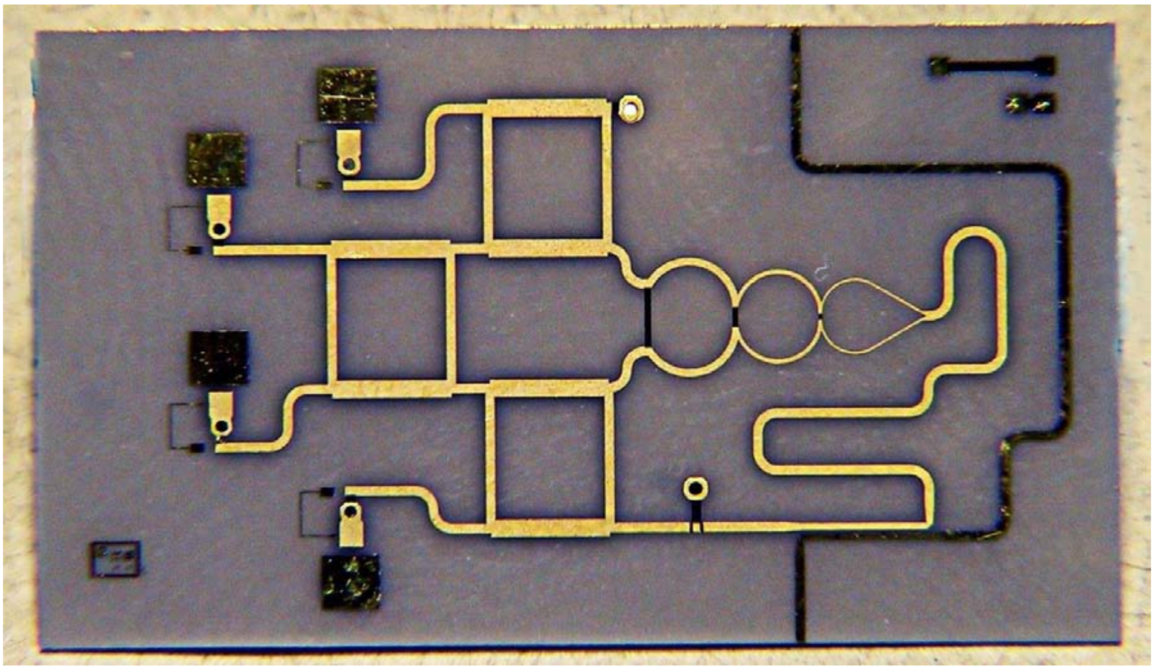

Figure 3.6 Quasi-optimal six-port junction designed in MHMIC technology using couplers and a multisection Wilkinson power divider. (© 1993 Wiley [20].)

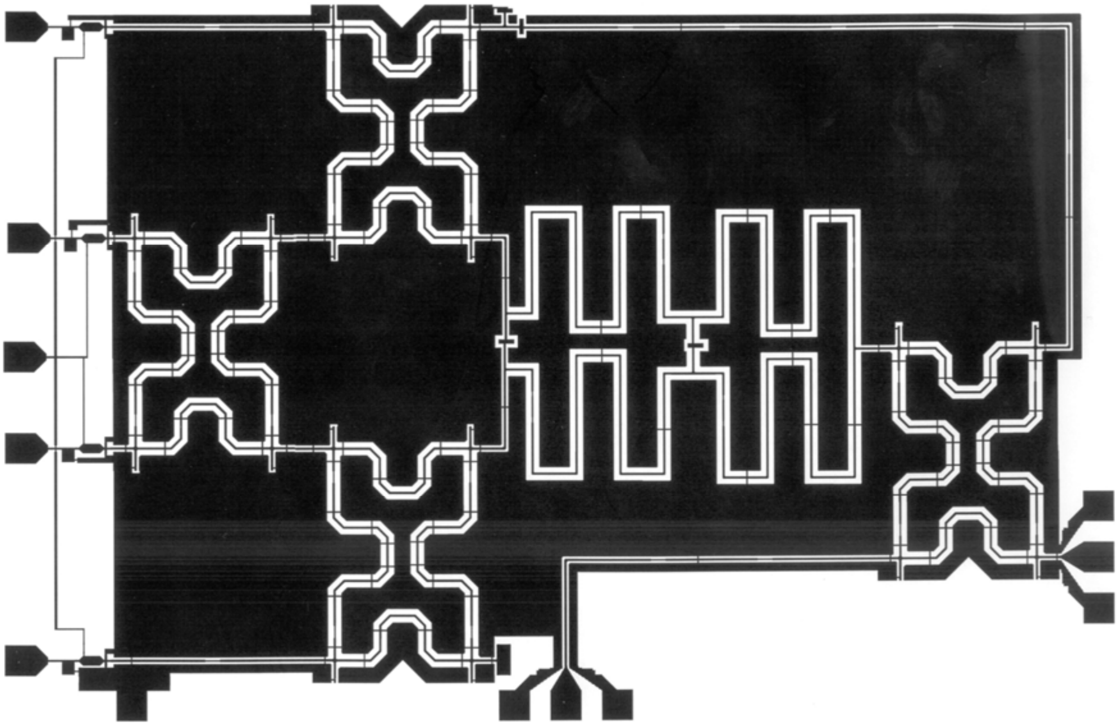

Figure 3.7 Six-port in MMIC technology. (© 1995 IEEE [21].)

3.5 A SIX-PORT JUNCTION BASED ON A SYMMETRICAL FIVE-PORT RING JUNCTION

The symmetrical lossless five-port ring junction can be used as the main component to design an optimal six-port junction. This junction incorporates a directional coupler to monitor the power level and the five-port symmetrical ring junction as shown in Figure 3.8.

The properties of the linear scattering matrix of the symmetrical five-port junction lead to the determination of the scattering parameters of the junction. The reciprocity condition provides:

$$s_{ij} = s_{ij} \tag{3.29}$$

with $i = 1, 2, 3, 4$, and 5, $j = 1, 2, 3, 4$, and 5, and $i \neq j$. The symmetrical condition of the five-port ring junction which has a sequential numbering of its port provides:

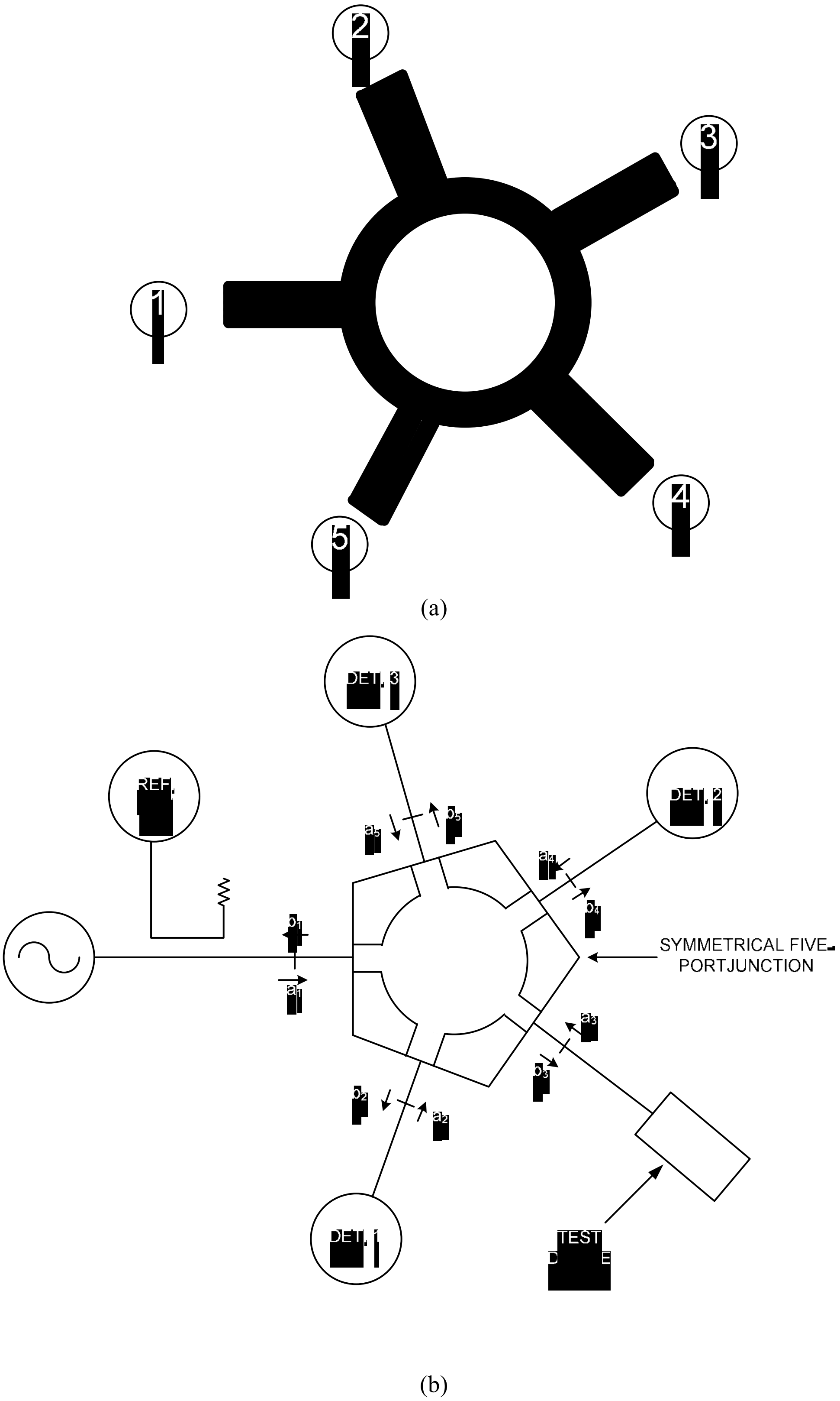

Figure 3.8 (a) Schematic of a symmetrical five-port ring junction. (b) A schematic of a symmetrical five-port ring based six-port junction.

$$s_{11} = s_{22} = s_{33} = s_{44} = s_{55} = \alpha \tag{3.30a}$$

$$s_{12} = s_{15} = s_{23} = s_{34} = s_{45} = \beta \tag{3.30b}$$

$$s_{13} = s_{14} = s_{24} = s_{25} = s_{35} = \delta \tag{3.30c}$$

From (3.30) one can conclude that only three independent *s* parameters are sufficient to form the **S** matrix:

$$\mathbf{S} = \begin{bmatrix} \alpha & \beta & \delta & \delta & \beta \\ \beta & \alpha & \beta & \delta & \delta \\ \delta & \beta & \alpha & \beta & \delta \\ \delta & \delta & \beta & \alpha & \beta \\ \beta & \delta & \delta & \beta & \alpha \end{bmatrix} \tag{3.31}$$

For a lossless junction, one can write that

$$|\alpha|^2 + 2|\beta|^2 + 2|\delta|^2 = 1 \tag{3.32}$$

The unitary condition of **S** matrix provides

$$\begin{cases} \alpha\beta^* + \beta\alpha^* + \delta\beta^* + \beta\delta^* + |\delta|^2 = 0 \\ \alpha\delta^* + \delta\alpha^* + \delta\beta^* + \beta\delta^* + |\beta|^2 = 0 \\ \alpha\delta^* + \beta\delta^* + \delta\beta^* + \delta\alpha^* + |\beta|^2 = 0 \\ \alpha\beta^* + \beta\delta^* + \delta\beta^* + \beta\alpha^* + |\delta|^2 = 0 \end{cases} \tag{3.33}$$

For a matched five-port ring junction ($\alpha = 0$), using (3.32) and (3.33) leads to

$$\begin{cases} \delta\beta^* + \beta\delta^* + |\delta|^2 = 0 \\ \delta\beta^* + \beta\delta^* + |\beta|^2 = 0 \\ 2|\beta|^2 + 2|\delta|^2 = 1 \end{cases} \tag{3.34}$$

The above set of equations gives:

$$\left|\beta\right| = \left|\delta\right| = 0.5 \tag{3.35}$$

By assuming that β is real and by substituting the value of β in one of the two first equations, one can easily deduce that:

$$\delta = 0.5\angle \pm 120^{\circ} \tag{3.36}$$

Finally, the **S** matrix of a six-port junction comprising a symmetrical and matched five-port ring junction and an ideal directional coupler connected to port 1 of the five-port junction as shown in Figure 3.8 is as follows:

$$\mathbf{S_{sp}} = \begin{bmatrix} 0 & t\delta & jc & t\beta & t\delta & t\beta \\ t\delta & 0 & 0 & \beta & \beta & \delta \\ jc & 0 & 0 & 0 & 0 & 0 \\ t\beta & \beta & 0 & 0 & \delta & \delta \\ t\delta & \beta & 0 & \delta & 0 & t\beta \\ t\beta & \delta & 0 & \delta & t\beta & 0 \end{bmatrix} \tag{3.37}$$

Using (1.13), one can deduce the positions of the three q_i points in the complex plane using the S parameters of the six-port junction:

$$q_4 = \frac{s_{41}}{-s_{21}s_{42}} = \frac{t\beta}{-t\delta\beta} = 2\angle 60^{\circ} \tag{3.38a}$$

$$q_5 = \frac{s_{51}}{-s_{21}s_{52}} = \frac{t\delta}{-t\delta\beta} = 2\angle 180^{\circ} \tag{3.38b}$$

and

$$q_6 = \frac{s_{61}}{-s_{21}s_{62}} = \frac{\beta}{-\delta^2} = 2\angle -60^{\circ} \tag{3.38c}$$

These values were calculated using $\delta = 0.5\angle 120^{\circ}$. The analytical development to obtain the above design specifications can be found in [10]. An optimal L-band microstrip line six-port junction designed on a 10 mil Alumina substrate, shown in Figure 3.9, is reported in [22]. It incorporates a 10 dB edge-line coupler and the symmetrical five-port ring. The interconnection lines were made using 50Ω microstrip lines. The junction is fitted in 3.5×3.2 cm^2.

A six-port junction was designed using Agilent ADS software. This six-port junction was fabricated and tested. The actual q_i point positions in the Γ over 1–2 GHz frequency band are deduced first using the simulated S parameters and (2.13), second, using the measured S parameters, and finally using the calibration parameters of the six-port reflectometer, obtained after its calibration using the six- to four-port reduction technique, in conjunction with (3.36). A good agreement was obtained between the three sets of results.

The accuracy of the reflectometer was checked by measuring the reflection coefficient of a short-circuited 6 dB attenuator standard measured at the Canadian Bureau of Standards. It was found that the measurement errors are within ± 0.05 for the amplitude of Γ and ± 1° for the phase of Γ over the operational frequency band 1–2.5 GHz.

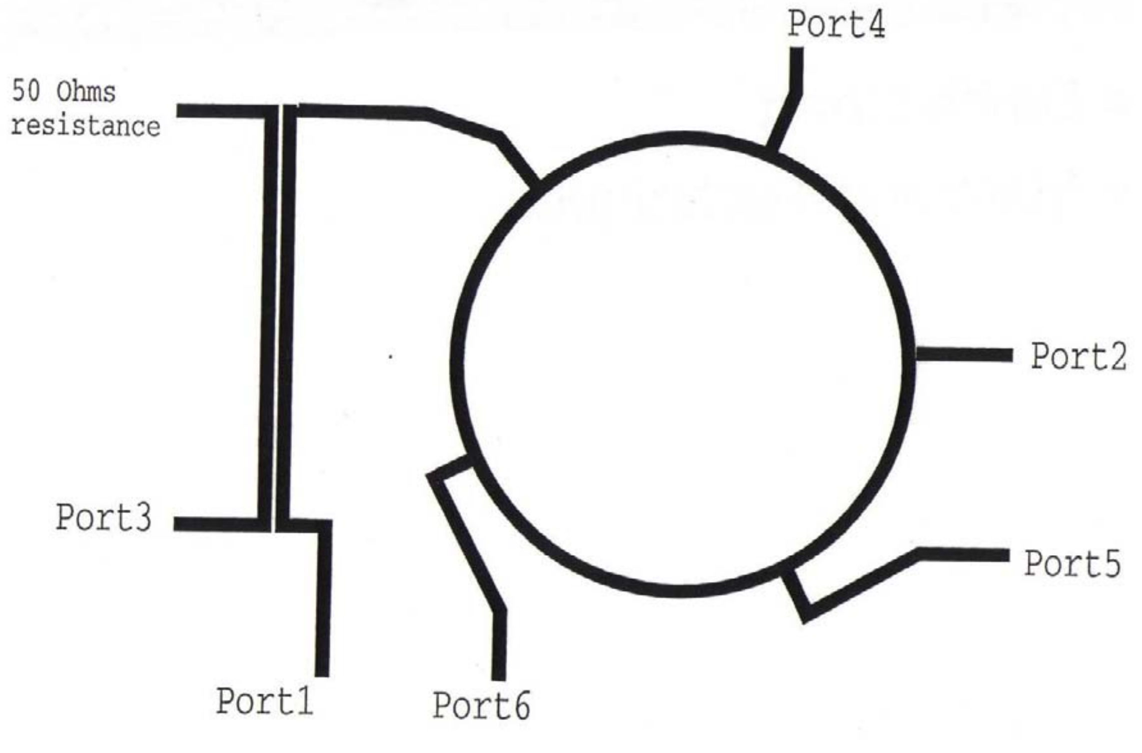

Figure 3.9 A symmetrical five-port ring based six-port junction in microstrip technology. (© 1994 Microwave & RF [22].)

3.6 HIGH POWER SIX-PORT JUNCTION IN HYBRID WAVEGUIDE/ STRIPLINE TECHNOLOGY

A high power six-port junction in hybrid waveguide stripline technology, using a stripline waveguide directional coupler and a nonsymmetrical stripline five-port ring junction, was designed and manufactured and tested at 2.45 GHz (ISM frequency). This junction is capable of handling power as much as the waveguide portion of the junction could handle. It is expected that this design could handle up to several kilowatts of power; the details of the design can be found in [23]. The block diagram is shown in Figure 3.10.

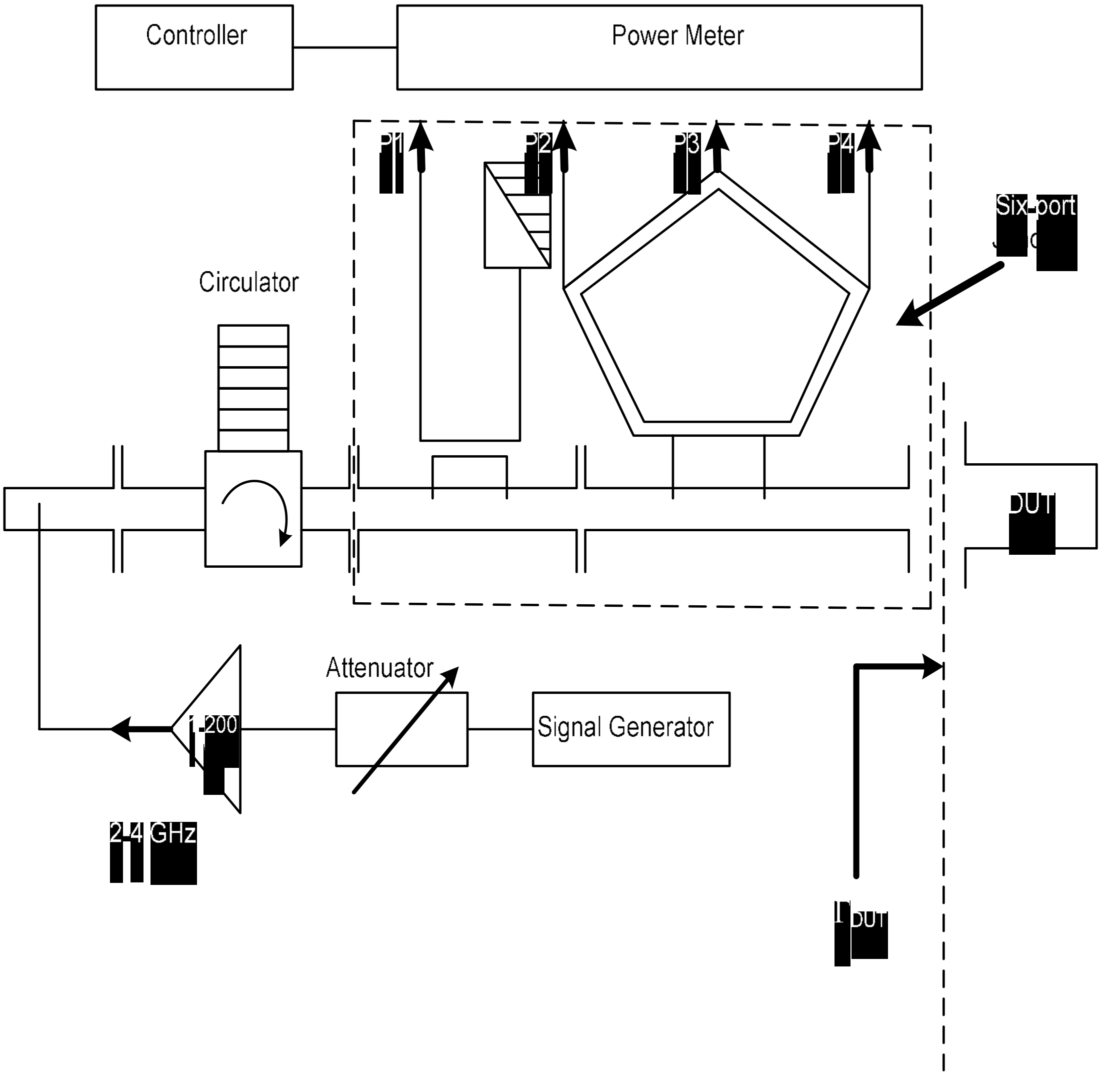

Figure 3.10 A high power six-port junction comprising a nonsymmetrical five-port ring junction in microstrip technology and hybrid stripline-waveguide directional coupler. (© 1994 IEEE [23].)

3.7 WORST-CASE ERROR ESTIMATION

It was shown in Chapter 2 that the six-port reflectometer can be linearly modeled by a 4×4 real matrix and the basic relation that governs its operation in (2.17) is repeated hereafter:

$$\underline{\mathbf{P}} = \rho \mathbf{C} \underline{\Gamma} \tag{3.39}$$

Also, it was shown that the calculation of the real and imaginary parts of the reflection coefficient can be realized by means of (2.19) repeated hereafter

$$R = \frac{\sum_{j=1}^{4} x_{3j} P_{j+2}}{\sum_{j=1}^{4} x_{1j} P_{j+2}} \quad \text{and} \quad I = \frac{\sum_{j=1}^{4} x_{4j} P_{j+2}}{\sum_{j=1}^{4} x_{1j} P_{j+2}} \tag{3.40}$$

In Chapter 2, it was shown that the q_i values of the six-port junction are related to the entries of matrix **C** by means of (2.18).

For a six-port junction that incorporates a reference port (port 3) to monitor the power level and which is completely isolated from the measuring port $(s_{32} \cong 0)$, and if the measuring port mismatch is not excessive $(s_{22} \cong 0)$, the module of q_3 becomes too large and the six-port junction is almost completely defined by the position of the three remaining q_4, q_5, and q_6. In such a case, the first row elements of **C** can be approximated by $c_{11} = 1$ and $c_{12} = c_{13} = c_{14} = 0$.

Figure 3.11 shows a geometrical representation of the different parameters involved in the worst case error estimation. Using some geometrical manipulations, it is simple to show that the expression of the relative error in amplitude measurements and the absolute error in phase measurements, in the worst-case situation, can be calculated using the absolute errors of the real and imaginary parts, $\Delta\mathrm{R}$ and $\Delta\mathrm{I}$ of the reflection coefficient $\Gamma = |\Gamma| \angle \varphi = R + jI$, as follows:

$$\frac{\Delta|\Gamma|}{|\Gamma|} = \max\left\{ \frac{\left||\Gamma_r| - |\Gamma|\right|}{|\Gamma|}, \frac{\left||\Gamma_b| - |\Gamma|\right|}{|\Gamma|} \right\} \tag{3.41a}$$

$$\Delta\varphi = \max\left(|\theta_n|, |\theta_v|\right) \tag{3.41b}$$

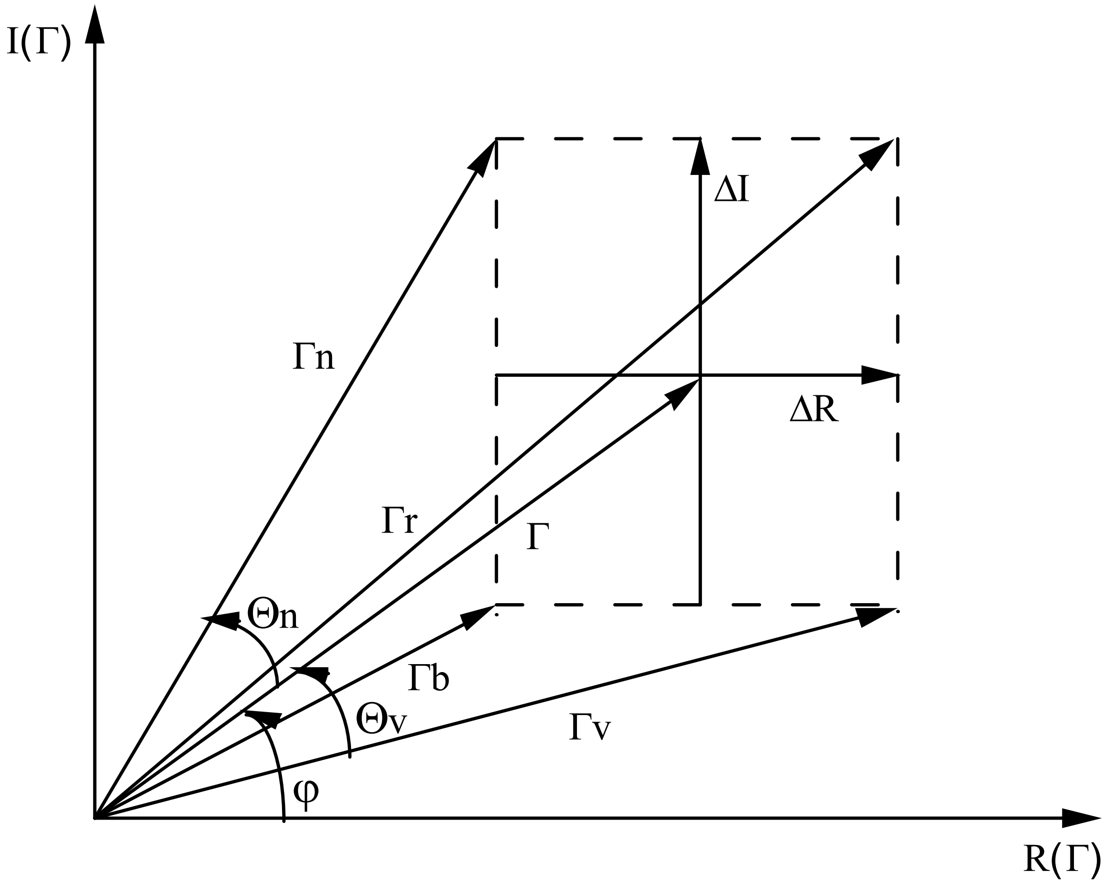

Figure 3.11 Geometrical representation of the different parameters involved in the worst-case error estimation.

where

$$\theta_n = \sin^{-1}\left\{\frac{\left[(\Delta R)^2+(\Delta I)^2\right]^{\frac{1}{2}}}{|\Gamma_n|}\sin\left(\frac{\pi}{2}+\varphi-\beta\right)\right\} \tag{3.42a}$$

$$\theta_v = \sin^{-1}\left\{\frac{\left[(\Delta R)^2+(\Delta I)^2\right]^{\frac{1}{2}}}{|\Gamma_v|}\sin\left(\frac{\pi}{2}+\varphi-\beta\right)\right\} \tag{3.42b}$$

$$|\Gamma_r|^2 = \left(|\Gamma|\cos\varphi+\Delta R\right)^2+\left(|\Gamma|\sin\varphi+\Delta I\right)^2 \tag{3.42c}$$

$$|\Gamma_v|^2 = \left(|\Gamma|\cos\varphi + \Delta\mathrm{R}\right)^2 + \left(|\Gamma|\sin\varphi - \Delta\mathrm{I}\right)^2 \tag{3.42d}$$

$$|\Gamma_n|^2 = \left(|\Gamma|\cos\varphi - \Delta\mathrm{R}\right)^2 + \left(|\Gamma|\sin\varphi + \Delta\mathrm{I}\right)^2 \tag{3.42e}$$

$$|\Gamma_b|^2 = \left(|\Gamma|\cos\varphi - \Delta\mathrm{R}\right)^2 + \left(|\Gamma|\sin\varphi - \Delta\mathrm{I}\right)^2 \tag{3.42f}$$

and

$$\beta = \tan^{-1}\left(\frac{\Delta\mathrm{R}}{\Delta\mathrm{I}}\right) \tag{3.42g}$$

Using (3.41), we can deduce the expression of the absolute errors of the real and imaginary parts of Γ as a function of the parameters of the six-port junction and the relative errors in the power readings as follows:

$$\Delta\mathrm{R} = \sum_{\mathrm{i}=3}^{6} \alpha_i P_i \left|\frac{\partial\mathrm{R}}{\partial P_i}\right| \tag{3.43a}$$

and

$$\Delta\mathrm{I} = \sum_{\mathrm{i}=3}^{6} \alpha_i P_i \left|\frac{\partial\mathrm{I}}{\partial P_i}\right| \tag{3.43b}$$

where

$$\frac{\partial\mathrm{R}}{\partial P_i} = \frac{\sum_{j=1}^{4}\left(x_{3,i-2}x_{1j} - x_{1,i-2}x_{3j}\right)P_{j+2}}{\left(\sum_{j=1}^{4} x_{1j}P_{j+2}\right)^2} \tag{3.44a}$$

$$\frac{\partial \mathrm{I}}{\partial P_i} = \frac{\sum_{j=1}^{4}\left(x_{4,i-2}x_{1j} - x_{1,i-2}x_{4j}\right)P_{j+2}}{\left(\sum_{j=1}^{4} x_{1j}P_{j+2}\right)^2} \tag{3.44b}$$

and

$$\alpha_i = \frac{\Delta P_i}{P_i},\ \text{i=3, 4, 5, and 6} \tag{3.44c}$$

To estimate the worst-case error in reflection coefficient measurements for a given six-port junction, it is sufficient to know the values of the q_i positions and the relative errors of the power detectors. The above formulation can be used to compare different six-port junction configurations, such as Engen's design or quasi-optimal design or other designs. A comparative study of some proposed six-port junction designs has been carried out in [24]. Constant contour plots, for amplitude and phase measurements, in the worst-case situation, have been obtained over the entire Smith chart and for different precision of power sensors. It was found that a dynamic range of 60 dB can be reached with a power sensor having a precision of 0.1%.

References

[1] Engen, G. F., "An Improved Circuit for Implementing the Six-Port Technique of Microwave Measurements," *IEEE Trans. on Microwave Theory & Tech.*, Vol. MTT 25, No. 12, pp. 1080–1083, December 1977.

[2] Griffin, E. J., "Six-Port Reflectometer Circuit Comprising Three Directional Coupler," *Electron Letts.*, pp. 491–493, 1982.

[3] Rafal, M. D., and Joines, W. T., "Optimizing the Design of the Six-Port Junction," *IEEE MTT-S Digest*, pp. 437–439, 1980.

[4] Collier, R. J., and N. A. Deeb, ""On the Use of a Microstrip Three Line System as a Six-Port Reflectometer," *IEEE Trans. on Microwave Theory & Tech.*, Vol. MTT-27, pp. 847–853, October 1979.

[5] Cullen, A. L., "Impedance Measurement Using Six-Port Directional Coupler," *IEE Proc.*, Vol. 127, Part H, No. 2, pp. 32–38, April 1980.

[6] Hansson, E. R. B., and G. P. Riblet, "An Ideal Six-Port Network Consisting of Matched Reciprocal Losses Five-Port and a Perfect Directional Coupler," *IEEE Trans. on Microwave Theory & Tech.*, Vol. 31, pp. 284–289, March 1983.

[7] Eda, K., "Miniature Hybrid Microwave IC's Using Novel Thin Film Technology," *MTT-S, International Microwave Symposium Digest*, pp. 419–422, 1990.

[8] Ghannouchi, F. M., S. Wang, and R. G. Bosisio, "A Preferred Frequency Balanced Six-Port Junction in Microstrip Line," *SMBO International Microwave Symposium Proceedings*, Vol. 1, pp. 285–290, July 1989.

[9] Cullen A. L., and A. J. Belfort, "Seven Port Millimeter-Wave Reflectometer," *Electronics Lett.,* Vol. 21, No. 3, January 1985.

[10] Riblet G. P., and E. R. B. Hansson, "An Ideal Six-Port Network Consisting of a Matched Reciprocal Lossless Five-Port and a Perfect Directional Coupler," *IEEE Tran. on Microwave Theory & Tech.*, Vol. MTT-31, No. 3, pp. 284–288, 1983.

[11] Robert, P. J., and J. E. Carroll, "Design Features of Multi-Port Reflectometers," *IEE Proc*., Vol. 129, Pt. H, No. 5, pp. 245–252, October 1982.

[12] Li, S. H., and R. G. Bosisio, "Analysis and Optimized Circuit of Six-Port Reflectometer," *Acta Electronica Sinica,* Vol. 11, No. 2, pp. 1–8, 1983.

[13] Wang, S., "A CAD/CAM Wideband Microwave Six-Port Junction," *Master thesis, École Polytechnique de Montreal*, February 1990.

[14] Griffin, E. J., G. J. Slack, and L. D. Hill, "Broadband Six-Port Reflectometer Junction," *Electron Lett.*, pp. 921–922, 1983.

[15] Feng, Z. H., "Broadband Dielectric Waveguide Coupler and Six-Port Network," *IEEE MTT-S Digest,* pp. 237–240, 1986.

[16] Malkomes, M., and R. Walsdorf, "Integrated Fin-Line 6-Ports for MM-Wave Network Analyzers," *IEEE MTT-S Digest,* pp. 669–671, 1986.

[17] Ohta, I., "A New Six-Port Microwave Network: Six-Port Magic Junction," *IEEE Tran. on Microwave Theory & Tech.*, Vol. MTT-36, pp. 859–864, May 1988.

[18] Berman, M., P. I. Somlo, and M. J. Buckley, "A Comparative Statistical Study of Some Proposed Six-Port Junction Designs," *IEEE Trans. on Microwave Theory & Tech.*, Vol. MTT-35, pp. 971–977, November 1987.

[19] Ghannouchi, F. M., R. G. Bosisio, and S. Wang "A CAD/CAM of an Optimum and Wideband Triplate Six Port Junction," International Conference on Millimeter Wave & Microwave (ICOMM-90), Dehra Dun, India, pp. 466–470, December 1990.

[20] Ghannouchi, F. M., R. G. Bosisio, D. Maurin, and M. Cuhaci, "A Design of Six-Port Junction on MHMIC Technology," Microwave *and Optical Tech. Letters,* Vol. 6, No.10, pp. 573–575, August 1993.

[21] Taymia, S. I., R. Hajji, and F. M. Ghannouchi, "A CAD/CAM of an Coplanar Wave Guide MMIC Six-Port Junction," *Canadian Conference in Electrical and Computer Engineering,* Montreal Canada, September 1995.

[22] Ghannouchi, F. M., "Compact Microwave Circuit Perform Swept Vector Measurements," *Microwave & RF*, pp. 67–68, February 1994.

[23] Akyel, C., F. M. Ghannouchi, and M. Caron, "A New Design for High-Power Six-Port Reflectometers Using Hybrid Stripline/Waveguide Technology," *IEEE Trans. on Instrumentation and Measurements*, Vol. 43, No. 2, pp. 316–321, April 1994.

[24] Ghannouchi, F. M., and R. G. Bosisio, "A Comparative Worst-Case Error Analysis of Some Proposed Six-Port Designs," *IEEE Trans. on Instrumentation and Measurements*, Vol. 37, No. 4, pp. 552–556, 1988.

Chapter 4

Calibration Techniques

In Chapter 2, the fundamentals of the six-port techniques have been presented and it has been shown that a calibration procedure to determine the parameters of the model of the six-port reflectometer is needed. Different methods have been proposed in the literature [1–14]. The number of known standards and the computation effort required are the most important parameters in selecting a calibration technique. Two categories of methods can be defined. The first category uses a linear formalism to solve for the calibration parameters, and the second category uses nonlinear formalism in conjunction with iterative numerical techniques to solve for the calibration parameters. In this chapter we will present five different calibration techniques as well as a calibration technique to increase the dynamic range of the six-port reflectometer. A calibration technique using active loads will be also presented.

4.1 CALIBRATION METHOD USING SEVEN STANDARDS

It was shown in Chapter 2 that the three normalized power readings are related to reflection coefficient of a DUT, Γ, as follows:

$$p_i = \left| \frac{d_i \Gamma + e_i}{c_3 \Gamma + 1} \right|^2 \quad i = 4, 5, \text{ and } 6 \tag{4.1}$$

By designating $\Gamma = x + jy$, $c_3 = c_{x3} + jc_{y3}$, $d_i = d_{xi} + jd_{yi}$, and $e_i = e_{xi} + je_{yi}$, and after algebraic manipulations, (4.1) can be written as follows:

$$\begin{aligned} &p_i \left(1 + |c_3|^2 \left(x^2 + y^2 \right) + 2 \left(c_{x3} x - c_{y3} y \right) \right) = \\ &|d_i|^2 \left(x^2 + y^2 \right) + |e_i|^2 + 2 \left(\eta_i x + \kappa_i y \right) \end{aligned}, \quad i = 4, 5, \text{ and } 6 \tag{4.2}$$

where $\eta_i = d_{xi}e_{xi} + d_{yi}e_{yi}$ and $\kappa_i = d_{xi}e_{yi} - d_{yi}e_{xi}$. The connection of a well-known standard having a reflection coefficient, Γ_k, to the measuring port of the six-port reflectometer gives

$$1+|c_3|^2\left(x_k^2+y_k^2\right)+2\left(c_{x3}x_k-c_{y3}y_k\right)=\frac{1}{p_{ik}}\left[|d_i|^2\left(x_k^2+y_k^2\right)+|e_i|^2+2\left(\eta_i x_k+\kappa_i y_k\right)\right]$$

$$\text{for} \quad i=4,\,5,\text{ and }6 \tag{4.3}$$

As we have mentioned before, the determination of the relative values of the calibration parameters is sufficient because the formalism that relates the reflection coefficient, Γ, to the calibration parameters is power independent; thus, one can deliberately set the value of the amplitude of c_3 to unity ($|c_3|=1$).

It is important to notice that for a given standard k, (4.3) provides only two independent equations, because the left-hand side of (4.3) is the same for the three equations. Therefore, *seven* standards are required to solve for the 14 real linearly independent calibration parameters $|d_i|^2$, $|e_i|^2$, c_{x3}, c_{y3}, η_i, and κ_i.

Alternatively, one can solve the set of 14 equations, obtained using (4.3) and seven standards, as a nonlinear set of 14 equations comprising fourteen independent unknowns $c_{x3}, c_{y3}, d_{xi}, d_{yi}, e_{xi}$, and e_{yi}; *i*= 4, 5, and 6. Writing (4.2) for *i* and *j* with *i*≠*j* and subtracting these equations, one can easily deduce that

$$x^2+y^2=\frac{ep_{ij}+\eta p_{ij}x+\kappa p_{ij}y}{-dp_{ij}} \tag{4.4}$$

Where $ep_{ij}=\frac{|e_i|^2}{p_i}-\frac{|e_j|^2}{p_j}$, $dp_{ij}=\frac{|d_i|^2}{p_i}-\frac{|d_j|^2}{p_j}$, $\eta p_{ij}=2\left(\frac{|\eta_i|^2}{p_i}-\frac{|\eta_j|^2}{p_j}\right)$, and

$\kappa p_{ij}=2\left(\frac{|\kappa_i|^2}{p_i}-\frac{|\kappa_j|^2}{p_j}\right)$ for $i=4$, 5, and 6; $j=4$, 5, and 6 and $i\neq j$.

Equation (4.4) leads to a set of two linear and independent equations in *x* and *y*

$$\begin{cases} dp_{46}\left(ep_{45}+\eta p_{45}x+\kappa p_{45}y\right)=dp_{45}\left(ep_{46}+\eta p_{46}x+\kappa p_{46}y\right) \\ dp_{56}\left(ep_{45}+\eta p_{45}x+\kappa p_{45}y\right)=dp_{45}\left(ep_{56}+\eta p_{56}x+\kappa p_{56}y\right) \end{cases} \tag{4.5}$$

The calculation of the real and imaginary parts of the reflection coefficient Γ of any DUT connected to the measuring port uses the three relative power readings and the calibration parameters as follows:

$$x = \frac{\left\{ \begin{array}{l} \left(ep_{45}dp_{56} - ep_{56}dp_{45}\right)\left(\kappa p_{56}dp_{46} - \kappa p_{46}dp_{56}\right) - \\ \left(ep_{46}dp_{56} - ep_{56}dp_{46}\right)\left(\kappa p_{56}dp_{54} - \kappa p_{45}dp_{56}\right) \end{array} \right\}}{\left\{ \begin{array}{l} \left(\eta p_{56}dp_{45} - \eta p_{45}dp_{56}\right)\left(\kappa p_{56}dp_{46} - \kappa p_{46}dp_{56}\right) - \\ \left(\eta p_{56}dp_{46} - \eta p_{46}dp_{56}\right)\left(\kappa p_{56}dp_{56} - \kappa p_{45}dp_{56}\right) \end{array} \right\}} \tag{4.6a}$$

and

$$y = \frac{\left\{ \begin{array}{l} \left(\eta p_{56}dp_{45} - \eta p_{45}dp_{56}\right)\left(ep_{46}dp_{56} - \kappa p_{56}dp_{46}\right) - \\ \left(ep_{45}dp_{56} - ep_{56}dp_{45}\right)\left(\eta p_{56}dp_{46} - \eta p_{46}dp_{56}\right) \end{array} \right\}}{\left\{ \begin{array}{l} \left(\eta p_{56}dp_{45} - \eta p_{45}dp_{56}\right)\left(\kappa p_{56}dp_{46} - \kappa p_{46}dp_{56}\right) - \\ \left(\eta p_{56}dp_{46} - \eta p_{46}dp_{56}\right)\left(\kappa p_{56}dp_{56} - \kappa p_{46}dp_{56}\right) \end{array} \right\}} \tag{4.6b}$$

This method requires a large number of well-known standards. The imprecision in the knowledge of their reflection coefficients has a direct effect on the accuracy of the calculation of the calibration parameters, consequently the accuracy of the reflection coefficient measurements. Therefore, it is more interesting, in practice, to minimize the number of the known calibration standards required in the calibration procedure. For this reason a calibration technique that requires only five standards is reported in the next section.

4.2 LINEAR CALIBRATION USING FIVE STANDARDS

It was shown in Chapter 2 that the six-port reflectometers can be modeled by a (4×4) real matrix, **C**, which relates the four power readings to the complex reflection coefficient Γ as follows:

$$\underline{\mathbf{P}} = \rho \mathbf{C} \underline{\mathbf{\Gamma}} \tag{4.7}$$

where $\underline{\mathbf{P}} = \left[p_3, p_4, p_5, p_6\right]^T$, $\underline{\mathbf{\Gamma}} = \left[1 \quad |\Gamma|^2 \quad \mathrm{Re}(\Gamma) \quad \mathrm{Im}(\Gamma)\right]^T$, and $\rho = |b_2|^2$. By connecting four different standards to the measuring port, one can write in an explicit manner:

$$\begin{bmatrix} p_{3k} \\ p_{4k} \\ p_{5k} \\ p_{6k} \end{bmatrix} = \rho_k \begin{bmatrix} c_{31} & c_{32} & c_{33} & c_{34} \\ c_{41} & c_{42} & c_{43} & c_{44} \\ c_{51} & c_{52} & c_{53} & c_{54} \\ c_{61} & c_{62} & c_{63} & c_{64} \end{bmatrix} \begin{bmatrix} 1 \\ |\Gamma_k|^2 \\ \mathrm{Re}(\Gamma_k) \\ \mathrm{Im}(\Gamma_k) \end{bmatrix} \quad k\text{=1, 2, 3, and 4} \tag{4.8}$$

By dividing each row of the above matrix equation by the first row one can obtain:

$$\begin{gathered} c_{j1} + c_{j2}|\Gamma_k|^2 + c_{j3}\mathrm{Re}(\Gamma_k) + c_{j4}\mathrm{Im}(\Gamma_k) = \\ \frac{p_{jk}}{p_{3k}}\left(c_{31} + c_{32}|\Gamma_k|^2 + c_{33}\mathrm{Re}(\Gamma_k) + c_{34}\mathrm{Im}(\Gamma_k)\right) \end{gathered} \tag{4.9}$$

with j = 4, 5, and 6 designating the power readings and k = 1, 2, 3, and 4 designating the calibration standards.

The above equations can be written in matrix format as follows

$$\underline{\mathbf{C}}_\mathbf{j} = \mathbf{G}^{-1}\mathbf{P}_\mathbf{j}\mathbf{P}_\mathbf{3}^{-1}\mathbf{G}\underline{\mathbf{C}}_\mathbf{3} \tag{4.10}$$

where $\underline{\mathbf{C}}_\mathbf{j} = \left[c_{j1}, c_{j2}, c_{j3} c_{j4}\right]^T$

$$\mathbf{G} = \begin{bmatrix} 1 & |\Gamma_1|^2 & \mathrm{Re}(\Gamma_1) & \mathrm{Im}(\Gamma_1) \\ 1 & |\Gamma_2|^2 & \mathrm{Re}(\Gamma_2) & \mathrm{Im}(\Gamma_2) \\ 1 & |\Gamma_3|^2 & \mathrm{Re}(\Gamma_3) & \mathrm{Im}(\Gamma_3) \\ 1 & |\Gamma_4|^2 & \mathrm{Re}(\Gamma_4) & \mathrm{Im}(\Gamma_4) \end{bmatrix} \quad \mathbf{P}_\mathbf{j} = \begin{bmatrix} p_{j1} & 0 & 0 & 0 \\ 0 & p_{j2} & 0 & 0 \\ 0 & 0 & p_{j3} & 0 \\ 0 & 0 & 0 & p_{j4} \end{bmatrix}$$

Using (4.10), it can be easily deduced that

$$\mathbf{P}_\mathbf{3}^{-1}\mathbf{G}\underline{\mathbf{C}}_\mathbf{3} = \mathbf{P}_4^{-1}\mathbf{G}\underline{\mathbf{C}}_4 = \mathbf{P}_5^{-1}\mathbf{G}\underline{\mathbf{C}}_5 = \mathbf{P}_6^{-1}\mathbf{G}\underline{\mathbf{C}}_6 = \underline{\mathbf{V}}_\mathbf{0} \tag{4.11}$$

where $\underline{\mathbf{V}}_\mathbf{0} = \left[\frac{1}{\rho_1}, \frac{1}{\rho_2}, \frac{1}{\rho_3}, \frac{1}{\rho_4}\right]^T$ is an unknown vector related to the power flow exciting the four standards during calibration procedure. Equation (4.11) leads to

$$\underline{\mathbf{C}}_\mathbf{j} = \mathbf{G}^{-1}\mathbf{P}_\mathbf{j}\underline{\mathbf{V}}_\mathbf{0}, j\text{=3, 4, 5, and 6} \tag{4.12}$$

After connecting a fifth standard to the measuring port, one can write

$$\underline{\mathbf{P}}_{\mathbf{5}} = \rho_5 \mathbf{C} \underline{\Gamma}_5 = \rho_5 \left[\underline{\mathbf{C}}_3, \underline{\mathbf{C}}_4, \underline{\mathbf{C}}_5, \underline{\mathbf{C}}_6 \right]^T \underline{\Gamma}_5 \tag{4.13}$$

Substituting (4.12) in (4.13), one can write

$$\underline{\mathbf{P}}_{\mathbf{5}} = \rho_5 \left[\mathbf{G}^{-1}\mathbf{P}_3 \underline{\mathbf{V}}_{\mathbf{0}}, \mathbf{G}^{-1}\mathbf{P}_4 \underline{\mathbf{V}}_{\mathbf{0}}, \mathbf{G}^{-1}\mathbf{P}_5 \underline{\mathbf{V}}_{\mathbf{0}}, \mathbf{G}^{-1}\mathbf{P}_6 \underline{\mathbf{V}}_{\mathbf{0}} \right]^T \underline{\Gamma}_5 \tag{4.14}$$

Rearranging (4.14), one can write

$$\underline{\mathbf{P}}_{\mathbf{5}} = \rho_5 \left[\underline{\mathbf{V}}_{\mathbf{0}}^T \mathbf{P}_3, \underline{\mathbf{V}}_{\mathbf{0}}^T \mathbf{P}_4, \underline{\mathbf{V}}_{\mathbf{0}}^T \mathbf{P}_5, \underline{\mathbf{V}}_{\mathbf{0}}^T \mathbf{P}_6 \right] \underline{\mathbf{S}} \tag{4.15}$$

where $\underline{\mathbf{S}} = \left[\mathbf{G}^{-1} \right]^T \underline{\Gamma}_5 = \left[a, b, c, d \right]^T$ is a known vector which can be calculated using the five reflection coefficients of the five calibration standards. Equation (4.15) can be written in an explicit manner as follows

$$\begin{bmatrix} p_{35} \\ p_{45} \\ p_{55} \\ p_{65} \end{bmatrix} = \begin{bmatrix} p_{31}a & p_{32}b & p_{33}c & p_{34}d \\ p_{41}a & p_{42}b & p_{43}c & p_{44}d \\ p_{51}a & p_{52}b & p_{53}c & p_{54}d \\ p_{61}a & p_{62}b & p_{63}c & p_{64}d \end{bmatrix} \begin{bmatrix} \rho_5/\rho_1 \\ \rho_5/\rho_2 \\ \rho_5/\rho_3 \\ \rho_5/\rho_4 \end{bmatrix} \tag{4.16}$$

The solution of the above matrix equation leads to the calculation of the relative values of the entries of vector $\rho_5 \underline{\mathbf{V}}_{\mathbf{0}}$. It was mentioned in Chapter 1 that the formalism to calculate the reflection coefficient is power level independent; therefore, the proportionality constant ρ_5 has no effect on the overall final results since it is automatically embedded in the calibration parameters c_{ij}.

Knowing $\rho_5 \underline{\mathbf{V}}_{\mathbf{0}}$ and using (4.12), one can deduce all the entries of the calibration matrix **C**. The calculation of the reflection coefficient for any DUT is as follows

$$\mathrm{Re}(\Gamma) = \frac{\sum_{j=1}^{4} x_{3j} P_{j+2}}{\sum_{j=1}^{4} x_{1j} P_{j+2}}, \quad \mathrm{Im}(\Gamma) = \frac{\sum_{j=1}^{4} x_{4j} P_{j+2}}{\sum_{j=1}^{4} x_{1j} P_{j+2}} \tag{4.17}$$

where x_{ij} are the entries of the inverse of the calibration matrix **C**. The power absorbed by the DUT can be calculated as follows:

$$P_{DUT} = |b_2|^2 \left(1 - |\Gamma_{DUT}|^2\right) = \left(1 - |\Gamma_{DUT}|^2\right)\left(\sum_{j=1}^{4} x_{1j} P_{j+2}\right) \tag{4.18}$$

4.3 NONLINEAR CALIBRATION USING FOUR STANDARDS

It was shown in Chapter 1 that the calibration matrix of the six-port reflectometers is the following:

$$\mathbf{C} = \begin{bmatrix} \alpha_3^2 |q_3|^2 & \alpha_3^2 & -2\alpha_3^2 \mathrm{Re}(q_3) & -2\alpha_3^2 \mathrm{Im}(q_3) \\ \alpha_4^2 |q_4|^2 & \alpha_4^2 & -2\alpha_4^2 \mathrm{Re}(q_4) & -2\alpha_4^2 \mathrm{Im}(q_4) \\ \alpha_5^2 |q_5|^2 & \alpha_5^2 & -2\alpha_5^2 \mathrm{Re}(q_5) & -2\alpha_5^2 \mathrm{Im}(q_5) \\ \alpha_6^2 |q_6|^2 & \alpha_6^2 & -2\alpha_6^2 \mathrm{Re}(q_6) & -2\alpha_6^2 \mathrm{Im}(q_6) \end{bmatrix} \tag{4.19}$$

One can deduce from (4.19) that the elements of each row are related by the following equation:

$$c_{j3}^2 + c_{j4}^2 - 4c_{j1}c_{j2} = 0 \text{ , } j = 3, 4, 5, \text{ and } 6 \tag{4.20}$$

On the other hand, it was also shown that

$$\underline{\mathbf{C}}_{\mathbf{j}} = \mathbf{H}^{\mathbf{j}} \underline{\mathbf{C}}_{\mathbf{3}} \quad ; j = 3, 4, 5, \text{ and } 6 \tag{4.21}$$

where $\mathbf{H}^{\mathbf{j}} = \mathbf{G}^{-1}\mathbf{P}_{\mathbf{j}}\mathbf{P}_{\mathbf{3}}^{-1}\mathbf{G}$ and $\mathbf{G}$ is a known matrix related to the four reflection coefficients of the four standards and their corresponding power readings. As we have mentioned before, the knowledge of the relative values of the entries of the calibration matrix of the six-port reflectometer is sufficient to perform measurements since the measurement equation is power independent. Therefore, without any constraint, we can fix c_{11} to unity.

The substitution of (4.21) into (4.20) and the writing of results in explicit manner give

$$\begin{aligned} &\delta_1^j + \delta_2^j c_{32}^2 + \delta_3^j c_{33}^2 + \delta_4^j c_{34}^2 + 2(\sigma_{23}^j c_{32} c_{33} + \sigma_{24}^j c_{32} c_{34} + \\ &\sigma_{34}^j c_{33} c_{34} + \sigma_{12}^j c_{32} + \sigma_{13}^j c_{33} + \sigma_{14}^j c_{34}) = 0 \end{aligned} \tag{4.22}$$

where $\delta_i^j = (h_{3i}^j)^2 + (h_{4i}^j)^2 - 4h_{1i}^j h_{2i}^j$, and $\sigma_{ik}^j = h_{3i}^j h_{3k}^j + h_{4i}^j h_{4k}^j - 2(h_{1i}^j h_{2k}^j + h_{2i}^j h_{1k}^j)$,

with $j = 3, 4, 5$, and 6.

Equation (4.22) is a set of four nonlinear equations comprising three unknowns: c_{32}, c_{33}, and c_{34}. In practical situations, the six-port junction incorporates a reference port, port 3, to monitor the power level; hence, the power reading P_3 is quasi-independent of the DUT. In such a case the entries of the first row can be approximated by $c_{31} \approx 1$, and $c_{32} \approx c_{33} \approx c_{34} \approx 0$. These values can be used as initial guests for the numerical algorithm needed to calculate the actual values of the three unknowns. The Newton-Raphson technique can be used for this purpose. Following the calculation of the entries of the first row of the **C** matrix, the values of the entries of the remaining rows can be straightforwardly calculated using (4.10). The calculation of the reflection coefficient of any DUT is then obtained using (4.17).

All the calibration and measurement methods described above require the use of well-known standards and relate explicitly in one step the reflection coefficient Γ to the power readings and the calibration parameters. The calibration and measurement procedures based on the six- to four-port reduction technique and the concept of de-embedding are more powerful and robust, in practice, since they require only three well-known standards.

4.4 NONLINEAR CALIBRATION USING THREE STANDARDS

It was mentioned in Chapter 1 that 11 real parameters are sufficient to model the six-port reflectometer. It also was mentioned that the embedded reflection coefficient, w_4, can be related to the reflection coefficient, Γ, via the three error box complex parameters (six real parameters). This is shown in Figure 4.1. Consequently, the partition of the calibration in two different steps is possible.

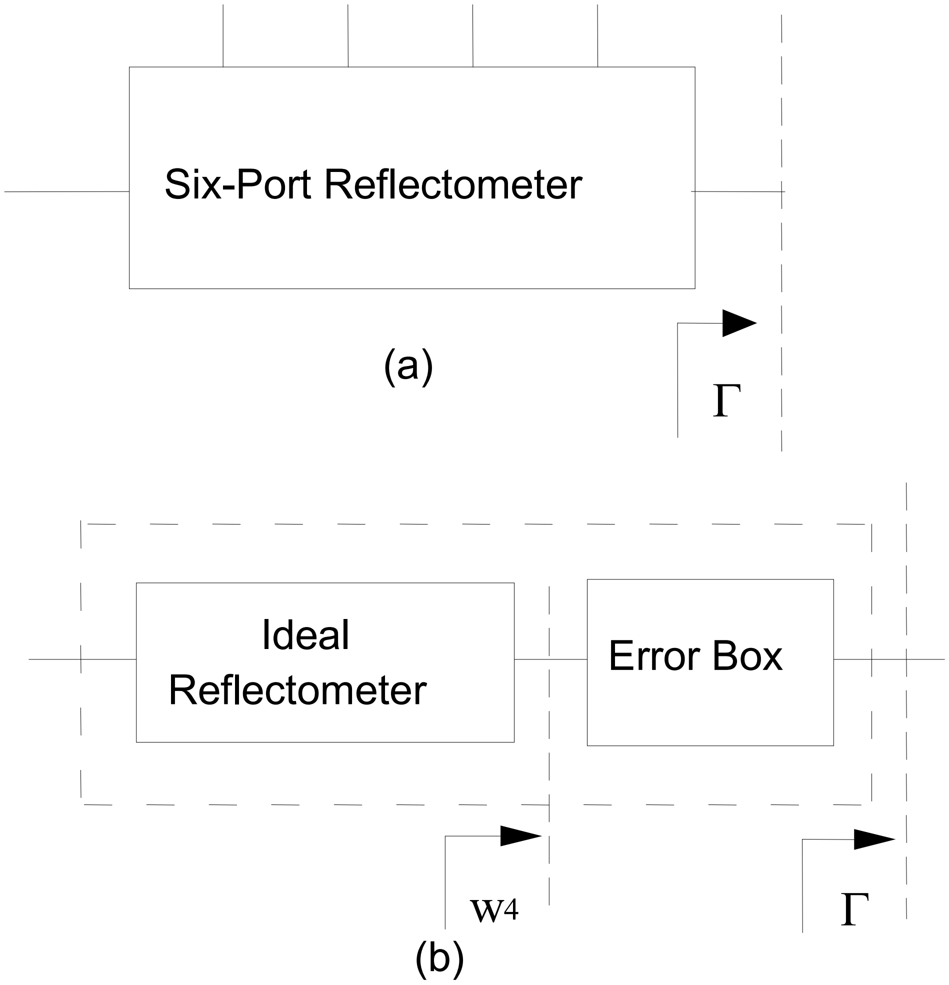

Figure 4.1 Modeling of a six-port reflectometer; (a) an actual six-port reflectometer, and (b) an ideal reflectometer followed by a two-port error box network.

The first step is to find five real parameters that relate the four power readings to the embedded reflection coefficient, w_4, and the second step is to find in the error box, three complex parameters, c, d, and e, which relate, w_4 to Γ via a bilinear transformation. By defining

$$w = w_4 e^{-j\varphi_m} \tag{4.24}$$

Equation (2.29) becomes

$$p_4 = |w|^2 \tag{4.25}$$

$$p_5 = \frac{1}{A_5^2}\left|w - |m|\right|^2 \tag{4.26}$$

$$p_6 = \frac{1}{A_6^2}\left|w - |n|\, e^{j(\varphi_n - \varphi_m)}\right|^2 \tag{4.27}$$

We notice that the second Q_i point in the W plane becomes real following the bilinear mapping. The graphical common intersection of these circles in the W plane gives the de-embedded reflection coefficient w shown in Figure 4.2. Equations (2.32) and (2.33) give explicit expressions for the calculation w_4 and can be used to calculate w providing that we substitute $|m|\angle\varphi_m$ and $|n|\angle\varphi_n$ by $|m|\angle 0^\circ$ and $|n|\angle(\varphi_n - \varphi_m)$ in (2.33), respectively. Therefore, the real and imaginary parts of the embedded reflection coefficient w can be calculated as follows:

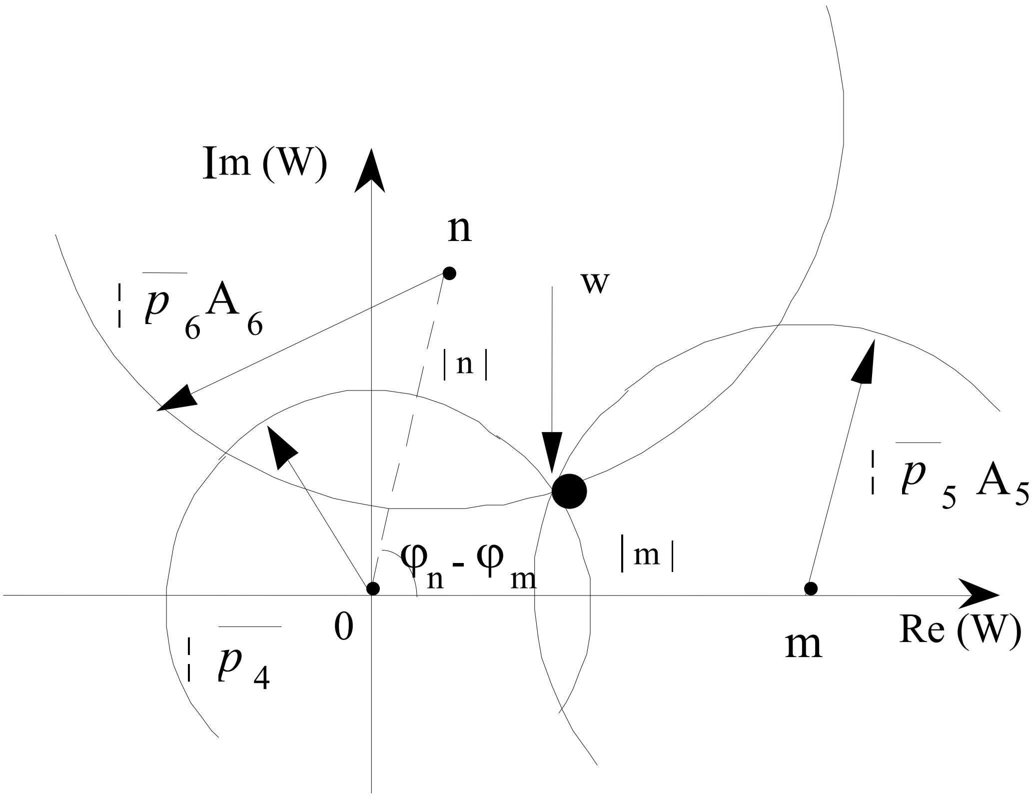

Figure 4.2 Graphical solution in the W plane.

$$\mathrm{Re}(w) = \frac{p_4 - A_5^2 p_5 + m^2}{2m} \tag{4.28}$$

$$\mathrm{Im}(w) = \frac{\left(p_4 - A_6^2 p_6 + |n|^2\right)}{2|n|\sin\left(\varphi_\mathrm{n} - \varphi_\mathrm{m}\right)} + \frac{\cos\left(\varphi_\mathrm{n} - \varphi_m\right)\left(p_4 - A_5^2 p_5 + m^2\right)}{2m\sin\left(\varphi_\mathrm{n} - \varphi_\mathrm{m}\right)} \tag{4.29}$$

Knowing that $p_4 = |w|^2 = \left(\mathrm{Re}(w)\right)^2 + \left(\mathrm{Im}(w)\right)^2$ and using (4.28) and (4.29), one can eliminate *w* and obtain a nonlinear equation function only of the power readings and the five calibration parameters as follows:

$$\begin{aligned} &|n|^2\left(p_4 - A_5^2 p_5 + m^2\right)^2 + m^2\left(p_4 - A_6^2 p_6 + |n|^2\right)^2 - 4m^2|n|^2 p_4\left(1 - z^2\right) \\ &-2m|n|\left(p_4 - A_5^2 p_5 + m^2\right)\left(p_4 - A_6^2 p_6 + |n|^2\right)z = 0 \end{aligned} \tag{4.30}$$

where $z = \cos\left(\varphi_\mathrm{n} - \varphi_\mathrm{m}\right)$. Equation (4.30) is the basis of six- to four-port reduction techniques. At least five different and unknown loads are required to generate a system of five equations in order to solve for the five calibration parameters $A_5, A_6, m, |n|$, and *z*.

It is clear from the (4.30) that the solution, $m = n = 0$, is the trivial one to avoid, since (4.30) will be equal to zero regardless of the values of the normalized power readings, p_4, p_5, and p_6 or the parameters A_5 and A_6. The calculation of the de-embedded reflection coefficient *w* as a function of the power readings and the five calibration parameters are as follows:

$$\mathrm{Re}(w) = \frac{p_4 - A_5^2 p_5 + m^2}{2m} \tag{4.31a}$$

$$\mathrm{Im}(w) = \frac{\pm 1}{\sqrt{1 - z^2}}\left(\frac{p_4 - A_6^2 p_6 + |n|^2}{2|n|} + \frac{z\left(p_4 - A_5^2 p_5 + m^2\right)}{2m}\right) \tag{4.31b}$$

The sign ambiguity can be resolved using a partially known reflection coefficient.

To obtain a good estimation of the embedded reflection coefficient, *w*, one can calculate the common intersection of the three radical axes as shown in Figure 4.3.

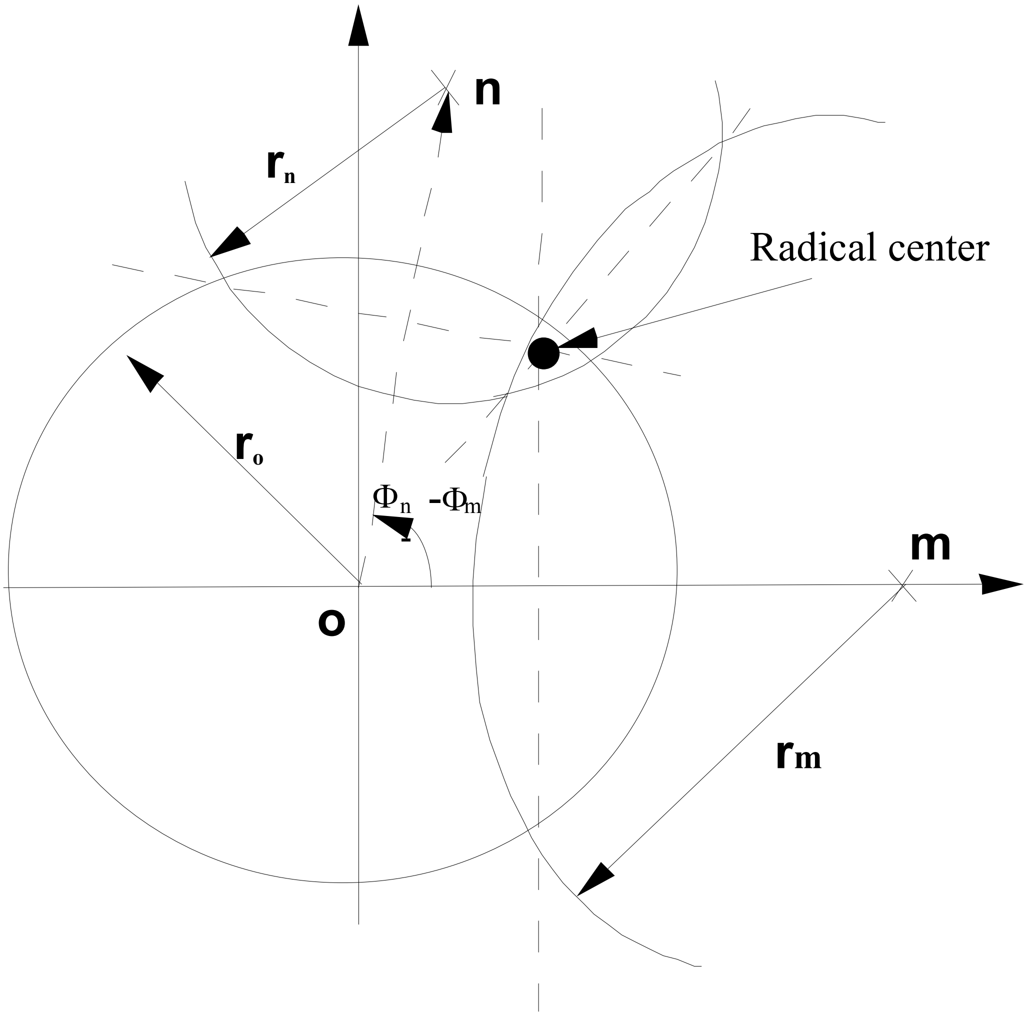

Figure 4.3 Common intersections of the three straight lines in the *W* complex plane.

Each straight line passes through the two common intersections of one pair of circles among the three pairs. This intersection is the radical center, r_c, of the three circles, and its coordinates are:

$$\operatorname{Re}\left(r_c\right) = \frac{r_0^2 - r_m^2 + m^2}{2m} \tag{4.32a}$$

$$\operatorname{Im}\left(r_c\right) = \frac{r_0^2 - r_n^2 + |n|^2 - 2\operatorname{Re}(r_c)|n|\sqrt{1-z^2}}{2z|n|} \tag{4.32b}$$

where $r_0^2 = p_4$ is the square of the first circle; $r_m^2 = A_5^2 p_5$ is the square of the second circle, and $r_n^2 = A_6^2 p_6$ is the square of the third circle.

In practice, the intersection of the three circles is not a clear point, but a small curvilinear triangle where the "true" embedded reflection coefficient should fall as shown in Figure 4.2. Equation (4.32) can be used to calculate an estimate of *w*. This estimate can be used as an initial guess for further iterative calculations to obtain the actual embedded reflection coefficient, *w*.

For the **omn** triangle in Figure 4.3, it easy to deduce that:

$$z = \cos\left(\varphi_{\mathrm{n}} - \varphi_{\mathrm{m}}\right) = \frac{|n|^2 + |m|^2 - |n-m|^2}{2|nm|} \tag{4.33}$$

By substituting (4.33) into (4.30), one can obtain an equivalent equation identical to the one published in [12, 15, and 16] as follows:

$$\begin{gathered} pp_4^2 + qA_5^4 p_5^2 + rA_6^4 p_6^2 + (r-p-q)A_5^2 p_4 p_5 + (q-p-r)A_6^2 p_4 p_6 \\ +(p-q-r)A_5^2 A_6^2 p_5 p_6 + p(p-q-r)p_4 + q(q-p-r)A_5^2 p_5 + \\ r(r-p-q)A_6^2 p_6 + pqr = 0 \end{gathered} \tag{4.34}$$

where $p = |n-m|^2$, $q = |n|^2$ and $r = |m|^2$.

By introducing new variables, (4.34) can be linearized as follows [15]:

$$\begin{gathered} x_1 p_4^2 + x_2 p_5^2 + x_3 p_6^2 + x_4 p_4 p_5 + x_5 p_5 p_6 + x_6 p_5 p_6 \\ + x_7 p_4 + x_8 p_5 + x_9 p_6 = -1 \end{gathered} \tag{4.35}$$

where

$$x_1 = 1/qr \tag{4.36a}$$

$$x_2 = A_5^4/pr \tag{4.36b}$$

$$x_3 = A_6^4/pq \tag{4.36c}$$

$$x_4 = (r-p-q)A_5^2/pqr \tag{4.36d}$$

$$x_5 = \left(q-p-r\right)A_6^2 \big/ pqr \tag{4.36e}$$

$$x_6 = \left(p-q-r\right)A_5^2 A_6^2 \big/ pqr \tag{4.36f}$$

$$x_7 = \left(p-q-r\right) \big/ qr \tag{4.36g}$$

$$x_8 = \left(q-p-r\right)A_5^2 \big/ pr \tag{4.36h}$$

$$x_9 = \frac{(r-p-q)A_6^2}{pq} \tag{4.36i}$$

In practice, nine or more different and unknown loads are needed to solve a linear system that can be formed using (4.35). The value obtained can be used to calculate an initial guess for the nonlinear system to be solved in the least squares sense as follows [15].

$$r = \frac{2x_5 - x_7x_9}{2x_1x_9 - x_5x_7} \tag{4.37a}$$

$$q = \frac{2x_4 - x_7x_8}{2x_1x_8 - x_4x_7} \tag{4.37b}$$

$$p = \frac{2x_5 - x_7x_9}{2x_1x_9 - x_5x_7} + \frac{2x_4 - x_7x_8}{2x_1x_8 - x_4x_7} + \frac{x_7}{x_1} \tag{4.37c}$$

$$A_5 = \left(x_2 \left(\frac{2x_5 - x_7x_9}{2x_1x_9 - x_5x_7} + \frac{2x_4 - x_7x_8}{2x_1x_8 - x_4x_7} + \frac{x_7}{x_1} \right) \left(\frac{2x_5 - x_7x_9}{2x_1x_9 - x_5x_7} \right) \right)^{\frac{1}{4}} \tag{4.37d}$$

$$A_6 = \left(x_3 \left(\frac{2x_5 - x_7 x_9}{2x_1 x_9 - x_5 x_7} + \frac{2x_4 - x_7 x_8}{2x_1 x_8 - x_4 x_7} + \frac{x_7}{x_1} \right) \left(\frac{2x_4 - x_7 x_8}{2x_1 x_8 - x_4 x_7} \right) \right)^{\frac{1}{4}} \tag{4.37e}$$

Using (4.24) and knowing from (2.24) and (2.27) that:

$$w = \frac{d\Gamma + e}{c\Gamma + 1} \text{ and } w_4 = \frac{d_4\Gamma + e_4}{c_3\Gamma + 1} \tag{4.38}$$

one can easily deduce that

$$d = d_4 e^{-j\varphi_m}, e = e_4 e^{-j\varphi_m} \text{ and } c = c_3 \tag{4.39}$$

From (4.39) it is clear that the effect of the rotation of plane W_4 by ϕ_m to obtain the W plane is automatically taken into account by the error box calibration procedure.

Using (2.34), one can easily deduce that

$$\Gamma = \frac{e - w}{cw - d} \tag{4.40}$$

The Q_i point's expression in the Γ plane can be deduced after performing calibration and error box measurement and calculations as follows:

$$q_{4/W} = 0 \rightarrow q_{4/\Gamma} = -\frac{e}{d} \tag{4.41a}$$

$$q_{5/W} = m \rightarrow q_{5/\Gamma} = \frac{e - m}{cm - d} \tag{4.41b}$$

and

$$q_{6/W} = |n| e^{j(\varphi_n - \varphi_m)} \rightarrow q_{6/\Gamma} = \frac{e - |n| e^{j(\varphi_n - \varphi_m)}}{c|n| e^{j(\varphi_n - \varphi_m)} - d} \tag{4.41c}$$

The advantage of the above calibration technique in comparison to other calibration techniques are: (1) the calibration requires only three well-known calibration standards for error box calibration procedure, and (2) the six- to four-port calibration procedure does not require any well-known calibration standards; however, it requires at least five unknown and different impedance terminations or excitation conditions.

In opposition to other calibration techniques, the measuring reference plane can be changed, for example, by adding a connector or a transition without a need to recalibrate the six-port reflectometer. Only a new error box calibration is required. The new error box calibration parameters and the "old" six- to four-port calibration parameters are needed to calculate the reflection coefficient of any DUT relative to the new measuring reference plane.

4.5 SELF-CALIBRATION BASED ON ACTIVE LOAD SYNTHESIS

It was mentioned earlier that the exact knowledge of the calibration standards used in six- to four-port reduction calibration technique is not required [16]. To insure stability of the numerical solvers, calibration standards with well-spaced reflection coefficients in the complex plane have to be used. These standards can be actively synthesized using the widely known active load concept and have been used in active load-pull systems.

The active load technique can lead, in principle, to the synthesis of any load (even outside the unit circle) over the Smith chart for calibration purposes [17]. With this method, all operations that are inherent to the reflectometer such as junction calibration become invisible to the user, leaving only a simple experimental procedure for error-box measurements [2] to be carried out, as in standard network analyzers. The block diagram of the system used is shown in Figure 4.4. It consists of the six-port reflectometer system (six-port junction, Schottky diode detectors, and CPU) and the controllable vector modulator (or a phase shifter and an attenuator).

The incoming signal from the source is split into two parts using a two-way power divider. One of them feeds port 1 of the junction, while the other passes through the modulator and feeds the measuring reference port 2.

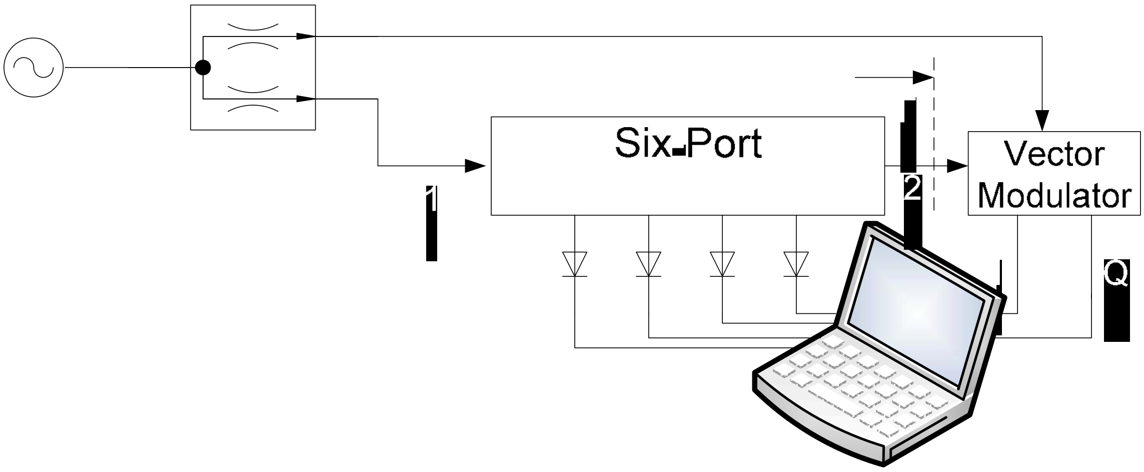

Figure 4.4 Block diagram of a self-calibration system for a six-port reflectometer.

The device used to control attenuation and phase shift in the loop is based on an in-phase and quadrature (IQ) vector modulator, which is controlled by two voltages (I and Q) and imposes attenuation and phase shift directly related to these two voltages. This relationship is theoretically described by the following equations

$$\phi = K \tan^{-1} \frac{I}{Q} \tag{4.42}$$

and

$$a = K^{/} \sqrt{I^2 + Q^2} \tag{4.43}$$

Where I and Q are the two control voltages, ϕ is the phase shift produced, and a is the attenuation. Thus, if a precise model of this device is available, that is, if the modulator follows exactly these equations and the constants K and K' are perfectly known, only one iteration measurement procedure is necessary to determine the necessary corrections to the reflection coefficient to bring it to the desired target. If the model is not precise enough, a few numbers of iterations will be needed to obtain reasonable precision on the targeted reflection coefficient [17].

With preliminary calibration data, the three measured power ratios are used to compute the value of the reflection coefficient seen at the measuring port [18]. After a comparison with the targeted reflection coefficient, appropriate instructions are sent to the attenuator and phase shifter to correct the coefficient and bring it to the desired value. In this way, the system can produce any reflection coefficient at the measuring port of the junction. Hence, the system is capable of successively producing the different standards needed in practice for a six- to four-port reduction technique [19].

The measurements taken after synthesizing each of the calibration loads constitute new updated calibration data, which can be used to update the previous calibration parameters. A six- to four-port reduction method cannot replace the error box procedure, which impacts the precision of the measurements and which is primordial for determining the reference plane [19]. As mentioned above, there is a need for a first manual calibration (e.g., [14, 20]), which can be seen as initial data provided by the system designer or manufacturer. This preliminary data need not be accurate, as the calibration loads must only be different, regardless of their absolute precise value. As the system parameters have a small drift in time, due to the numerous possible alterations to the working environment of the junction (such as temperature variations, detector aging, and so forth), this calibration data will grow "old," but can still be used as initial data for self-calibration, knowing that, as mentioned above, its absolute precision is not that important. An interesting property of the setup that can be stated is its ability to synthesize active loads positioned even outside the unit circle on the Smith chart. Experimentation shows that the measurement precision is excellent in the regions where the calibration loads were situated [17].

4.6 DYNAMIC RANGE EXTENSION

To obtain a good accuracy during measurements near the center of the Smith chart, it is recommended that one use a matched load among the standards required for the calibration procedure. In practice, the reflection due to the non-ideal matched load is added to the one due to the connector. This results in an overall residual error, $\Delta\Gamma$, which is added to the intrinsic reflection coefficient, Γ. The measured reflection coefficient Γ_m is the vector addition of both reflection coefficients shown in Figure 4.5. This results in a finite directivity of the measurement system, hence, the limitation of the dynamic range of the six-port reflectometer. The use of a sliding load in opposition to a fixed load can overcome this difficulty, and the dynamic range of the six-port reflectometer can be extended.

The basic relationship describing the behavior of the six-port reflectometer was reported in Chapter 2 as (2.21) and is repeated here

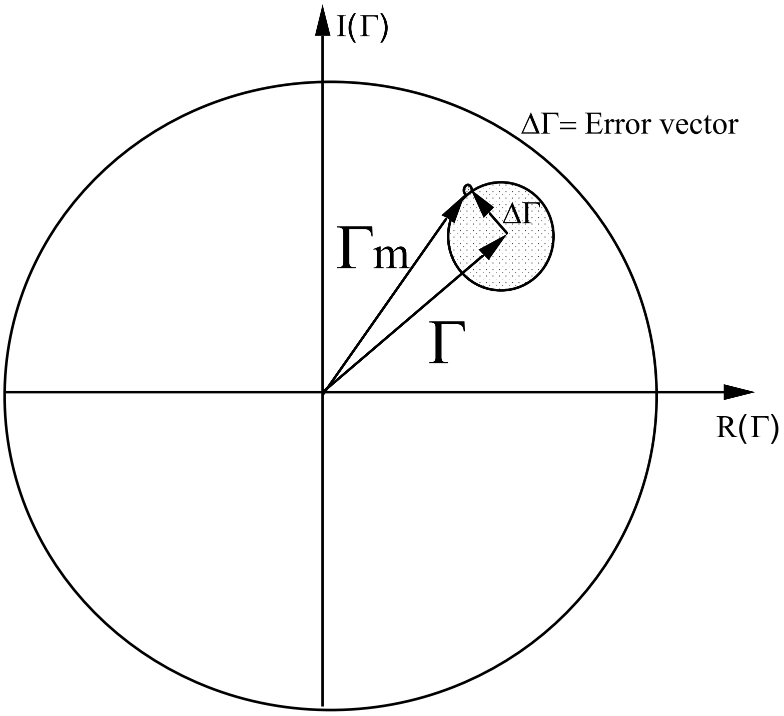

Figure 4.5 Residual reflection's error effect on the six-port measurement accuracy.

$$P_i = \alpha_i^2 \left|b_2\right|^2 \left|\Gamma - q_i\right|^2,\ i = 3, 4, 5, \text{ and } 6 \tag{4.44}$$

It can be easily shown that the power reading P_i corresponding to a device under test having an impedance near the center of the Smith chart $(\Gamma \approx 0)$ can be approximated with a good accuracy as follows:

$$P_i \cong P_i' - P_{oi} \cos\left(\theta_\Gamma - \theta_{q_i}\right) \tag{4.45}$$

where

$$P_i' = \alpha_i^2 \left|b_2\right|^2 \left|q_i\right|^2 \tag{4.46a}$$

$$P_{oi} = 2\alpha_i^2 \left|b_2\right|^2 \left|q_i\right| \left|\Gamma\right| \tag{4.46b}$$

and θ_Γ and θ_{q_i} are, respectively, the arguments of Γ and q_i. From (4.46) one can deduce that the variation of P_i as function of θ_Γ is sinusoidal and P_i' represents the power that should be detected when an ideal matched load $(\Gamma = 0)$ is connected to the measuring port.

In order to calculate P_i', three measurements of power readings are required. These measurements correspond to three different positions of the sliding load separated by known relative phase shifts α and β. Considering that the initial setting of the sliding load corresponds to the phase θ and the actual power level readings corresponding to $\theta, \alpha,$ and β are P_{i1}, P_{i2}, and P_{i3}, respectively, are as follows:

$$P_{i1} \cong P_i' - P_{oi}\cos(\theta) \tag{4.47a}$$

$$P_{i2} \cong P_i' - P_{oi}\cos(\theta + \alpha) \tag{4.47b}$$

$$P_{i3} \cong P_i' - P_{oi}\cos(\theta + \beta) \tag{4.47c}$$

Equation (4.40) forms a set of three equation with three unknowns θ, $P^{'}_{i}$, and P_{oi}. The analytical solution of this set leads to:

$$\theta = \cot^{-1}\left(\frac{(P_{i3} - P_{i1})\sin\alpha + (P_{i1} - P_{i2})\sin\beta}{(P_{i1} - P_{i3})(1 - \cos\alpha) + (P_{i2} - P_{i1})(1 - \cos\beta)}\right) \tag{4.48a}$$

$$P_i' = P_{i2}' + \frac{(P_{i3} - P_{i1})\cos(\alpha + \beta)}{\sin\theta\sin\beta - \cos\theta(1 - \cos\beta)} \tag{4.48b}$$

Equation (4.48) gives a close form expression to calculate the four power readings corresponding to an ideal matched load from the actual nine power readings corresponding to three positions of the sliding load. This technique has been experimentally implemented and validated [20]. It was found that the use of a sliding load in conjunction with the method described in this section enhances the accuracy of the six-port reflectometer for the measurements near the center of the Smith chart, hence increasing its dynamic range by at least 10 dB.

4.7 DIODE LINEARIZATION TECHNIQUE

It has been mentioned that the calibration and measurement calculations are based on the normalized value of the power readings and not on their absolute values. In addition, power detectors using bolometers or thermistors are slow; hence, for many applications they are not acceptable. The use of four Schottky diode detectors in place of four power detectors presents a cost-effective solution and offers a good alternative for applications where speed is important. Nevertheless, Schottky diode detectors do not have a linear voltage-power characteristic P-V over their whole dynamic range. In most cases, they present a linear characteristic at low power levels and a square law characteristic at high power levels. Therefore, an extra numerical correction is needed to take this deviation from the linear behavior into account. The general relationship between input power and output voltage of a Schottky diode detector can be expressed as follows:

$$P = CV\exp\left(\sum_{i=1}^{N} a_i V^i\right) \tag{4.49}$$

where C and a_i are the parameters of the diode's model, V is the output voltage, P is the input power, and N is the order of the polynomial series; typically $N = 10$ is enough to obtain a good accuracy. The calculation of the absolute value of P using (4.49) requires the knowledge of C and a_i, which have to be determined in advance using an appropriate calibration technique.

In a six-port measurement technique, only normalized power readings are required for the calibration and measurement calculations.

For each detector, *k*, one can write:

$$P_k = C_k V_k \exp\left(\sum_{i=1}^{N} a_{ki} V_k'^{i}\right) \tag{4.50a}$$

with

$$V_k' = \mathrm{Ln}\left(\frac{V_k}{d} + 1\right) \tag{4.50b}$$

The introduction of the variable V' in place of V in (4.49) ensures the convergence of the series. The d parameter is introduced to normalize the voltage in such a way that V' is less than 1 for the whole dynamic range of the diode detector.

The linearization technique is based on the fact that the six-port junction is a passive and linear junction; therefore, for a given load, the power reading ratio $p_k = P_k / P_3$ is independent of the power level.

By connecting a passive load at the measuring port and sweeping the power level of the source, for two different power levels of the generator, *j* and *j+1*, one can write:

$$\frac{P_{k,j+1}}{P_{k,j}} = \frac{C_k V_{k,j+1} \exp\left(\sum_{i=1}^{N} a_{ki} V'^{i}_{k,j+1} \right)}{C_k V_{k,j} \exp\left(\sum_{i=1}^{N} a_{ki} V'^{i}_{k,j} \right)} \tag{4.51}$$

Consequently, the normalized power readings are constant, $p_{k,j} = p_{k,j+1}$, and are not functions of the power level; thus, one can write

$$\frac{C_k V_{k,j} \exp\left(\sum_{i=1}^{N} a_{ki} V'^{i}_{k,j} \right)}{C_3 V_{3,j} \exp\left(\sum_{i=1}^{N} a_{3i} V'^{i}_{3,j} \right)} = \frac{C_k V_{k,j+1} \exp\left(\sum_{i=1}^{N} a_{ki} V'^{i}_{k,j+1} \right)}{C_3 V_{3,j+1} \exp\left(\sum_{i=1}^{N} a_{3i} V'^{i}_{3,j+1} \right)} \tag{4.52}$$

After simplifying and evaluating the logarithm of the right-hand and the left-hand sides of (4.52), we obtain:

$$\sum_{i=1}^{N} \left(a_{ki} \left(V'^{i}_{k,j} - V'^{i}_{k,j+1} \right) \right) - \left(a_{3i} \left(V'^{i}_{3,j} - V'^{i}_{3,j+1} \right) \right) = \mathrm{Ln}\left(\frac{V_{k,j+1} V_{3,j}}{V_{3,j+1} V_{k,j}} \right) \tag{4.53}$$

Equation (4.53) is a linear one for the unknowns a_{ki} and a_{3i}. By using a different load and different power level, one can form a set of linear equations to be able to solve for the parameters (a_{ki}, a_{3i}). It is important to notice that three different sets of parameters a_{3i} have to be calculated. Each set is associated with one pair of power detectors (D_4, D_3), (D_5, D_3), and (D_6, D_3). In practice, three different loads, (open, short, and matched load) and a power step of 1 dB are sufficient to obtain accurate solutions for the linear system (4.53), which offers a reasonable precision in the measurements.

Once all three sets of coefficient $\left(a_{ki}, a_{3i}\right)$ are obtained, one can calculate the following power ratio:

$$\frac{V_k \exp\left(\sum_{i=1}^{N} a_{ki} V_k'^{i}\right)}{V_3 \exp\left(\sum_{i=1}^{N} a_{3i} V_k'^{i}\right)} = \upsilon_k \frac{P_k}{P_3} \tag{4.54}$$

where $\upsilon_k = \frac{C_3}{C_k}$ and υ_k is a real parameter that can be embedded in the five calibration parameters.

The normalized power readings, p_k', required to calibrate the six-port reflectometer, to perform error box calculation, and to calculate the complex reflection coefficient can be calculated using only voltage measurements as follows:

$$p_k' = V_k / V_3 \exp\left(\sum_{i=1}^{N} \left(a_{ki} - a_{3i}\right) V_k'^{i}\right) \tag{4.55}$$

The advantages of the technique described above are: (1) no power meter is needed for the linearization technique, and (2) no precise variable attenuator is required during the linearization procedure.

In addition, in case the four diode detectors are quasi-identical, there would be no need for any further corrections to be taken into account for the effect of the environment temperature or operating frequency.

It is also worth mentioning that the computation effort needed for the linearization and the measurement procedures is relatively insignificant.

4.8 POWER CALIBRATION TECHNIQUE

It was shown that the six-port reflectometer can be used to calculate the power flow propagating toward the device under test (DUT). A power calibration, which calculates an extra real parameter, α_3^2, is needed for that purpose. In the case of a six-port reflectometer fitted with four diode detectors, the power calibration calculation is different.

Using (2.39), the absorbed power by any load can be calculated as follows:

$$P_L = \frac{|c|^2\left(1-|\Gamma_L|^2\right)P_3}{\alpha_3^2\,|c\Gamma+1|^2} = \frac{|c|^2\left(1-|\Gamma_L|^2\right)C_3V_3\exp\left(\sum_{i=1}^{N} a_{3i}V_k'^{\,i}\right)}{\alpha_3^2\,|c\Gamma+1|^2} \qquad (4.56)$$

The only unknown quantities are the ratio C_3/α_3^2 and the coefficients a_{3i}. It is assumed herein that c is the parameter of the error box.

It was mentioned above that the six-port junction is a linear one. Therefore, for a fixed load connected to the measuring port, the ratio of the power absorbed by the load for two different levels of the generator is the same as the ratio of the third power readings corresponding to these power levels of the generator. Therefore, one can deduce:

$$\frac{P_L^{j+1}}{P_L^{j}} = \frac{C_3V_{3,j+1}\exp\left(\sum_{i=1}^{N} a_{3i}V_{3,j+1}'^{\,i}\right)}{C_3V_{3,j}\exp\left(\sum_{i=1}^{N} a_{3i}V_{3,j}'^{\,i}\right)} \qquad (4.57)$$

By connecting an absolute power meter to the measuring port and after simplifying and evaluating the logarithm of the right-hand and the left-hand sides of (4.57), one can deduce the following equation

$$\sum_{i=1}^{N}\left(a_{3i}\left(V_{3,j}'^{\,i} - V_{3,j+1}'^{\,i}\right)\right) = \mathrm{Ln}\left(\frac{P_{PM,j}V_{3,j+1}}{P_{PM,j+1}V_{3,j}}\right) \qquad (4.58)$$

where $P_{PM,j}$ and $P_{PM,j+1}$ are the two power readings given by the power meter.

By sweeping the power level of the source, one can generate a set of equations, similar to (4.58), which can be grouped to form a linear system. The solution of this linear system gives the coefficients a_{3i} needed to calculate the power absorbed by the load in (4.56). Once these coefficients are obtained, for a given power level, *i*, of the source, one can write

$$\frac{C_3}{\alpha_3^2} = \frac{P_{PM,i}\,|c\Gamma_{PM}+1|^2\,|c|^2}{|c|^2\left(1-|\Gamma_{PM}|^2\right)V_{3,i}\exp\left(\sum_{i=1}^{N} a_{3i}V_k'^{\,i}\right)} \qquad (4.59)$$

where the remaining unknown ratio C_3/α_3^2 can be calculated.

References

[1] Ghannouchi, F. M., and R. G. Bosisio, "An Alternative Explicit Six-Port Matrix Calibration Formalism Using Five Standards*," IEEE Trans. Microwave Theory Tech.*, Vol. 36, No. 3, pp. 494–498, March 1988.

[2] Engen, G. F., "Calibrating the Six-Port Reflectometer by Means of Sliding Terminations," *IEEE Trans. Microwave Theory Tech.*, Vol. MTT-26, pp. 951–957, 1978.

[3] Susman, L., "Calibration of Six-Port Reflectometer Using Projection Geometry Concept," *Electronic Letters*, Vol. 20, No. 1, pp. 9–11, 1984.

[4] Somlo, P. I., and J. D. Hunter, "A Six-Port Reflectometer and Its Complete Characterization by Convenient Calibration Procedures," *IEEE Trans. Microwave Theory Tech.*, Vol. MTT-30, No. 2, pp. 186–192, February 1982.

[5] Hunter, J. D., and P. I. Somlo, "An Explicit Six-Port Calibration Method Using Five Standards," *IEEE Trans. Microwave Theory Tech.*, Vol. MTT-33, No. 1, pp.69–71, January 1985.

[6] Qian, C. Z., "An Improved Method for Six-Port Reflectometer Calibration," *IEEE Trans. Instr. & Meas*., Vol. IM-34, No. 4, pp. 611–615, December1985.

[7] Ghannouchi, F. M., and R. G. Bosisio, "Calibration and Measurement of Six-Port Reflectometer Using a Matrix Approach," *Technical Report EPM-86/48, Ecole Polytechnique of Montreal*, October 1986.

[8] Engen, G. F., "An Improved Circuit for Implementing the Six-Port Technique of Microwave Measurements," *IEEE Trans. Microwave Theory Tech.*, Vol. MTT-25, No. 12, pp. 1080–1083, December 1977.

[9] Ghannouchi, F. M., and R. G. Bosisio, "Calibration and Measurement of Six-Port Reflectometer Using a Matrix Approach," *Technical Report EPM/RT-86/46, Report EPM/RT-86/47 and Report EPM/RT-86/48, Ecole Polytechnique of Montreal*, October 1986.

[10] Hoer, C. A., "Choosing Line Lengths for Calibrating Network Analyzers," *IEEE Trans. Microwave Theory Tech.,* Vol. 31, pp. 76–77, January 1983.

[11] Ghannouchi, F. M., and R. G. Bosisio, "An Improved Load Formulation for Use in Six-Port Calibration Methods," *Alta Frequenza*, Vol. 57, No. 8, pp. 497–499, 1988.

[12] Engen, G. F., "A Least Square Solution for Use in the Six-Port Measurement Technique," *IEEE Trans. Microwave Theory Tech.*, Vol. MTT-28, pp. 1473–1477, December 1980.

[13] Riblet, G. P., and E. R. B. Hansson, "Aspects of the Calibration of a Single Six-Port Using a Load and Offset Reflection Standards," *IEEE Trans. Microwave Theory Tech.*, Vol. MTT-30, pp. 2120–2125, 1982.

[14] Ghannouchi, F. M., and R. G. Bosisio, "The Six Port Reflectometer and Its Complete Calibration by Four Standard Terminations," *IEE Proceedings-H: Microwaves, Antennas and Propagation*, Vol. 135, No. 4, pp. 285–288, August 1988.

[15] Hodgetts, T. E., and E. J. Griffin, "An Unified Treatment of the Theory of Six-Port Reflectometer Calibration Using The Minimum of Standards," *Royal Signals and Radar Establishment, UK, Report 83003,* 1983.

[16] Potter, C. M., and G. Hjipieris, "A Robust Six- to Four Reduction Algorithm," *IEEE MTT Symposium Proceedings* , Vol. 3, pp. 1263–1266, 1993.

[17] Yakabe, T., F. M. Ghannouchi, E. E. Eid, K.Fujii, and H. Yabe, "Six-Port Self-Calibration Based on Active Loads Synthesis," *IEEE Trans. Microwave Theory Tech.,* Vol. 50, No. 4, pp. 1237–1239, April 2002.

[18] Ghannouchi, F. M., and R. G. Bosisio, "A Wide Band Millimeter Wave Six-Port Reflectometer Using Four Diode Detectors Calibrated Without Power Ratio Standard," *IEEE Trans. Instrumentation and Measurement,*. Vol. 40, pp. 1043–1046, Decemeber 1991.

[19] Le, D. L., and F. M. Ghannouchi, "Source–Pull Measurements Using Reverse Six-Port Reflectometers with Application to MESFET Mixer Design," *IEEE Trans. Microwave Theory Tech.*, Vol. 42, pp. 1589–1595, September. 1994.

[20] Yakabe, T., M. Kinoshita, and H. Yabe, "Complete Calibration of a Six-Port Reflectometer with One Sliding Load and One Short," *IEEE Trans. Microwave Theory Tech.*, Vol. 42, pp. 2035–2039, November 1994.

Chapter 5

Six-Port Network Analyzers

In the previous chapters, the fundamentals, the calibration techniques, and the design of six-port reflectometers have been presented and discussed. This chapter presents the theory and discusses the design and the calibration of six-port based network analyzer. The theory and the calibration of a two-port six-port vector network analyzer are presented. A six-port based de-embedding technique needed for the measurement of devices without coaxial terminals is also presented. The theory, the measurement, and the calibration of a tri-six-port-based network analyzer are presented. An N-six-port measurement technique, which requires only a one-step connection, is also presented and discussed. Finally, a single six-port junction based N-port vector network analyzer is presented in which the six-port junction is used as a complex wave comparator.

5.1 GENERAL FORMULATION

It was shown in Chapter 1 that the six-port reflectometer is capable of making simultaneous power flow and impedance measurements using only amplitude measurements while no phase measurements are required. The use of two six-port reflectometers in conjunction with an appropriate calibration procedure can lead to the determination of the four scattering parameters of any two-port device under test (DUT) [1-4]. The general block diagram of a two-port six-port based network analyzer is shown in Figure 5.1.

CNT1 and CNT2 are two repeatable phase and amplitude controllers inserted in branch 1 and branch 2 of the six-port network analyzer (SPNA). CNT1 and CNT2 are used to vary the amplitude and the phase of the emerging signal a_1 and a_2 from the two measuring ports of the two six-port junctions, SP1 and SP2.

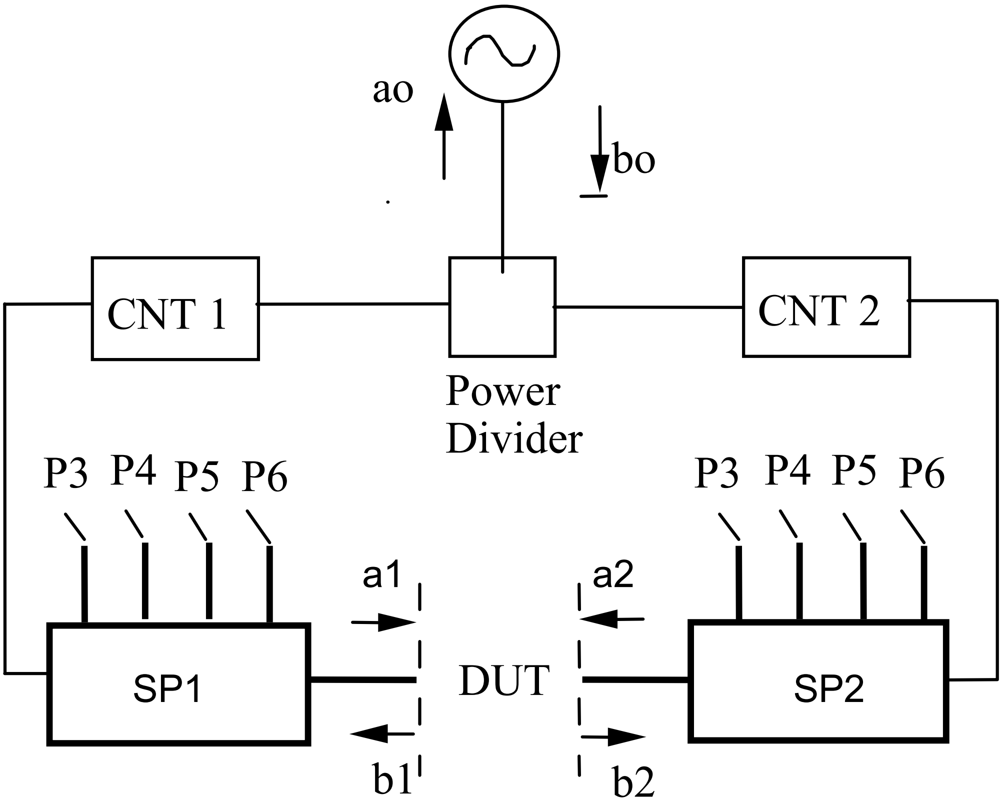

Figure 5.1 Block diagram of a six-port based two-port network analyzer.

For a given setting, k, of CNT1 and CNT2, the incident signals a_{1k} and a_{2k} and the reflected signals, b_{1k} and b_{2k} at the measuring planes of the two six-port reflectometers are related through the four scattering parameters, s_{ij}, of the DUT as follows:

$$\begin{bmatrix} b_{1k} \\ b_{2k} \end{bmatrix} = \begin{bmatrix} s_{11} & s_{12} \\ s_{21} & s_{22} \end{bmatrix} \begin{bmatrix} a_{1k} \\ a_{2k} \end{bmatrix} \tag{5.1}$$

Knowing that the measured reflection coefficients by the two six-port reflectometers are

$$\Gamma_{1k} = \frac{b_{1k}}{a_{1k}} \tag{5.2a}$$

$$\Gamma_{2k} = \frac{b_{2k}}{a_{2k}} \tag{5.2b}$$

one can rewrite (5.1) in the following format

$$\Gamma_{1k} - s_{11} = s_{12} g_k \tag{5.3a}$$

$$\Gamma_{2k} - s_{22} = s_{21} / g_k \tag{5.3b}$$

where $g_k = \frac{a_{2k}}{a_{1k}}$. The use of two different settings for the amplitude and phase controllers, k=1, and 2, leads to obtaining a set of four linear equations similar to (5.3). The solution of this set gives the four unknown s_{ij} parameters.

5.2 CASE OF A RECIPROCAL TWO-PORT DUT

The multiplication of (5.3a) by (5.3b) allows the elimination of g_k and gives the following equation:

$$s_{11}\Gamma_{2k} + s_{22}\Gamma_{1k} - \Delta = \Gamma_{1k}\Gamma_{2k} \tag{5.4}$$

where $\Delta = s_{11}s_{22} - s_{12}s_{21}$. Equation (5.4) can be used to calculate the S parameters of a reciprocal two-port DUT$(s_{12} = s_{21})$. In such a case three excitations, k =1, 2, and 3, are required to form a set of three complex linear equations with three unknowns s_{11}, s_{22}, and Δ. The solution of this linear system leads to a complete knowledge of s_{11} and s_{22} and to a partial knowledge of s_{21}.

$$|s_{21}| = \left|\sqrt{s_{11}s_{22} - \Delta}\right| \tag{5.5a}$$

$$\arg(s_{21}) = \arg\left(\sqrt{s_{11}s_{22} - \Delta}\right) + n\pi \tag{5.5b}$$

with n =1, 2, ..., N. The nonambiguous determination of the phase of s_{21} requires multifrequency measurements or the knowledge of an approximate value for the phase of s_{21}.

It is important to notice that in cases of a reciprocal DUT, no extra calibration, besides the calibration of each six-port reflectometer for reflection measurements, is required to determine the S parameters of the two-port device under test.

5.3 CASE OF AN ARBITRARY TWO-PORT DUT

In the case of an arbitrary DUT, (5.3) can be rewritten as follows:

$$\begin{bmatrix} s_{11} & s_{12} \\ s_{21} & s_{22} \end{bmatrix} \begin{bmatrix} 1 \\ g_k \end{bmatrix} = \begin{bmatrix} \Gamma_{1k} \\ g_k \Gamma_{2k} \end{bmatrix} \tag{5.6}$$

Equation (5.6) shows that the measurements of Γ_{1k} and Γ_{2k}, at two different excitations, k =1 and 2, are sufficient to determine the four S parameters of any DUT provided that g_k is known for these two excitations. The determination of S parameters is based on the solution of a set of four complex linear equations with four unknowns. At this stage, g_k is still unknown and has to be calculated using the calibration parameters of the SPNA which should be obtained in advance using the procedure explained next.

The determination of the excitation g_k, when the DUT is connected to the SPNA and when the branch controllers are set at condition k, is based on the characterization of the calibration of three-port network resulting from the two measuring planes, 1 and 2, and the reference plane at the output of the RF signal generator, plane 0, as shown in Figure 5.2.

The relationships between the incident b_{ik} and the reflected a_{ik} waves at the two measuring planes 1 and 2 are:

$$a_{1k} = u_{10}^{k} b_{0k} + u_{11}^{k} b_{1k} + u_{12}^{k} b_{2k} \tag{5.7a}$$

$$a_{2k} = u_{20}^{k} b_{0k} + u_{21}^{k} b_{1k} + u_{22}^{k} b_{2k} \tag{5.7b}$$

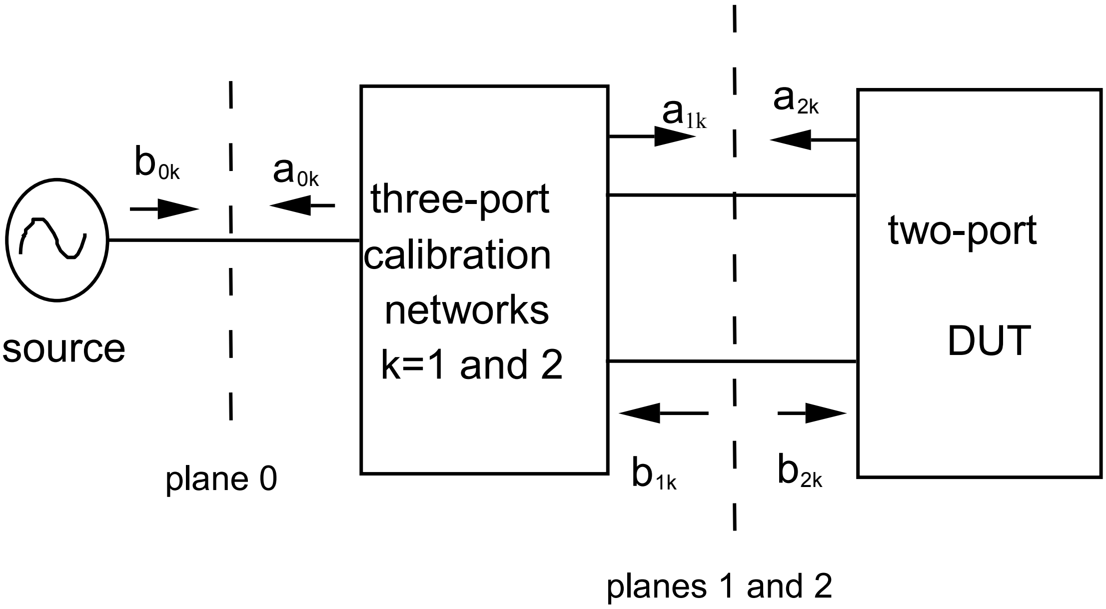

Figure 5.2 The three-port network needs to be characterized at both controller settings.

where u_{ij}^{k} represent the scattering parameters of the three-port network at excitation *k*. Equation (5.7) can be rewritten in matrix format as follows:

$$\begin{bmatrix} 1-u_{11}^{k}\Gamma_{1k} & -u_{12}^{k}\Gamma_{2k} \\ -u_{21}^{k}\Gamma_{1k} & 1-u_{22}^{k}\Gamma_{2k} \end{bmatrix} \begin{bmatrix} a_{1k} \\ a_{2k} \end{bmatrix} = b_{0k} \begin{bmatrix} u_{10}^{k} \\ u_{20}^{k} \end{bmatrix} \tag{5.8}$$

Using Crammer's rules and after algebraic manipulations, one can obtain:

$$g_k = \frac{\left(B_k/A_k\right)+\left(D_k/A_k\right)\Gamma_{1k}}{1+\left(C_k/A_k\right)\Gamma_{2k}} \tag{5.9}$$

where

$$A_k = u_{10}^{k},\ \ B_k = u_{20}^{k},\ \ C_k = u_{20}^{k}u_{12}^{k} - u_{10}^{k}u_{22}^{k}$$

and

$$D_k = u_{10}^{k}u_{21}^{k} - u_{20}^{k}u_{11}^{k}$$

The calculation of g_k needed for the determination of the DUT's S parameters is straightforward using the measured reflection coefficients Γ_{1k} , and Γ_{2k}, when the DUT is connected to the measuring planes, and the calibration parameters of the SPNA B_k/A_k , C_k/A_k , and D_k/A_k . The determination of these parameters is based on the following equation obtained by substituting (5.9) into (5.3a) and by replacing $g_k = \frac{a_{2k}}{a_{1k}}$ by its equivalent expression deduced using (5.3a), and which is equal to $\left(\Gamma_{1k} - s_{11}\right)/s_{12}$:

$$s_{12}^{s}\frac{B_k}{A_k} + \left(\Delta^{s} - s_{22}^{s}\Gamma_{1k}^{s}\right)\frac{C_k}{A_k} + s_{12}^{s}\Gamma_{1k}^{s}\frac{D_k}{A_k} = \Gamma_{1k}^{s} - s_{11}^{s} \tag{5.10}$$

with s= 1, 2, and 3 and k= 1 and 2, and s_{ij}^{s} are the scattering parameters of the standards. The use of the same three known and different two-port standards (s=1, 2, and 3) for both excitations (k=1 and 2) provides two sets of linear equations, one set per excitation. Each set includes three equations and three unknowns (B_k/A_k, C_k/A_k ,D_k/A_k). The solution of these sets allows the calculation of the six calibration parameters, three per excitation.

Alternatively, it is possible to use three unknown reciprocal two-port standards and three different excitations in place of two known two-port standards and two excitations to solve for the six calibration parameters. The procedure to determine the S parameters of a reciprocal two-port standard, described in Section 5.2, can be applied to calculate the S parameters of the three standards before solving the linear system (5.10) for B_k/A_k , C_k/A_k, and D_k/A_k . The calibration technique is general in the sense that no assumption is made regarding the isolation between branches and it is applicable whenever the bandwidth of the hardware is appropriate: six-port junctions, controllers, and so forth.

5.4 SIX-PORT BASED DE-EMBEDDING TECHNIQUE: THEORY

S-parameter measurements of devices whose terminals are noncoaxial (e.g., microstrip lines, coplanar waveguide lines, rectangular or circular waveguides, and fin lines) require the use of a test fixture with suitable transitions between the DUT terminals and the coaxial terminals of the measurement system [6]. Several de-embedding techniques have been used to extract the de-embedded (intrinsic) S parameters of the noncoaxial DUT from the embedded (raw) S' parameters obtained using a network analyzer for the DUT mounted in an appropriate test fixture [7–11]. Based on the above methods, a six-port based technique that requires three reciprocal unknown two-port standards, a through connection, a matched two-port standard, and an unmatched two-port standard, is presented in this section.

The relationship between the scattering parameter matrix entries and the transmission parameters matrix entries of an arbitrary two-port device is the following:

$$\mathbf{D}=\begin{bmatrix} d_{11} & d_{12} \\ d_{21} & d_{22} \end{bmatrix}=\frac{1}{s'_{12}}\begin{bmatrix} -s'_{22}s'_{11}+s'_{21}s'_{12} & s'_{11} \\ -s'_{22} & 1 \end{bmatrix} \tag{5.11}$$

Figure 5.3 shows a typical setup for S parameters de-embedding purposes. Let **A** and **B** be the transmission matrices associated to the left and right parts of the test fixture, respectively, and **D** be the DUT transmission matrix. The incident signals at the DUT (test fixture) reference planes are a_A and a_B (a'_A, a'_B), respectively, and the reflected signals at the DUT (test fixture) reference planes are b_A and b_B (b'_A, b'_B), respectively, as shown in Figure 5.3. **A**, **D,** and **B** are related to the incident and reflected signals as follows:

$$\begin{bmatrix} b'_A \\ a'_A \end{bmatrix}=\mathbf{A}\begin{bmatrix} b_A \\ a_A \end{bmatrix} \tag{5.12a}$$

$$\begin{bmatrix} b_A \\ a_A \end{bmatrix}=\mathbf{D}\begin{bmatrix} b_B \\ a_B \end{bmatrix} \tag{5.12b}$$

$$\begin{bmatrix} b'_B \\ a'_B \end{bmatrix}=\mathbf{B}\begin{bmatrix} b_B \\ a_B \end{bmatrix} \tag{5.12c}$$

Using (5.12), one can write

$$\begin{bmatrix} b'_A \\ a'_A \end{bmatrix}=\mathbf{ADB}^{-1}\begin{bmatrix} b'_B \\ a'_B \end{bmatrix}=\mathbf{M}\begin{bmatrix} b'_B \\ a'_B \end{bmatrix} \tag{5.13}$$

M represents the transmission matrix of the test fixture holding the DUT.

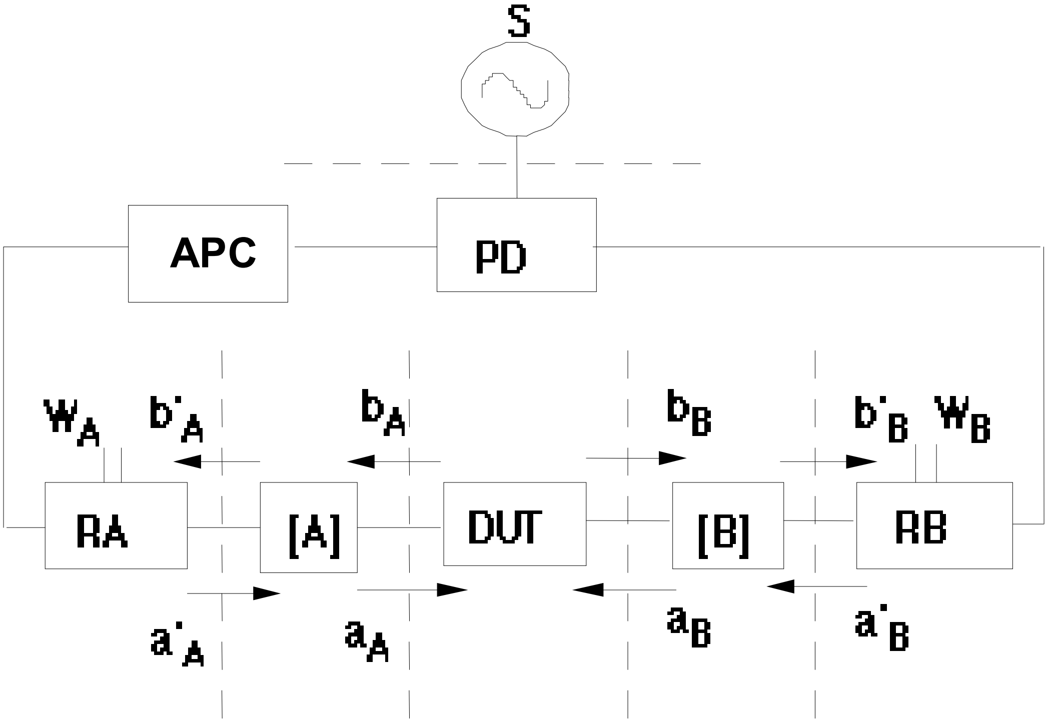

Figure 5.3 General representation of the de-embedding problem.

The two embedded reflection coefficients w_A and w_B can be measured by the two reflectometers SPA and SPB for two different excitations, $k = 1$, and 2. These excitations are obtained by changing the setting of the amplitude and phase controllers CNT1 and CNT2, shown in Figure 5.1. This leads to a system of equations (similar to (5.6)), including four linear equations with four unknowns, which are the embedded scattering parameters of the test fixture holding the DUT s'_{11}, s'_{12}, s'_{21}, and s'_{22} :

$$\begin{bmatrix} s'_{11} & s'_{12} \\ s'_{21} & s'_{22} \end{bmatrix} \begin{bmatrix} 1 \\ g'_k \end{bmatrix} = \begin{bmatrix} w_{Ak} \\ g'_k w_{Bk} \end{bmatrix}, k = 1 \text{ and } 2 \tag{5.14}$$

where $w_{Ak} = \frac{b'_{Ak}}{a'_{Ak}}$, and $w_{Bk} = \frac{b'_{Bk}}{a'_{Bk}}$ are, respectively, the embedded reflection coefficients measured by the two reflectometers SPA and SPB, respectively, and $g'_k = \frac{a'_{Bk}}{a'_{Ak}}$ are the two excitation parameters that should be calculated using the calibration technique described in section 5.9. The same three reciprocal two-port standards, which will be introduced in the next section, can be used to calculate the calibration parameters B_k'/A_k', C_k'/A_k', and D_k'/A_k' of the three-port calibration network needed for the calculation of g_k'.

The solution of (5.14) leads to the determination of S' parameters of the test fixture holding the DUT.

To be able to recover the de-embedded S parameters of the DUT from the embedded S' parameters and transmission matrices **A** and **B**, which model, respectively, the right and the left sides of the test fixture delimited by the actual measuring planes of SPA and SPB, the reference planes of the device under test (see Figure 5.3) have to be determined in advance. This step constitutes the calibration procedure which has to be carried out before measuring any DUT.

5.5 TWO-PORT DE-EMBEDDING TECHNIQUE

As mentioned above, the calibration procedure consists of using three unknown reciprocal two-port standards needed to calculate the entries of the **A** and **B** transmission matrices:

1. A through connection standard:

$$\mathbf{S}_1 = \begin{bmatrix} 0 & 1 \\ 1 & 0 \end{bmatrix} \tag{5.15a}$$

2. A matched reciprocal two-port standard:

$$\mathbf{S}_2 = \begin{bmatrix} 0 & f \\ f & 0 \end{bmatrix} \tag{5.15b}$$

3. An unmatched reciprocal two-port standard:

$$\mathbf{S}_3 = \begin{bmatrix} g & h \\ h & g \end{bmatrix} \tag{5.15c}$$

Notice that the determinants of the transmission matrices $\mathbf{D}_1$, $\mathbf{D}_2$, and $\mathbf{D}_3$ corresponding to these standards are equal to unity.

After placing the three standards successively in the test fixture and measuring their corresponding embedded reflection coefficients for two different excitations and applying (5.14) to calculate their corresponding S' parameters, one can construct three different transmission matrices, one for each standard, $\mathbf{M}_1$, $\mathbf{M}_2$ and $\mathbf{M}_3$ using the standard transformation between scattering parameters and transmission parameters shown here:

$$\mathrm{M} = \frac{1}{s'_{12}} \begin{bmatrix} -s'_{22}s'_{11} + s'_{21}s'_{12} & s'_{11} \\ -s'_{22} & 1 \end{bmatrix} \tag{5.16}$$

A second way to calculate the **M** matrix is based on the following: from (5.16), one can see that the knowledge of s'_{11}, s'_{22}, and Δ' ($\Delta' = s'_{11}s'_{22} - s'_{12}s'_{21}$) leads to the partial knowledge of the matrix **M**. Only a normalizing parameter s'_{12} corresponding to each standard is still an unknown. These normalizing parameters can be embedded, respectively, in the matrices $\mathbf{D}_2$, $\mathbf{D}_3$ and $\mathbf{T}$ defined below. In such a case the entries of the nonnormalized transmission matrix **M** can be found directly from the solution of a set of linear systems obtained for three different excitations when the standard, or the DUT, is connected to the measuring ports as follows:

$$s'_{11}w_{Bk} + s'_{22}w_{Ak} - \Delta' = w_{Ak}w_{Bk}\text{, } k = 1, 2, \text{and } 3 \tag{5.17}$$

Let **P**, **Q**, **R**, and **T** be:

$$\mathbf{M}_2\mathbf{M}_1^{-1} = \mathbf{P} \tag{5.18a}$$

$$\mathbf{M}_3\mathbf{M}_1^{-1} = \mathbf{Q} \tag{5.18b}$$

$$\mathbf{M}_3\mathbf{M}_2^{-1} = \mathbf{R} \tag{5.18c}$$

$$\mathbf{D}_3\mathbf{D}_2^{-1} = \mathbf{T} \tag{5.18d}$$

where $\mathbf{D}_2$ and $\mathbf{D}_3$ are the corresponding transmission matrices of the second and the third standards, respectively.

By using the three equations obtained by means of (5.13), for the three standards, in conjunction with (5.16), one can derive the following equations:

$$\mathbf{AD_2} = \mathbf{PA} \tag{5.19a}$$

$$\mathbf{AD_3} = \mathbf{QA} \tag{5.19b}$$

$$\mathbf{AT} = \mathbf{RA} \tag{5.19c}$$

Each of the three matrix equations includes a pairs of similar matrices, (**D₂, P**), (**D₃, Q**), and (**R, T**), which have been shown mathematically to have the same trace, determinant, and sign values. The trace invariance property for such matrices yields the following equation:

$$\Sigma u_{ii} = \Sigma v_{ii} \tag{5.20}$$

where u_{ii} and v_{ii} are the diagonal entries of a pair of similar matrices ($\mathbf{U}$, $\mathbf{V}$).

Applying that property to (5.19a) to calculate the s'_{21} parameter of the matched standard, it is found that two values for f can satisfy the trace invariance property;

$$f_1 = \frac{\left(p_{11}+p_{22}\right)+\sqrt{\left(p_{11}+p_{22}\right)^2-4}}{2} \tag{5.21a}$$

$$f_2 = \frac{\left(p_{11}+p_{22}\right)-\sqrt{\left(p_{11}+p_{22}\right)^2-4}}{2} \tag{5.21b}$$

where p_{ij} are the entries of matrix **P**. One way to resolve this ambiguity is to utilize the fact that, in practice, the entries of the transmission matrix **A** for an appropriate test fixture should satisfy the following equation:

$$\left|\frac{a_{12}}{a_{22}}\right| \le \left|\frac{a_{11}}{a_{21}}\right| \tag{5.22}$$

This inequality is equivalent to:

$$\left|\frac{p_{12}}{1/f_i - p_{11}}\right| \le \left|\frac{f_i - p_{22}}{p_{21}}\right|, \; i = 1 \text{ and } 2 \tag{5.23}$$

Using (5.19b) and (5.19c), and after some algebraic manipulations, one can calculate the remaining unknown parameters of the third standard as follows:

$$h = \frac{1-f^2}{\left(q_{11}+q_{22}\right)-f\left(r_{11}+r_{22}\right)} \tag{5.24}$$

where q_{ii} and r_{ii} are the entries of matrices **Q** and **R,** respectively.

For the s_{11} parameter of the unmatched standard, two values for *g* can satisfy the trace invariance property:

$$g_1 = \left(-fh\left(r_{11}+r_{22}\right)+f^2+h^2\right)^{\frac{1}{2}} \tag{5.25a}$$

$$g_2 = -\left(-fh\left(r_{11}+r_{22}\right)+f^2+h^2\right)^{\frac{1}{2}} \tag{5.25b}$$

Again, the sign ambiguity can be resolved knowing that, in practice, the measured value of s_{11}, of the third standard, should be comparable to the value of *g*, in amplitude and in phase. Therefore, one can use the following criterion to select *g*:

$$\left|s_{11}-g_i\right| \le \left|s_{11}+g_i\right|, \; i = 1 \text{ and } 2 \tag{5.26}$$

We assume that the impedances of both the test-ports of SPA and SPB are equal to the line characteristic impedance, which is 50Ω in practice.

5.6 CALCULATION OF THE ERROR-BOX PARAMETERS

Knowing the parameters of all standards used, we are able now to determine the a_{ij} entries of matrix **A** by means of (5.18). Each matrix equation can be written as a set of four homogenous linear complex equations with four unknowns. Assembling these four sets into one leads to an overdetermined homogenous complex linear system with four unknowns, a_{ij}, and 12 equations:

$$\mathbf{C}\underline{\mathbf{A}} = 0 \tag{5.27}$$

where $\underline{\mathbf{A}} = \left[a_{11} \quad a_{12} \quad a_{21} \quad a_{22}\right]^T$ and **C** is a known (12×4) complex matrix.

A singular value decomposition (SVD) technique can be used to solve the above system to insure a reliable and good solution even if the matrix **C** presents a bad condition number. The transmission matrix **B**, which models the right-hand side of the test fixture, can easily be calculated using **A** and **M** as follows:

$$\mathbf{B}=\mathbf{M}^{-1}\mathbf{A} \tag{5.28}$$

5.7 DETERMINATION OF S PARAMETERS OF AN ARBITRARY DUT

To be able to calculate the S parameters of any DUT, we first need to determine the S' matrix of the test fixture holding the DUT using (5.14). This procedure requires the use of good quality phase and amplitude controllers CNT1 and CNT2 with reliable repeatability.

Using the transmission matrices of the two error box networks **A** and **B**, the transmission matrix of the DUT can be obtained using the following equation:

$$\mathbf{D} = \mathbf{A}^{-1}\mathbf{MB} \tag{5.29}$$

where **M** is the transmission matrix of the test fixture holding the DUT and is related to its S' parameters via (5.14).

The standard transformation between the transmission parameter matrix and the scattering parameter matrix allows the calculation of the de-embedded S parameters of the DUT as follows:

$$s_{11} = \frac{d_{12}}{d_{22}} \tag{5.30a}$$

$$s_{12} = d_{11} - \left(\frac{d_{12}d_{21}}{d_{22}}\right) \tag{5.30b}$$

$$s_{21} = \frac{1}{d_{22}} \tag{5.30c}$$

and

$$s_{22} = -\frac{d_{21}}{d_{22}} \tag{5.30d}$$

The above calibration and de-embedding procedures can be implemented on a network analyzer comprising two reflectometers (e.g., six-port network analyzers), or can also be implemented on four CNAs that directly provide the embedded S' parameters. In this case, the four measurement matrices $\mathbf{M}_1$, $\mathbf{M}_2$, $\mathbf{M}_3$, and **M** can be directly calculated using (5.16). When a four-channel network analyzer is used, only excitation 1 and excitation 2 are needed to compute the S parameters of an arbitrary DUT.

In the case of a purely reflecting DUT $\left(s'_{12} = s'_{21} = 0\right)$, the transformation between the scattering matrix, **S**, and the transmission matrix **D** becomes singular, as can be deduced from (5.28). Therefore, a test to detect such a situation is required and an alternative method for calculating s_{11} and s_{22} should be included in the algorithm. A test may consist of checking whether the determinant of **M** in (5.14) goes to zero, and in a such a case, the following relationships can be used to calculate s_{11} and s_{22}.

$$s_{11} = \frac{w_A - \alpha_{11}}{-\det[\alpha] + \alpha_{22} w_A} \tag{5.31a}$$

and

$$s_{22} = \frac{w_\mathrm{B} - \beta_{11}}{-\det[\beta] + \beta_{22} w_B} \tag{5.31b}$$

where α_{ij} and β_{ij} are the entries of the scattering matrices $\mathbf{A}'$ and $\mathbf{B}'$ associated with the error box matrice **A** and **B**, which can be easily calculated using the transmission matrices **A** and **B** and the embedded reflection coefficient w_A and w_B measured when the DUT is connected to one of the measuring reference planes.

It is important to notice that the through connection standard can be replaced by a delay line as in the line reflect line (LRL) technique. In this case, the equivalent reference plane of a virtual through connection positioned at the middle of this delay line is considered in the computation. The difference between the delay line and the matched standard electrical length is considered as the electrical length of the matched standard in the computation.

5.8 TRI-SIX-PORT NETWORK ANALYZER

The block diagram of the three-six-port network analyzer (TSPNA) is shown in Figure 5.4 [15]. The basic relationship that relates the incident signals to the reflected signals for a given three-port DUT is

$$\underline{\mathbf{b}} = \mathbf{S}\underline{\mathbf{a}} \tag{5.32}$$

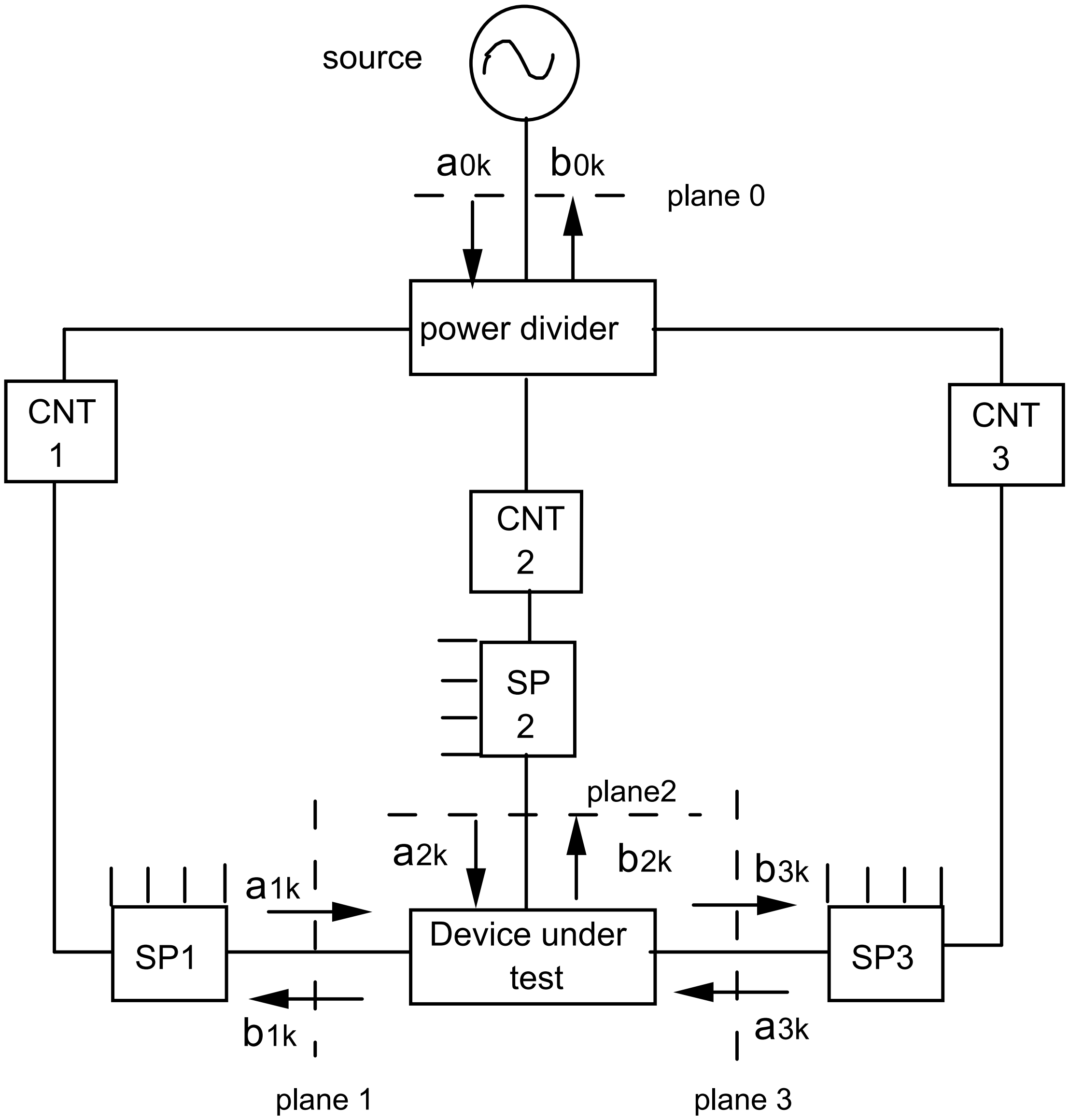

Figure 5.4 Block diagram of TSPNA.

where $\underline{\mathbf{a}} = \left(a_1, a_2, a_3\right)^T$, and $\underline{\mathbf{b}} = \left(b_1, b_2, b_3\right)^T$. When the amplitude and phase controllers, CNT1, CNT2, and CNT3, are set at condition *k*, (5.32) can be reexpressed as follows:

$$\mathbf{S}\underline{\mathbf{G}}_k = \underline{\mathbf{G}}'_k \tag{5.33}$$

where $\underline{\mathbf{G}}_k = \left(1_1, g_{2k}, g_{3k}\right)^T$, $\underline{\mathbf{G}}'_k = \left(\Gamma_{1k}, g_{2k}\Gamma_{2k}, g_{3k}\Gamma_{3k}\right)^T$, $g_{ik} = \frac{a_{ik}}{a_{1k}}$, and $\Gamma_{ik} = \frac{b_{ik}}{a_{ik}}$ with i = 1, 2, and 3; and k = 1, 2, and 3.

Γ_{ik} is the reflection coefficient measured by SPI, for the excitation k. The three six-port reflectometers are assumed to be calibrated for reflection measurements.

For the four-port network delimited by the three measuring planes (planes 1, 2, and 3) and the reference plane at the output of the RF signal generator (plane 0) shown in Figure 5.4, the following equation can be written:

$$\mathbf{U_k}\,\underline{\mathbf{a}}_\mathbf{k} = b_{ok}\,\underline{\mathbf{U}}_\mathbf{0}^\mathbf{k} \tag{5.34a}$$

where

$$\mathbf{U_k} = \begin{bmatrix} 1-u_{11}^k\Gamma_{1k} & -u_{12}^k\Gamma_{2k} & -u_{13}^k\Gamma_{3k} \\ -u_{21}^k\Gamma_{1k} & 1-u_{22}^k\Gamma_{2k} & -u_{23}^k\Gamma_{3k} \\ -u_{31}^k\Gamma_{1k} & -u_{32}^k\Gamma_{2k} & 1-u_{33}^k\Gamma_{3k} \end{bmatrix} \tag{5.34b}$$

and $\underline{\mathbf{a}}_k = \left(a_{1k}, a_{2k}, a_{3k}\right)^\mathbf{T}$ and $\underline{\mathbf{U}}_\mathbf{0}^\mathbf{k} = \left(u_{10}^k, u_{20}^k, u_{30}^k\right)^\mathbf{T}$ and b_{ok} is the incident signal at the generator port of the four-port network.

Solving (5.34a) for a_{ik} using Crammer's rules, one can easily write

$$g_{ik} = \frac{a_{ik}}{a_{1k}} = \frac{\dfrac{\det\left(\mathbf{U_{ik}}\right)}{\mathrm{b}_{0k}\det\left(\mathbf{U_k}\right)}}{\dfrac{\det\left(\mathbf{U_{1k}}\right)}{\mathrm{b}_{0k}\det\left(\mathbf{U_k}\right)}} = \frac{\det\left(\mathbf{U_{ik}}\right)}{\det\left(\mathbf{U_{1k}}\right)} \tag{5.35}$$

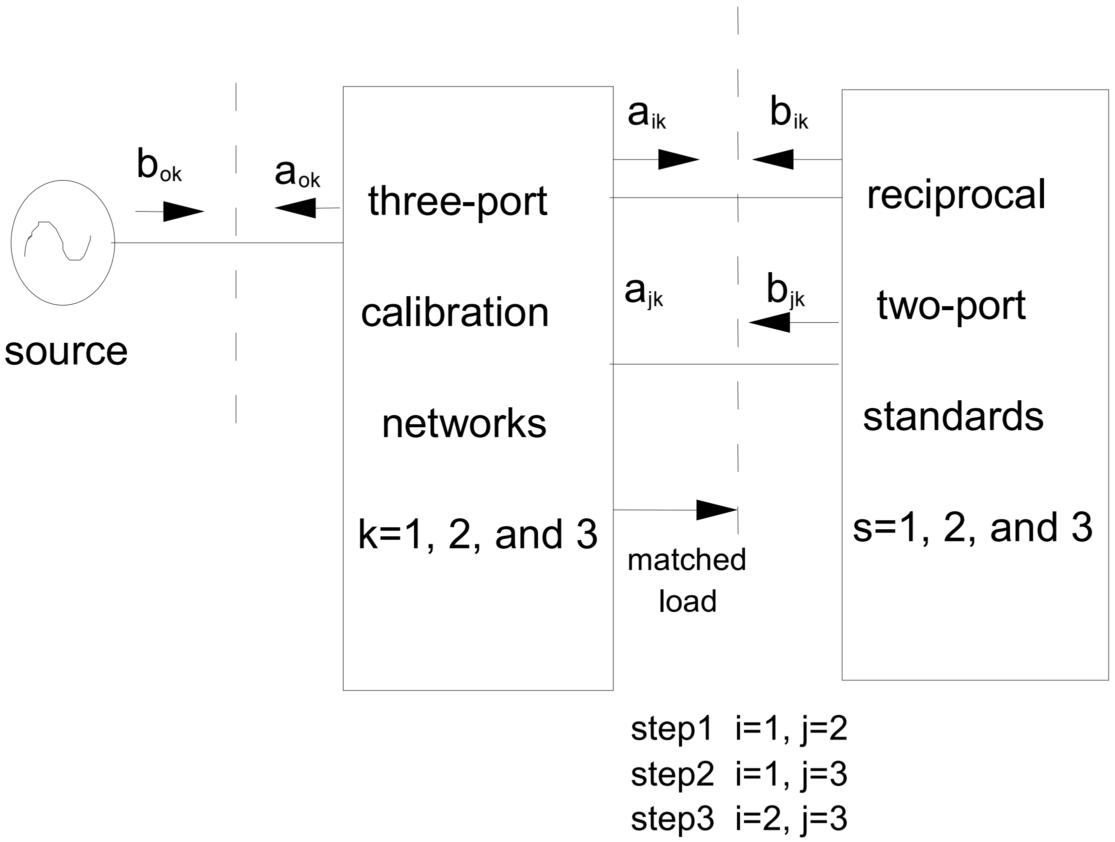

Figure 5.5 Calibration of the TSPNA.

Here $\det\left(\mathbf{U_{ik}}\right)\left(\det\left(\mathbf{U_{1k}}\right)\right)$ is the determinant of matrix $\mathbf{U_k}$ with its *i*th (first) column replaced by a column vector $\underline{\mathbf{U}}_{\mathbf{0}}^{\mathbf{k}}$. The assembling of (5.33) obtained for three different excitations, in one matrix equation gives:

$$\begin{bmatrix} 1 & g_{21} & g_{31} & 0 & 0 & 0 & 0 & 0 & 0 \\ 0 & 0 & 0 & 1 & g_{21} & g_{31} & 0 & 0 & 0 \\ 0 & 0 & 0 & 0 & 0 & 0 & 1 & g_{21} & g_{31} \\ 1 & g_{22} & g_{32} & 0 & 0 & 0 & 0 & 0 & 0 \\ 0 & 0 & 0 & 1 & g_{22} & g_{32} & 0 & 0 & 0 \\ 0 & 0 & 0 & 0 & 0 & 0 & 1 & g_{22} & g_{32} \\ 1 & g_{23} & g_{33} & 0 & 0 & 0 & 0 & 0 & 0 \\ 0 & 0 & 0 & 1 & g_{23} & g_{33} & 0 & 0 & 0 \\ 0 & 0 & 0 & 0 & 0 & 0 & 1 & g_{23} & g_{33} \end{bmatrix} \begin{bmatrix} s_{11} \\ s_{12} \\ s_{13} \\ s_{21} \\ s_{22} \\ s_{23} \\ s_{31} \\ s_{32} \\ s_{33} \end{bmatrix} = \begin{bmatrix} \Gamma_{11} \\ g_{21}\Gamma_{21} \\ g_{31}\Gamma_{31} \\ \Gamma_{12} \\ g_{22}\Gamma_{22} \\ g_{32}\Gamma_{32} \\ \Gamma_{13} \\ g_{23}\Gamma_{23} \\ g_{33}\Gamma_{33} \end{bmatrix} \quad (5.36)$$

The solution of the linear system (5.36) provides the nine unknown S parameters of the three-port DUT.

The calculation of the six g_{ik} (i = 1 and 2; k = 1, 2, and 3) is easily obtained using (5.35). For example, g_{23} should be calculated as follows:

$$g_{23} = \frac{\begin{vmatrix} 1-u_{11}^3\Gamma_{13} & 1 & -u_{13}^3\Gamma_{33} \\ -u_{21}^3\Gamma_{13} & u_{20}^3/u_{10}^3 & -u_{23}^3\Gamma_{33} \\ -u_{31}^3\Gamma_{13} & u_{30}^3/u_{10}^3 & 1-u_{33}^3\Gamma_{33} \end{vmatrix}}{\begin{vmatrix} 1 & -u_{12}^3\Gamma_{23} & -u_{13}^3\Gamma_{33} \\ u_{20}^3/u_{10}^3 & 1-u_{22}^3\Gamma_{23} & -u_{23}^3\Gamma_{33} \\ u_{30}^3/u_{10}^3 & -u_{32}^3\Gamma_{23} & 1-u_{33}^3\Gamma_{33} \end{vmatrix}} \tag{5.37}$$

The calibration of the TSPNA can be subdivided into three parts. As shown in Figure 5.5, each part is equivalent to the calibration of a dual six-port network analyzer. By connecting a matched load at one port of the four-port network shown in Figure 5.5, the four-port network will be reduced to a three-port network, which can be characterized by determining its nine parameters, three for each excitation, using the method explained in section 5.2. The rotation of this matched load between the measuring ports of the three reflectometers and the calculation of the corresponding calibration parameters u_{ij}^k ,and u_{j0}^k/u_{i0}^k lead to the complete determination of the 27 calibration parameters, 9 per excitation, needed for the operation of the TSPNA.

u_{ij}^k , and u_{j0}^k/u_{i0}^k can be deduced from the calibration parameters of each pair of six-port reflectometers (*SPi*, *SPj*), $(B_k/A_k)_{ij}$, $(C_k/A_k)_{ij}$, and $(D_k/A_k)_{ij}$ as follows.

$$\frac{u_{j0}^k}{u_{i0}^k} = (B_k/A_k)_{ij} \tag{5.38a}$$

and

$$u_{ij}^k = \begin{cases} (D_k/A_k)_{ij} + (B_k/A_k)_{ij}\, u_{jj}^k ; i > j \\ \left[(C_k/A_k)_{ij} + u_{jj}^k\right] / (B_k/A_k)_{ij} ; j > i \end{cases} \tag{5.38b}$$

with u_{jj}^k as the reflection coefficient of the *j*th port of the four-port network when all the remaining ports are terminated by matched loads. These parameters can be easily measured in advance, using a calibrated six-port reflectometer. In conclusion, three steps are required for the calibration of TSPNA:

Step 1: Calibration of (SP1, SP2), as explained in section 5.2, while SP3 is terminated by a matched load for each excitation (*k* = 1, 2, and 3). This step gives the following nine complex parameters $\left(u_{20}^{k}/u_{10}^{k}, u_{21}^{k}, u_{12}^{k}\right)$.

Step 2: Calibration of (SP1, SP3), as explained in section 5.2, while SP2 is terminated by a matched load for each excitation (*k* = 1, 2, and 3). This step gives the following nine complex parameters $\left(u_{30}^{k}/u_{10}^{k}, u_{31}^{k}, u_{13}^{k}\right)$.

Step 3: Calibration of (SP2, SP3), as explained in section 5.2, while SP1 is terminated by a matched load for each excitation (*k* = 1, 2, and 3). This step gives the following nine complex parameters $\left(u_{30}^{k}/u_{20}^{k}, u_{32}^{k}, u_{23}^{k}\right)$.

The method to determine the 27 calibration parameters required to calculate the six excitation parameters g_{ik} ($i = 2$ and 3; $k = 1, 2$, and 3) is explicit, rigorous, and does not requires any isolation between branches. Only three unknown reciprocal two-port standards, three repeatable and absorptive switches, and two repeatable amplitude and phase controllers are required for the operation of the TSPNA.

5.9 N-SIX-PORT NETWORK ANALYZER

The above described technique for the calibration and measurements of the TSPNA can be easily extended to handle the N-six-port network analyzer (NSPNA). The block diagram of the NSPNA is shown in Figure 5.6. The number of the six-port reflectometers and the number of excitations required should be equal to the number of ports, *N*, of the DUT, and the calibration procedure includes C_n^2 steps. Each step is to calibrate each pair of six-port reflectometers and to deduce the *3N* complex parameters $\left(u_{i0}^{k}/u_{j0}^{k}, u_{ij}^{k}, u_{ji}^{k}\right)$, $k = 1, 2, 3, ..., N$. The calibration procedure of the NSPNA is illustrated in Figure 5.6.

Therefore, the total number of the calibration parameters is $3NC_n^2$ and the linear system to be solved for the calculation should include N^2 equations to solve for the N^2 unknown S parameters.

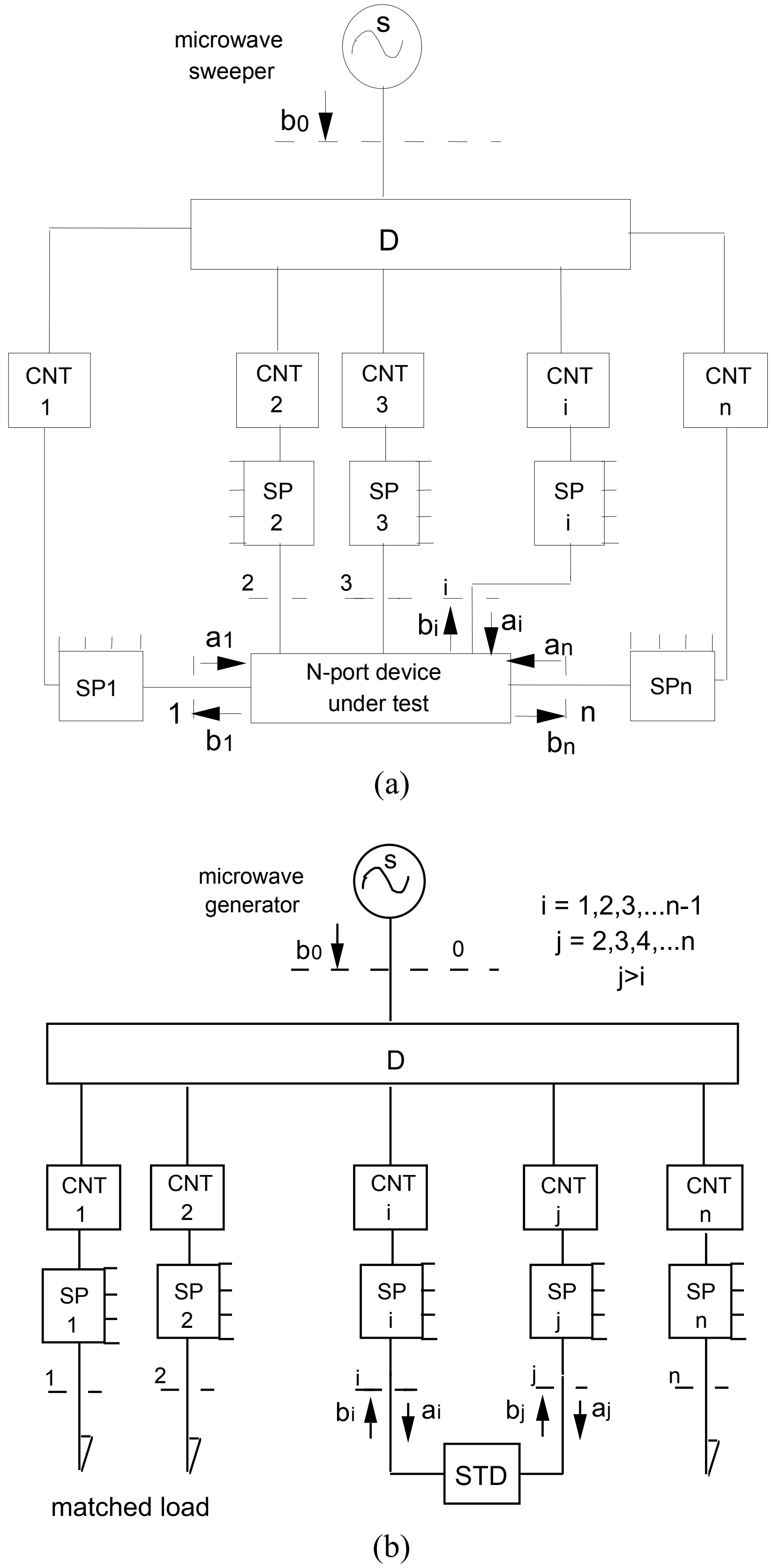

(a)

(b)

Figure 5.6 (a) Block diagram of the NSPNA. (b) Calibration procedure of the NSPNA.

5.10 A SINGLE SIX-PORT N-PORT VECTOR NETWORK ANALYZER

The six-port junction operates as a relative two-channel receiver in this application [16]. As explained, the six-port can perform reflection coefficient measurements at the test port while the input port is connected to an RF generator and the four remaining ports to power/voltage detection sensors. In this configuration, shown in Figure 5.7, incident and reflected waves a_{in} and a_{out} are completely independent and the six-port junction reflectometer operates as a wave comparator providing the ratio a_{out}/ a_{in}. This ratio is a function of the measured reflection coefficient and the calibration parameters, which have to be determined in advance, as follows

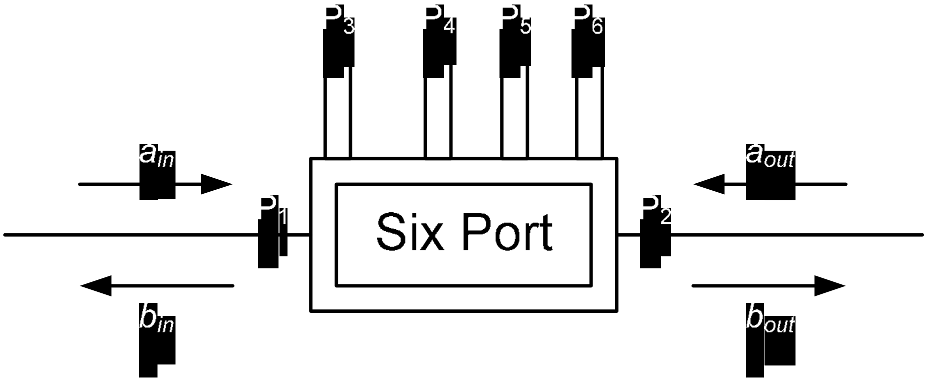

Figure 5.7 A six-port wave comparator.

$$\frac{a_{out}}{a_{in}} = \frac{C_1\Gamma_{out}}{\left(1-C_2\Gamma_{out}\right)} \tag{5.39}$$

where $\Gamma_{out} = \frac{a_{out}}{b_{out}}$, C_1 and C_2 are the calibration parameters characterizing the two-port network constituted by the six-port junction when the four reading ports are terminated by the four power/voltage sensors. These parameters have to be determined in advance, and Γ_{out} is the measured reflection coefficient at port 2 of the six-port junction. According to Chapter 4, when the six-port junction includes a reference port, the reflection coefficient measurement is independent from the generator impedance. Using this hypothesis and a very simple flow graph, the coefficients C_1 and C_2 can be related directly to the S parameters of six-port reflectometer as follows:

$$C_1 = S_{21,SP} \text{ and } C_2 = S_{22,SP} \tag{5.40}$$

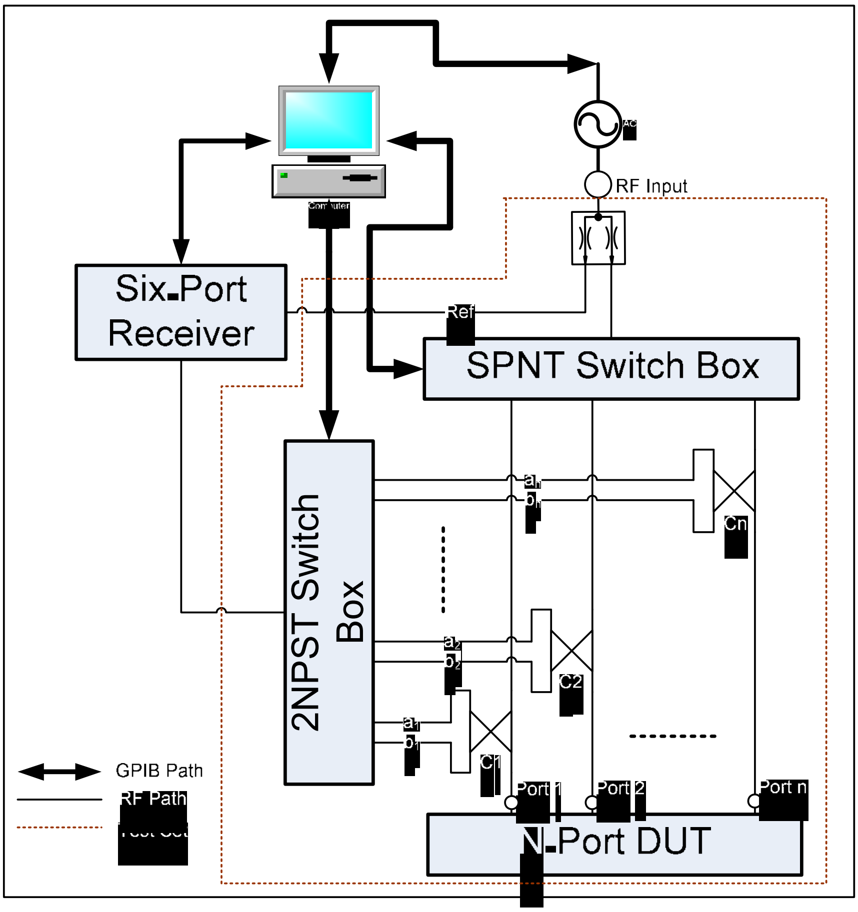

Figure 5.8 A six-port automated network analyzer.

Using the six-port as a two-channel receiver and adding an appropriate test set designed using switches and couplers and power dividers, a single six-port junction N-port vector network analyzer can be designed. The block diagram of the proposed system is shown in Figure 5.8.

For calibration and measurement purposes of S parameters, the incidents and/or the reflected waves a_i and b_i are sampled via N two-dual directional couplers. Using the primary SPNT absorptive switch box, the signal generator is routed successively to the P_i ports of the DUT. For a given setting of the latter switch box, the secondary absorptive 2NPST switch box is used to route all a_i and b_i to the measuring port (port 2) of the six-port junction, respectively. The ratio between the raw a_{ir} or b_{ir} and the reference wave a_{Ref} feeding port 1 of the six-port junction can be provided by the two-channel six-port receiver as follows by the six-port receiver:

$$R = \frac{b_i \text{ or } a_i}{a_{ref}} = \frac{s_{21,SP}\Gamma}{\left(1 - S_{22,SP}\Gamma\right)} \tag{5.41}$$

with $\Gamma = \frac{b_2}{a_2}$, where Γ is the measured reflection coefficient at the output of six-port. For full vector calibration and de-embedding purposes needed to transfer the measurement's reference planes form the inputs of the six port junction to the DUT, the technique presented in Section 5.5 or several established techniques such as QSOLT [9] or TRL [17] can be used as in the case of two-port commercial VNA. For multiport VNA the calibration algorithm presented in the next section can be used to de-embed the raw S parameters measured at the SPR ports to the N-port of the DUT.

5.11 N-PORT CALIBRATION ALGORITHM

In the proposed setup, the measurements are performed at the SPR as ratios between channel 1 as a receiver for the incident and reflected waves and channel 2 as a reference. This first requires calibration of the six-port junction as a reflectometer using one of the techniques reported in Chapter 3 [12, 13, 17]. Then the raw S parameters measured at the SPR ports have to be de-embedded to get the true S parameters of the DUT [5, 14, 15].

The calibration algorithm used in this measurement setup is based on making full calibration for port 1 using OSL standards and then making two-port calibration using a (THRU) standard. The block diagram of the *N*-port calibration procedure is shown in Figure 5.9. The calibration steps can be described as follows.

Step 1: Performing OSL at port 1

This step is performed to calculate the parameters (e_1^{11}, e_1^{22}, and $\Delta e = e_1^{11} e_1^{22} - e_1^{21} e_1^{12}$) of the error box representing the transfer from port 1 to the six-port receiver (SPR) reference plane as shown in Figure 5.9. These parameters can be calculated by measuring the reflection coefficients of OSL at port 1 at each frequency point using (5.33)–(5.36).

The reflection coefficient at the standard connected to port 1 plane (Γ_{STD}) can be described as a function of the measured reflection coefficient at the SPR plane (Γ_m) and the error box matrix e_1^{ij} as follows:

$$\Gamma_m = e_1^{11} + \frac{e_1^{12} e_1^{21} \Gamma_{STD}}{1 - e_1^{22} \Gamma_{STD}} = \frac{-\Delta e_1 \Gamma_{STD} + e_1^{22}}{-e_1^{22} \Gamma_{STD} + 1} \tag{5.42}$$

Using open, short, and load standards, one can write

$$\begin{bmatrix} e_1^{11} \\ e_1^{22} \\ \Delta e \end{bmatrix} = \begin{bmatrix} 1 & \Gamma_{open} * \Gamma_{Mopen} & -\Gamma_{open} \\ 1 & \Gamma_{short} * \Gamma_{Mshort} & -\Gamma_{short} \\ 1 & \Gamma_{load} * \Gamma_{Mload} & -\Gamma_{load} \end{bmatrix}^{-1} \begin{bmatrix} \Gamma_{Mopen} \\ \Gamma_{Mshort} \\ \Gamma_{Mload} \end{bmatrix} \tag{5.43}$$

The error box E_i models the interconnection between the SPR measurement port and the port *i* of the DUT and relates the reflected to the incident waves, defined according the following equation

$$\begin{bmatrix} b_{mi} \\ a_{duti} \end{bmatrix} = E_i \cdot \begin{bmatrix} a_{mi} \\ b_{duti} \end{bmatrix} \tag{5.44}$$

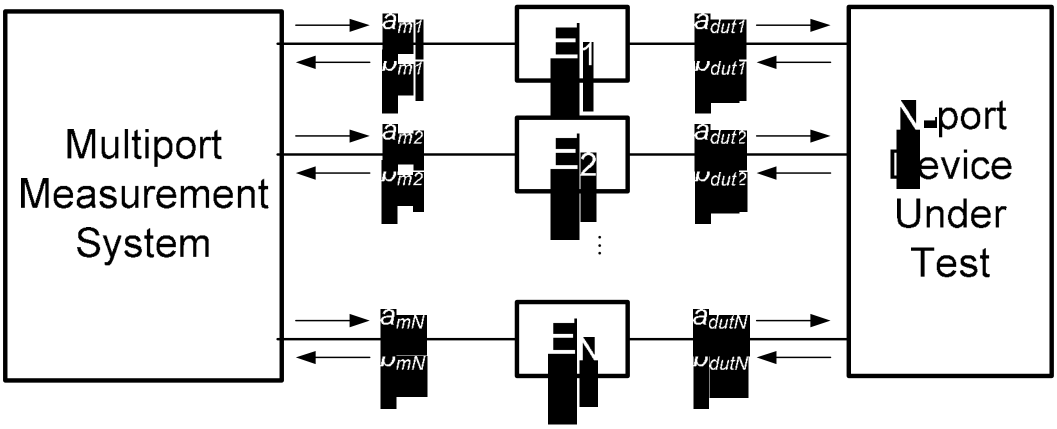

Figure 5.9 Block diagram of the *N*-port calibration procedure.

where Γ_{open}, Γ_{short}, and Γ_{load} are the actual reflection coefficients of the OSL standards. Γ_{Mopen}, Γ_{Mshort}, and Γ_{Mload} are the measured reflection coefficients of the OSL standards using SPR.

Step 2: THRU Connection between port 1 and each port of the N-ports

By performing this step, the parameters of the remaining error boxes between the N-ports and the SPR can be calculated as functions of the measured S parameters of the THRU using the following relations:

$$e_K^{22} = \frac{S_{mKK}^{T1N} - e_1^{11}}{t_{11} + e_1^{22}(S_{m11}^{T1K} - e_1^{11})} \tag{5.45}$$

$$e_K^{11} = S_{mKK}^{T1K} - \frac{t_{KK} e_1^{22}}{1 - e_1^{22} e_K^{22}} \tag{5.46}$$

$$T_{KK} = S_{mK1}^{T1K} S_{m1K}^{T1K} - \frac{\left(1 - e_1^{22} e_K^{22}\right)^2}{t_{11}} \tag{5.47}$$

$$T_{1K} = S_{m1K}^{T1K}\left(1-e_1^{11}e_K^{11}\right) \text{ and } T_{K1} = S_{mK1}^{TK1}\left(1-e_1^{11}e_K^{11}\right) \tag{5.48}$$

where *k* is the port number and S_m are the measured S-parameters of the THRU connected between port 1 and port *K*. Step 2 will be repeated until *K*=*N* where *N* is the number of ports.

Step 3: Calculation of the term T_{KJ} *, which characterizes the path between port k and port j*

$$T_{KJ} = e_k^{12}e_j^{21} = \frac{T_{K1}T_{1J}}{t_{11}} \tag{5.49}$$

Step 4:De-embedding of the DUT's S parameters

After calculating all the parameters of the error boxes, the de-embedded S parameters of the DUT can be calculated using (5.40).

$$S = A*(I+\Gamma_{11}*A)^{-1} \tag{5.50}$$

where

$$A = \begin{bmatrix} \frac{\left(S_{m11}-e_1^{11}\right)}{t_{11}} & \cdots & \cdots & \frac{S_{m1N}}{t_{1N}} \\ \frac{S_{m21}}{t_{21}} & \frac{\left(S_{m22}-e_1^{11}\right)}{t_{22}} & \cdots & \frac{S_{m2N}}{t_{2N}} \\ \vdots & \vdots & \vdots & \vdots \\ \frac{S_{mN1}}{t_{N1}} & \cdots & \cdots & \frac{\left(S_{mNN}-e_N^{11}\right)}{t_{NN}} \end{bmatrix} \tag{5.51}$$

$$\Gamma_{11} = \text{diag}(e_1^{11}, e_2^{11}, e_3^{11} \ldots, e_N^{11}) \tag{5.52}$$

and *I* is the identity matrix. This calibration algorithm has the advantage of taking the cross-talk between ports into consideration, which leads to accurate results compared to other calibration algorithms. It also avoids the problem of impractical line lengths when using the TRL method at relatively low frequencies.

References

[1] Kaliouby, L., and R. G. Bosisio, "A New Method for Six-Port Swept Frequency Automatic Network Analysis," *IEEE Trans. on Microwave Theory and Tech.,* Vol. 32, No. 12, pp. 1678–1682, December 1984.

[2] Cronson, H. M., and L. Susman, "A Six-Port Automatic Network Analyzer," *IEEE Trans. on Microwave Theory and Tech.,* Vol. MTT-25, pp. 1086–1091, December 1977.

[3] Engen, G. F., and C. A. Hoer, "Thru-Reflect-Line: An Improved Technique for Calibrating the Dual Six-Port Automatic Network Analyzer," *IEEE Trans. on Microwave Theory and Tech.,* Vol. MTT-27, pp. 987–992, 1979.

[4] Li, S., and R. G. Bosisio, "A Calibration of Multiport Reflectometer by Means of Four Open/Short Circuit," *IEEE Trans. on Microwave Theory and Tech.,* Vol. MTT-30, pp. 1085–1090, July 1982.

[5] Li, S. H., and R. G. Bosisio, "The Automatic Measurement of N-Port Microwave Junction by Means of the Six-Port Technique," *IEEE Trans. Instr. Meas*., Vol. IM-31, No. 1, pp. 40–43, 1982.

[6] Maury, M. A., S. L. March, and G. R. Simpson, "TRL Calibration of Vector Automatic Network Analyzers," *Microwave Journal,* Vol. 30, No. 5, pp. 387–382, May 1987.

[7] Rubin, D., "De-Embedding MM-Wave MICs with TRL," *Microwave Journal*, Vol. 33, No. 6, pp. 141–150, June 1990.

[8] Locatelli, G. P., "De-Embedding Techniques for Device Characterization," *ALTA FREQ*., Vol. 57, No. 5, pp. 267–272, June 1988.

[9] Engen, G.F. and C.A. Hoer, "Thru-Reflect-Line: An Improved Technique for Calibrating the Dual Six-Port Automatic Network Analyzer," *IEEE Trans. on Microwave Theory and Tech.,* Vol. 27, pp. 987–993, December 1979.

[10] Williams, D. F., "De-Embedding and Un-Terminating Microwave Fixtures with Nonlinear Least Squares," *IEEE Trans. on Microwave Theory and Tech.*, pp. 787–792, June 1990.

[11] Reeve, G., R. B. Marks, and D. Blackburn, "Microwave Monolithic Integrated Circuit-Related Metrology at NIST," *IEEE Trans. Instr. Meas*., pp. 958–961, December 1990.

[12] Eul, H. J., and B. Schiek, "A Generalization Theory and New Calibration Procedures for Network Analyzer Self-Calibration," *IEEE Trans. on Microwave Theory and Tech.,* Vol. MTT-39, pp. 724–731, April 1991.

[13] Soares, R. A., P. Gouzien, P. Legaud, and G. Follot, "A Unified Mathematical Approach to Two-Port Calibration Techniques and Some Applications," *IEEE Trans. Microwave Theory Tech.,* Vol. MTT-37, pp. 1660–1674, November 1989.

[14] Ghannouchi, F. M., Y. Xu, and R. G. Bosisio, "A One-Step Connection Method for the Measurement of N-Port Microwave Networks Using of Six Port Techniques," *IEE Proceedings Part-H. Microwave, Antenna & Propagation,* Vol. 141, No. 4, pp. 285–289, August 1994.

[15] Ghannouchi, F. M., "A Calibration and Measurement Method of a Tri-Six-Port Network Analyzer Suitable for On Wafer Characterization of Three Port Devices," *IEEE Trans. Instrum. Meas. ,*Vol. 42, No. 4, pp. 864–866, August 1993.

[16] Khouaja, S. and F. M. Ghannouchi, “A Single Six-Port Based Automated Network Analyzer,” *IEEE MTT-S*, pp. 1503–1506, 1998.

[17] Engen, G .F., “Calibrating the Six-Port Reflectometer by Means of Sliding Termination,” *IEEE Trans. Microwave Theory.*, pp. 951–957, December 1978.

Chapter 6

Source-Pull and Load-Pull Measurements Using the Six-Port Technique

In previous chapters, it has been shown that a six-port reflectometer can be used to simultaneously perform impedance and power flow measurements. A straightforward application of such capability of six-port technique is the load-pull measurements of microwave transistors. Typical setups for passive and active load-pull measurements as well as the extension of this technique to perform harmonic load-pull measurements will be described in this chapter. The on-wafer load-pull measurements on chip devices require special attention, and an alternative approach for impedance and power flow calibration using a reflection-based technique will be presented.

6.1 PRINCIPLES OF SOURCE-PULL/LOAD-PULL MEASUREMENTS

The object of load/source-pull measurements is the experimental determination of the performances of a device in large-signal operation mode and the identification of the conditions that yield the optimum or desired performance in terms of power, power efficiency or linearity or a trade-off between them. Load-pulling means varying the output load, that is, the load at the output side of the device under test (DUT), and source-pulling means varying the input load, that is, the load at the source side of the DUT. In fact, the load-pull measurements on a microwave transistor consist essentially of plotting the constant power contour absorbed the load seen by the DUT which can span the whole Smith chart for given bias point and input power level. Different setups have been used in the past for such measurements. A typical load-pull/measurement system is shown in Figure 6.1. One could split these techniques into two types: passive source-pull/load-pull setups and active source-pull/load-pull setups.

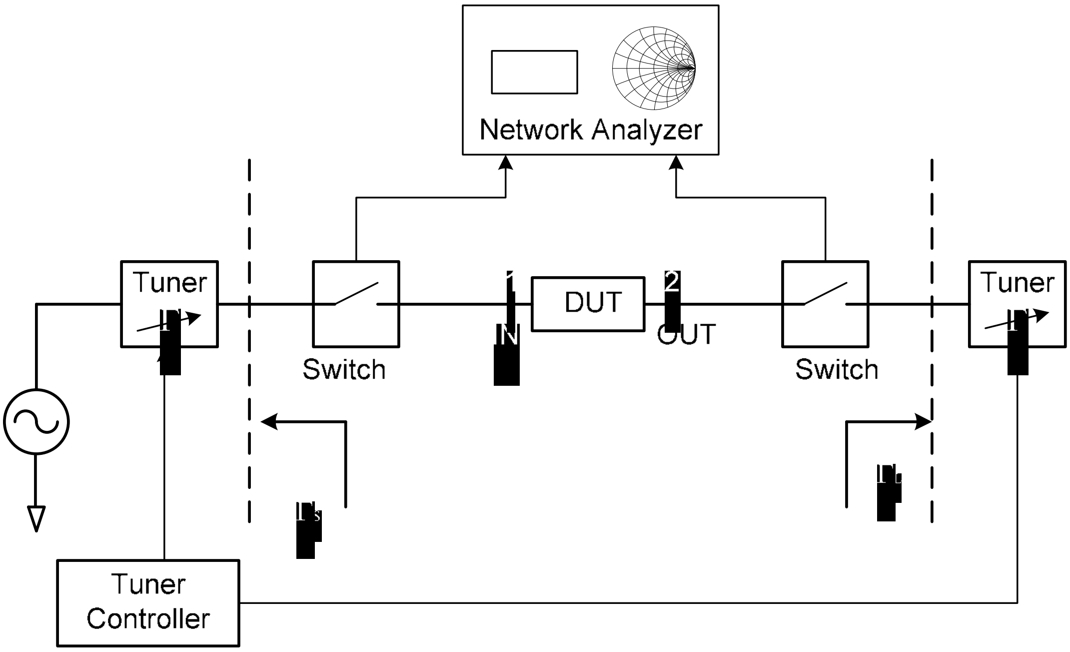

Figure 6.1 A typical load-pull/source-pull measurement system.

Indeed, any load-pull system should be capable of measuring the input impedance of the DUT, the load impedance seen by the DUT at its output, Z_L, the source load impedance presented to the DUT at its input, Z_S, the input power absorbed by the DUT, P_{in}, and the power delivered to load, P_L. In addition, any load-pull system has to monitor the voltage and currents across both the input and output of the DUT for any pair of (Z_S , Z_L) to be able to plot the power-added efficiency in the Smith chart. In some circumstances, measurement and monitoring of the linearity of the device are also required. Several metrics' linearity can be used depending on the application such as AM/AM and AM/PM distortions, carrier to third-order intermodulation products (C/IMD$_3$), adjacent channel power ratio (ACPR), and error vector magnitude (EVM).

6.2 IMPEDANCE AND POWER FLOW MEASUREMENTS WITH AN ARBITRARY TEST PORT IMPEDANCE

Six-port measurement techniques have been used for linear S parameters' measurements of microwave circuits. Figure 6.2 shows a six-port reflectometer. It has been shown in previous chapters that the measurements of the complex S parameters of *N*-port network require 4N power readings.

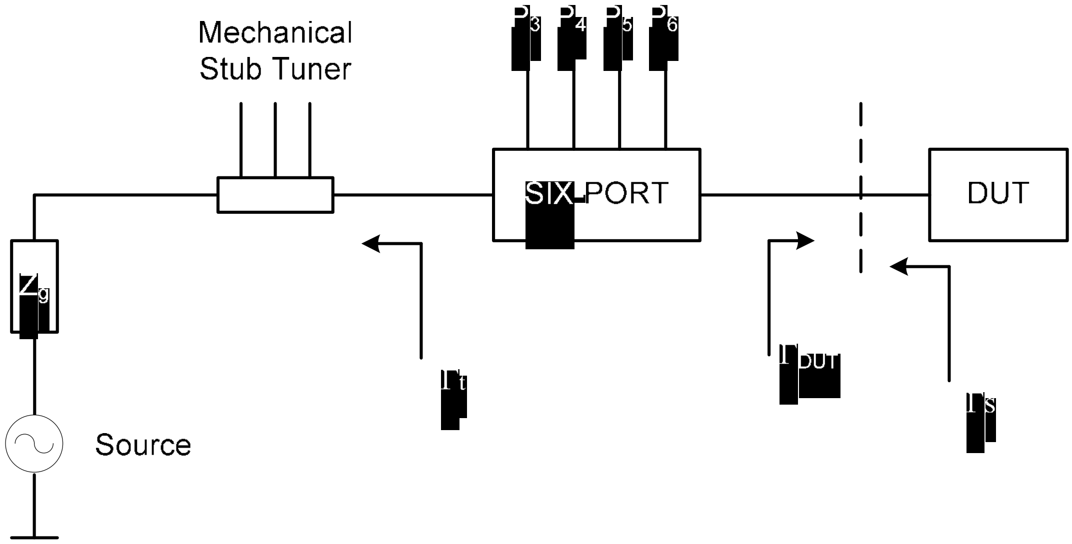

Figure 6.2 A six-port reflectometer with variable test port impedance.

Phase information is derived without any need to convert RF signal down to IF frequency or baseband. Moreover, it has also been shown that the calibration and measurement calculations are not a function of the source impedance presented to the input port of the six-port reflectometer; hence, one could change such a source impedance by using a passive tuner inserted before the input port of the six-port reflectometer. The power flow exciting the device under test connected to the measuring port of the six-port junction can be calculated using the expression obtained in Chapter 2 and reported here:

$$\Gamma_{DUT}(f)=\frac{w(f)-e(f)}{-c(f)w(f)+d(f)} \tag{6.1}$$

$$P_{DUT}(f)=\frac{k(f)P_r(f)}{\left|1+c(f)\Gamma_{DUT}(f)\right|^2} \tag{6.2}$$

where $c(f)$, $d(f)$, and $e(f)$ are the error box parameters, $w(f)$ is the embedded reflection coefficient, $k(f)$ is the power calibration parameter that has to be determined at each measurement's frequency, $P_{REF}(f)$ is the power reading measured by the reference port of the six-port junction, and $\Gamma_{DUT}(f)$ is the reflection coefficient measured by the six-port reflectometer.

$\Gamma_s(f)$, shown in Figure 6.2, is the source impedance seen by the DUT. The complex value of $\Gamma_s(f)$ is related to the tuner impedance, $\Gamma_t(f)$, and the S parameters, s_{ij}, of the two-port network delimited by the input and the output ports of the six-port junction when the remaining ports of the six-port junction are terminated by the 50 Ω power sensors. $\Gamma_s(f)$ can be obtained as:

$$\Gamma_s(f) = s_{22}(f) + \frac{s_{12}(f)s_{21}(f)\Gamma_t}{1 - s_{11}(f)\Gamma_t} = \frac{\alpha(f)\Gamma_t + \beta(f)}{\mu(f)\Gamma_t + 1} \tag{6.3}$$

where $\alpha(f)$, $\beta(f)$, and $\mu(f)$ are directly related to the two-port network delimited by the input and the output reference planes of the six-port junction.

If the six-port junction is designed to be transparent in such a way that the input and measuring port of the six-port junction are both situated in the main direct line of 50 Ω $\left(|s_{12}| = |s_{21}| \cong 1; |s_{11}| \cong |s_{22}| \cong 0\right)$, a good approximation of the module of $\Gamma_s(f)$ is

$$|\Gamma_s(f)| \cong |\Gamma_t(f)| \tag{6.4}$$

Such a configuration allows online impedance and power flow measurements while the impedance presented to the DUT can be changed arbitrarily over the whole Smith chart. This assumes that the tuner was precalibrated and the impedance corresponding to Γ_t is known for any position of the stubs of the used tuner.

6.3 OPERATION OF A SIX-PORT IN REVERSE CONFIGURATION

Generally, a six-port junction is built with physically assigned input, output, power reference port, and three other power detection ports. The normal use of a six-port reflectometer requires the connection of the signal generator at the input port and the DUT to the output port of the six-port junction, as shown in Figure 6.3(a).

Microwave signals are injected from the input through the output; the six-port measures the reflection coefficient Γ of the DUT and the power flow at the output port. It was demonstrated in Chapter 4 that the signal generator impedance can be arbitrary and has no effect on the six-port calibration and measurement calculations [8]. This configuration of the six-port reflectometer can be considered as the direct configuration. However, if the signal generator is connected to the output and the DUT to the input of the six-port and the microwave signal is injected from the output port through the input port, then the six-port junction is considered in a reverse configuration as shown in Figure 6.3(b).

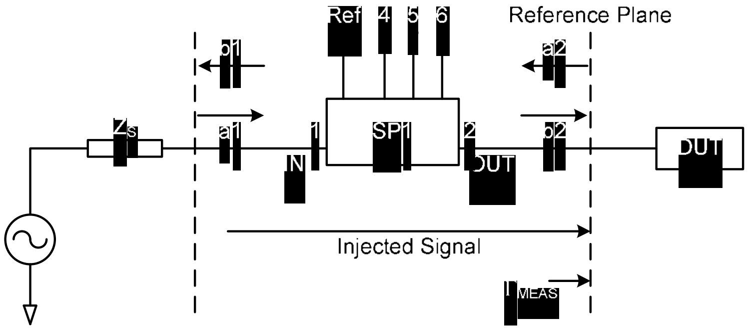

DIRECT SIX-PORT REFLECTOMETER
(a)

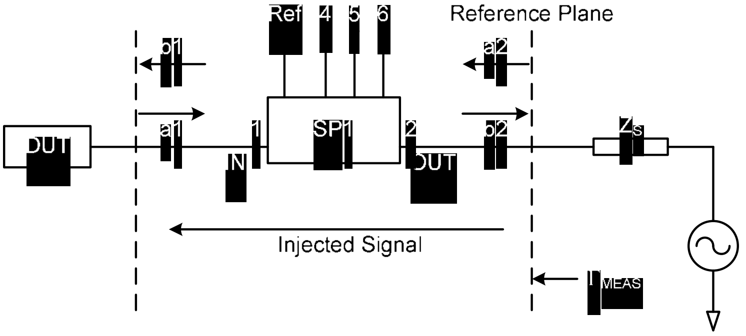

REVERSE SIX-PORT REFLECTOMETER
(b)

Figure 6.3 Six-port reflectometer: (a) direct and (b) reverse configurations. (Copyright 1994 IEEE from [9].)

In this configuration, the six-port would measure the reflection coefficient of the DUT, seen at the reference plane located at the output port (port 2) of the six-port junction. The calibration procedure of the six-port reflectometer used in this reverse configuration is divided into two steps: (1) the classical six-port to four-port reduction technique using 13 unknown and well distributed loads, and (2) a new error box procedure using three well-known standards [9]. The determination of these error box parameters are based on those obtained in direct configuration and on some analytical manipulations.

Figure 6.4 shows the different steps required for the calibration, de-embedding, and measurement procedures of the reverse six-port reflectometer. The calibration and de-embedding procedures characterize the six-port junction and fix the reference plane for the measurements; see Figure 6.4(a, b). A self-calibration approach [10,11], contrary to an explicit calibration method [12], can be used in this context. Notice that a -10 dB directional coupler is added to the output in the de-embedding procedure. This coupler will allow the use of the six-port junction in reverse configuration, as shown in Figure 6.4(c). This configuration consists of a generator connected to the output port of the six-port reflectometer via the -10 dB directional coupler.

The six-port junction measures the reflection coefficient of the tuner that is shifted from the input port (port 1) to the reference plane at the output port (port 2). The microwave signal injected through the coupler excites the DUT. A part of this signal is reflected toward the six-port and allows the latter to measure the reflection coefficient of the tuner connected to the input port. The six-port junction was designed to be transparent $\left(|s_{12}| = |s_{21}| \cong 1; |s_{11}| \cong |s_{22}| \cong 0\right)$, in order to minimize the insertion loss allowing the tuner to cover a wider area on the Smith chart. The measured tuner reflection coefficient is shifted to the reference plane defined by the de-embedding procedure at the right-hand side of the six-port and the directional coupler.

Note that at first the six-port reflectometer is calibrated in the direct configuration and next is used in the reverse configuration. Thus, this measurement technique can be justified if we can establish a relation between the calibration and the de-embedding of the direct and the reverse six-port junctions.

6.3.1 Six-Port Reflectometer Calibration in Reverse Configuration

Generally, the six-port is constructed with a power reference port and three remaining detection ports (ports 4, 5, and 6) such that the power readings at the six-ports obey the following expressions:

$$P_{ref} = P_3 = \beta_3 \left|1 + a_3 \Gamma_L\right|^2 \left|b_2\right|^2 \tag{6.5a}$$

$$P_i = \beta_i \left|1 + a_i \Gamma_L\right|^2 \left|b_2\right|^2, \ i = 4,5,6 \tag{6.5b}$$

where β_i are real constants, a_i are complex constants that characterize the six-port junction, b_2 is the outgoing wave at the output port (port 2, in Figure 6.4), and Γ_L is the reflection coefficient of the DUT. Dividing P_i by P_{ref}, the ratio of P_i / P_3 can next be written as 13:

$$\frac{P_4}{P_{ref}} = \alpha_4 \left|\Gamma_L - Q_4\right|^2 \tag{6.6a}$$

$$\frac{P_5}{P_{ref}} = \alpha_5 \left|\Gamma_L - Q_5\right|^2 \tag{6.6b}$$

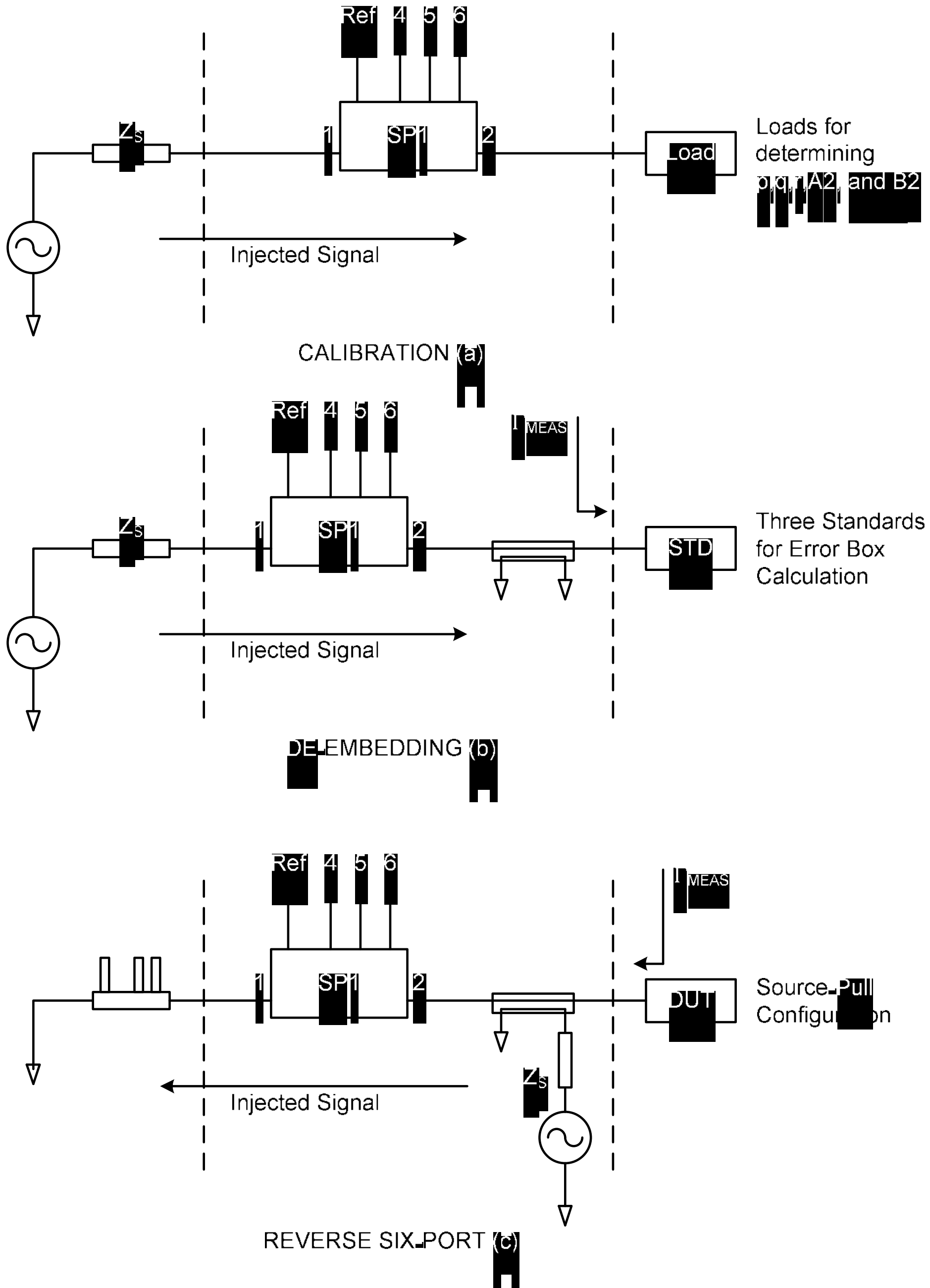

Figure 6.4 Reverse six-port reflectometer measurements: (a) calibration in direct configuration; (b) de-embedding in direct configuration; and (c) measuring in reverse configuration. (Copyright 1994 IEEE from [9].)

and

$$\frac{P_6}{P_{ref}} = \alpha_6 \left|\Gamma_L - Q_6\right|^2 \tag{6.6c}$$

where α_i and Q_i are complex constants. The reflection coefficient Γ_L of the load is determined by the intersection of three circles using the six- to four-port reduction technique similar to technique explained in Chapter 4 as

$$\begin{bmatrix} \dfrac{P_4}{P_{ref}} \\ \dfrac{P_5}{P_{ref}} \\ \dfrac{P_6}{P_{ref}} \end{bmatrix} = \begin{bmatrix} \alpha_4 \left|Q_4\right|^2 \\ \alpha_5 \left|Q_5\right|^2 \\ \alpha_6 \left|Q_6\right|^2 \end{bmatrix} + \begin{bmatrix} \alpha_4 & -\alpha_4 Q_4^* & -\alpha_5 Q_4 \\ \alpha_5 & -\alpha_5 Q_5^* & -\alpha_5 Q_5 \\ \alpha_6 & -\alpha_6 Q_6^* & -\alpha_6 Q_6 \end{bmatrix} \begin{bmatrix} \left|\Gamma_L\right|^2 \\ \Gamma_L^* \\ \Gamma_L \end{bmatrix} \tag{6.7a}$$

$$\begin{bmatrix} \left|\Gamma_L\right|^2 \\ \Gamma_L^* \\ \Gamma_L \end{bmatrix} = \begin{bmatrix} \alpha_4 & -\alpha_4 Q_4^* & -\alpha_5 Q_4 \\ \alpha_5 & -\alpha_5 Q_5^* & -\alpha_5 Q_5 \\ \alpha_6 & -\alpha_6 Q_6^* & -\alpha_6 Q_6 \end{bmatrix}^{-1} \begin{bmatrix} \dfrac{P_4}{P_{ref}} - \alpha_4 \left|Q_4\right|^2 \\ \dfrac{P_5}{P_{ref}} - \alpha_5 \left|Q_5\right|^2 \\ \dfrac{P_6}{P_{ref}} - \alpha_6 \left|Q_6\right|^2 \end{bmatrix} \tag{6.7b}$$

Examining (6.7), we note that the product of rows two and three is equal to row one. Hence, after some algebraic manipulation, we eliminate Γ_L and obtain the following relation:

$$\begin{aligned} & p\left[\frac{P_4}{P_{ref}}\right]^2 + q(A^2)^2\left[\frac{P_5}{P_{ref}}\right]^2 + r(B^2)^2\left[\frac{P_6}{P_{ref}}\right]^2 + (r-p-q)A^2\left[\frac{P_4}{P_{ref}}\right]\left[\frac{P_5}{P_{ref}}\right] + \\ & (q-p-r)B^2\left[\frac{P_4}{P_{ref}}\right]\left[\frac{P_6}{P_{ref}}\right] + (p-q-r)A^2B^2\left[\frac{P_5}{P_{ref}}\right]\left[\frac{P_6}{P_{ref}}\right] + \\ & p(p-q-r)\left[\frac{P_4}{P_{ref}}\right] + q(q-p-r)A^2\left[\frac{P_5}{P_{ref}}\right] + r(r-p-q)B^2\left[\frac{P_6}{P_{ref}}\right] + pqr = 0 \end{aligned} \tag{6.8}$$

where the real quantities p, q, r, A^2,B^2 are the calibration constants related to α_i and Q_i and associated with the physical structure of the six-port junction [10].

These parameters are determined by the six-port to four-port reduction theory: for each specified frequency, at least five measurements for different distributed loads that lead to a set of five nonlinear equations are needed to solve this set of equations [10,11]. The explicit knowledge of the impedance values of these distributed loads is not required in the calculation of p, q, r, A^2, and B^2. As discussed earlier, in practice, 13 loads are employed to improve the accuracy of the calibration over the entire Smith chart.

The elimination of $|b_2|^2$ in (6.5) makes the quantities p, q, r, A^2, and B^2 completely independent of the choice of port 1 or port 2 for the test port of the six-port junction. Hence, if the power reference and the remaining detection ports are fixed, the calibration of the six-port, which aims at the determination of p, q, r, A^2, and B^2, will normally give the same value of these parameters for a six-port used in either direct or reverse configurations.

6.3.2 Error Box Calculation for Reverse Six-Port Measurements

Once the calibration constants are found, the six-port can measure an embedded reflection coefficient $w = g(P_i/P_{ref}, p, q, r, A^2, B^2)$ at an unknown reference plane [10]. The error box calculation (or de-embedding procedure) determines the three complex constants c, d, and e, which relate w to the reflection coefficient, Γ, at a chosen reference plane by the following relation:

$$w = \frac{d\Gamma + e}{c\Gamma + 1} \tag{6.9}$$

With three well-known standards and with their measured embedded reflection coefficients w_i given by the six-port, one can easily find c, d, and e by solving the linear system given here:

$$\begin{aligned}
w_1\Gamma_1^{std}c - \Gamma_1^{std}d - e &= -w_1 \\
w_2\Gamma_2^{std}c - \Gamma_2^{std}d - e &= -w_2 \\
w_3\Gamma_3^{std}c - \Gamma_3^{std}d - e &= -w_3
\end{aligned} \tag{6.10}$$

Referring to Figure 6.4(c), for a reverse six-port, the microwave signal must be injected from the output port (port 2) to the input port (port 1) and we must present the three de-embedding standards at the left side of the reference plane, which is physically impossible. To overcome this difficulty, a direct six-port error box, as shown in Figure 6.4(b), with the three standards connected successively to the measuring port at the right side of the reference plane is used. For the reverse six-port error box calculation, the system (6.10) is replaced by the following:

$$
\begin{aligned}
w_1 \frac{c'}{\Gamma_1^{std}} - \frac{d'}{\Gamma_1^{std}} - e' &= -w_1 \\
w_2 \frac{c'}{\Gamma_2^{std}} - \frac{d'}{\Gamma_2^{std}} - e' &= -w_2 \\
w_3 \frac{c'}{\Gamma_3^{std}} - \frac{d'}{\Gamma_3^{std}} - e' &= -w_3
\end{aligned}
\tag{6.11}
$$

where the value Γ_i^{std} of the three standards in (6.10) are replaced by $1/\Gamma_i^{std}$ in (6.11). Note that using the value of Γ_i^{std} is equivalent to presenting these standards at the left side of the reference plane, which is valid when Γ is referred to the same characteristic impedance (50 Ω).

In practice, it is usually convenient to use a short circuit, an open circuit, and a matched load of 50 Ω ($\Gamma = 0$) as the three de-embedding standards. Unfortunately, for a reverse six-port error box procedure, the matched load needs to be replaced by another standard to avoid the $1/\Gamma$ singularity. To circumvent this difficulty, one can determine the reverse six-port error box by first finding the coefficients *c, d,* and *e* of the conventional error box procedure and next deducing the coefficient *c', d',* and *e'* of the reverse six-port error box using the following relations:

$$c' = 1/c;\ d' = 1/d;\ e' = 1/e \tag{6.12}$$

These relations can be easily derived by comparing the two sets of linear equations, (6.10) and (6.11). Measurement results obtained by a reverse six-port calibrated and de-embedded according to the above procedures confirm the validity of this technique [9]. The reverse six-port reflectometer is suitable for performing source-pull measurements at the input of the DUT. The measurement technique consists of a signal injected into the DUT via the directional coupler. The reflected signal from the input port of the DUT allows the six-port to perform measurements in the opposite direction. It should be mentioned that when the DUT is well matched, the six-port reflectometer will not be powered and will not operate. However, source-pull measurements are only useful when the DUT input is mismatched.

6.3.3 Discussion

In light of (6.9) and (6.12), we can easily see that $\Gamma' = 1/\Gamma$ where Γ' and Γ are, respectively, the reflection coefficients measured by a six-port in reverse and in direct configurations. It may seem that this relation can be equally obtained by just taking $\Gamma = b / a$ and $\Gamma' = a / b$ (where a and b are, respectively, the incident and the reflected wave), but this is not true. For example, in the case of a direct six-port measurement, $1/\Gamma_{meas.}$ does not lead to the impedance of the generator and has no physical significance. In a direct six-port configuration, the DUT is connected to port 2 of the six-port reflectometer that measures the ratio of a_2 / b_2, the incoming and outgoing waves at the output of the junction (port 2, in Figure 6.10). This ratio a_2 / b_2 represents the reflection coefficient of the DUT, seen from the left side of the reference plane. In a reverse six-port configuration, the reference plane is always located at port 2 but the output port of the reflectometer becomes port 1.

Thus, the reverse six-port junction measures the ratio of a_1 / b_1 rather than a_2 / b_2. The ratio a_1 / b_1 shifted to port 2 of the six-port junction by the de-embedding procedure then represents the reflection coefficient of the test port of the six-port reflectometer, seen from the load side of the reference plane. Therefore, the inverse value b_1 / a_1 cannot yield the reflection coefficient of the device under test connected to port 2. In summary, reverse six-port reflectometer measurements require a conventional calibration procedure to characterize the six-port junction and a special error box to fix the reference plane. This error box can be obtained either by using the relations given by (6.12) or by inverting the actual reflection coefficient Γ of the standards used to calculate the parameters *c, d,* and *e* of the direct error box.

6.4 SOURCE-PULL CONFIGURATION USING SIX-PORT

The source-pull measurement is aimed at evaluating linear/nonlinear device performance as a function of source impedance [1]. In source-pull measurement, the input load varies as a load at the source side. The source-pull is measured using six-port technique both in passive and active configurations.

6.4.1 Passive Source-Pull Configuration

The passive source-pull techniques are based on the use of a tuner. Figure 6.5 shows the setup for a passive source-pull: the input signal is injected into the device under test (DUT) via a directional coupler, and the source impedance is set with a stub tuner. The six-port in such an arrangement is operated in reverse configuration and measures the source impedance seen at the reference plane.

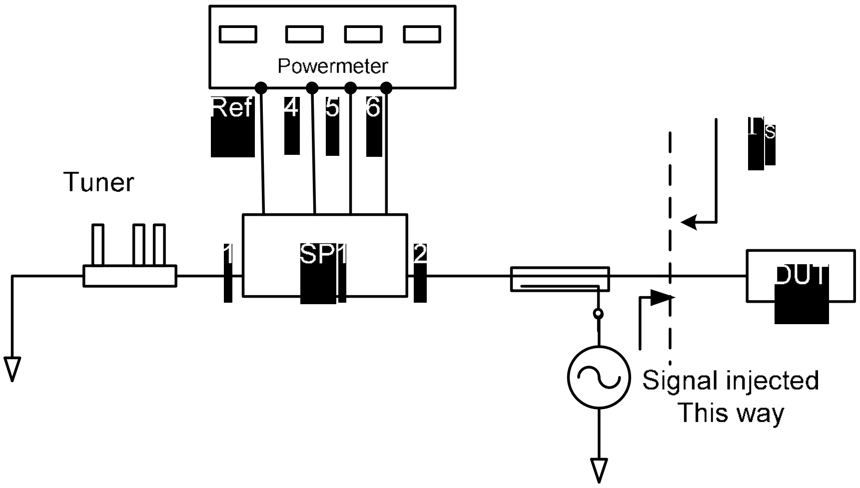

Figure 6.5 A passive source-pull measurement system.

6.4.2 Active Source-Pull Configuration

Figure 6.6 shows the setup for an active source-pull measurement. This setup uses a variable attenuator and a variable phase shifter. The attenuator and phase shifter values can be varied during the measurement.

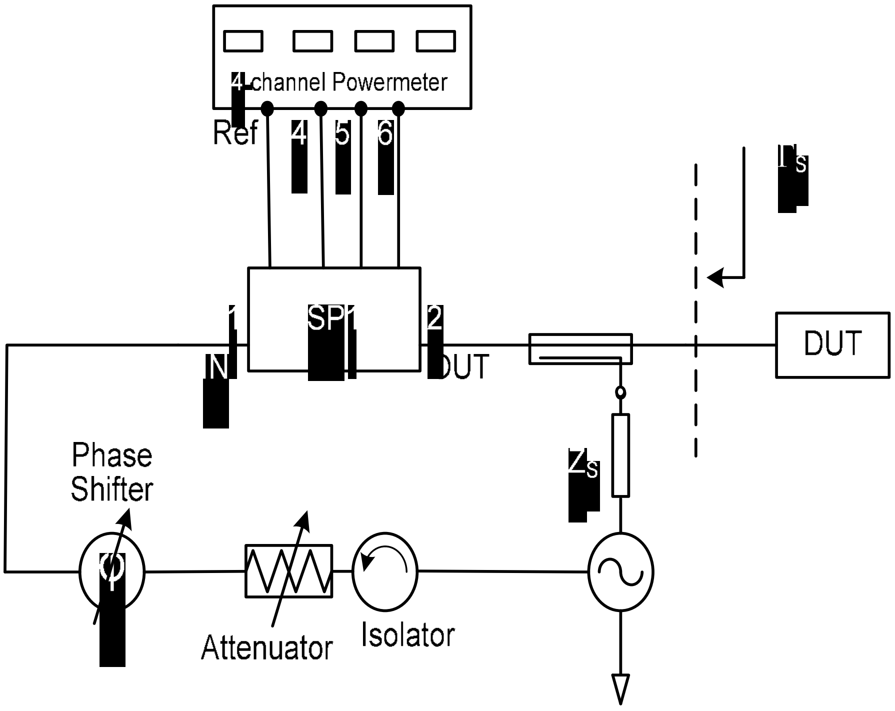

Figure 6.6 An active source-pull measurement system.

The six-port in this setup is used in reverse configuration allowing the measurements of the source impedance seen at the reference plane. As may be seen, the active source-pull configuration has more flexibility and accuracy in comparison to the conventional passive source-pull technique.

6.5 LOAD-PULL CONFIGURATION USING SIX-PORT

The load-pull measurement evaluates linear/nonlinear device performance as a function of load impedance. Both passive and active load-pull measurement setups can be realized using the six-port technique.

6.5.1 Passive Load-Pull Configuration

The passive load-pull configuration, as shown in Figure 6.7, comprises two six-port junctions, SP1 and SP2 and two tuners, T1 and T2. This configuration allows the evaluation of a large-signal input impedance $\Gamma_{in}(f)$ of the TUT and the power delivered to it $P_{in}(f)$ by means of SP1 as shown in the Figure 6.7.

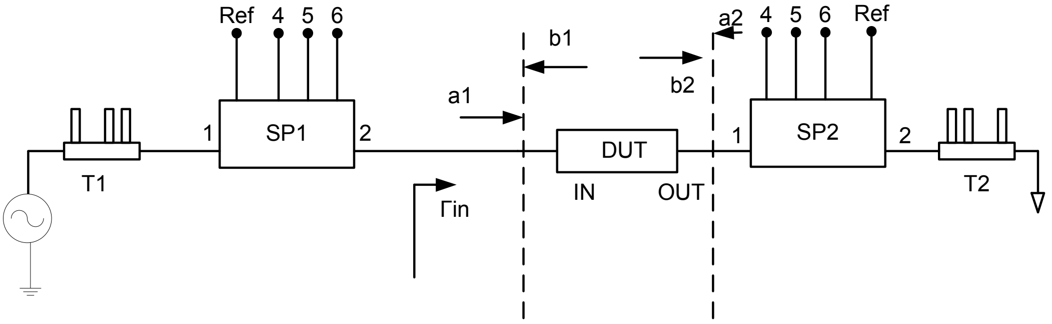

Figure 6.7 Six-port based passive load-pull measurement configuration.

The source impedance seen by the DUT at its input can be changed by varying the stub positions of T1 as follows:

$$\Gamma_{in}(f) = b_1/a_1 = \Gamma_1(f) \tag{6.13}$$

$$P_{in}(f)=\frac{1}{2}(|a_1|^2-|b_1|^2)=\frac{k_1(f)P_{r1}(f)\left(1-|\Gamma_{in}(f)|^2\right)}{|1+c_1(f)\Gamma_{in}(f)|^2} \tag{6.14}$$

In opposition to $\Gamma_{in}(f)$, the source impedance $\Gamma_s(f)$ cannot be determined online using the conventional calibration and measurement approaches describing the operation of the six-port reflectometer in direct or forward mode. As presented in the previous chapters, a straightforward technique to solve such a problem is to perform a precalibration of T1 using a network analyzer that gives the impedance of the tuner's port connected to the TUT DUT as a function of the tuner's stub positions. This technique requires a repeatable and high quality computer driven tuner.

The reflection coefficient associated with load impedance and the power absorbed by the load, are measured with SP2 operated in direct configuration (port 1 is connected to the DUT and port 2 to the load) and can be calculated as follows:

$$\Gamma_L(f)=a_2(f)/b_2(f) \tag{6.15}$$

$$P_L(f)=\frac{1}{2}(|b_2|^2-|a_2|^2)=\frac{k_2(f)P_{r2}(f)(1-|\Gamma_L(f)|^2)}{|1+c_2(f)\Gamma_L(f)|^2} \tag{6.16}$$

SP2 operated in forward configuration provides the value of Γ_2; consequently, Γ_L can be easily obtained as follows:

$$\Gamma_L=\frac{\alpha\Gamma_2+\beta}{\delta\Gamma_2+1} \tag{6.17}$$

where α, β, and δ are the complex coefficients modeling the two-port network delimited by the reference planes where Γ_L and Γ_2 are defined and measured. α, β, and δ parameters can be determined beforehand using the short open load de-embedding technique. Section 6.6 provides the necessary equations to de-embed both the reflection coefficient and the power flow measurements between different reference planes and through different error networks.

The passive source-pull tuning configuration, as shown in Figure 6.5, and explained in section 6.3.1, allows the measurements of the source impedance, which has to be retuned for every load impedance to maximize the power absorbed by the DUT. In case of a DUT that can be considered unilateral (s_{12}~0), the position of this input tuner can fixed once for a maximum power transfer at the input of the transistor ($\Gamma_s = \Gamma_{in}{}^*$).

6.5.2 Active Branch Load-Pull Configuration

The active load-pull measurement system is basically a six-port network analyzer that incorporates two six-port junctions including phase and amplitude signal controllers inserted in one branch. The active load-pull configuration is shown in Figure 6.8.

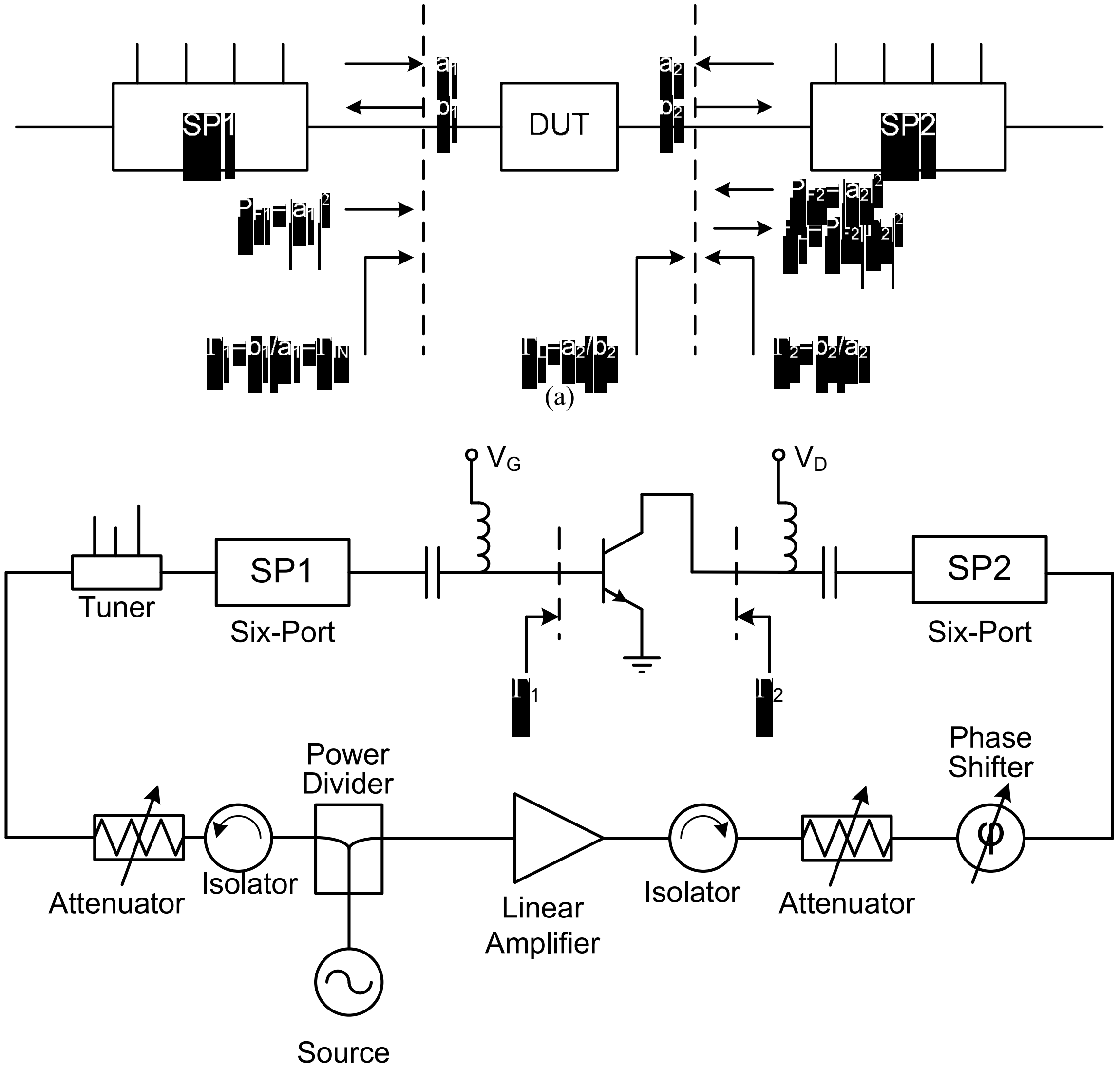

(b)

Figure 6.8 Six-port based active load-pull measurement : (a) configuration and (b) measurement systems.

The two six-port junctions are calibrated independently for impedance and power flow measurements in a reflection mode operation. The active load-presented to the TUT, $Z_L(f)$, can be varied by changing the phase and the amplitude of the injected signal $a_2(f)$ at the output of the TUT. The active load-pull measurement system is presented in Figure 6.8.

The complex value of $Z_L(f)$ can be deduced from the measured reflection coefficient, $\Gamma_2(f)$, obtained by the second six-port reflectometer SP2 as follows:

$$Z_L(f) = Z_0 \frac{1+\Gamma_L(f)}{1-\Gamma_L(f)} \tag{6.18}$$

$$\Gamma_L(f) = \frac{1}{\Gamma_2(f)} \tag{6.19}$$

The absorbed power by the active (electronic) load presented to the DUT can be calculated using the following expression:

$$P_L(f) = P_2(f)\left|\Gamma_2(f)\right|^2 \tag{6.20}$$

6.5.3 Active Loop Load-Pull Configuration

An alternative technique to realize active load-pull measurement is the active loop method. The active loop architecture is shown in Figure 6.9; a directional coupler placed at the output of the DUT (the *loop coupler*) takes part of the signal and sends it to a variable attenuator, a phase shifter, a tunable filter, and an amplifier. The loop also uses a circulator upstream from the amplifier. Then, the signal is re-injected back in to the DUT output. In this configuration, the reflection coefficient provided to the DUT does not change with the output power if the loop amplifier is in the linear region and has a constant gain [2].

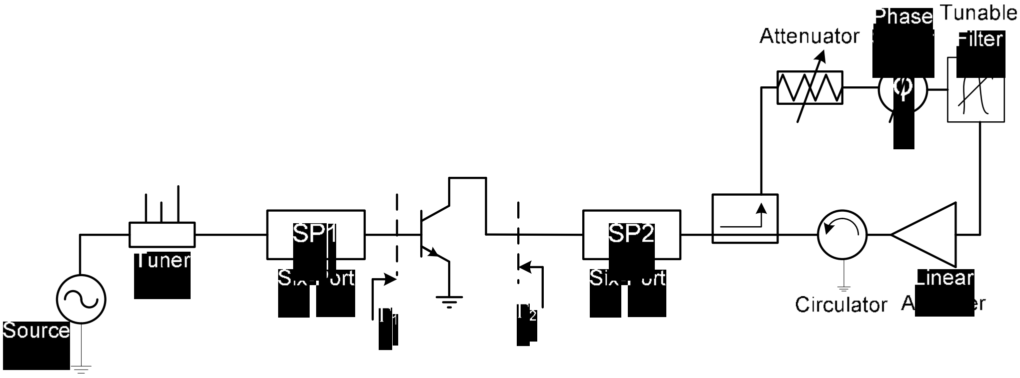

Figure 6.9 Six-port active loop load-pull measurement system.

6.6 SOURCE-PULL/LOAD-PULL CONFIGURATION USING SIX-PORT

The source-pull/load-pull technique is a characterization method of DUT based on the output performance's optimization by tuning output and input impedances seen at DUT accesses. Similar to the load impedance, the impedance of the source providing the input signal for the DUT also plays a role in its behavior. The source impedance presented at the device input can influence output characteristics like linearity or optimum load impedance.

A passive source-pull/load-pull configuration is shown in Figure 6.10. The input and output tuners may be replaced with active source and active load configurations. To implement a source-pull/load-pull measurement system, the source switch position 1 is used. In this position, the switch connects the source signal in the load-pull configuration. In such a configuration, one can measure directly (Γ_{in}, P_{in}) and (Γ_L, P_L) using SP1 and SP2 operated both in the forward configuration for a fixed position of the input tuner presenting Γ_s to the input of the DUT. Knowing Γ_L, one can easily obtain Γ_{out} using (6.17) along with the SOLT de-embedding technique to determine the three error box parameters.

$$\Gamma_{out} = \frac{\alpha\Gamma_L + \beta}{\delta\Gamma_L + 1} \tag{6.21}$$

where α, β, and δ are the complex coefficients modeling the two-port network delimited by the reference planes where Γ_L and Γ_{out} are defined and measured.

The Γ_s presented to the device can be determined by operating the input six-port SP1 in reverse configuration through the appropriate setting of the three switches connected to the input tuner, the generator, and the input directional coupler in position 0.

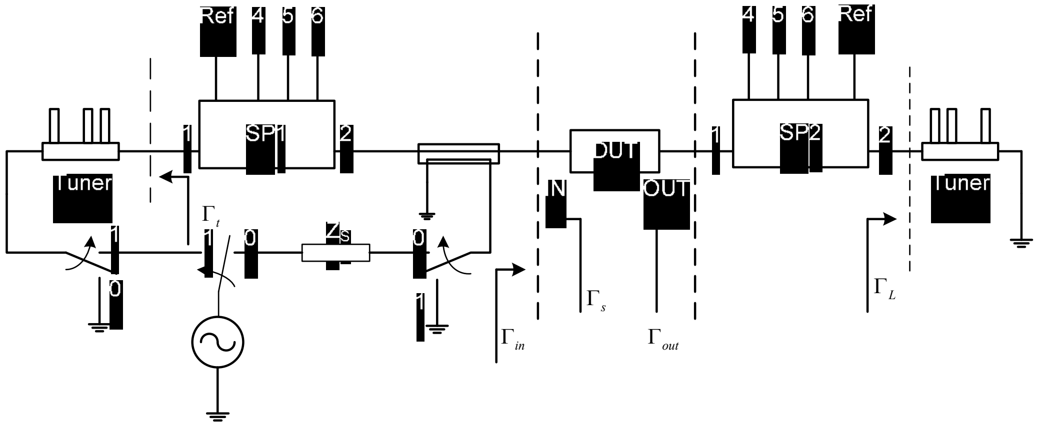

Figure 6.10 A block diagram of source-pull/load-pull configuration.

Hence, the source impedance can be varied and adjusted for any position of the load impedance. Accordingly, the source-pull/load-pull provides a solution for simultaneous measurement of both the input reflection coefficient of the device under test (DUT) and the reflection coefficient of the synthesized source with variable impedance [1,3].

6.7 A DE-EMBEDDING TECHNIQUE FOR ON-WAFER LOAD-PULL MEASUREMENTS

An absolute de-embedding technique for simultaneous impedance and power measurements suitable for on-wafer load-pull measurements of microwave transistors is proposed [1,3-7]. This technique allows one to perform impedance and power calibration of a network analyzer directly from the embedded reflection coefficient measurements. This technique requires two sets of open-short-load calibration standards, one coaxial and one noncoaxial such as coplanar (CPW). An absolute power calibration performed at the coaxial reference planes using a standard power meter is also required for accurate power flow measurement purposes at the coplanar reference planes of the microwave probes needed for on-wafer measurements.

6.7.1 Calibration and Measurement Techniques

A general formulation of the problem is illustrated in Figure 6.11, where $\left(\mathbf{A},\mathbf{B}\right)$ are two error box networks delimited by the network analyzer reference planes and the coaxial reference planes; $\left(\mathbf{A}',\mathbf{B}'\right)$ are two error box networks delimited by the coaxial reference planes and the coplanar reference planes at the tips of the microwave probes. Let $\left([\mathbf{A}],[\mathbf{B}]\right)$ and $\left([\mathbf{A}'],[\mathbf{B}']\right)$ designate the transmission matrices of these two pairs of error box networks.

The reflection coefficients at both coaxial and coplanar reference planes are related, respectively, to the reflection coefficients at the network analyzer reference planes and the coaxial reference planes (see Figure 6.11) as follows:

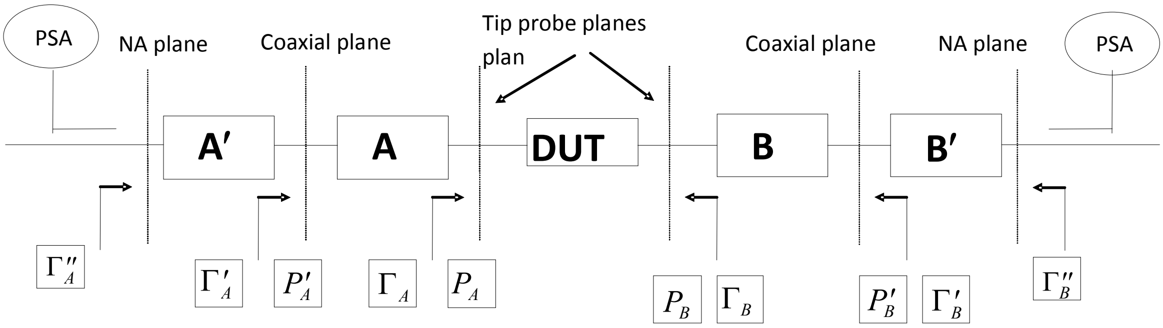

Figure 6.11 On-wafer impedance and absolute power calibration procedure.

$$\Gamma'_A = \frac{\alpha_1 \Gamma_A + \alpha_2}{\alpha_3 \Gamma_A + 1} \tag{6.22a}$$

$$\Gamma''_A = \frac{\alpha'_1 \Gamma'_A + \alpha'_2}{\alpha'_3 \Gamma'_A + 1} \tag{6.22b}$$

$$\Gamma'_B = \frac{\beta_1 \Gamma_B + \beta_2}{\beta_3 \Gamma_B + 1} \tag{6.22c}$$

$$\Gamma''_B = \frac{\beta'_1 \Gamma'_B + \beta'_2}{\beta'_3 \Gamma'_B + 1} \tag{6.22d}$$

where α_i, α'_i, β_i, and β'_i are the error box parameters, which can be calculated using four OSL calibrations, two at the coaxial reference planes and two at the coplanar reference planes.

The two power flows at the coaxial reference planes can be calculated as follows [6]:

$$P'_A = \frac{k'_A P_{SA}}{\left|1 + \alpha'_3 \Gamma'_A\right|^2} \tag{6.23a}$$

$$P'_B = \frac{k'_B P_{SB}}{\left|1 + \beta'_3 \Gamma'_B\right|^2} \tag{6.23b}$$

where P_{SA} and P_{SB} are two power readings sampled by two directional couplers as shown in Figure 6.1. These directional couplers can be placed within the network analyzer or can be inserted between the coaxial reference planes and the coplanar reference planes and k'_A, k'_B are power calibration factors which can be calculated by connecting an absolute power meter successively at both coaxial reference planes as follows:

$$k'_A = \frac{P_{APM} \left|1 + \alpha'_3 \Gamma'_{APM}\right|^2}{P_{SAPM} \left(1 - \left|\Gamma'_{APM}\right|^2\right)} \tag{6.24a}$$

$$k'_B = \frac{P_{BPM} \left|1 + \beta' \Gamma'_{BPM}\right|^2}{P_{SBPM} \left(1 - \left|\Gamma'_{BPM}\right|^2\right)} \tag{6.24b}$$

where P_{APM} and P_{BPM} are the power readings of a standard power meter when it is connected to successively to the coaxial reference planes; P_{SAPM} and P_{SBPM} are the two sampled power readings, and Γ'_{APM} and Γ'_{BPM} are the measured reflection coefficients when the standard power meter is connected successively to the coaxial reference planes. The power flow at the coplanar reference planes can be calculated as follows:

$$P_A = \frac{k_A P_{SA}}{\left|1+\alpha''\Gamma_A\right|^2} \tag{6.25a}$$

$$P_B = \frac{k_B P_{SB}}{\left|1+\beta''\Gamma_B\right|^2} \tag{6.25b}$$

where the value of k_A , k_B , α'' , and β'' can be calculated using the following expressions written below and without any need to perform extra power calibration at the coplanar reference planes:

$$k_A = \frac{\left|\alpha_1 - \alpha_2\alpha_3\right| k'_A}{\left|1+\alpha'_3\Gamma_A\right|^2} \tag{6.26a}$$

$$\alpha'' = \frac{\alpha_3 + \alpha'_3\alpha_1}{\alpha'_3\alpha_2 + 1} \tag{6.26b}$$

$$k_B = \frac{\left|\beta_1 - \beta_2\beta_3\right| k'_B}{\left|1+\beta'_3\Gamma_B\right|^2} \tag{6.26c}$$

$$\beta'' = \frac{\beta_3 + \beta'_3\beta_1}{\beta'_3\beta_2 + 1} \tag{6.26d}$$

In this section, an alternative technique for the on-wafer de-embedding of impedance and power flow measurements is proposed This technique requires two OSL sets of calibration standards, one coaxial and one coplanar. A coaxial power detector is also needed for power flow calibration purposes. The main advantage of this technique is that no second power calibration at the tips of the coplanar probes is needed. Such a power calibration is almost impossible to perform because there is no accurate coplanar power sensor that can be connected to the tip of the probes to calculate k_A and k_B .

6.8 APPLICATIONS OF SOURCE-PULL MEASUREMENTS

In the conventional application of a six-port to characterize a DUT, the microwave signal generator is connected to the input port, the DUT is connected to the output port, and the four remaining measuring ports are used for power detection purposes. This configuration allows the six-port to measure the power absorbed by the device under test and of the generator has no effect on the measurement of the six-port; therefore, it is impossible to get information about the effect of the source impedance on the performance of the DUT.

In certain situations, such as in the characterization of mixers, oscillators, or noise measurements, it is more desirable to vary the generator impedance and measure its reflection coefficient than to measure the reflection coefficient of the DUT. Such source-pull characterization is not possible, either by using an automatic vector network analyzer or by using the conventional six-port configuration. In this section, an approach for source-pull measurements of active two-port devices using a six-port reflectometer in reverse configuration is presented. The microwave source, the DUT, and the measuring reference plane are all placed at the output of the six-port junction. A tuner is connected at the input of the six-port junction. In this arrangement, the six-port can drive simultaneously the input of the DUT and perform source-pull measurements.

6.8.1 Low Noise Amplifier Characterization

An important part of low noise amplifier design is the measurement of the transistor's noise figure and the determination of noise parameters. Figure 6.12 shows a setup for noise characterization using the reverse six-port source-pull measurement technique. The six-port junction is calibrated at all test frequencies and measures the source impedance seen by the DUT. Obviously, the microwave generator must be turned off when the noise source is on for noise measurement and vice versa. The stability of the DUT is also important during this characterization. The noise figure can be determined using the noise source and a noise meter and a standard measurement procedure.

The noise figure is obtained as [14]

$$NF_{DUT} = 10\log\{\frac{G_{DUT}N_{in} + N_{added}}{G_{DUT}N_{in}}\} \tag{6.27}$$

where N_{added} is the difference between measured output noise level and the noise level at the input of the device, G_{DUT} is the gain of the DUT, and N_{in} is the available noise power at input of the DUT.

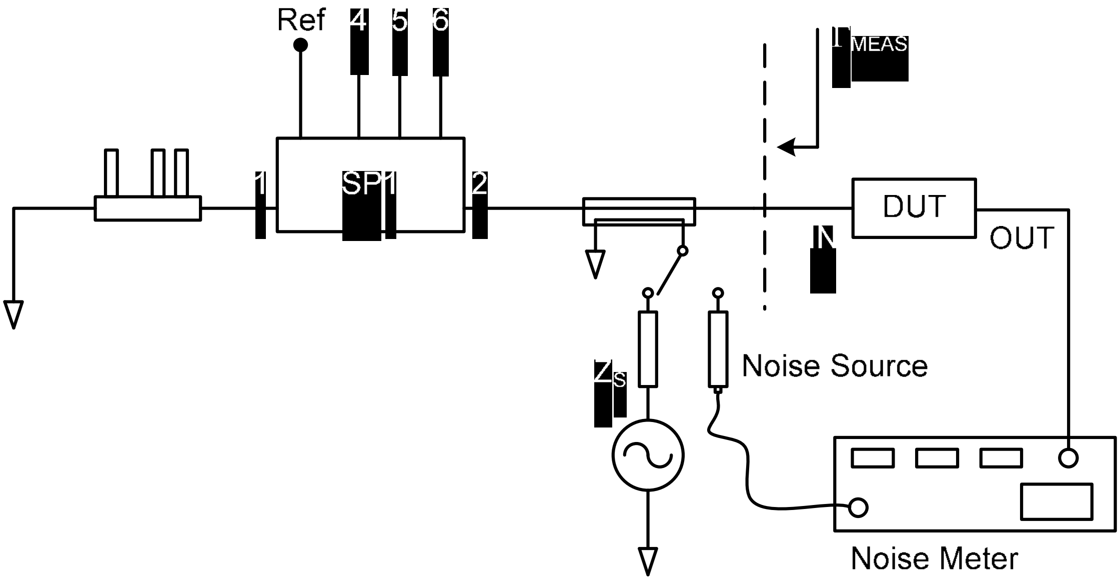

Figure 6.12 Using a reverse six-port reflectometer for noise characterization. (Copyright 1995 IEEE from [14].)

The advantage of the six-port source-pull based noise measurement is that the six-port in reverse configuration gives the source impedance for any tuner position without any need to premeasure and calibrate the tuner in advance using the network analyzer. In addition in this setup tuner repeatability is not an issue at all.

6.8.2 Mixer Characterization

Mixers employ mostly the nonlinearity of the active device to generate intermodulation products. Thus, their behavior depends strongly on the load and the LO and RF source impedance terminations. Computer-aided design approaches using harmonic balance methods allow the optimization of the input and output matching impedances, but the accuracy of the analysis relies on the device modeling.

In practice, it is possible to optimize, at the same time, the input and the output impedances by using a reverse six-port reflectometer to perform source-pull

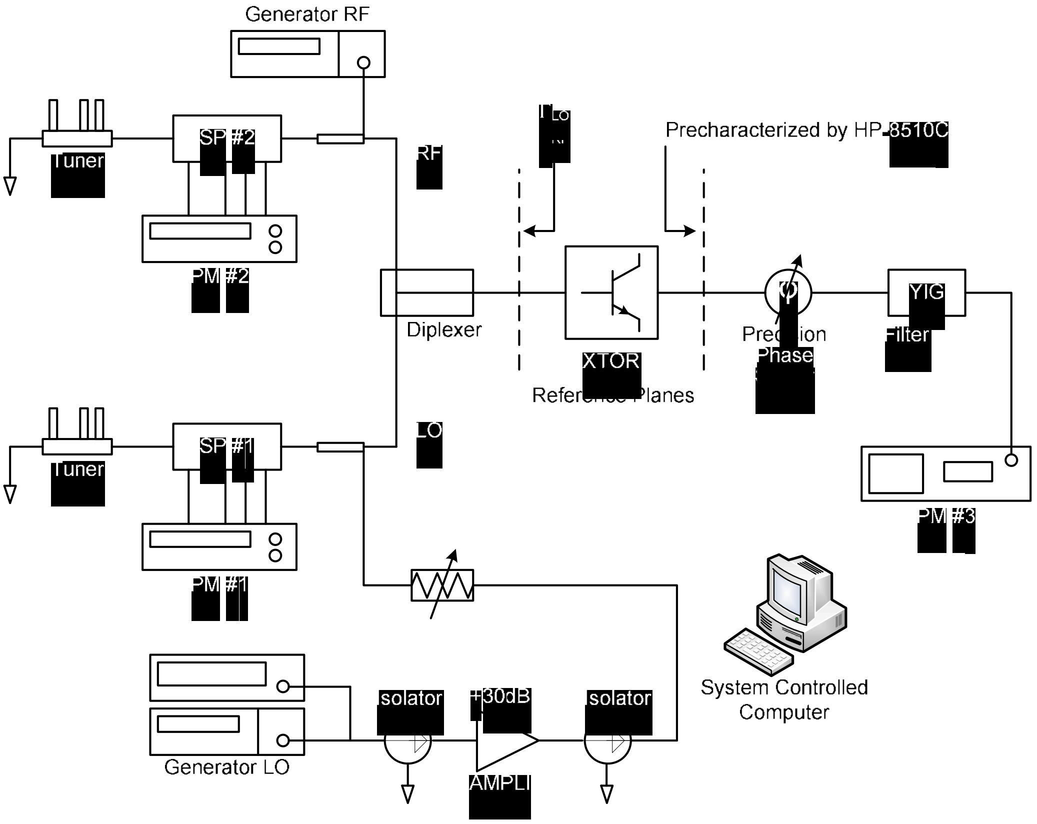

Figure 6.13 Experimental setup for the source-pull characterization of MESFET gate mixer. (© 1994 from IEEE [9].)

measurements at the input and a direct six-port reflectometer to obtain load-pull measurements [15] at the output of the DUT.

The mixer performance can be optimized by increasing its conversion gain, by improving return losses at its ports or even its linearity. The advantage of the six-port source-pull based mixer characterization is that the six-port in the reverse configuration gives the source impedance for any tuner position without the need to premeasure and calibrate the tuner in advance of using the network analyzer.

In addition, in this set-up tuner repeatability is not important. The experimental source-pull/load-pull characterization of a GaAs MESFET as a mixer is shown in Figure 6.13. This technique can be used to find the optimal input RF and LO load impedances of a MESFET gate mixer. The measurement results of the characterization of the mixer are presented in [9].

6.8.3 Power Amplifier Characterization

Figure 6.14 shows a common setup for power amplifier characterization. The use of reverse six-port reflectometers allows for the measurement of the source and load impedances presented to the transistor by input and output tuning.

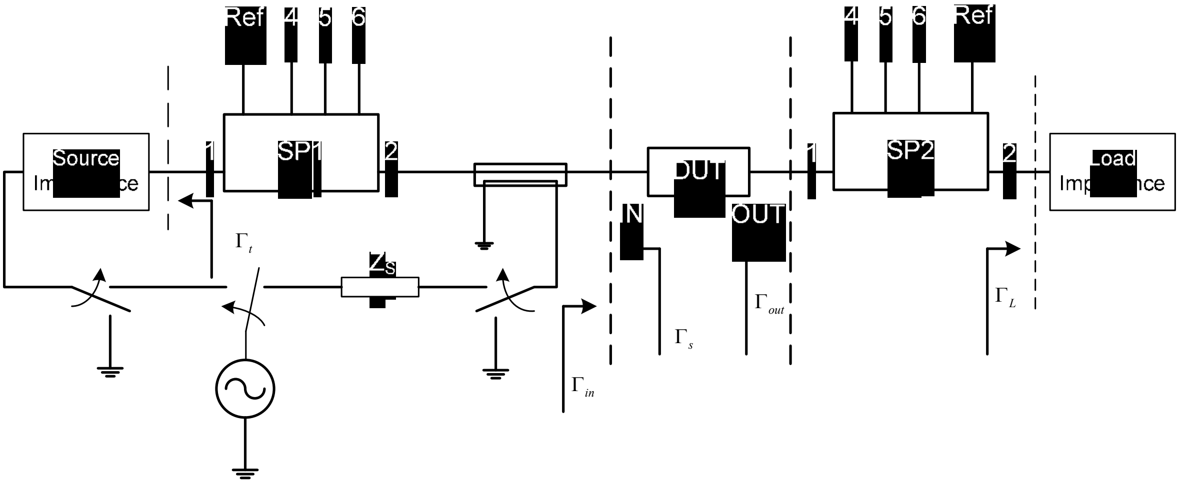

Figure 6.14 Two reverse six-port reflectometers for power amplifier characterization.

The PA designer can verify the transistor sensitivity in power gain versus termination impedances and can easily optimize the output power, the amplifier gain, the power-added efficiency, or the intercept point of the transistor [16]. The power relations are obtained as follows:

$$P_{out}(f) = |b_2|^2 (1 - |\Gamma_L(f)|^2) \tag{6.28a}$$

$$P_{in}(f) = |a_1|^2 (1 - |\Gamma_{in}(f)|^2) \tag{6.28b}$$

$$Power - gain = \frac{P_{out}}{P_{in}} \tag{6.28c}$$

$$PAE = \frac{P_{out} - P_{in}}{P_{dc}} \tag{6.28d}$$

where it is assumed that the dissipated dc power is known to calculate the power-added efficiency (PAE).

6.9 SOURCE-PULL/LOAD-PULL OSCILLATOR MEASUREMENTS

The characterization of active microwave devices is generally done by the measurement of S parameters using automatic network analyzers (ANA). The test port impedance of the ANA seen by the active device under test is the normal line characteristic impedance of the measurement system (50Ω). It must be noted that such a test port impedance cannot normally be varied during measurements. This constraint is not convenient when measuring active devices with a negative resistance (e.g., diode, transistors, and so forth), because oscillations might occur during characterization whenever the negative resistance of the device exceeds 50Ω. In this section a six-port reflectometer with variable test port impedance is considered. The six-port junction was specially designed to allow the variation of the test port impedance over almost the entire Smith chart. Such a reflectometer is found suitable for a large signal active microwave device characterization such as microwave source-pull/load-pull oscillator measurements [17].

6.9.1 Six-Port Reflectometer with Variable Test Port Impedance

By using the transparent six-port assumption, from (6.4) it can be seen that to obtain a variation of the test port impedance, it is sufficient to vary the internal impedance of the generator [17]. The variation of the test port impedance can be performed by the use of a three-stub tuner inserted between the signal generator and the input port of the six-port junction, as shown in Figure 6.2.

The generator and the three-stub tuner can be considered equivalent to a generator with variable test port impedance. Based on the above consideration and by using an appropriate calibration method, nonsensitive to the source power level variation and to the internal source impedance [11], the calibration parameters of the six-port reflectometer obtained for given tuner stub positions are valid for any position of the stubs.

6.9.2 Oscillator Measurements

Source-pull/load-pull oscillator measurements monitor both the oscillator power and the frequency as a function of the load impedance seen by the oscillator under test. The impedance seen by the oscillator can be changed and, at the same time, known over the quasi-entire Smith chart, by simultaneously changing and measuring the test port impedance of the six-port junction.

Figure 6.15 shows a block diagram of an experimental setup for source-pull/load-pull oscillator characterization using the reflectometer with variable test port impedance. The reflection coefficient associated with the load impedance Z_L seen by the oscillator is directly deduced from the measured reflection coefficient Γ_m as follows:

$$Z_L = Z_o \frac{\Gamma_m + 1}{\Gamma_m - 1} \tag{6.29}$$

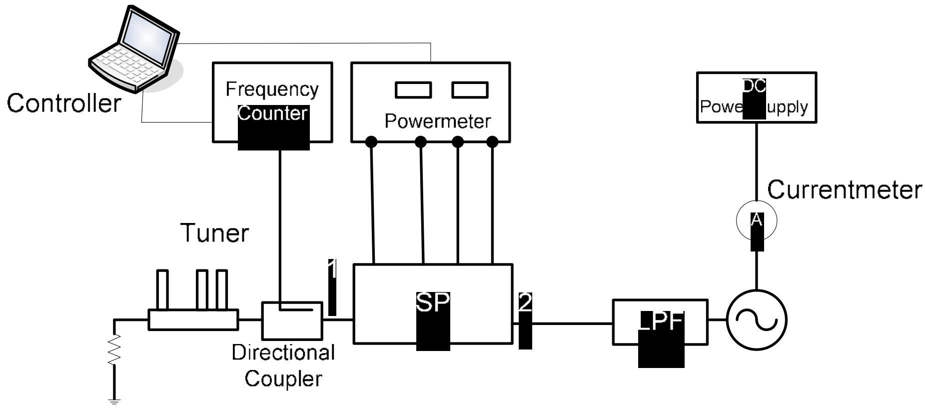

Figure 6.15 A block diagram of the experimental setup for source-pull/load-pull oscillator measurements. (© 1992 IEEE from [17].)

where Z_o is the characteristic impedance of the measurement system (50Ω). The available power P_a from the oscillator can be calculated using the six-port calibration parameters and the power calibration parameter as follows [18]:

$$P_a(f) = \frac{k(f) P_3(f) \left|\Gamma_m(f)\right|^2}{\left|1 + c(f)\Gamma_m(f)\right|^2} \tag{6.30}$$

where $c(f)$ is the de-embedding calibration parameter obtained by the six-port error box calibration at the oscillator frequency f, $k(f)$ is a scalar parameter obtained by the power calibration at the oscillator frequency f, $P_3(f)$ is the power reading at port 3 of the six-port junction at the oscillator frequency f, and $\Gamma_m(f)$ is the reflection coefficient measured by the six-port reflectometer at the oscillator frequency f.

The impedance seen by the oscillator can be simultaneously varied and measured over the quasi-entire Smith chart by changing the tuner stub positions and measuring the test port impedances of the six-port junction. The available power from the oscillator under test P_a is easily obtained at any tuner stub position and at any operating oscillator frequency using (6.29) and (6.30).

The oscillator frequency is measured by using a directional coupler and a frequency counter as shown in Figure 6.15. The six-port reflectometer is calibrated at discrete frequency points centered on the nominal oscillator frequency. The measurement results of the characterization of an oscillator are presented in [17].

6.10 AM-AM/AM-PM DISTORTION MEASUREMENTS OF MICROWAVE TRANSISTORS USING ACTIVE LOAD-PULL

Low phase distortion MESFET power amplifiers and limiters are key components in systems where the information is related to the phase of the microwave signal. For an accurate and quick design of linear solid state power amplifiers (SSPAs) and power limiters in hybrid microwave integrated circuits (HMIC) and monolithic microwave integrated circuits (MMIC) technologies, transistor characterization in terms of phase distortion measurements is highly recommended. The AM/PM distortion behavior can be described by the relative phase shift versus input power, $\phi(P_{in})$ and the AM/PM conversion coefficient k is in degrees per dB. Various methods for measuring the AM-PM conversion coefficients at intermediate frequencies have been published [19,20].

However, for microwave/millimeter wave amplifiers, it is less complex and tedious to obtain the characteristic $\phi(P_{in})$, by single-carrier power sweep measurements [21]. Then, if needed, k can be found by derivation of ϕ with respect to $P_{in}(d\phi / dP_{in})$. Actually, the measured $\phi(P_{in})$ curve as a phase transfer function is more general to characterize the AM-PM distortion performance of microwave transistors and power amplifiers. In addition, the $\phi(P_{in})$ characterization is especially useful for microwave limiters, where the variation range of the phase shift over a given power range beyond saturation is the main concern [22].

This section presents an approach to simultaneously investigate the AM/PM characteristics along with the AM-AM characteristics as the functions of the power level and the load impedance over the Smith chart using the six-port. For a designed performance in terms of output power, efficiency, and AM-PM distortion, this comprehensive characterization can provide data for improving the design of limiting amplifier or SSPAs driven by time-variable envelop signals. The proposed approach is based on the principles of a dual six-port network analyzer [21] and the active loading technique [23]. In comparison with the setups employing heterodyne network analyzers, the advantages of this measurement setup are: (1) the impedance and power measurements are performed at the actual power level of the device, and no extra attenuators are needed for power device characterization; (2) the AM-PM characterizations are carried out at the input and output reference planes of the device under test, loaded by arbitrary impedances; and (3) the cost of this system is much lower than the cost of the setups using two automatic network analyzers for AM-PM distortion load-pull measurements.

6.10.1 Principle of Operation

The measurement system is shown in Figure 6.16. As shown, two six-port junctions, associated with the amplitude and phase controllers, can be utilized for

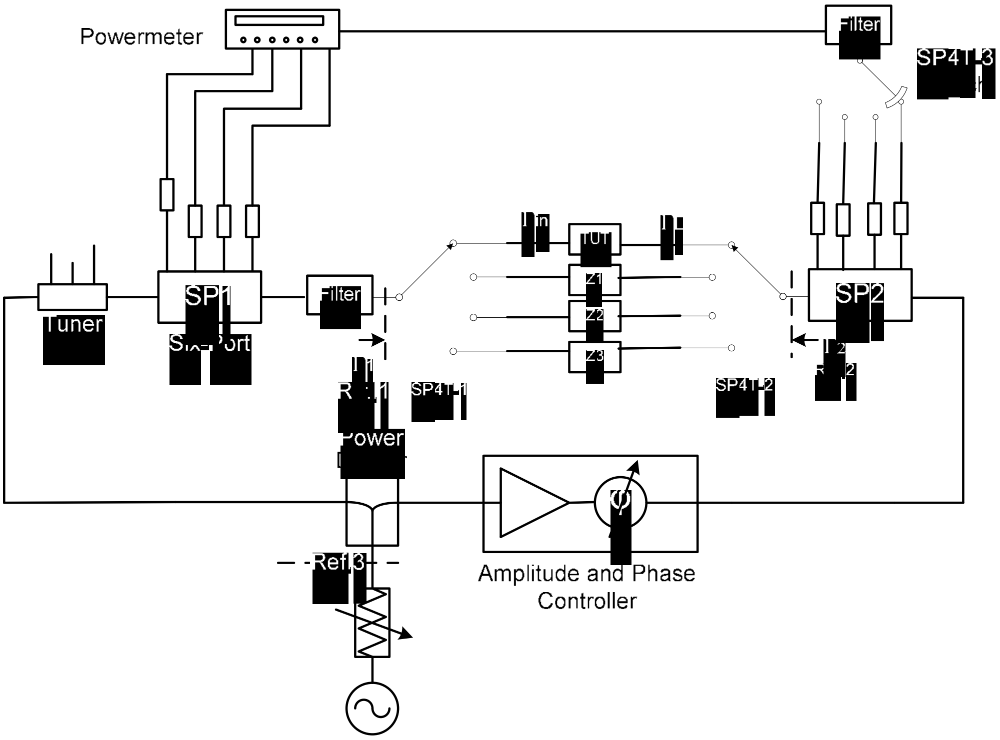

Figure 6.16 Block diagram of load-pull phase of distortion measurement system. (© 1995 IEEE from [21].)

active load-pull techniques. Meanwhile, the measurement system can be viewed as a three-port network with reference planes 1, 2, and 3. In order to measure the input-output phase shift of the transistor under test (TUT), three two-port passive standards, Z1, Z2, and Z3, are introduced to obtain a calibration coefficient. Due to the fact that the three-port network has fixed network scattering parameters during the four measurements of the TUT, Z1, Z2, and Z3 for a fixed setting of the amplitude and phase controllers, we can obtain the following equations expressed in matrix format [10].

$$\begin{bmatrix} S_{12}(1) & \Delta(1)-\Gamma_1(1)S_{22}(1) & S_{12}(1)\Gamma_1(1) \\ S_{12}(2) & \Delta(2)-\Gamma_1(2)S_{22}(2) & S_{12}(2)\Gamma_1(2) \\ S_{12}(3) & \Delta(3)-\Gamma_1(3)S_{22}(3) & S_{12}(3)\Gamma_1(3) \end{bmatrix} \begin{bmatrix} x_1 \\ x_2 \\ x_3 \end{bmatrix} = \begin{bmatrix} \Gamma_1(1)-S_{11}(1) \\ \Gamma_1(2)-S_{11}(2) \\ \Gamma_1(3)-S_{11}(3) \end{bmatrix} \tag{6.31}$$

where x_i is related to scattering parameters of the three-port network for a given amplitude and phase setting; $\Delta(k) = S_{11}(k)S_{22}(k) - S_{12}(k)S_{21}(k)$ and $S_{ij}(k)$ k, = 1, 2, and 3 are the known S parameters of three standards Z_1, Z_2, and Z_3. $\Gamma_1(k)$, $k = 1$, 2, and 3 are measured by six-port 1, when the test path is connected to Z_1, Z_2, or Z_3, respectively.

The three two-port standards, Z_1, Z_2, and Z_3, are three coaxial transmission lines with different lengths. Note that we have purposely selected them to make the phase of $S_{12}(1)$, $S_{12}(2)$, $S_{12}(3)$ deviate from each other about 120°, in order to ensure a good condition number of (6.31). The following equation can also be derived [4] to calculate the coefficient g, that is, the ratio of the incident waves at reference planes 2 and 1, as shown in Figure 6.17.

$$g = \frac{a_2'}{a_1'} = \frac{x_1 + x_3\Gamma_1(T)}{1 + x_2\Gamma_2(T)} \tag{6.32}$$

where x_i is obtained by solving (6.31); $\Gamma_1(T)$ and $\Gamma_2(T)$ are measured by six-ports 1 and 2, respectively, when the test path is connected to the DUT.

Then, the coefficient g has to be de-embedded to the input and output ports of the DUT (reference planes T_1 and T_2). As shown in Figure 6.17, the DUT includes a transistor. The network M (or N) consists of the single-pole four-throw switch SP4Tl (or SP4T2), the bias tee, and a half part (input or output) of the test fixture.

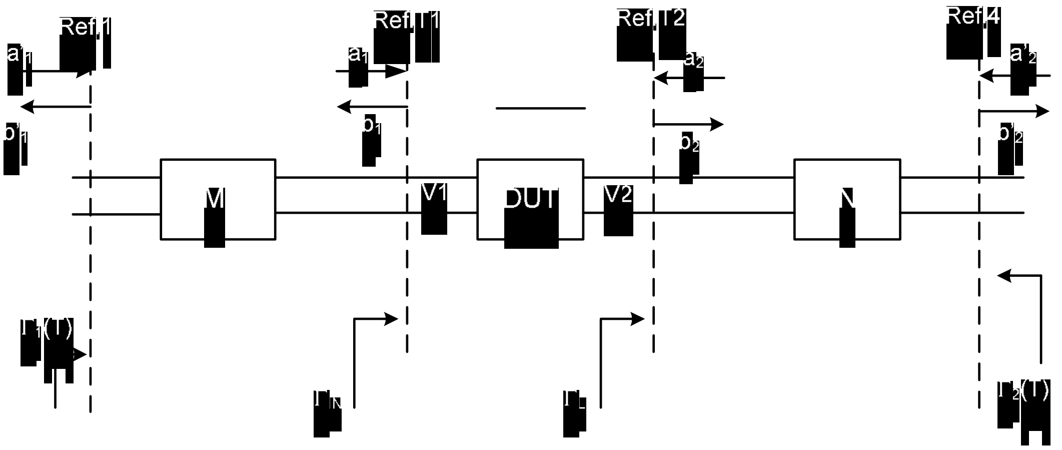

Figure 6.17 Error-box models for de-embedding procedures and computations.

We obtain

$$b_1' = S_{11}^m a_1' + S_{12}^m b_1 \tag{6.33a}$$

$$a_1 = S_{21}^m a_1' + S_{22}^m b_1 \tag{6.33b}$$

and

$$a_2 = S_{11}^n b_2 + S_{12}^n a_2' \tag{6.34a}$$

$$b_2' = S_{21}^n b_2 + S_{22}^n a_2' \tag{6.34b}$$

where S_{ij}^m and S_{ij}^n are the S parameters of the networks *M* and *N.* Also, we have $\Gamma_1(T) = b_1' / a_1'$ and $\Gamma_2(T) = b_2' / a_2'$. From the above equations, a_2/a_1 can be developed and related to coefficient *g* as follows:

$$\frac{a_2}{a_1} = g.\frac{S_{12}^m}{S_{21}^n}.\frac{\Gamma_2(T)S_{11}^n - \Delta^n}{\Gamma_1(T)S_{22}^m - \Delta^m} \tag{6.35}$$

where $\Delta^m = S_{11}^m S_{22}^m - S_{12}^m S_{21}^m$ and $\Delta^n = S_{11}^n S_{22}^n - S_{12}^n S_{21}^n$. Since the switches SP4T1 and SP4T2 are operated under linear conditions, the S parameters of networks *M* and *N* are constants when P_{in}, sweeps, and they can be obtained using de-embedding method such as TRL [24].

According to the definition of the normalized waves *a* and *b*, the ratio of the voltages at the output and input ports of the DUT for any arbitrary load at a given P_{in} is determined as follows:

$$\frac{V_2}{V_1} = \frac{a_2 + b_2}{a_1 + b_1} = \frac{a_2}{a_1}.\frac{1 + 1/\Gamma_L}{1 + \Gamma_{in}} \tag{6.36}$$

where a_2 / a_1 is obtained by (6.35), Γ_{in} is the input reflection coefficient of the DUT, and Γ_L is the load reflection coefficient presented to the TUT.

In brief, by means of the switches, $\Gamma_1(1)$, $\Gamma_1(2)$, $\Gamma_1(3)$, $\Gamma_2(1)$, $\Gamma_2(2)$, $\Gamma_2(3)$, $\Gamma_1(T)$, and $\Gamma_2(T)$ can be measured when the Z_1, Z_2, Z_3 and DUT are inserted in turn for a fixed setting of the amplitude and phase controllers. Meanwhile, it's easy to obtain Γ_{in}, P_{in} and Γ_L, P_L with the de-embedding techniques when $\Gamma_1(T)$ and $\Gamma_2(T)$ are measured by six-port 1 and six-port 2 [13]. Therefore, the phase shift of the DUT can be determined by (6.31 through 6.36). The harmonics are filtered, as shown in Figure 6.14, to ensure that the signals detected by the power-meter are the fundamental components only.

The phase distortion, ϕ, is defined as an input-output phase shift, relative to the reference phase shift value at a given lower input power P_{in}^{ref} (small-signal operation mode) for a given load impedance. Thus, the pertinent relative phase shift corresponds to the change of the angle of V_2/V_1 when P_{in} increases. The measurement ($\phi = f(P_{in})$) of the AM-PM distortion behavior, followed by the calculation of the derivative $(d\phi / dP_{in})$, provides the AM-PM conversion coefficient. Similarly, the AM-AM distortion is described by the deviation of the gain from its value at a small-signal input power level. Due to the fact that P_L and P_{in} are already measured, the operating power gain ($G_p = g(P_{in})$) can be deduced and the AM-AM conversion coefficient can be determined by the derivative (dG_p / dP_{in}) [19, 21].

6.10.2 Measurement Procedure

Traditionally, the load-pull has to be carried out for each given P_{in} with variable Γ_L. This results in a large number of measurements and adjustments. The present experimental procedure performs the active load-pull measurements by fixing the positions of the amplitude and phase controllers and sweeping the input power. In such conditions Γ_L changes, as P_{in} is swept. Then, the amplitude and phase controllers are adjusted at new positions and the measurements are performed with another sweep of P_{in}. Finally, the load-pull contours for a given P_{in} can be extracted from the recorded measurement database.

In addition, the characteristics ($P_L \sim P_{in}$) and ($\phi \sim P_{in}$) for a given Γ_L can be obtained as a postmeasurement calculation result. The power-added efficiency PAE and G_P can also be deduced. It is known that in an active load-pull system, when P_{in} changes it is difficult to maintain the required Γ_L value by adjusting the amplitude and phase controllers. This problem can be circumvented by means of the above alternative procedure. The error sources in the proposed approach are mainly due to the following four aspects. First, the measurements are made by increasing the input power and not by amplitude modulation as in the actual operation mode. Therefore, the dynamic effect of the AM modulation, which becomes more significant by increasing the modulation bandwidth, is ignored. Second, the self-heating effect can introduce a drift in the electrical operational conditions. To minimize this effect, the temperature of the fixture of the transistor investigated has to be maintained almost constantly by circulating a flux of air during characterization. Third, the measurement accuracy can also be diminished if the power level exceeds the operational range where the switches are linear. It is preferable to use mechanical switches instead of solid-state switches when characterizing high-power devices. Fourth, the extraction of the pertinent data from the raw database and the postmeasurement calculations using interpolation routines might introduce error. This effect can be reduced by increasing the amount of experimental data.

6.11 TIME-DOMAIN WAVE-CORRELATOR FOR POWER AMPLIFIER CHARACTERIZATION AND OPTIMIZATION

Time-domain waveform measurement techniques are considered one of the most useful methods for characterizing nonlinear microwave devices and amplifiers. This is especially important for switching-mode and harmonic-controlled circuits. The principle of highly efficient operation is to allow for a specific amount of higher harmonic content in the current and voltage waveforms at the transistor output terminals. In this way, power dissipation in the device is minimized by avoiding the simultaneous presence of high currents and voltages in the device.

In order to verify proper operating conditions or to tune a circuit, it is essential to measure and analyze the waveforms. Moreover, information about the amount of magnitude and phase of spectral components in the output waveforms of a nonlinear device under a large-signal stimulus is important for a better understanding of the electrical behavior and for accurate large signal modeling of the device under test (DUT). At microwave and millimeter frequencies, high-speed sampling oscilloscopes [25], special vector network analyzer (VNA) setups, optical sampling systems [26], and microwave transition analyzer (MTA) techniques [27, 28] have been used.

In this section, an approach for high-frequency time-domain voltage and current waveform measurements using six-port junction is described [29]. The advantage of this waveform measurement setup is its relatively low implementation cost compared to all the above-mentioned measurement techniques, especially at millimeter-wave frequencies.

6.11.1 Time-Domain Waveform Measurement

One method of determining time-domain voltage and current waveforms consists of measuring the complex Fourier coefficients of the waves in the frequency domain. By accurately determining the magnitude of the dc component (V_o , I_o), as well as the magnitude and phase of the fundamental (V_1, I_1) and harmonic frequency components (V_n, I_n), the time-domain waveforms can be calculated from the measured coefficients by using the well-known inverse Fourier transformation

$$v(t) = \mathrm{Re}\{\sum_{n=0}^{m} V_n e^{j2\pi n f_0 t}\} \tag{6.37}$$

and

$$i(t) = \mathrm{Re}\{\sum_{n=0}^{m} I_n e^{j2\pi n f_0 t}\} \tag{6.38}$$

where n denotes the harmonic order, f_0 is the fundamental frequency, and m is the total number of included harmonics. The dc components, V_o, I_o, are routinely measured directly with a biasing instrument; however, the measurement of the complex Fourier coefficients V_n, I_n for $n \geq 1$ is more difficult. Here, these measurements with a deliberately modified six-port reflectometer have been performed. To be able to determine the waveforms at the DUT output plane, the measurement of the complex voltage traveling waves, also called pseudo-waves [30], is performed at the fundamental (f_0), second ($2f_0$), and third ($3f_0$) harmonic frequencies.

At a given reference plane, V_n and I_n in (6.33) and (6.34) are related to the incident and reflected voltage traveling waves by [30,31]

$$V_n = a_n + b_n \tag{6.39}$$

and

$$I_n = \frac{a_n - b_n}{Z_c} \tag{6.40}$$

where Z_c is the characteristic impedance of the system, typically 50Ω. By measuring the pseudo-reflection coefficient $\Gamma_n = a_n / b_n$, the magnitude and phase of the voltage traveling wave a_n can easily be determined if the voltage traveling wave b_n is delivered by a reference generator, that is, its magnitude and phase of its harmonic contents are well known. By measuring the pseudoreflection coefficient Γ_n at a given reference plane by means of a six-port reflectometer, the voltage and the current frequency components can be deduced according to (6.39) and (6.40).

A multiharmonic generator is used to generate the harmonic-rich voltage wave with well-known magnitude and phase components, as a reference signal generator for the time-domain waveform calibration [29]. It is preferable that the reference generator consists of a step recovery diode (SRD) excited by a continuous wave (CW) RF signal at the fundamental frequency GHz. In most cases, to reach an adequate input drive level for the SRD, a high-gain amplifier is required.

6.11.2 Multiharmonic Six-Port Reflectometer

As discussed in Chapter 3, six-port junctions are in most cases designed using directional couplers and power dividers that can cover several octaves of bandwidth. However, the detection block of a conventional six-port reflectometer is not able to discriminate the different spectral components because it only detects the total power at the detection ports. Time-domain waveform measurements, however, require the measurement of a few complex Fourier coefficients of the signal. In order to perform this measurement, the power detection block of the six-port reflectometer is modified, as shown in Figure 6.18, to become frequency selective and, hence, allow for multiharmonic measurements.

The power detection block consists of a single-pole-four-through (SP4T) switch, a tunable yttrium–iron–garnet (YIG) filter, and a power meter. For harmonic measurements, the YIG filter is adjusted to pass only one harmonic frequency component at a time from the output of the SP4T switch to the power meter. Using the SP4T switch to successively switch from Ports 3 to 6 and detect the powers, the reflection coefficient $\Gamma = b/a$ can be measured in magnitude and phase according to (6.37). The measurement procedure is detailed next. The YIG filter is centered at f_0. Port 3 is selected by means of the switch SP4T and the power is measured. Before tuning the YIG filter to $2f_0$, the powers at Port, 4, 5, and 6 are measured. In the following measurement cycle, the filter is adjusted to $2f_0$ and the powers at Ports 3, 4, 5, and 6 are determined. Finally, the filter is set to $3f_0$ and the power detection steps are repeated.

Before every measurement, the repeatability of the YIG filter adjustment and the switch contact quality has to be checked. The multiharmonic six-port reflectometer is calibrated at f_0, $2f_0$, and $3f_0$. The relationship between the measured powers at Ports 3, 4, 5, and 6 (P_{3n}, P_{4n}, P_{5n}, and P_{6n}) and the output power, $P_{OUT\,n}$ and the reflection coefficient, Γ_{Ln} , are given by [29]:

$$\frac{P_{in}}{P_{3n}} = k_{in}\left|\frac{1+A_{in}\Gamma_{sn}}{1+A_{3n}\Gamma_{sn}}\right|^2 \tag{6.41}$$

where $\Gamma_{sn} = \dfrac{1}{\Gamma_{Ln}}$ and

$$P_{OUTn} = k_{Pn}\frac{P_{3n}}{\left|1+A_{3n}\Gamma_{sn}\right|}(1-\left|\Gamma_{Sn}\right|^2) \tag{6.42}$$

k_{in} and A_{in} (for $i = 4, 5, 6$) are determined by the six-port calibration procedure. The constants k_{Pn} are determined by an absolute power calibration method using a reference power meter; n represents the harmonic order.

The six-port reflectometer calibration principles for time-domain voltage and current waveform measurements are shown in Figure 6.19. The Fourier coefficients of the harmonic-rich reference voltage wave A_n generated by G_{ref} have to be well known in both magnitude and phase. Unlike A_n, the spectral content of B_n, generated by G_{unk}, does not have to be known. Therefore, it can be any arbitrary multiharmonic generator [29].

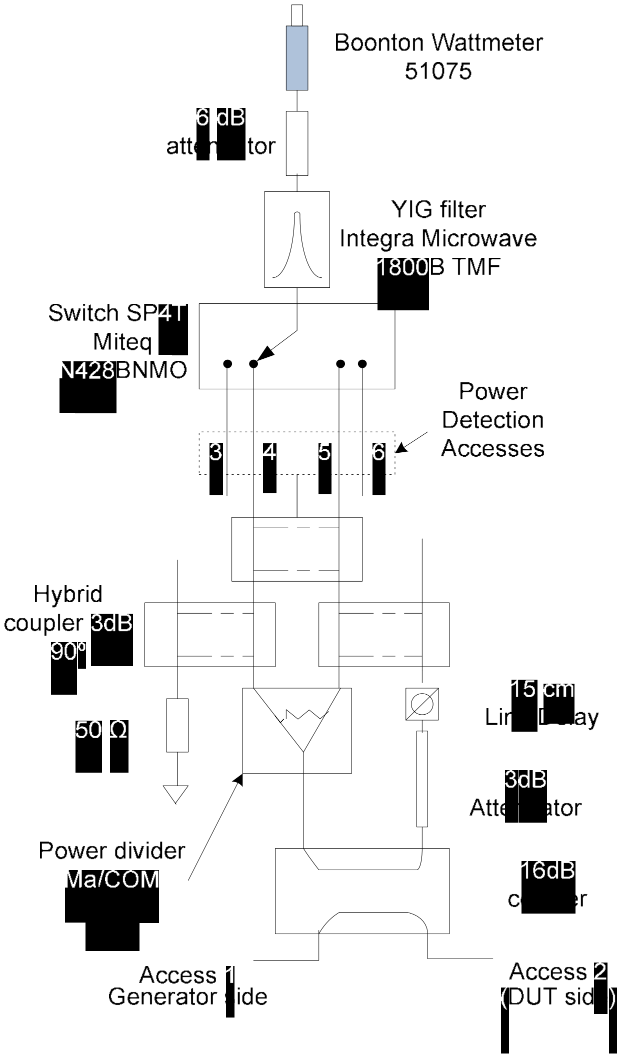

Figure 6.18 Multiharmonic SP reflectometer topology. (© 2008 IEEE [29].)

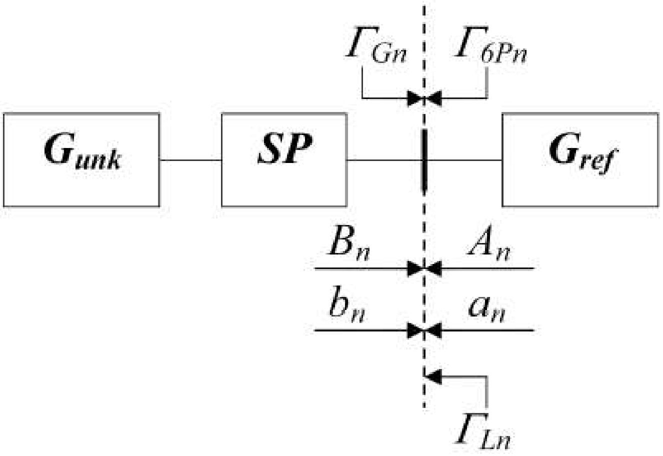

Figure 6.19 Definition of the calibration principle of the SP reflectometer for time-domain voltage and current waveform measurements.

6.11.3 Time-Domain Voltage and Current Measurements

The complete architecture of the proposed source-pull and load-pull measurement system suitable for determining high-frequency time-domain waveform measurements is shown in Figure 6.20 [29].

In the time-domain measurement plane, Γ_{DUTn} represents the reflection coefficient presented by the DUT output impedance. Γ_{6pn} represents the reflection coefficient presented by the source impedance of the six-port reflectometer SP3 when the harmonic generator is OFF (i.e., B_n=0.) Γ_n is the reflection coefficient measured by SP3 in reverse configuration, when the DUT, multiharmonic generator, and the load impedance tune system are in operation.

The waves B_n and $K_n b_{2n}$ are injected by the multiharmonic generator and DUT, respectively. If the directional coupler C1 provides high directivity, K_n is a complex constant. Otherwise, K_n is not constant, but rather a function of the reflection coefficient provided by the load impedance tune system. a_n and b_n in Figure 6.20 are defined as total voltage waves in the time-domain measurement plane traveling toward SP3 and the DUT, respectively.

A similar equation to (6.40) can be derived to express the voltage wave reflected from the output of the DUT and is denoted as b_{2n} in Figure 6.20 as follows:

$$b_{2n} = \frac{B_n}{K_n} \frac{(\Gamma_{DUTn}\Gamma_n - 1)}{(\Gamma_{6Pn} - \Gamma_n)} \tag{6.43}$$

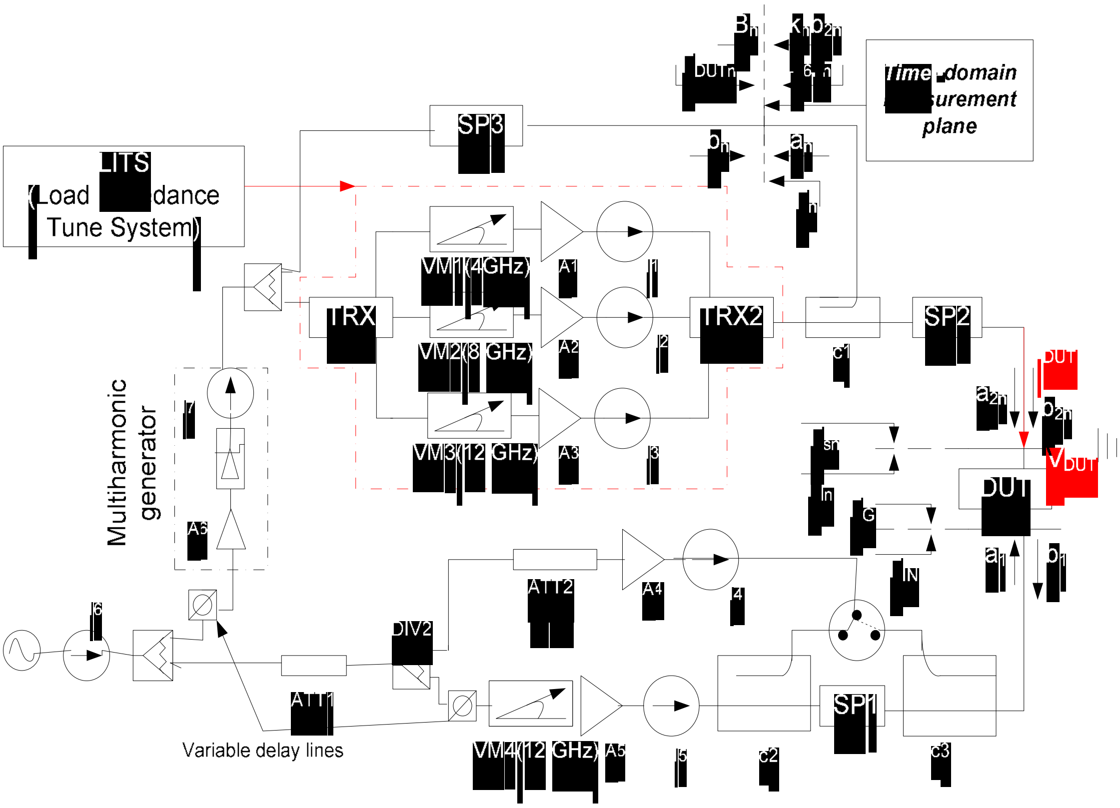

Figure 6.20 Complete architecture of the proposed source-pull and load-pull measurement system suitable for determining high-frequency time-domain waveform measurements. (© 2008 IEEE [29].)

Whereas B_n in (6.43) has been determined in the calibration procedure by replacing the DUT with a reference generator, K_n, Γ_{DOUTn}, and Γ_{6pn} need to be measured with either a six-port reflectometer or a VNA. b_{2n} can now be determined and can be calculated according to

$$a_{2n} = b_{2n}\Gamma_{Ln} \tag{6.44}$$

where Γ_{Ln} is measured by the six-port reflectometer SP2 in Figure 6.20. A drawback of measurement systems using SP reflectometers in a reverse configuration is the drastic loss of measurement accuracy in a 50Ω environment. This is not an issue, however, for source-pull and load-pull systems since the impedance levels are typically different form the system reference impedance, ensuring sufficient precision for the reflection coefficient measurement in the proposed setup. Finally, voltage and current waveforms at the DUT output port are obtained using (6.39) and (6.40) as follows:

$$V_n = b_{2n} + a_{2n} \tag{6.45}$$

$$I_n = \frac{a_{2n} - b_{2n}}{Z_C} \tag{6.46}$$

Depending on the bandwidth of the six-port junction, the frequency selective detection module, and the fundamental frequency, in most cases measurements of V and I at three to five harmonics are sufficient to determine the shape of time-domain voltage and current waveforms accurately for amplifier design applications.

The instantaneous voltage V_{DUT} and the current I_{DUT} waveforms at the output terminal of the DUT are given by

$$V_{DUT}(t) = \mathrm{Re}\{\sum_{n=0}^{3} V_n e^{j2\pi n f_0 t}\} \tag{6.47}$$

and

$$I_{DUT}(t) = \mathrm{Re}\{\sum_{n=0}^{3} I_n e^{j2\pi n f_0 t}\} \tag{6.48}$$

and V_n, I_n (n=1,2,3) are measured with SP2 and SP3, whereas V_0, I_0 are measured with a bias instrument. This setup was implemented and used for a medium-power device optimized for maximum efficiency to demonstrate the capability of the measurement system.

Time-domain voltage and current waveform measurements were performed with the setup and compared to those obtained with a microwave transition analyzer (MTA) based system. The measured time-domain voltage and current waveforms at the output terminal of the FET are presented in Figure 6.21. The maximum relative error of the measured waveforms is approximately 4% [29].

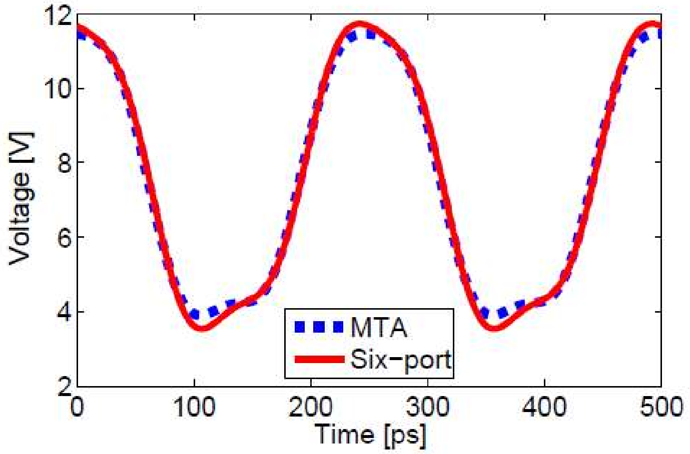

(a) Voltage waveform

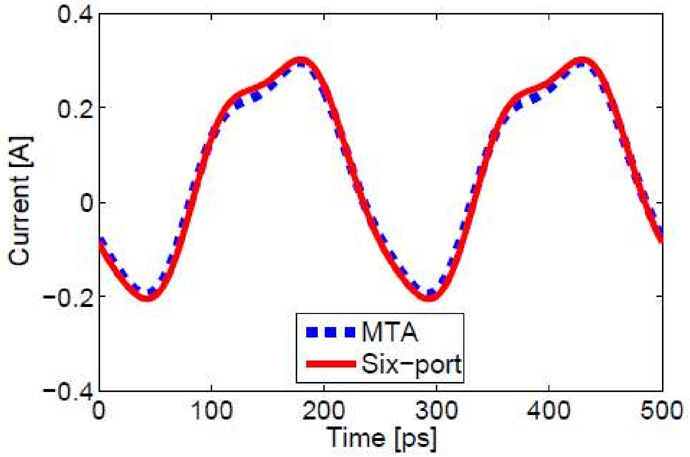

(b) Current waveform

Figure 6.21 Comparison of voltage and current waveforms measured with the time-domain setup and an MTA. (a) Voltage waveform. (b) Current waveform. (© 2008 IEEE [29].)

References

[1] Le, D., and F. M. Ghannouchi, "Multitone Characterization and Design of FET Resistive Mixers Based on Combined Active Source Source–Pull Load–Pull Techniques," *IEEE Trans. Instrument Meas.,* Vol. 46, No. 9, pp. 1201–1208, September 1998.

[2] Teppati, V., A. Ferrero, and U. Pisani, "Recent Advances in Real-Time Load-Pull Systems," *IEEE Trans. on Instrumentation and Measurement,* Vol. 57, pp. 2640–2646, November 2008.

[3] Berghoff, G., E. Bergeault, B. Huyart, and L. Jallet, "Automated Characterization of HF Power Transistors by Source–Pull and Multiharmonic Load–Pull Measurements Based on Six-Port

Techniques," *IEEE Trans. on Microwave Theory and Techniques,* Vol. 46, No. 12, pp. 2068–2073, December 1998.

[4] Soares, R. A., P. Gouzien, P. Legaud, and G. Follot, "A Unified Mathematical Approach to Two-Port Calibration Techniques and Some Applications," *IEEE Trans. Microwave Theory Tech.*, Vol. MTT-37, pp. 1660–1674, November 1989.

[5] Ghannouchi, F. M., F. Beauregard, R. Hajji, and A. Brodeur, "A De-Embedding Technique for Reflection-Based S-Parameters Measurements of HMICs and MMICs," *Microwave & Optical Tech. Letters,* Vol. 10, No. 4, pp. 218–222, November 1995.

[6] Ghannouchi, F. M., G. Zhao, and F. Beauregard, "Simultaneous Load-Pull of Intermodulation and Output Power Under Two Tone Excitation for Accurate SSPA Design," *IEEE Trans. Micro. Theory & Tech,* Vol. 42, No. 6, pp. 943–950, June 1994.

[7] Ferrero, A., and U. Pisani, "An Improved Calibration Technique for On-Wafer Large-Signal Transistor Characterization," *IEEE Trans. Inst. & Meas.,* Vol. 42, No.2, pp. 360–364, April 1993.

[8] Somlo, P. I., and J. D. Hunter, "Microwave Impedance Measurement," *IEE Electrical Measurement Series 2,* London: Peter Peregrinus, 1985.

[9] Luan, D., and F. M. Ghannouchi, "Source-Pull Measurements Using Reverse Six-Port Reflectometers with Application to MESFET Mixer Design," *IEEE Trans. Microwave Theory Tech.*, Vol. 42, pp. 1589–1595, 1994.

[10] Hodgetts, T. E., and G. J. Griffin, "A Unified Treatment of the Six-Port Reflectometer Calibration Using a Minimum of Standards," *Royal Signals and Radar Establishment Rep. No. B3003*, 1983.

[11] Engen, G. F., "Calibrating the Six-port Reflectometer by Means of Sliding Terminations," *IEEE Microwave Theory Tech.*, Vol. 26, pp. 951–957, December 1978.

[12] Hunter, J. D., and P. I. Somlo, "Explicit Six-Port Calibration Method Using Five Standards," *IEEE Microwave Theory Tech.,* Vol. MTT-33, pp. 69–72, January1985.

[13] Engen, G. F., "The Six-Port Reflectometer: An Alternative Network Analyzer," *IEEE Microwave Theory Tech.,* Vol. 25, pp. 1075–1080, December 1977.

[14] Le, D., and F. M. Ghannouchi, "Noise Measurements of Microwave Transistors Using an Uncalibrated Mechanical Stub Tuner and a Built-In Reverse Six-Port Reflectometer," *IEEE Trans. Instrument Meas.,* Vol. 44. No. 4, pp. 847–852, August 1995.

[15] Ghannouchi, F. M., R. Larose, and R. G. Bosisio, "A New Multiharmonic Loading Method for Large Signal Microwave Transistor Characterization," *IEEE Microwave Theory Tech.,* Vol. 39, pp. 986–992, June 1991.

[16] Gonzalez, G., *Microwave Transistor Amplifiers Analysis and Design,* Second Ed., Englewood Cliffs, NJ: Prentice-Hall, 1996.

[17] Ghannouchi, F. M., and R. G. Bosisio, "Source-Pull/Load-Pull Oscillator Measurements at Microwave/MM Wave Frequencies," *IEEE Trans. Instrument Meas.,* Vol. 41, pp. 32–35, February 1992.

[18] Yakabe, T., M. Kinoshita, and H. Yabe, "Complete Calibration of a Six-Port Reflectometer with One Sliding Load and One Short," *IEEE Trans. Microwave Theory Tech.*, Vol. 42, pp. 2035–2039, November 1994.

[19] Koyama, K., T. Kawasaki, and J. E. Hanely, "Measurement of AM-PM Conversion Coefficients," *Telecommun.,* Vol. 12, No. 6, pp. 25–28, June 1978.

[20] Moss, J. F., "AM-AM and AM-PM Measurements using the PM Null Technique," *IEEE Trans. Microwave Theory Tech* ,Vol. MTT-35, No. 8, pp. 780–782, 1987.

[21] Ghannouchi, F. M., G. Zhao, and F. Beauregard, "Simultaneous AM-AM/AM-PM Distortion Measurements of Microwave Transistors Using Active Load-Pull and Six-Port Techniques," IEEE *Trans. Microwave Theory Tech.* Vol. 43, No.1, pp.1584–1588, July 1995.

[22] Parra, T., et al., "X-Band Low Phase Distortion MMIC Power Limiter," *IEEE Trans. Microwave Theory Tech.* Vol. 41, No. 5, pp. 876–879, 1993.

[23] Ghannouchi, F. M., and R. G. Bosisio, "An Automated Millimeter-Wave Active Load-Pull Measurement System Based on Six-Port Techniques," *IEEE Trans. Instrum. Meas*., Vol. 41, No. 6, pp. 957–962, 1992.

[24] Engen, G. F., and C. A. Hoer, "Thru-Reflect-Line: An Improved Technique for Calibrating the l Dual Six-port Automatic Network Analyzer," *IEEE Trans. Microwave Theory Tech.,* Vol. MTT-27, pp. 987–993, 1979.

[25] Sipila, M., K. Lehtinen, and V. Pora, "High Frequency Periodic Time-Domain Waveform Measurement System," *IEEE Trans. Microw. Theory Tech.*, Vol. 36, No. 10, pp. 1397–1405, October 1988.

[26] Weiss, M., and Z. Popovic, "Time-Domain Optical Sampling of Nonlinear Microwave Power Amplifiers," *IEEE MTT-S Int. Microw. Symp. Dig.*, pp. 889–892, June 1999.

[27] Raay, F. V., and G. Kompa, "A New On-wafer Large-Signal Waveform Measurement System with 40 GHz Harmonic Bandwidth," *IEEE MTT-S Int. Microw. Symp. Dig.*, pp. 1435–1438, June 1992.

[28] Verspecht, J., P. Debie, A. Barel, and L. Martens, "Accurate on Wafer Measurement of Phase and Amplitude of the Spectral Components of Incident and Scattered Voltage Waves at the Signal Ports of Nonlinear Microwave Device," *IEEE MTT-S Int. Microw. Symp. Dig*., pp. 1029–1032, May 1995.

[29] Bensmida, S., P. Poiré, R. Negra, F. M. Ghannouchi, and G. Brassard, "New Time-Domain Voltage and Current Waveform Measurement Setup for Power Amplifier Characterization and Optimization," *IEEE Trans. Microwave Theory Tech.*, Vol. 56, No. 1, pp. 224–231, January 2008.

[30] Marks, R. B., and D. F. Williams, "A General Waveguide Circuit Theory," *J. Res. Nat. Inst. Standards Technol.,* Vol. 97, No. 5, pp. 533–562, September 1992.

[31] Verspecht, J., "Large-Signal Network Analysis," *IEEE Microwave*, vol. 6, no. 4, pp. 82–92, December 2005.

Chapter 7

Six-Port Wireless Applications

There is increasing demand for reduced complexity and power consumption in the design of wireless terminals. Furthermore, wideband, compact-sized, and low-cost digital transceivers are required to expand mobile and wireless communications. Use of a multiport homodyne technique is interesting in wireless communications due to the utilization of power detectors instead of mixers. This technique provides simpler circuits in comparison with its heterodyne counterpart. The advantages of such an approach are manifold. First of all, the broadband specifications can be easily achieved by passive elements. Moreover homodyne technique ensures low power consumption. In addition, its hardware architecture is proposed as a means to avoid more costly transceivers. The objective of this chapter is to study the multiport transceivers and their wireless applications.

7.1 MULTIPORT TRANSCEIVER

In this section, the operation of multiport structures as modulators and demodulators is discussed.

7.1.1 Multiport Modulator

In a multiport modulator, some versions of the LO signal under various amplitudes/phase angles are discussed, where the amplitude and phase of the collected signal are properly achieved. The multiport transmitter uses some variable reflectors and one collector, instead of conventional mixers. Figure 7.1 shows the functional block diagram of a multiport modulator, which consists of one input, one output, and *N* reflection ports. The input signal is the local reference signal, $a_{LO}(t)$. The multiport structure produces *N* various versions of the LO signal and combines them in the output ports.

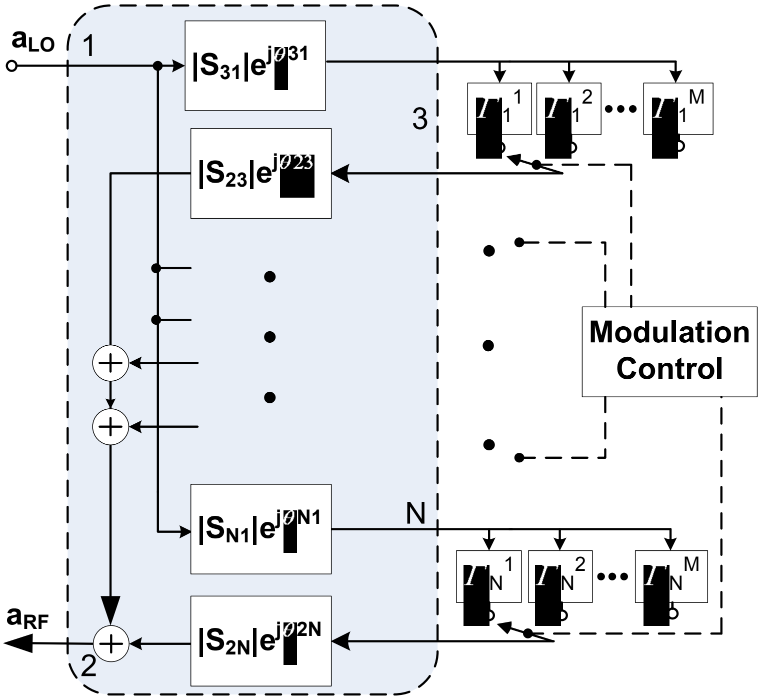

Figure 7.1 Functional block diagram of an *N*-port modulator.

The multiport junction is assumed to be a linear network, so the output signal of the multiport structure is as follows:

$$a_{RF} = \sum_{i=1}^{N} S_{i1} S_{2i} \Gamma_i^k a_{LO} \quad , \quad k = 1,2,...,M$$
$$\begin{cases} S_{i1} = |S_{i1}| e^{j\phi_{i1}} \\ S_{2i} = |S_{2i}| e^{j\phi_{2i}} \end{cases} \tag{7.1}$$

where S_{ij} are the scattering parameters of the multiport structure, and Γ_i^k is the kth value of the reflection coefficient at the ith port using K reflection states. The input and output signals are shown as a_{LO} and a_{RF}, respectively. For a specific multiport structure, where the scattering parameters are given, the distinct values for Γ_i^k can be calculated for each desired modulation scheme.

Figure 7.2 is a diagram of the six-port direct QPSK modulator. It consists of a six-port circuit, a switch matrix, and open and short terminations. The circuit operates as follows: port 1 is fed with a carrier signal, which is routed to ports 3, 4, 5, and 6 through the different branches of the six-port circuit. Signals present at ports 3 to 6 are routed to different terminations by the switch matrix, controlled by baseband data.

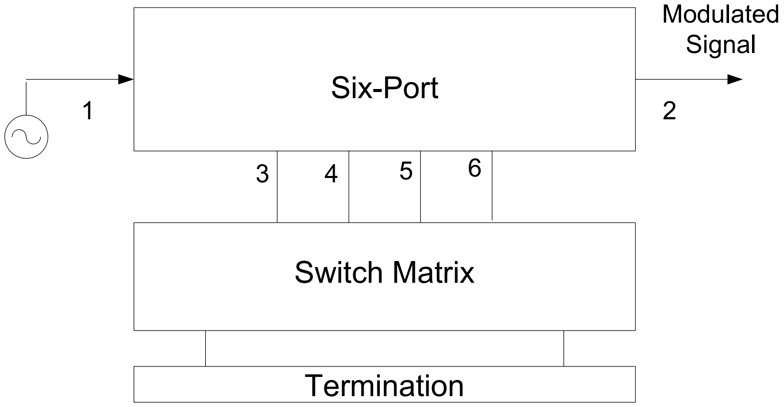

Figure 7.2 Six-port direct modulator architecture.

Those reflected signals are then summed at port 2, which is the output for the modulated signal. The output signal acquires different phases depending on the terminations applied at ports 3–6 [1]. A six-port direct 16QAM modulator is also recently introduced by the use of a similar concept [2].

7.1.2 Multiport Demodulator

In a multiport demodulator, the received RF signal is summed with a local oscillator signal under various phase angles. The multiport receiver uses power detectors instead of conventional mixers. Figure 7.3 shows the functional block diagram of a multiport demodulator, which consists of two inputs and N outputs. The input signal is the received RF signal, $a_{RF}(t)$, and the local reference signal is $a_{LO}(t)$.

The multiport structure produces N various combinations of RF and LO signals and directs them to N power detectors. Therefore, N scalar outputs can be obtained. The multiport junction is assumed to be a linear network. The N signal levels off the multiport structure outputs, detected using Schottky diode detectors, and the expression of demodulation equations can be derived as:

$$I=\sum_{i=1}^{N}\alpha_i P_{oi} \tag{7.2a}$$

$$Q=\sum_{i=1}^{N}\beta_i P_{oi} \tag{7.2b}$$

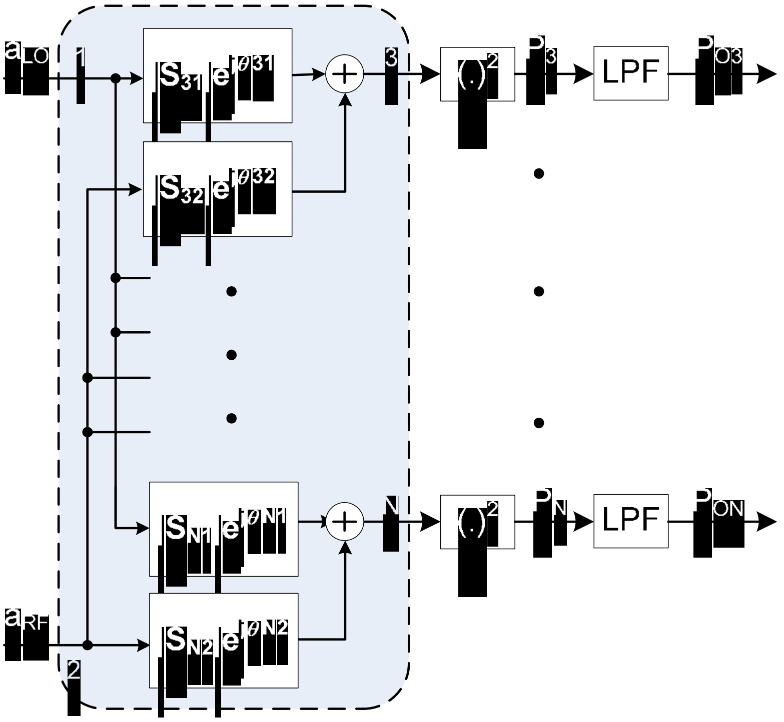

Figure 7.3 Functional block diagram of an *N*-port demodulator.

where *I* and *Q* are the in-phase and quadrature components of the modulated signal, and α_i and β_i are the demodulation coefficients.

7.2 SIX-PORT RECEIVER

A multiport receiver consists of two inputs and *N* outputs. In direct-conversion receiver applications, the RF and LO signals are applied to two input ports as two complex inputs shown in Figure 7.4. The multiport structure produces *N* various combinations of RF and LO signals and injects them to *N* power detectors, so that *N* outputs can be obtained [3, 4]. If the multiport junction is a linear network, *N* outputs of the multiport structure will be as follows:

$$P_i = \left|S_{i1}\overline{a}_{LO} + S_{i2}\overline{a}_{RF}\right|^2 \qquad i = 1,2,...,N \tag{7.3a}$$

$$S_{i1} = \left|S_{i1}\right| e^{j\phi_{i1}} \tag{7.3b}$$

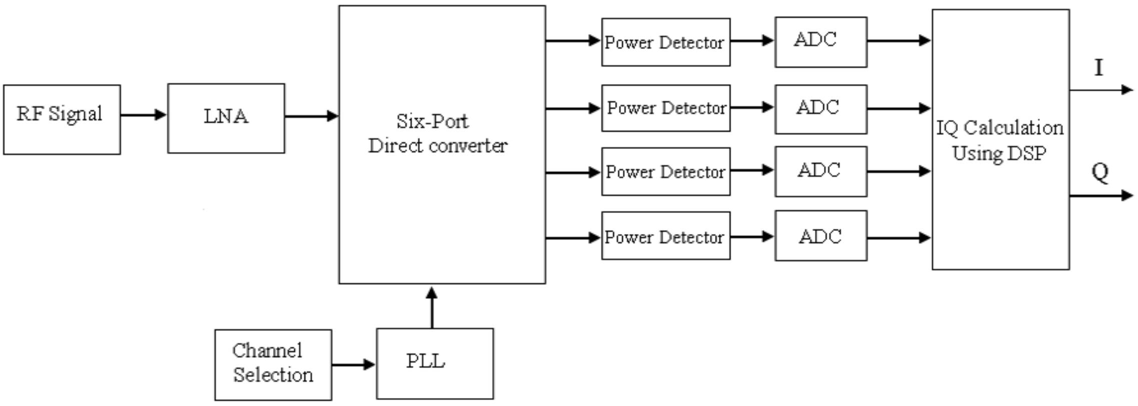

Figure 7.4 Direct conversion receiver based on six-port.

$$S_{i2} = |S_{i2}| e^{j\phi_{i2}} \tag{7.3c}$$

where S_{ij} is the scattering parameter of the multiport structure. Assuming that the RF signal with digital modulation has the same frequency as the LO signal, the RF and LO signals can be represented by:

$$a_{LO} = \frac{1}{\sqrt{2}} |a_{LO}| e^{j\varphi_{LO}} \tag{7.4}$$

$$a_{RF} = \frac{1}{\sqrt{2}} |a_{RF}| \sqrt{I^2 + Q^2}\, e^{j\varphi_{RF}} \tag{7.5}$$

where I and Q are in-phase and quadrature-phase modulating signals. By substituting (7.4) and (7.5) in (7.3) and by use of the relations:

$$I = \sqrt{I^2 + Q^2} \cos(\varphi_{RF}) \tag{7.6a}$$

$$Q = -\sqrt{I^2 + Q^2} \sin(\varphi_{RF}) \tag{7.6b}$$

the expressions of output powers can be derived as

$$P_i = \frac{1}{2}|S_{i1}|^2 |a_{LO}|^2 + \frac{1}{2}|S_{i2}|^2 |a_{RF}|^2 \left(I^2 + Q^2\right) \\ + |S_{i1}||S_{i2}||a_{RF}||a_{LO}|\left(I\cos\left(\varphi_i\right) + Q\sin\left(\varphi_i\right)\right) \tag{7.7}$$

where $\varphi = \varphi_{RF} - \varphi_{LO}$ and $\varphi_i = \varphi_{i1} - \varphi_{i2}$. Assuming that the LO power is known, the unknown parameters will be (I^2+Q^2), I, and Q. Thus, (7.7) can be rewritten as follows:

$$\begin{gathered} P_i = M_i + L_i\left(I^2 + Q^2\right) + N_i\cos\left(\varphi_i\right)I + N_i\sin\left(\varphi_i\right)Q \\ M_i = \frac{1}{2}|S_{i1}|^2 |a_{LO}|^2,\ L_i = \frac{1}{2}|S_{i2}|^2 |a_{RF}|^2, N_i = |S_{i1}||S_{i2}||a_{RF}||a_{LO}| \\ \varphi_i = \varphi_{i1} - \varphi_{i2}, for \quad i = 1,2,\ldots,N \end{gathered} \tag{7.8}$$

where M_i, L_i, and N_i are constant governing parameters for given operating conditions, which are functions of scattering parameters and the power of LO and received RF signals. Equation (7.8) presents N equations with three unknown parameters. From (7.8), the six-port equations can be written in matrix form:

$$\begin{bmatrix} 1 \\ \left(I^2 + Q^2\right) \\ I \\ Q \end{bmatrix} = D_T^{-1} \cdot \begin{bmatrix} P_1 \\ P_2 \\ P_3 \\ P_4 \end{bmatrix} \tag{7.9}$$

where $\mathbf{D_T}$ is a matrix defined as:

$$\mathbf{D_T} = \begin{bmatrix} M_1 & L_1 & N_1\cos(\phi_1) & N_1\sin(\phi_1) \\ M_2 & L_2 & N_2\cos(\phi_2) & N_2\sin(\phi_2) \\ M_3 & L_3 & N_3\cos(\phi_3) & N_3\sin(\phi_3) \\ M_4 & L_4 & N_4\cos(\phi_4) & N_4\sin(\phi_4) \end{bmatrix} \tag{7.10}$$

If the determinant of the $\mathbf{D_T}$ matrix is nonzero, (7.9) can be solved with respect to the unknown parameters:

$$I = \alpha_1' P_1 + \alpha_2' P_2 + \alpha_3' P_3 + \alpha_4' P_4 \tag{7.11a}$$

$$Q = \beta_1' P_1 + \beta_2' P_2 + \beta_3' P_3 + \beta_4' P_4 \tag{7.11b}$$

Equation (7.9) shows the general demodulation equations in six-port structures. As seen from (7.9), there is a dependent equation that leads to a fixed value in the first element of the calculated matrix [4, 5]. This dependent equation is the result of the known LO power. This assumption is reasonable, because the LO power is known to the receiver designer and can be removed from unknown parameters.

Nevertheless, if the LO power is so unstable that it cannot be treated as a constant, the DC terms of each output can be easily removed by DC cancellation methods (in a simple case, by a capacitor), which always are used in direct-conversion receivers for the DC offset cancellation. Therefore, the slow variation of the LO signal with the other DC terms will be removed, and it is not necessary to know or calibrate the LO power exactly. Note that blindly removing the LO power cannot cause any problems, since the information needed for *I/Q* detection exists in terms of the AC outputs. Note that the (I^2+Q^2) parameter is variable and cannot be removed from demodulation calculations.

This is the reason for reducing the number of outputs from four to three; therefore, (7.9) may be changed to:

$$\begin{bmatrix} \left(I^2+Q^2\right) \\ I \\ Q \end{bmatrix} = \mathbf{D}^{-1}. \begin{bmatrix} P_1 - M_1 \\ P_2 - M_2 \\ P_3 - M_3 \end{bmatrix} \tag{7.12}$$

where the matrix **D** is defined as:

$$\mathbf{D} = \begin{bmatrix} L_1 & N_1\cos\left(\phi_1\right) & N_1\sin\left(\phi_1\right) \\ L_2 & N_2\cos\left(\phi_2\right) & N_2\sin\left(\phi_2\right) \\ L_3 & N_3\cos\left(\phi_3\right) & N_3\sin\left(\phi_3\right) \end{bmatrix} \tag{7.13}$$

where the determinant of the **D** matrix is nonzero. Therefore, the demodulation equations will be:

$$I = \alpha_1 P_1 + \alpha_2 P_2 + \alpha_3 P_3 - c_1 \tag{7.14a}$$

$$Q = \beta_1 P_1 + \beta_2 P_2 + \beta_3 P_3 - c_2 \tag{7.14b}$$

where:

$$Q = \beta_1 P_1 + \beta_2 P_2 + \beta_3 P_3 - c_2 \tag{7.15a}$$

$$I = \alpha_1 P_1 + \alpha_2 P_2 + \alpha_3 P_3 - c_1 \tag{7.15b}$$

Thus, it can be inferred that multiport structures require at least three independent outputs for *I* and *Q* signal calculation. Each additional output port adds another dependent equation into (7.12); hence, the five-port structure has the minimum possible outputs among the multiport structures. Therefore, it can be emphasized that any multiport structure with *N* output ports presents *N* equations with respect to the three unknown parameters. The three independent equations can be chosen between all of the *N* equations and the remainder (*N*-3) can be derived from these three independent equations.

It should be mentioned that the additional equation in the common six-port structure is only used to simplify *I/Q* calculations. In this case, it is sometimes better to reduce the number of ports from six to five, if the complexity of calculation remains the same. In regards to (7.9) and (7.12), the additional equation in the six-port architecture leads to more calibration parameters, which may increase the errors of the *I/Q* calculations due to errors in the calibration procedure.

7.2.1 Five-Port Receiver

There is a simple way to choose three independent outputs between output ports in conventional six-port structure. Using the same notation as Hoer [6], it can be shown that a set of four independent outputs are obtained by choosing one equation from each group in Table 7.1, plus a fourth equation from unselected equations.

Table 7.1
Six-Port Independent Output Selection

Group 1	*Group 2*	*Group 3*
$\lvert a_{LO}\rvert^2$	$P_1 = \lvert a_{LO} - a_{RF}\rvert^2$	$P_3 = \lvert a_{LO} - ja_{RF}\rvert^2$
$\lvert a_{RF}\rvert^2$	$P_2 = \lvert a_{LO} + a_{RF}\rvert^2$	$P_4 = \lvert a_{LO} + ja_{RF}\rvert^2$

Therefore, the independent ports are members of the different groups. As a good design, a member of group 2 (P_1 or P_2), a member of group 3 (P_3 or P_4), and both members of group 1 ($\lvert a_{LO}\rvert^2, \lvert a_{RF}\rvert^2$) can be chosen in which LO power is known ($\lvert a_{LO}\rvert^2$). In case the LO power is known, the four outputs are reduced to three.

Although there are various methods to implement a five-port architecture, nevertheless, it is important to choose an efficient architecture to provide accurate performance. Some criteria to design the five-port architecture are as follows:

1. It is necessary to choose three independent outputs that provide three independent equations for calculating the *I*, *Q* signals. If three power outputs are not independent, *I*, *Q* demodulation will be impossible.

2. The most important source of error in *I*, *Q* demodulation equations is due to the calibration procedure. To reduce the impact of these errors the nonzero elements of the D matrix should be minimized. Thus, an optimum five-port structure with minimum error in calibration procedure is a junction that presents a sparse D matrix.

3. Because the five-port structure falls in the direct conversion category, the DC offset is one of the most critical parameters that must be limited. Since the main source of DC offset is LO leakage to the RF port and vice versa, it is required to have a high isolation between two input ports.

4. The output reduction in a five-port should not increase the complexity of *I*, *Q* calculation. Therefore, a five-port structure is preferable to six-port structures in software defined radio applications if the complexity of the *I*, *Q* calculation remains the same.

Figure 7.5 shows a practical implementation of a five-port receiver [7]. Supposing that all elements are ideal in this architecture, the equations of output power can be written as:

$$P_{RF} = \frac{1}{2}\left|\bar{a}_{RF}\right|^2 = \frac{1}{4}\left|a_{RF}\right|^2\left(I^2 + Q^2\right) \tag{7.16a}$$

$$\begin{aligned} P_2 &= \left|\frac{1}{2}\bar{a}_{LO} + \frac{1}{2\sqrt{2}}\bar{a}_{RF}\right|^2 \\ P_2 &= \frac{1}{8}\left|a_{LO}\right|^2 + \frac{1}{16}\left|a_{RF}\right|^2\left(I^2 + Q^2\right) + \frac{1}{8\sqrt{2}}\left|a_{RF}\right|\left|a_{LO}\right| I \end{aligned} \tag{7.16b}$$

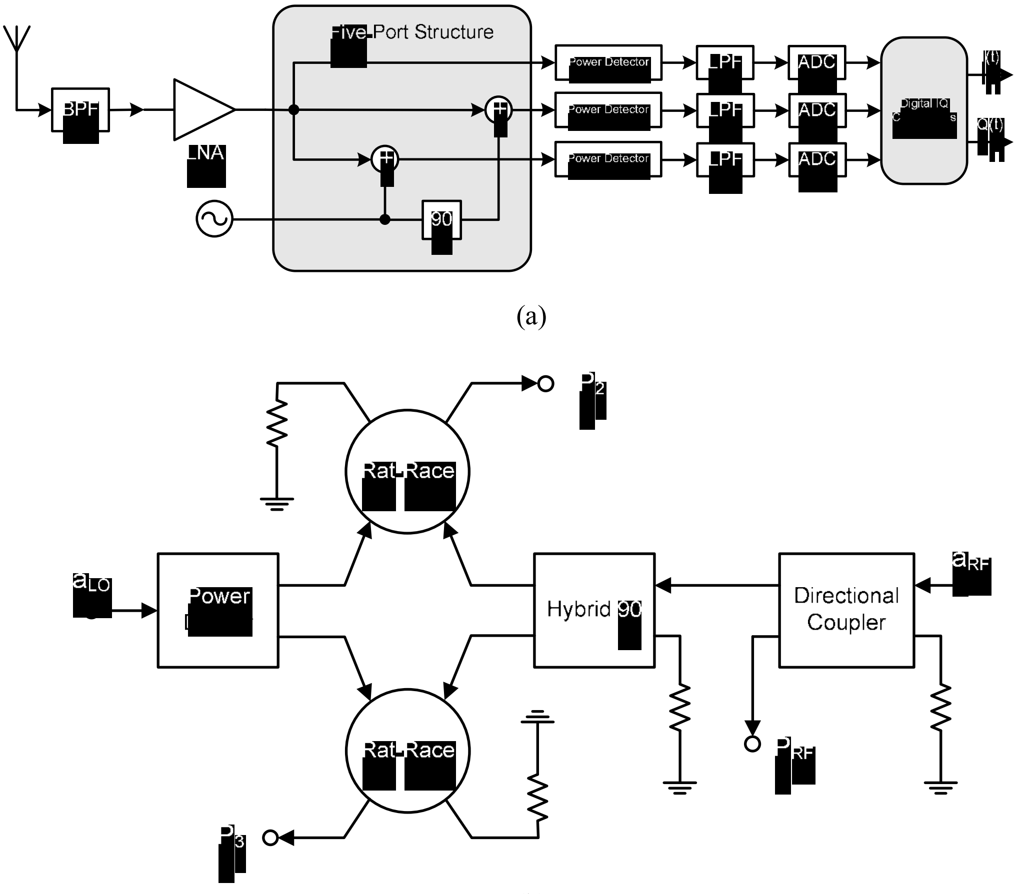

(a)

(b)

Figure 7.5 (a) A five-port receiver. (b) A practical implementation of five-port architecture. (© 2007 IET [7].)

$$P_3 = \left| \frac{1}{2}\bar{a}_{LO} - j\frac{1}{2\sqrt{2}}\bar{a}_{RF} \right|^2$$

$$P_3 = \frac{1}{8}\left|a_{LO}\right|^2 + \frac{1}{16}\left|a_{RF}\right|^2\left(I^2+Q^2\right) + \frac{1}{8\sqrt{2}}\left|a_{RF}\right|\left|a_{LO}\right|Q \qquad (7.16c)$$

Hence, the demodulated signal can be written as:

$$\begin{bmatrix} I^2+Q^2 \\ I \\ Q \end{bmatrix} = \mathbf{D}^{\mathbf{-1}} \cdot \begin{bmatrix} P_{RF} \\ P_2 \\ P_3 \end{bmatrix} - C \tag{7.17}$$

where

$$\mathbf{D}^{\mathbf{-1}} = \frac{8\sqrt{2}}{|a_{RF}||a_{LO}|} \begin{bmatrix} \dfrac{|a_{LO}|}{2\sqrt{2}|a_{RF}|} & 0 & 0 \\ -\dfrac{1}{4} & 1 & 0 \\ -\dfrac{1}{4} & 0 & 1 \end{bmatrix}, \quad C = \frac{8\sqrt{2}|a_{LO}|}{|a_{RF}|} \begin{bmatrix} 0 \\ \dfrac{1}{8} \\ \dfrac{1}{8} \end{bmatrix}$$

As seen from (7.17), the five-port structure has a sparse $\mathbf{D}^{-1}$ matrix due to the zero setting of $\mathbf{D}^{-1}$'s elements. According to (7.17), only five constant parameters are needed to be determined in practical conditions. Note that the elements of the C matrix are not needed to be determined, because they can be removed by subtracting a constant or DC cancellation in DSP. The parameter reduction in $\mathbf{D}^{-1}$ matrix makes the calibration procedure easier and mitigates the errors of demodulation equations due to the calibration procedure.

7.2.2 Noise in Six-Port Receiver

Assuming the RF signal with digital modulation has the same frequency as the LO signal, the RF signal plus noise can be represented by

$$a_{RF} = |a_{RF}| \left\{ \left[I(t) + n_I(t) \right] \cos(\omega_c t + \phi_{RF}) + \left[Q(t) - n_Q(t) \right] \sin(\omega_c t + \phi_{RF}) \right\} \tag{7.18}$$

where I and Q are in-phase and quadrature components of the modulated signal. The noise components are

$$n_I(t) \overset{\Delta}{=} n_C(t) / |a_{RF}| \tag{7.19a}$$

$$n_Q(t) \overset{\Delta}{=} n_S(t) / |a_{RF}| \tag{7.19b}$$

where

$$
\begin{aligned}
n(t) &= |n(t)|\cos(\omega_C t+\phi_{RF}+\varphi_n) \\
&= |n(t)|\cos(\varphi_n)\cos(\omega_C t+\phi_{RF}) - |n(t)|\sin(\varphi_n)\sin(\omega_C t+\phi_{RF}) \\
&\overset{\Delta}{=} n_C(t)\cos(\omega_C t+\phi_{RF}) - n_S(t)\sin(\omega_C t+\phi_{RF})
\end{aligned}
$$

By substituting (7.19) into (7.18), the expressions of output powers are

$$
\begin{aligned}
P_i &= \frac{1}{2}|S_{i1}|^2|a_{LO}|^2 + \frac{1}{2}|S_{i2}|^2|a_{RF}|^2\left[(I+n_I)^2+(Q-n_Q)^2\right] \\
&\quad + |S_{i1}||S_{i2}||a_{RF}||a_{LO}|\left[(I+n_I)\cos(\phi-\varphi_i)+(Q-n_Q)\sin(\phi-\varphi_i)\right] \\
&\quad + \text{high frequency terms.}
\end{aligned}
\tag{7.20}
$$

where $\phi=\phi_{RF}-\phi_{LO}$ and $\varphi_i=\varphi_{i1}-\varphi_{i2}$.

By using lowpass filters to remove the high frequency components, baseband output is obtained as

$$
\begin{aligned}
P_{oi} &= \frac{1}{2}|S_{i1}|^2|a_{LO}|^2 + \frac{1}{2}|S_{i2}|^2|a_{RF}|^2\, LP\left\{(I+n_I)^2+(Q-n_Q)^2\right\} \\
&\quad + |S_{i1}||S_{i2}||a_{RF}||a_{LO}|\left[(I+n_I)\cos(\phi-\varphi_i)+(Q-n_Q)\sin(\phi-\varphi_i)\right]
\end{aligned}
\tag{7.21}
$$

where $LP\{.\}$ is the lowpass component. Since the square operator increases frequency contents of its input signal, then, $LP\left\{(I+n_I)^2+(Q-n_Q)^2\right\}$ could be not equal to $\left\{(I+n_I)^2+(Q-n_Q)^2\right\}$. We assume that the local oscillator power level is known and does not change; thus, (7.21) can be rewritten as follows:

$$
\begin{aligned}
P_{oi} &= M_i + L_i \cdot |a_{RF}|^2\, LP\left\{(I+n_I)^2+(Q-n_Q)^2\right\} \\
&\quad + N_i\,|a_{RF}|\left\{\cos(\phi-\varphi_i)(I+n_I)+\sin(\phi-\varphi_i)(Q-n_Q)\right\}
\end{aligned}
\tag{7.22}
$$

where $M_i=\frac{1}{2}\left|S_{i1}\right|^2\left|a_{LO}\right|^2$, $L_i=\frac{1}{2}\left|S_{i2}\right|^2$, $N_i=\left|S_{i1}\right|\left|S_{i2}\right|\left|a_{LO}\right|$. M_i, L_i, and N_i are constant parameters, which are functions of scattering parameters and the power of the LO signal. Neglecting noise, this result is the same as the one presented in [8]. System of linear equations expressed in (7.22) consist of N equations, N is the number of output ports, with three unknown parameters $LP\ \{I^2+Q^2\}$, I, and Q. Hence, in-phase (I) and quadrature (Q) signals can be obtained after simple mathematical calculations in the form of a linear composition of N output voltages. In a general case demodulation equations can be derived as

$$I'=\left|a_{RF}\right|(I+n_I)=\sum_{i=1}^{N}\alpha_i P_{oi} \tag{7.23a}$$

$$Q'=\left|a_{RF}\right|(Q-n_Q)=\sum_{i=1}^{N}\beta_i P_{oi} \tag{7.23b}$$

where I', Q' are demodulated data, and α_i and β_i are called demodulation coefficients.

In conventional six-port structures [4,8] the phase shifts between the LO and RF signal at output ports 3 through 6 are selected multiples of $\pi/2$.

$$\begin{aligned}
&\varphi_{1,LO}=\pi,\ \varphi_{1,RF}=0\\
&\varphi_{2,LO}=\pi/2,\ \varphi_{2,RF}=0\\
&\varphi_{3,LO}=\pi/2,\ \varphi_{3,RF}=\pi/2\\
&\varphi_{4,LO}=0,\ \varphi_{4,RF}=\pi/2
\end{aligned} \tag{7.24}$$

According to (7.22) and assumption of $\phi=0$, a linear system of equations can be constructed as

$$P_{o1}=M_1+L_1\left|a_{RF}\right|^2 LP\left\{(I+n_I)^2+(Q-n_Q)^2\right\}-\left|a_{RF}\right|N_1(I+n_I) \tag{7.25a}$$

$$P_{o2}=M_2+L_2\left|a_{RF}\right|^2 LP\left\{(I+n_I)^2+(Q-n_Q)^2\right\}+\left|a_{RF}\right|N_2(Q-n_Q) \tag{7.25b}$$

$$P_{o3}=M_3+L_3\left|a_{RF}\right|^2 LP\left\{(I+n_I)^2+(Q-n_Q)^2\right\}+\left|a_{RF}\right|N_3(I+n_I) \tag{7.25c}$$

$$P_{o4}=M_4+L_4\left|a_{RF}\right|^2 LP\left\{(I+n_I)^2+(Q-n_Q)^2\right\}-\left|a_{RF}\right|N_4(Q-n_Q) \qquad (7.25\text{d})$$

where M_i, L_i are defined in (7.22). For a general structure, I and Q can be obtained using the above equations by a simple matrix calculation called the demodulation process. Finally, demodulated data can be written as a linear composition of known parameters, P_{oi} .

$$I'=\left|a_{RF}\right|(I+n_I)=\alpha_1 P_{o1}+\alpha_4 P_{o2}+\alpha_3 P_{o3}+\alpha_4 P_{o4} \qquad (7.26\text{a})$$

$$Q'=\left|a_{RF}\right|(Q-n_Q)=\beta_1 P_{o1}+\beta_2 P_{o2}+\beta_3 P_{o3}+\beta_4 P_{o4} \qquad (7.26\text{b})$$

The above demodulation equations are simplified for symmetrical structure. For a symmetrical structure, we can write

$$M_i = M_j, L_i = L_j, N_i = N_j \qquad i,j = 1,2,3,4 \qquad (7.27)$$

Hence, $\alpha_3=-\alpha_1=\beta_2=-\beta_4=1/(2N_1)$, $\alpha_2=\alpha_4=\beta_1=\beta_3=0$, and demodulation equations are in a simplest form as:

$$I'=(P_{o3}-P_{o1})/(2N_1) \qquad (7.28\text{a})$$

$$Q'=(P_{o2}-P_{o4})/(2N_1) \qquad (7.28\text{b})$$

Using additional ADCs and DSP units, these demodulation equations can be implemented with accurate results. A low-cost implementation of (7.28) is the conventional op-amp circuits [9], although the accuracy may be slightly reduced. The system of linear equations in (7.25) has four equations and three unknown parameters, so there is a dependent equation that can be eliminated. One way to reduce the receiver's cost and complexity is to eliminate one of the outputs, which eliminates one power detector and one ADC. For example, by the elimination of P_{o4} , the demodulation equations can be rewritten as

$$I'=(P_{o3}-P_{o1})/(2N_1) \qquad (7.29\text{a})$$

$$Q'=[2P_{o2}-(P_{o3}+P_{o1})]/(2N_1) \qquad (7.29\text{b})$$

These equations convert six-port structure to five-port structure. For cost reduction, we can implement these equations by an electronic circuit which can be realized using conventional operational amplifiers as shown in Figure 7.6. In this circuit we use variable resistors to remove the unwanted constant DC components. The calibration process can be done by varying the value of the resistors in horizontal arms. Moreover, there are various I/Q generation algorithms that may be used for six-port and five-port receivers [10–12].

Beside the noise, in the case of nonideal phase shift, additional terms appeared in (7.25) as

$$\begin{aligned} P_{oi}=&M_i+L_i\left|a_{RF}\right|^2 LP\left\{(I+n_I)^2+(Q-n_Q)^2\right\} \\ &+\left|a_{RF}\right|C_iN_i(I+n_I)+\left|a_{RF}\right|S_iN_i(Q-n_Q), \qquad i=1,2,3,4 \end{aligned} \tag{7.30}$$

where $C_i=\cos\left(\phi-\varphi_i\right)$ and $S_i=\sin\left(\phi-\varphi_i\right)$ are constants for a six-port architecture with specific phase deviations.

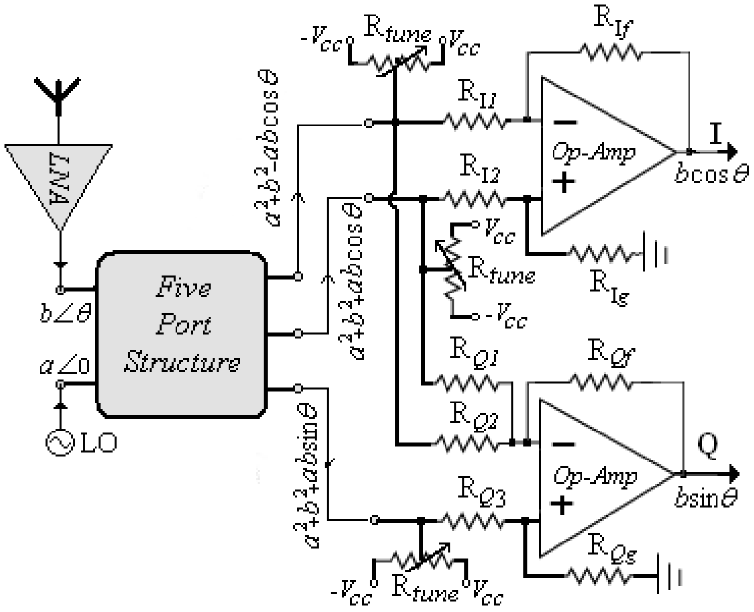

Figure 7.6 Baseband circuit for a five-port structure (*I/Q* calculation block). (© 2009 IET [16].)

Therefore, a combination of at least three outputs is required in demodulation process, and in this general case, the demodulation equation is rewritten as

$$I'=\left|a_{RF}\right|(I+n_I)=\alpha_1P_{o1}+\alpha_2P_{o2}+\alpha_3P_{o3} \tag{7.31a}$$

$$Q'=\left|a_{RF}\right|(Q-n_Q)=\beta_1P_{o1}+\beta_2P_{o2}+\beta_3P_{o3} \tag{7.31b}$$

which can be implemented by a simple modification in an electronic circuit of *IQ* calculation.

7.2.3 Six-Port Receiver Calibration

To have an optimal receiver, the demodulation coefficients must be found for each carrier frequency to minimize BER. Here, a calibration method is described based on S-parameters of multiport linear structure as well as the characteristics of nonlinear power detectors. The S-parameters of structures can be obtained from simulation or measurement. At first stage, the output powers are calculated for each constellation points using S-parameters and the characteristics of power detectors. The calibration is performed using the video signals. Accordingly, for each constellation point, *I*, *Q*, and P_{oi} are known. Considering *M* as *constellation* points ($M \geq N$), a system of linear equations *B*=*A*.*X* must be solved for demodulation purpose. The matrices *A* and *X* are as follows:

$$A=\left[\begin{array}{cccc|cccc} P_{o11} & P_{o12} & \cdots & P_{o1N} & P_{o11} & P_{o22} & \cdots & P_{o1N} \\ P_{o21} & P_{o22} & \cdots & P_{o2N} & P_{o21} & P_{o22} & \cdots & P_{o2N} \\ \vdots & \vdots & \ddots & \vdots & \vdots & \vdots & \ddots & \vdots \\ P_{oM1} & P_{oM2} & \cdots & P_{oMN} & P_{oM1} & P_{oM2} & \cdots & P_{oMN} \end{array}\right],$$

$$X=\begin{bmatrix} \alpha_1 \\ \alpha_4 \\ \vdots \\ \alpha_N \\ \text{—} \\ \beta_1 \\ \beta_4 \\ \vdots \\ \beta_N \end{bmatrix} \text{ and } B=\begin{bmatrix} I_1 \\ I_2 \\ \vdots \\ I_M \\ \text{—} \\ Q_1 \\ Q_2 \\ \vdots \\ Q_M \end{bmatrix} \qquad (7.32)$$

The system must be solved to obtain demodulation coefficients α_i and β_i. For a five-port receiver, this system of equations is simplified to match the one presented earlier in [13]. As may be seen, the number of equations is greater than unknown parameters. Accordingly, a least squares solution must be implemented to find the unknown coefficients. Therefore, a calibration procedure to solve the least squares solution *X* that minimizes the norm of {*B*-*A***X*} is required. This calibration procedure can be repeated when any change in system or channel has occurred. A real-time calibration method based on the above technique for six-port receiver has been presented in [14].

7.2.4 Six-Port Structure Bandwidth

Several multiport receivers have been developed for microwave and millimeter-wave communications [14, 15]. However, it is important to choose an efficient architecture to provide a suitable performance for a broadband transceiver. Figure 7.7 shows a common six-port structure [15] and various five-port structures [9, 16, and 17].

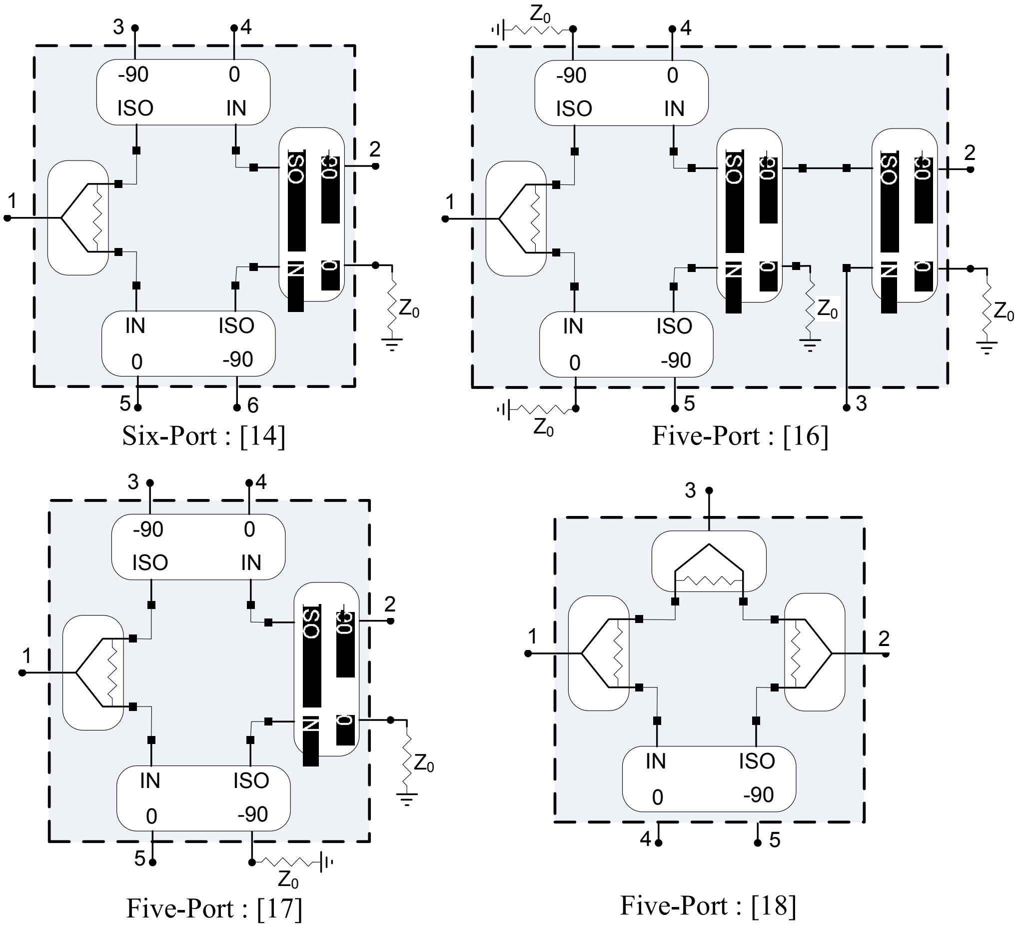

Six-Port : [14]

Five-Port : [16]

Five-Port : [17]

Five-Port : [18]

Figure 7.7 Geometry of some five- or six-port structures.

These structures are implemented from several standard quadrature hybrid couplers and power dividers. To obtain simpler demodulation equations, these circuits are designed in the way that power is divided equally between the output ports for signals that originate from input ports. To compare the presented structures, a simple procedure will be followed. First, the main components of the multiport structures are designed in a desired frequency f_0 (4.5 GHz is selected in this work) and implemented with transmission lines to obtain complete structure. Then the S-parameter of each structure is obtained from RF simulations.

Using these parameters and the characteristics of power detectors, the output powers are calculated for each constellation point (specific I and Q) in a QAM modulation scheme. By known values of I, Q, and P_{oi}, the linear system of equations in (7.2) can be solved to obtain the demodulation coefficients α_i and β_i. Then, the circuit is investigated in the different frequencies and the average of error vector magnitudes (EVM) in QAM constellation points are calculated for various structures. The EVM is calculated using

$$EVM = \frac{\sqrt{(I' - I)^2 + (Q' - Q)^2}}{\sqrt{I^2 + Q^2}} \tag{7.33}$$

where I' and Q' are demodulated values which are calculated by (7.2), using the demodulation coefficients from the previous step and output powers for I and Q in new operational frequencies.

Figure 7.8 shows an average EVM for various structures in a frequency band of $0.8f_0$ to $1.2f_0$. The demodulation coefficients have been calculated for f_0. As may be seen, the EVM for all structures is equal to the expected value of zero at f_0. As may be seen, the smaller and larger bandwidths are obtained from five-port structures presented in [9] and [17], respectively. The six-port circuit of [15] supports a smaller bandwidth than the five-port circuit of [17].

7.3 SIX-PORT IN SOFTWARE RADIO APPLICATIONS

Due to various wireless communication standards, achieving a multi-mode and multistandard receiver is desirable. Such receivers must satisfy the requirements to have broadband or multi-band RF stages, to have low cost, size, and power consumption, and to be compatible with the digital signal processing section. In order to obtain these properties, the RF stage architecture must be chosen properly. It is obvious that the conventional superheterodyne architectures are not suitable solutions for satisfying these requirements because they require to several image rejection filters to eliminate image responses [18].

Moreover, when the receiver switches to another standard, it needs to use a new image rejection filter. This problem can be solved by direct conversion architectures because they have no image response, and thus do not require any image rejection filters. In addition, the direct conversion architectures have more integrated size and lower power consumption than the superheterodyne ones [18].

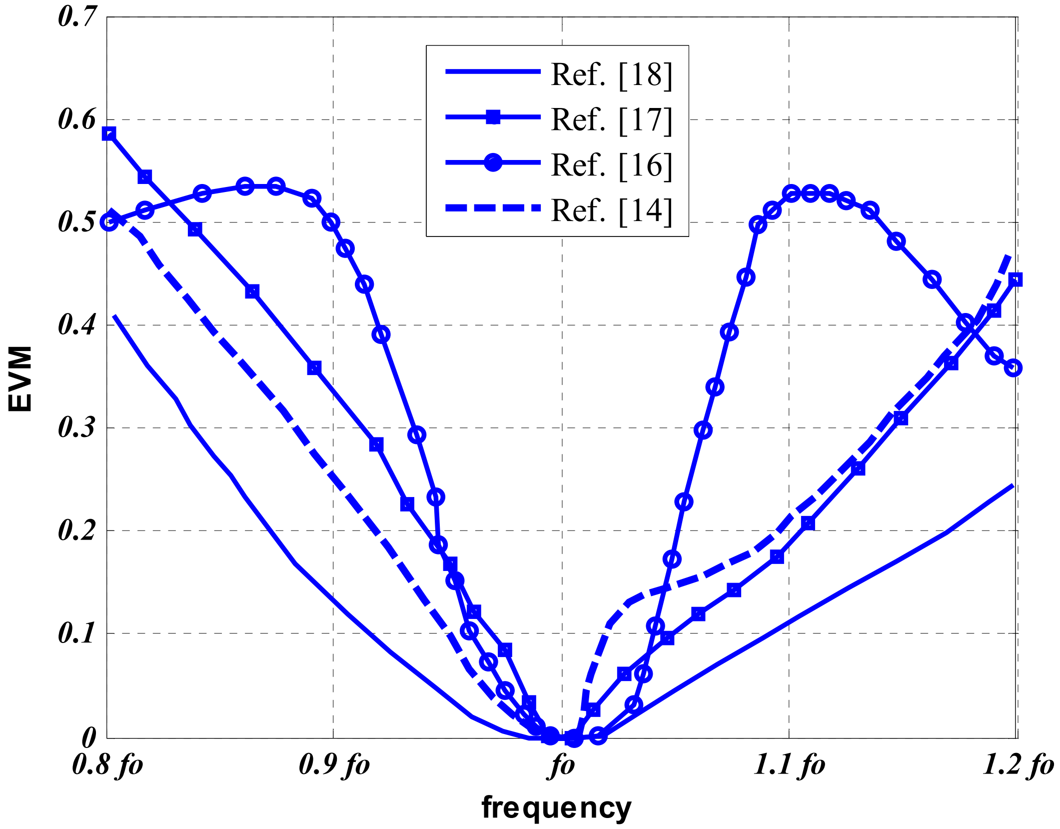

Figure 7.8 Average EVM for various multiport structures.

Software defined radio is the main architecture for future advanced radio systems [19]. A software defined radio (SDR) is a radio in which the operating parameters,including the frequency range, modulation type, and maximum radiated or conducted output power can be altered by making a change in the software without making any hardware changes [20]. The advantages of six-port architecture such as compatibility with DSP, ultra low power consumption, and broadband specifications make it very suitable for software defined radio applications. Figure 7.9(a) shows the structure of a six-port SDR receiver [20, 21].

The RF front-end consists of a low-noise amplifier (LNA), a BPF, a six-port junction, and four power detectors. The six-port junction works as an RF downconverter in the proposed receiver. Port 2 connects to the RF signal and port 1 connects to the local oscillator (LO); the other four ports are connected to RF power detectors. The output voltages of the RF power detectors represent power levels of the four output ports of the six-port circuit. Signals from ports 1 and 2 are directly downconverted from RF to baseband frequency in the form of the output of power detectors. The signals from power detectors are then sent to the DSP section after passing a set of BPFs and baseband amplifiers.

The DSP section is responsible for the baseband signal processing such as demodulation and decoding. The receiver is designed to operate at the microwave frequency and operates over a wideband for multimode schemes. For an SDR receiver platform, the DSP computation algorithms and calibration methods are crucial.

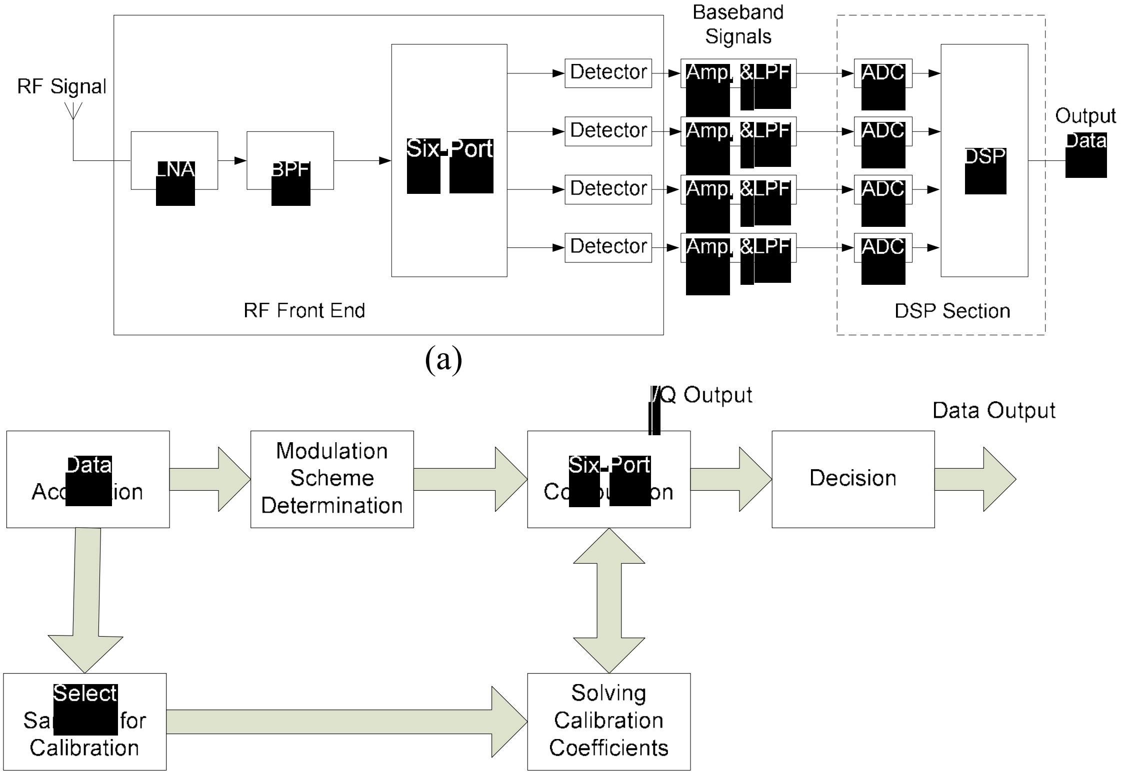

(a)

(b)

Figure 7.9 (a) Architecture of six-port software receiver. (b) Six-port receiver algorithm.

Figure 7.9(b) shows the algorithm flowchart of the SDR six-port receiver [21]. Subsequent to the data acquired from the antenna, some samples are selected for calibration. This six-port calibration provides the coefficients needed for computation to calculate the in-phase and quadrature (I/Q) data. Following a decision algorithm, the signals are then demodulated. This process is a universal demodulation algorithm for six-port receivers. A calibration method free from any external connection must be used. In this receiver platform, a real-time six-port calibration method [14] is adopted and the demodulation results for different modulation schemes are analyzed.

7.3.1 Five-Port Structure in Software Defined Radio Applications

The performance of the five-port structure has been studied as a software radio receiver as well [4]. The center frequency was considered to be 2.4 GHz, and the symbol rate was assumed to be 10 Msymbol/sec. The received signals were investigated with a signal-to-noise ratio (SNR) of 20 dB. The direct-conversion five-port receiver for this application is shown in Figure 7.10(a).

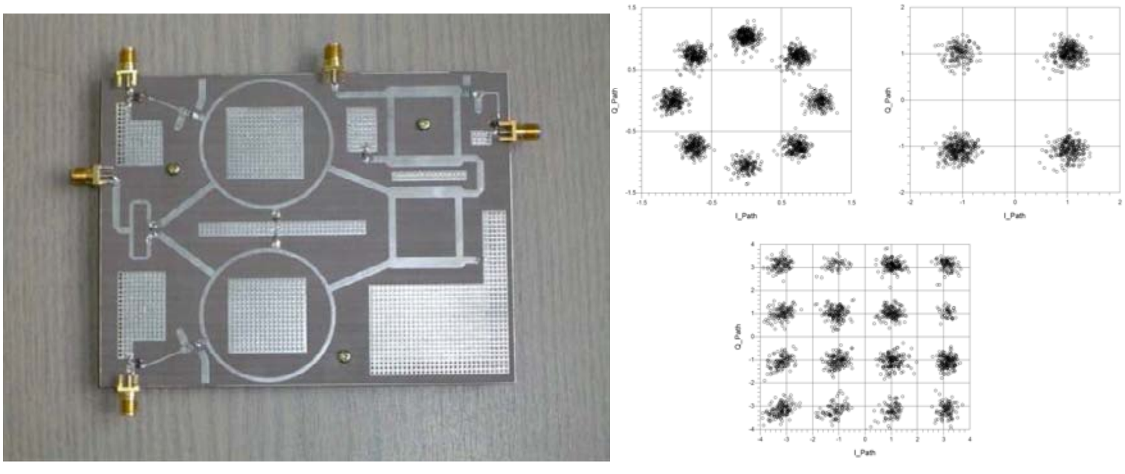

(a) (b)

Figure 7.10 (a) Five-port direct-conversion receiver, and (b) QPSK, 8PSK, and 16QAM constellations using a five-port receiver with SNR = 20 dB.(©2007 IET [16].)

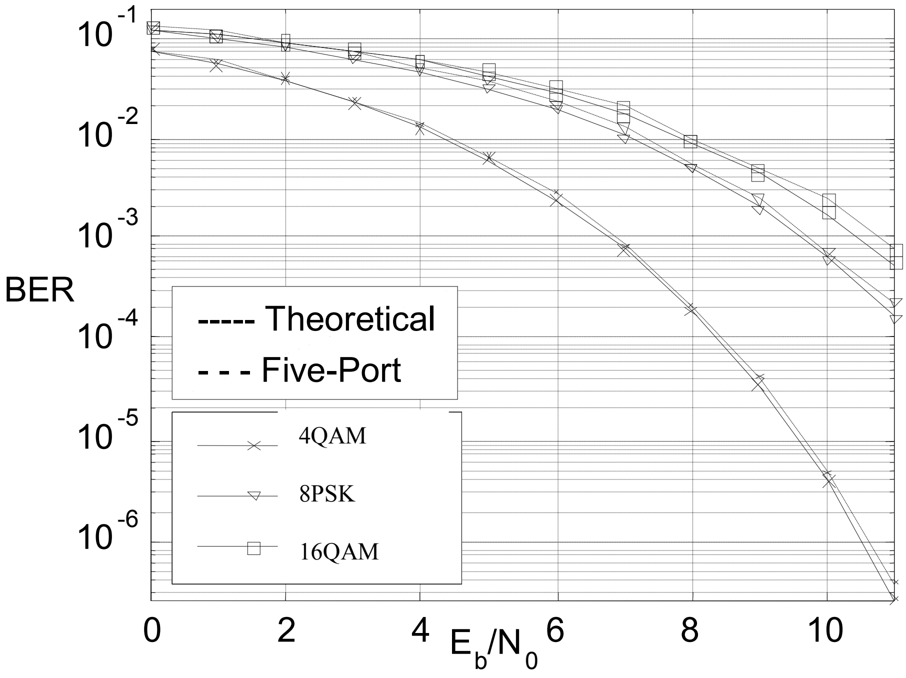

Figure 7.11 BER of QPSK, 8PSK, and 16QAM constellations using a five-port receiver.

The constellation diagrams for various modulation schemes (QPSK, 8PSK, and 16QAM) using the five-port receiver are shown in Figure 7.10(b). The results imply that it is possible to implement the five-port circuit precisely in MQAM and MPSK demodulators, and it can be used as a direct demodulator receiver. Theoretical and simulated BERs versus E_b/N_0 for different modulation schemes (QPSK, 8PSK, and 16QAM) are illustrated in Figure 7.11.

7.4 SIX-PORT IN UWB APPLICATIONS

The recent allowance of frequencies between 3 GHz and 10 GHz for UWB applications would allow higher data throughput up to 500 Mbps over short distances [22]. Apart from high data rates, the other compelling features of UWB would be potentially lower cost and higher levels of integration. Ideal targets for UWB systems are low power, low cost, high data rates, precise positioning capability, and extremely low interference [22, 23]. The common choices of the modulation scheme in UWB communication are pulse position modulation (PPM), pulse amplitude modulation (PAM), and pulse shape modulation (PSM) [24]. The long-term vision for UWB is a low power high-speed standard that provides wireless connectivity for battery operated devices.

Pulse-based systems are one approach for implementing UWB systems to use the UWB bands. A pulse-based system may use a modulated pulse to transfer information. Such systems require RF front-end to support a wideband signal. Therefore, a conventional design technique as well as RF front-end architecture for narrowband applications must be modified and improved to overcome obstacles in implementing RF front-end for emerging wideband applications. Because of the characteristics of the pulse, the RF front-end of such systems tends to be simple, using direct conversion methods. However, processing these extremely wideband signals using an ADC would be quite challenging.

It is important to choose an efficient architecture to provide the suitable performance for a UWB transceiver. The six-port structure is implemented for UWB [18]. This receiver and transmitter architecture uses six-port circuits to digitally modulate and demodulate a full 1-GHz phase spectrum. The six-port impulse radio block diagram is shown in Figure 7.12. Differences between six-port impulse radios and other UWB radios are in the modulation and demodulation schemes including related radio hardware/software/signal processing. It consists of a wideband six-port circuit, a switch matrix, and open and short terminations.

Each component has wideband characteristics. The impulse radio hardware and software for direct modulation and demodulation are experimentally investigated for UWB applications [18]. The radio demonstration platform contained two six-port interferrometers (one for modulation and the other for demodulation), four-channel digital signal processors, four single-pole double throw (SPDT) switches, two antennas (Rx/Tx), and various minor components such as wideband short and open circuit terminations. The radio is designed to operate in wideband channels (over 500 MHz per channel) as required in UWB communication systems.

7.4.1 Six-Port Impulse Radio Modulator

Figure 7.12 shows the six-port impulse radio modulator. The modulator operates as follows: port 1 is fed with a pulse signal, which is routed to ports 3–6 through the different branches of the six-port circuit.

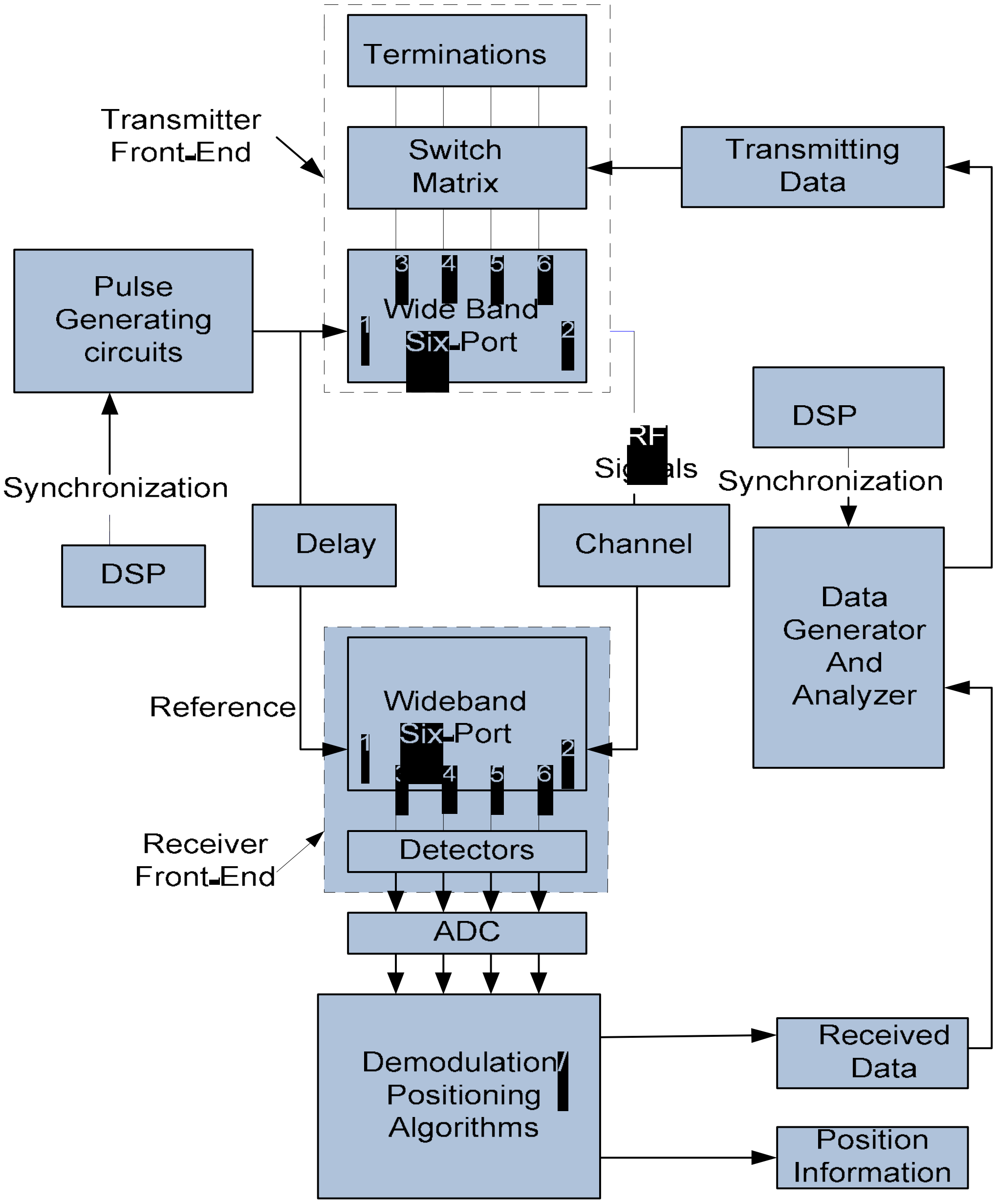

Figure 7.12 The six-port impulse radio test block diagram.(© 2008 IEEE [18].)

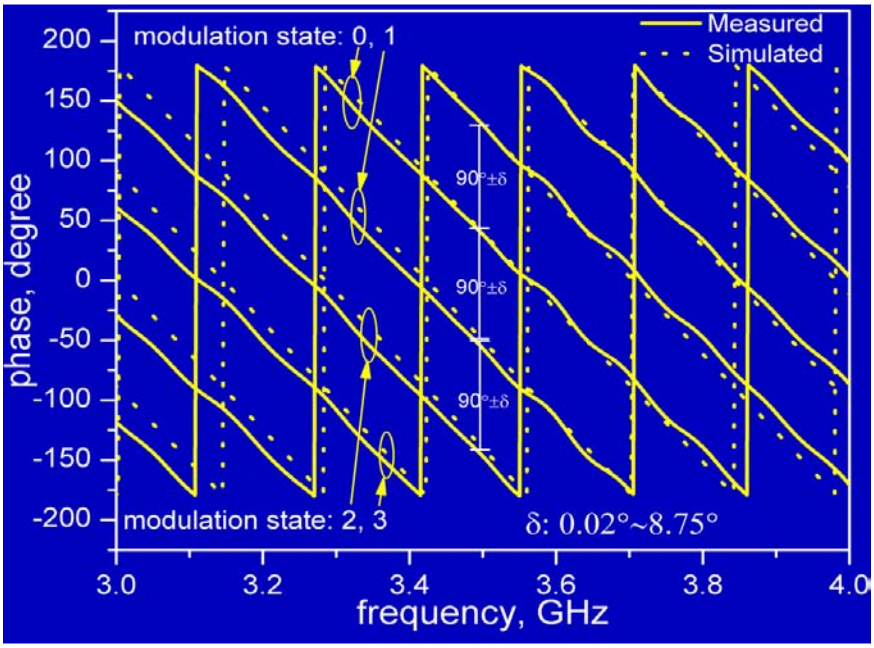

(a)

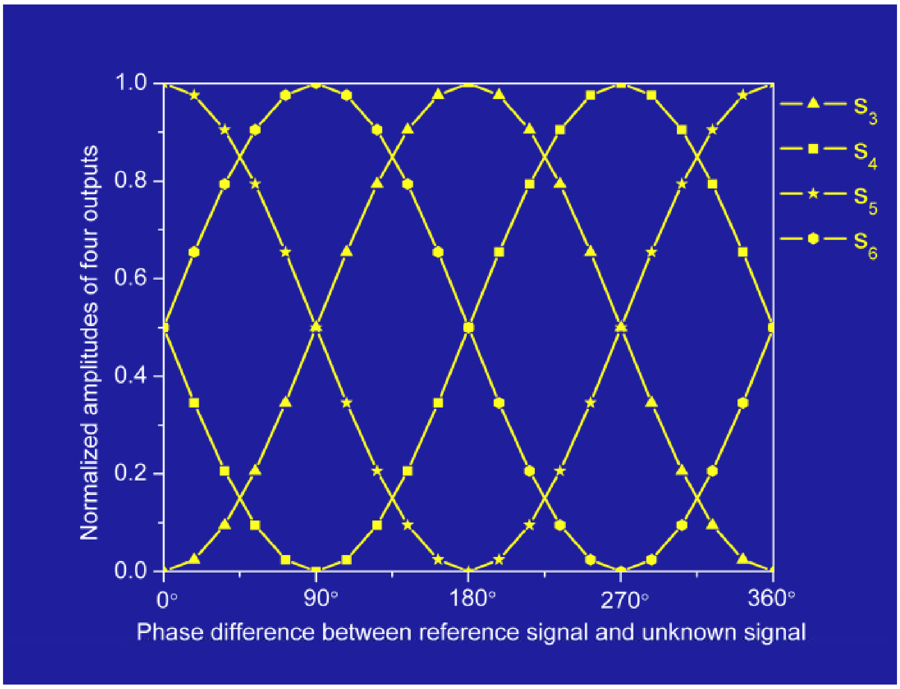

(b)

Figure 7.13 (a) Six-port impulse radio QPSK modulator measurements and simulations from 3 GHz to 4 GHz. (b) Demodulator test results showing normalized output voltages of detectors versus phase difference between two input signals taken at any frequency within the operating channel (3 GHz to 4 GHz).(© 2008 IEEE [18].)

Signals present at ports 3–6 are routed to different terminations by the switch matrix, which is controlled by baseband data. Port 2 outputs the digitally modulated signal, which acquires different phase states depending on the terminations applied at ports 3–6. The six-port circuit used in the modulator is composed of one power divider and three hybrid couplers. Figure 7.13 shows the measured phase changes over a wide operating band for QPSK modulation.

7.4.2 Six-Port Impulse Radio Demodulator

The six-port impulse radio demodulator shown in Figure 7.12 is composed of a six-port circuit using the same structure as the modulator. Ports 1 and 2 are fed with the modulated and reference signals, respectively. Ports 3–6 simultaneously provide four signals to power detectors composed of zero-biased Schottky diodes. Output signals from power detectors are then sampled and fed into a field-programmable gate-array (FPGA) processor for demodulation.

The adoption of the DSP in the proposed six-port impulse radio is for the purpose of increasing the flexibility of the system. Synchronization of reference CW (or pulsed) signals with received signals presents the same challenge in the new radio as in any radio.

7.4.3 Five-Port Receiver in UWB

Figure 7.14(a) shows a receiver circuit using a five-port structure as an RF demodulator. As shown in Figure 7.14(b), the five-port structure has one quadrature hybrid coupler and three Wilkinson power dividers. The five-port circuit needs broadband components in UWB applications. Hence, several sections are required to increase the bandwidth of the circuits. This circuit is designed, optimized, and fabricated for a wide bandwidth from 3 GHz to 6 GHz using the substrate RO 4003 with ε_r=3.38 and H=20 mil. The simulation using the method of moment (MOM) of S-parameters is shown in Figure 7.15.

The simulated return loss at the two input ports and the isolation between the LO port and the RF port are given in Figure 7.15(a). Figure 7.15(b) indicates that the signals from both input ports, LO and RF, are attenuated about 6 dB at the output ports 3 through 5. According to this figure, the isolation and reflection for input ports are at least 15 dB. This five-port structure is used as an RF demodulator. The received SNR=20 dB. The power detector circuit is realized using Schottky detector diodes (HSMS-2852).

The theoretical and simulation results of BER versus E_b/N_0 are compared in Figure 7.16. As may be seen, the simulation curve fits very well with the theoretical values.

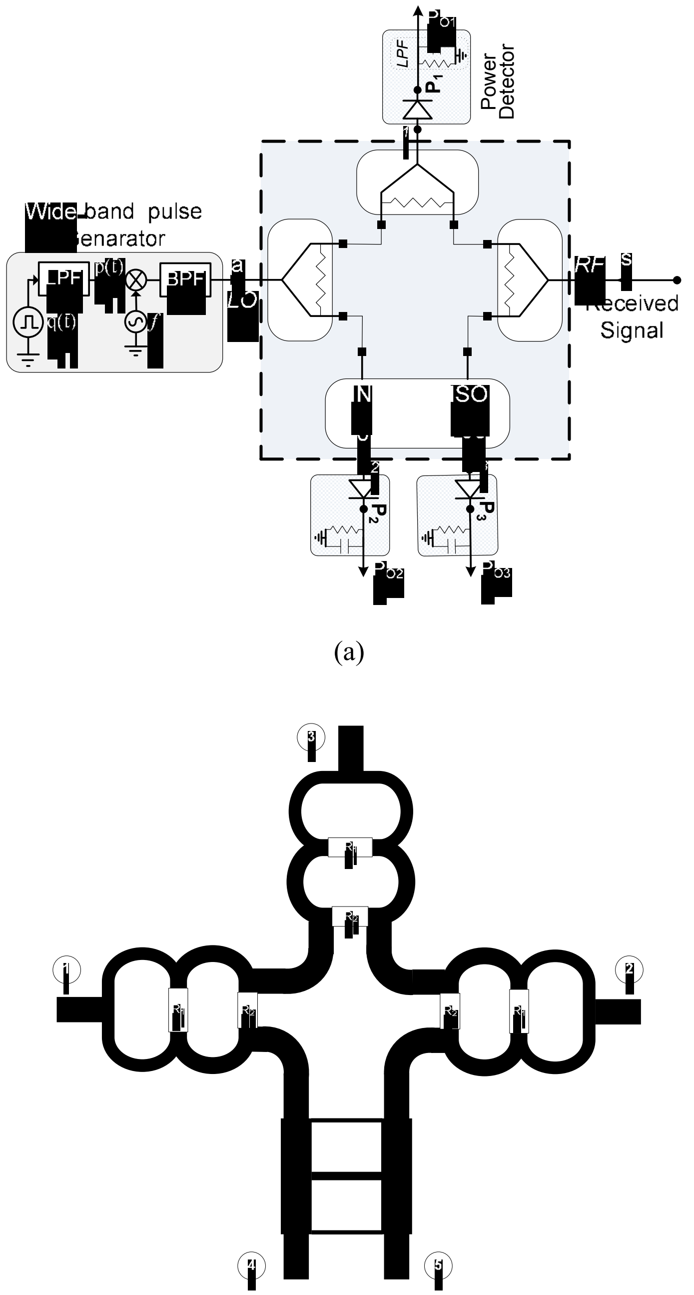

(a)

(b)

Figure 7.14 A five-port UWB receiver. (a) Functional block diagram. (b) The microstrip layout.

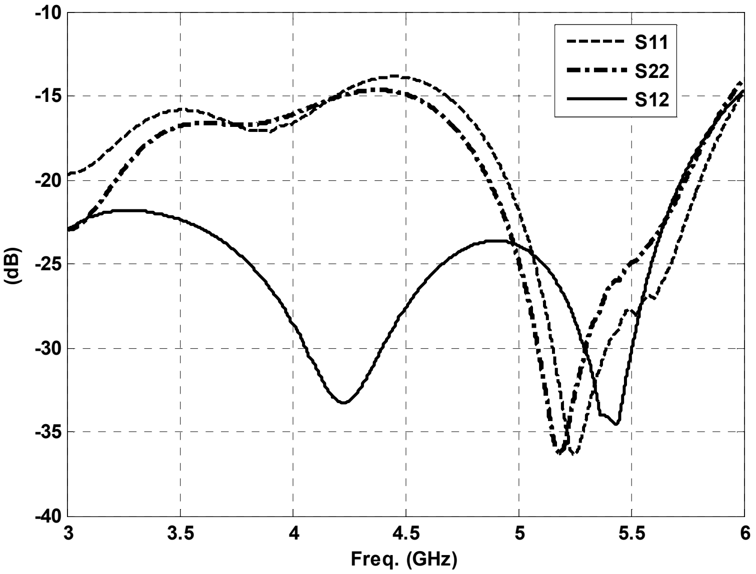

(a)

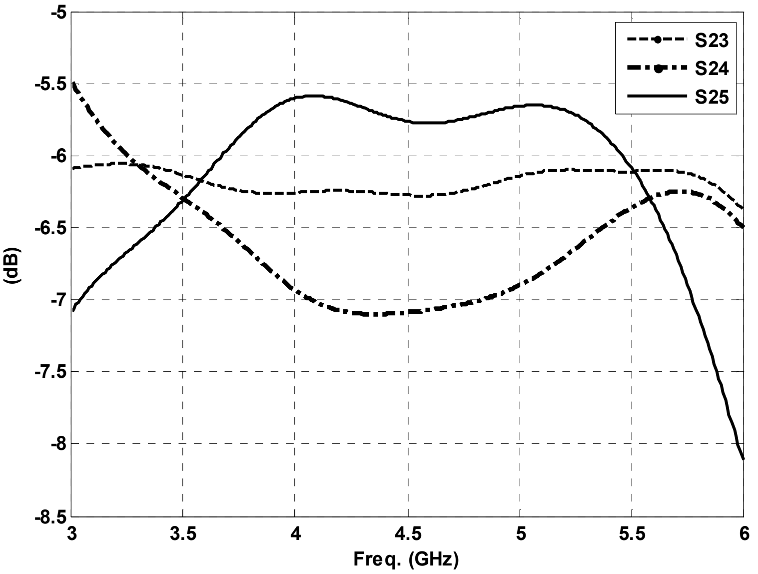

(b)

Figure 7.15 A five-port UWB receiver. (a) Reflection coefficients and isolation for the input port. (b) Transmission coefficients from the input to the output port.

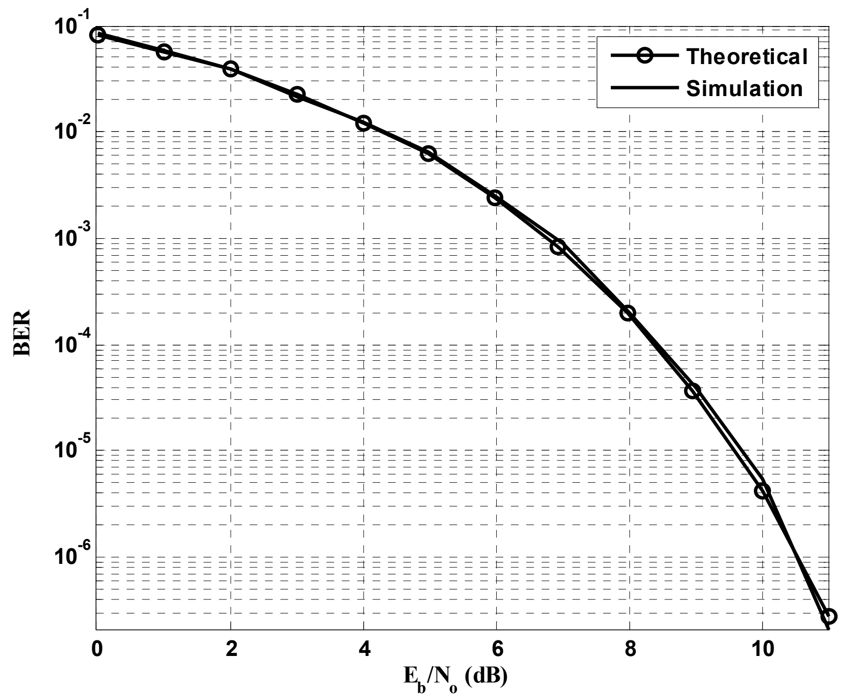

Figure 7.16 Comparison between theoretical and simulated BER in a five-port UWB receiver.

7.5 SIX-PORT IN MILLIMETER-WAVE RADIOS

It has already been shown that six-port architecture can be used effectively in millimeter-wave frequencies [25-27]. Moreover, the five-port architecture has been used successfully in millimeter-wave applications [16]. Figure 7.17 shows the microstrip layout of the fabricated Ka-band five-port structure and its baseband section. The accuracy of the transmission lines was ±50 μm; accordingly, this uncertainty led to some changes in the S-parameters. Therefore, imbalances in the transmissions' magnitude and phase may occur, which can easily be removed with the calibration of multiport receivers [16, 21, 28].

Figure 7.18(a) presents the measured isolation between input ports and the transmission from input ports to output ports. The two input ports were well isolated, showing an isolation of greater than 20 dB from 23 GHz through 29 GHz between the LO and RF ports.

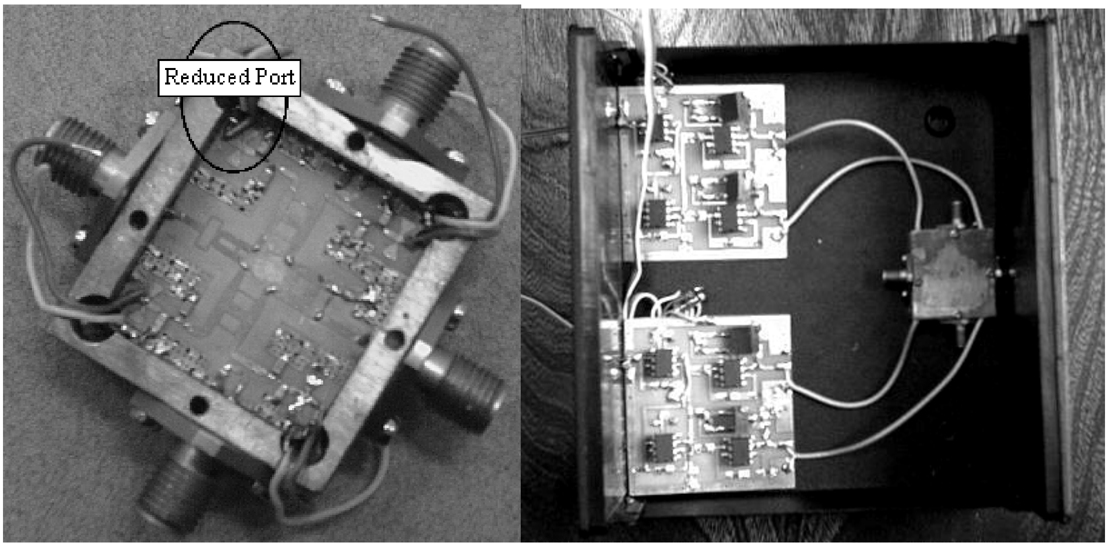

Figure 7.17 A Ka-band receiver fabricated using a microstrip line. (© 2009 IET [16].)

These measurement results indicate an attenuation of approximately 10 dB. Figure 7.18(b) also shows the absolute measured phase shift from the input ports to ports 3 and 4. The desired 180° phase difference between RF signals at ports 3 and port 4 was achieved, and the LO signal had the same phase shift at two output ports. Finally, the circuit was tested as a direct demodulator of a 2 Mbit/s QPSK modulated signal.

The RF and LO input levels were set to -20 dBm at center frequency. The I and Q signals were obtained using an electric circuit shown in Figure 7.18(c). Using the XY display of the oscilloscope, the *I/Q* constellation can be achieved from analog output signals, as shown. The demodulated QPSK signal confirmed the accuracy of the five-port receiver in millimeter-wave applications.

A six-port transceiver has been implemented using CMOS technology in 60 GHz [26]. The target is to provide a very low-cost, miniaturized, and low DC power consumption transceiver for IEEE 802.15 applications. The transmitter is composed of a reflection-type *I/Q* modulator and a buffer amplifier, while the receiver consists of an LNA and a six-port demodulator.

An on-chip VCO provides the LO signals for the transmitter and receiver and an SPDT switch is used to select the transmitting or receiving path. This block diagram of the transceiver and its chip photo are shown in Figure 7.19. The total DC power consumption of the transceiver is less than 100 mW.

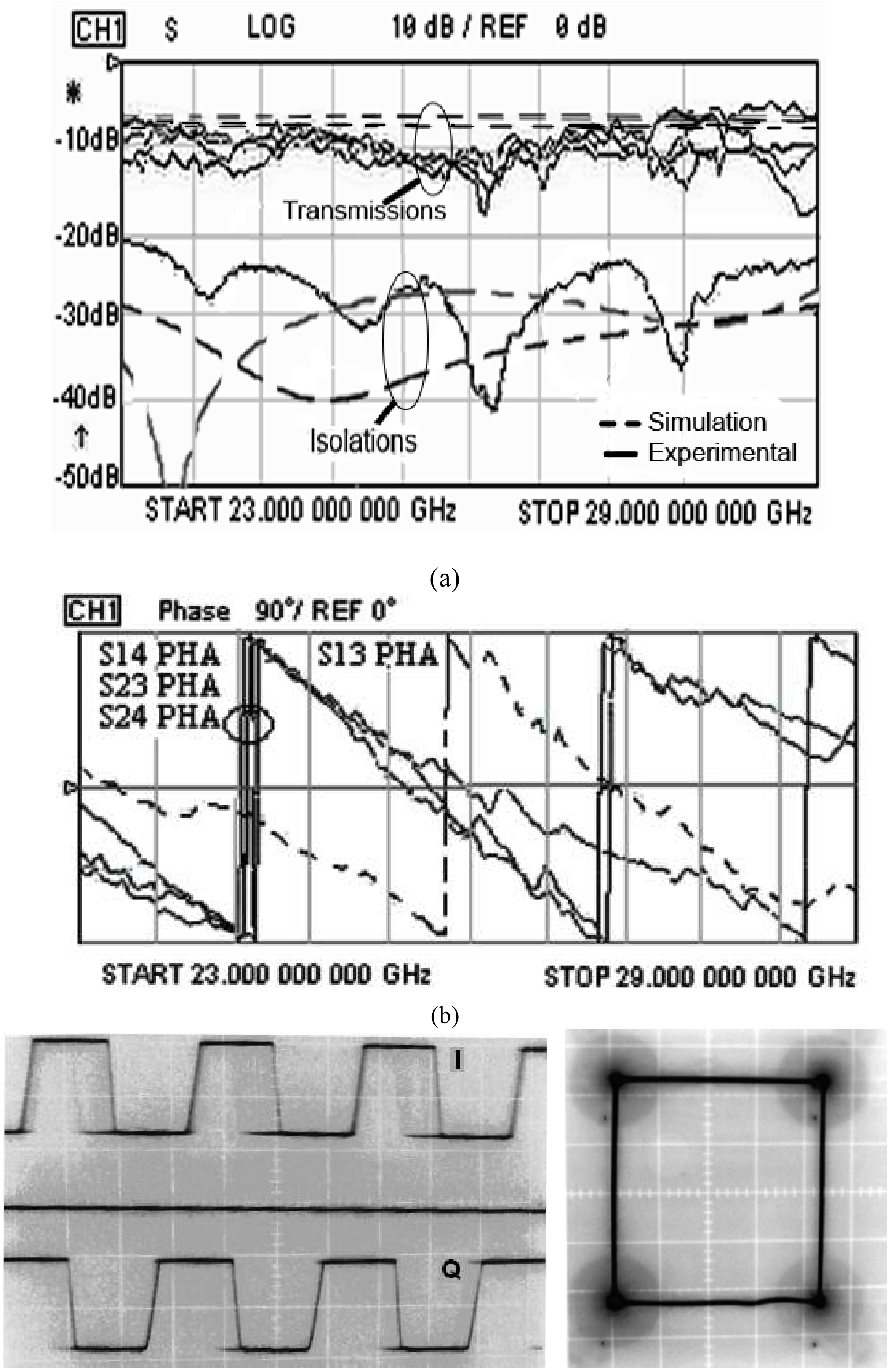

(a)

(b)

(c)

Figure 7.18 (a) The Ka-band receiver, (b) the measured values for transmission and isolation for the Ka band five-port receiver, and (c) The constellation diagram for demodulated I and Q signals of QPSK modulation.(© IET 2009 [16].)

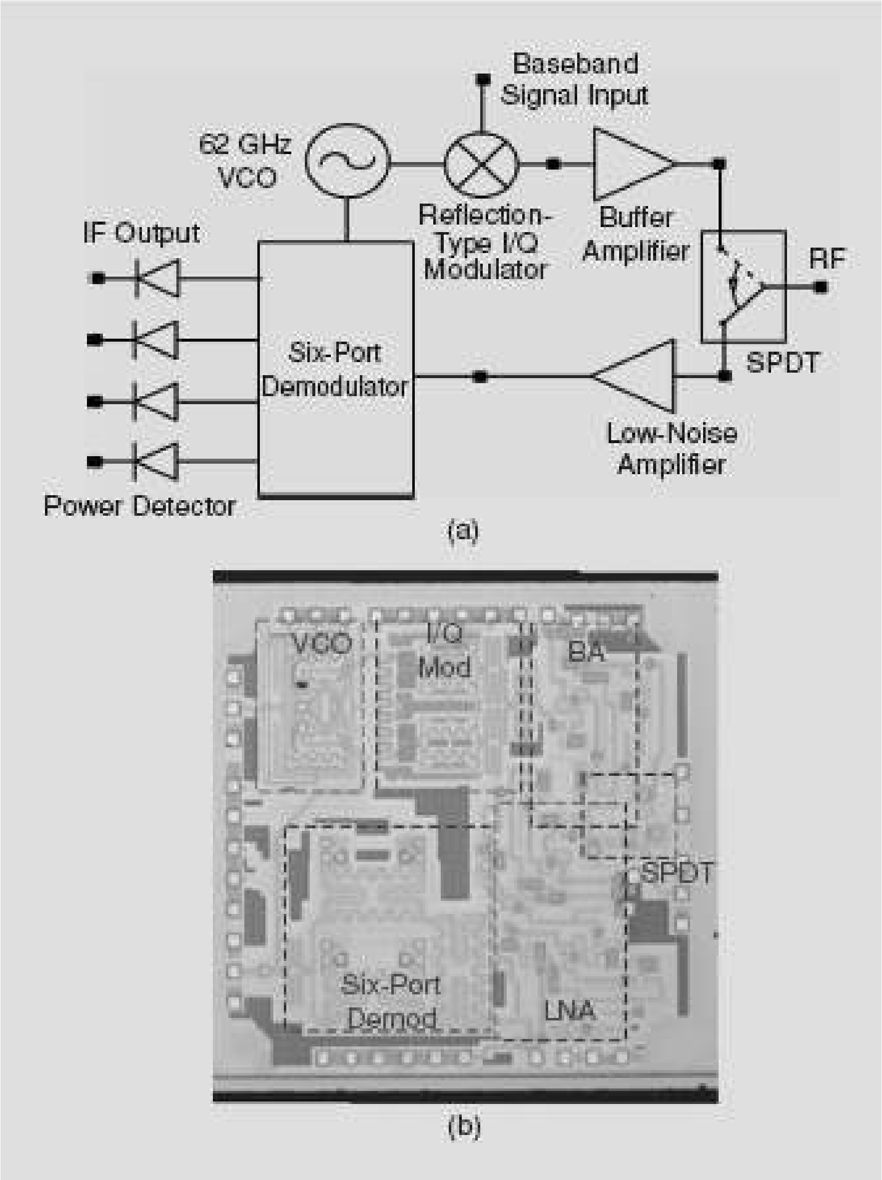

Figure 7.19 (a) Block diagram and (b) chip photo of the 60-GHz CMOS six-port transceiver. The transmitter is composed of a reflection-type I/Q modulator and a buffer amplifier while the receiver consists of an LNA and a six-port demodulator. An on-chip VCO provides the LO signals for the transmitter and receiver and an SPDT switch is used to select the transmitting or receiving path. (© 2009 IEEE [26].)

7.6 COMPARISON BETWEEN SIX-PORT AND CONVENTIONAL RECEIVERS

Six-port microwave receivers push the boundaries regarding price and the upper frequency limit. To enable a serious validation of the six-port technology, we have to benchmark it with existing receiver architectures [27]. This section compares the six-port receiver with conventional receivers [27, 29].

7.6.1 RF Performance

Phase Accuracy

In a conventional receiver, the phase noise of the local oscillator (LO) will be directly transformed to the phase noise in the baseband. This will lead to neighbor channel interference, caused by reciprocal mixing, and therefore reduce the selectivity of the receiver. In the six-port receiver, as in the direct conversion receiver, additional phase inaccuracy will be introduced. Because of this unavoidable phase imbalance, phase distortion can be generated. However, phase distortion can be reduced by performing an accurate calibration.

Noise Figure

The noise figure is usually defined by the LNA in a receiver. If no LNA is used, we have to compare the noise of a mixer to the noise of a power detector receiver. For frequencies beyond 50 GHz, both are usually built up using Schottky diodes. The noise figure for diode mixers is comparable to its conversion loss which is typically about 7 dB. Simulations on microwave power detectors using a beam lead GaAs Schottky diode have shown that the noise figure goes down to 4.8 dB for input powers smaller than -20 dBm.

LO Power

For most mixers to obtain a good conversion gain, the power of the local oscillator should be in the range of 0 to 10 dBm [30]. On the other hand, a suitable condition for six-port receivers is an LO power in the area of the receiver input power which is much lower in practical applications (less that -20 dBm).

In-Band Dynamic Range

For six-port receivers this dynamic range is mainly limited by the accuracy of the calibration and the detector sensitivity. First trials have shown a dynamic range of 40 dB [31, 32]. Calibration will also limit the linearity of the receiver. For mixer-based receivers the dynamic range is limited by the linearity. This results in a dynamic range of about 90 to 100 dB for a signal bandwidth of 10 MHz. The dynamic range of the receiver can also be increased well above 70 dB with an AGC inserted within the LNA [33].

Self Mixing Effects

Direct coupling and external reflections lead to a DC offset for a direct conversion receiver and a six-port receiver. Direct conversion receivers usually contain some signal processing unit to cope with this effect. It was recently shown that six-port receivers are less sensitive to DC offset in comparison to subharmonically pumped direct conversion receivers [29].

7.6.2 Boundary Limitations

Size

The size of mixer-based architectures is mainly given by active components and filters. The usual setup of a six-port is about ¾ λ in square. For V-, W-, and D-band applications it is very possible to integrate the six-port on a chip.

Cost

The cost of a direct conversion receiver depends very much on the frequency range. Especially for frequencies in the W- and D-bands, mixers become rare and expensive, whereas power detectors are available for higher frequencies. For millimeter-wave signal generation usually a lower frequency LO is followed by a frequency multiplier, which produces a small LO power. The six-port receiver will have a cost advantage by reduced LO power requirements.

In conclusion, six-port receivers are a suitable and cost-effective alternative to existing mixer-based receiver architectures, especially in the millimeter-wave and sub-millimeter-wave range. In this frequency range we usually do not have to cope with strong neighbor channel interference, so the reduced dynamic range will be acceptable. Moreover, it has recently been shown that the six-port receiver architecture is less sensitive to LO power variations and phase errors than the antiparallel diode receivers [29].

7.7 SIX-PORT IN PHASED-ARRAY SYSTEMS

Six-port junctions have been primarily used as reflectometers [34, 35], that is, to measure the reflected-to-incident waves ratio at one port of the junction. Alternatively, one can measure the complex ratio of incident waves at two different ports of the junction [36, 37]. In the case of a linear array, the array factor can be fully determined if the signals radiated by the elements are related to each other by complex ratios. These ratios depend on the feed network but also on the coupling between the array elements. This is represented as a coupling network box in Figure 7.20. Let us assume that all the active elements have the same radiation pattern and that waves a_1 and a_2 are not reflected back to the antenna. The goal herein is to determine the ratio a_1/a_2 from the power readings. If we can determine this ratio for all the element pairs of the array, it will be possible to calculate the array factor. To illustrate the procedure, let us consider the two-branch network of Figure 7.20 where waves a_1 and a_2 are absorbed by matched terminations. Using the superposition of sources, we can write:

$$a_i = M_i b_7 + N_i b_8, i = 1, 2, \ldots, 6 \tag{7.34}$$

From (7.34) with $i = 1$ and $i = 2$, we have:

$$\begin{aligned} b_7 &= (a_1 N_2 - a_2 N_1)/(M_1 N_2 - N_1 M_2) \\ b_8 &= (a_1 M_1 - a_1 M_2)/(M_1 N_2 - N_1 M_2) \end{aligned}$$

Using these expressions for b and b_s, (7.34) can be rewritten as

$$a_i = P_i a_1 + Q_i a_2, i = 3, \ldots, 6 \tag{7.35}$$

Equation (7.35) has the classic form of six-port relations [36]. It relates the incident signals on the power detectors to the waves radiated by elements 1 and 2. Using (7.35), it is easy to implement the calibration technique for six-port reflectometers given in [18] or [38] by replacing the unknown reflection coefficient (b_2/a_2) by the ratio of interest, namely a_2/a_1. The remaining difficulty is the establishment of accurate a_1/a_2 ratios to be used as standards in the calibration.

In the case of an antenna array, the a_n values used in the calibration of the junctions embedded between each pair of elements can be determined by measuring the radiation pattern of the array. For an N-element linear array, we can write the following expression for the θ-component of the radiated far-field $E(\theta, r)$ in the XZ plane:

$$E(\theta, r) = K(\theta) \frac{e^{-j\beta r}}{r} \sum_{n=1}^{N} a_n e^{j\beta n d \sin\theta} \tag{7.36}$$

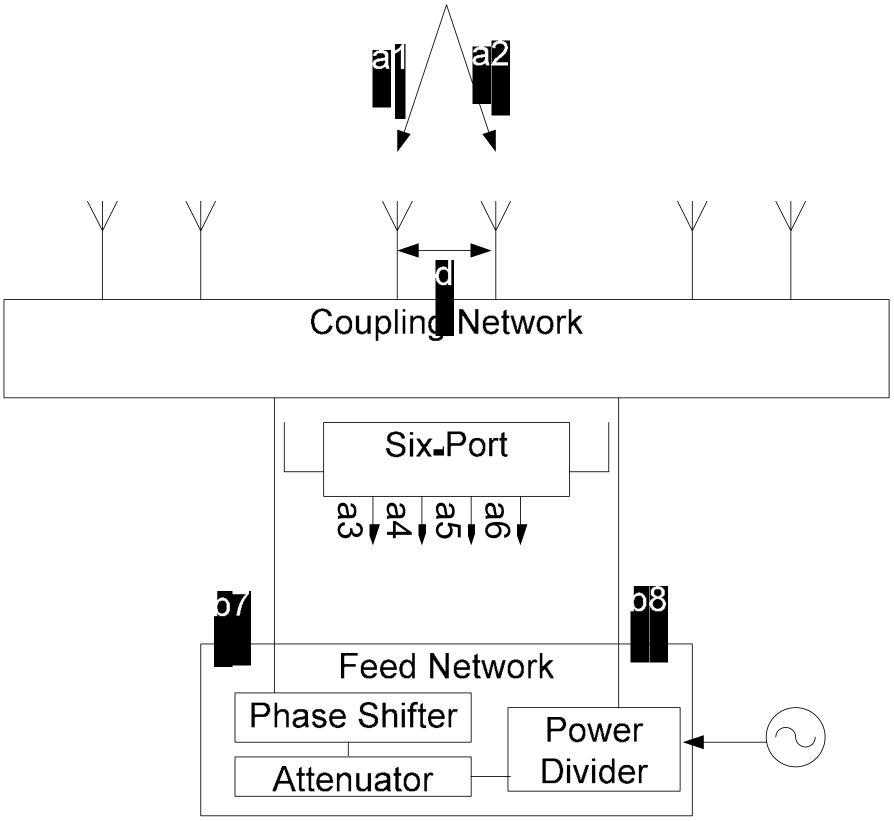

Figure 7.20 Six-port in phased-array systems.

where $K(\theta)$ includes all the constants and the array-element factor. $K(\theta)$ can be measured by feeding only one element of the array. When all the active elements are fed simultaneously, we can measure $E(\theta, r)$ for N different values of angle θ and build a system of N linear equations. This system can then be solved to give one set of a_ns. All the data necessary to calibrate the N-1 six-port junctions can be obtained from four far-field pattern measurements [39]. In a phased array, we arbitrarily choose four different settings of the phase shifters. For each setting, both the phase and magnitude patterns of the array are measured and the $[a_n]$ vectors are determined by solving the linear system of equations. The power readings of the six-port junctions are also recorded. This data can then be used to calibrate each one of the junctions with the procedure given in [29]. Once the junctions are calibrated, all the a_i values can be related to each other for any state of the feed network since the six-port measurements can be used to calculate the ratio of each pair of adjacent signals. This allows a real-time determination of the array factor [40, 41].

References

[1] Zhao, Y., C. Viereck, J. F. Frigon, R. G. Bosisio, and K. Wu, “Direct Quadrature Phase Shift Keying Modulator Using Six-Port Technology,” *Electronics Letters*, Vol. 41, No. 21, pp. 1180–1181, October. 2005

[2] Lou, B., and M.Y. Chia, “Direct Quadrature 16QAM Six-Port Modulator,” *Electronics Letters*, Vol. 44, No. 15, July 2008.

[3] Boulajfen, N., F. M. Ghannouchi, and A. B. Kouki, “A Homodyne Multiport Network Analyzer for S-Parameter Measurements of Microwave N-port Circuits/Systems,” *Microwave Opt. Technol. Lett.*, Vol. 24, No. 1, pp. 63–67, January 2000.

[4] Mohajer, M., A. Mohammadi, and A. Abdipour, “Direct Conversion Receivers Using Multi-Port Structures for Software Defined Radio Systems,” *IET Microwaves, Antennas & Propagation,* 2007, Vol. 1, No.2, pp. 363–372*,* April 2007.

[5] Tatu, S. O., K. Wu, and T. Denidni, “Multi-Band Multi-Port Direct Conversion Receiver: Design, Implementation and Demodulation Results,” *Microwave and Optical Technology Letter*, Vol. 48, No. 4, pp. 817–822, April 2006.

[6] Hoer, C. A., and K. C. Roe, “Using an Arbitrary Six-Port Junction to Measure Complex Voltage Ratios,” *IEEE Trans. Microwave Theory & Tech.,* Vol. MTT-23, pp. 978–984, December 1975.

[7] Mohajer, M., and A. Mohammadi, “A Novel Architecture for Six-Port Direct Conversion Receiver,” *IEEE PIMRC 2004,* Vol .4, pp. 2705–2709, September 2004.

[8] Buracchini, E., “The Software Radio Concept,” *IEEE Communication Magazine,* Vol. 38, pp. 138–143*,* September 2000.

[9] Mohajer, M., A. Mohammadi, and A. Abdipour, “A Software Defined Radio Direct Conversion Receiver,” *European Microwave Conference, EUMC 2005,* Vol. 3, pp. 1823–1826, 2005.

[10] Huang, X., D., Hindson, M., de Leseleuc, and M., Caron., “I/Q-Channel Regeneration in 5-Port Junction Based Direct Receivers,” *IEEE MTT-S 1999*, pp. 169–173, February 21-24, 1999.

[11] Cho, Y. H., B. W. Kim, and D. J. Park, “ I/Q Regeneration Algorithm for Direct Conversion Receiver Using 5-Port Junction,” *2006 8th International Conference on Signal Processing*, November 2006.

[12] Hentschel, T., “A Simple IQ-Regeneration Technique for Six-Port Communication Receivers,” *First International Symposium on Control, Communications and Signal Processing,* pp. 311–314, 2004.

[13] Neveux, G., B. Huyart, and G. J. Rodriguez-Guisantes, “Wide-Band RF Receiver Using the Five-Port Technology,” *IEEE Transactions on Vehicular Technology*, Vol. 53, No. 5, September 2004.

[14] Y. Xu, and R. G. Bosisio, “On the Real-Time Calibration of Six-Port Receivers (SPRs),” *Microwave and Optical Technology Letters*, Vol. 20, No. 5, March 5, 1999.

[15] Zhao, Y., J .F. Frigon, K. Wu, and R. G. Bosisio, “Multi(Six)-Port Impulse Radio for Ultra-Wideband,” *IEEE Trans. Microwave Theory & Tech*., Vol. 54, No. 4, June 2006, pp. 1707–1712.

[16] Mirzavand, R., A. Mohammadi, and A. Abdipour, “Low-cost Implementation of Broadband Microwave Receiver in Ka Band Using Multi-Port Structures,” *IET Microwaves, Antennas & Propagation,* Vol. 3, No. 3, pp. 483–491, 2009.

[17] Mirzavand, R., A. Mohammadi, and A. Abdipour, "Five-Port Transceiver for WiMAX Applications," *17th International Conference on Microwaves, Radar and Wireless* Communications *MIKON*, Wroclaw, Poland, pp. 19–21 May 2008.

[18] Bosisio, R. G., Y. Y. Zhao, X. Y. Xu, S. Abielmona, E. Moldovan, Y. S. Xu, M. Bozzi, S. O. Tatu, J. F. Frigon, C. Caloz, and K. Wu, "New-Wave Radio," *IEEE Microwave Magazine,* pp. 89–100, February 2008.

[19] Ghannouchi, F. M., "Software Defined Radio Transmitters for Advanced Wireless and Satellite Communications Systems," *Microwave Journal*, Vol. 51, No. 5, pp. 202–216, May 2008.

[20] Chang, K., *Encyclopedia of RF and Microwave Engineering*, New York: Wiley, 2005.

[21] Xu, X., R. G. Bosisio, and K. Wu, "Analysis and Implementation of Six-Port Software-Defined Radio Receiver Platform," *IEEE Trans. Microwave Theory & Tech.*, Vol. 54, No. 7, 2006, pp. 2937–2943.

[22] Yang, L., and G.B. Giannakis, "Ultra-Wideband Communications: an Idea Whose Time Has Come," *IEEE Signal Processing Magazine*, Vol. 21, No. 6, pp. 26–54, November 2004.

[23] Bellorado, J., S. S. Ghassemzadeh, L. J. Greenstein, T. Sveinsson, and V. Tarokh, "Coexistence of Ultra-Wideband Systems with IEEE 802-11a Wireless LANs," *IEEE Global Telecommunications Conference*, Vol. 1, pp. 410–414, December 2003.

[24] Da Silva, J. A. N., and M. L. R. de Campos, "Performance Comparison of Binary and Quaternary UWB Modulation Schemes," *Proc. IEEE GLOBECOM Conf.*, San Francisco, CA, 2003, pp. 789–793.

[25] Li, J., R. G. Bosisio, and K. Wu, "Computer and Measurement Simulation of a New Digital Receiver Operating Directly at Millimeter Wave Frequencies," *IEEE Trans. Microwave Theory Tech.*, Vol. 43, No. 12, pp. 2766–2772, December 1995..

[26] Wang, H., K. Lin, Z. Tsai, L. Lu, H. Lu, C. Wang, J. Tsai, T. Huang, and Y. Lin, "MMICs in the Millimeter-Wave Regime," *IEEE Microwave Magazine,* pp. 99–117, February 2009.

[27] Eireiner, T., and T. Müller, "Six-Port Receiver for mm-Wave – Concept, Evaluation and Implementation," *IEEE MELECON 2006*, Benalmádena (Málaga), Spain, May 16-19, 2006.

[28] Ghannouchi, F. M., and R. G. Bosisio, "An Alternative Explicit Six Port Matrix Calibration Formalism Using Five Standards," *IEEE Trans. MTT*, Vol. 36, No. 3, pp. 494−498, 1988.

[29] Khaddaj Mallat, N., E. Moldovan, and S. O. Tatu, "Comparative Demodulation Results for Six-Port and Conventional 60 GHz Direct Conversion Receivers," *Progress in Electromagnetics Research, PIER,* Vol. 84, pp. 437–449, 2008.

[30] Hewlett Packard, "The Schottky Diode Mixer," Application Note 995.

[31] Jürgensen, J.-U., D. Krupezevic, M. Ratni, and Z. Wang, "Baseband Aspects of a Direct Conversion Receiver Concept Using Five-Port Technology," *2nd Karlsruhe Workshop on Software Radio*, Karlsruhe, March 2002.

[32] Demers, Y., R. G. Bosisio, and F. M. Ghannouchi, "Repetitive and Single Shot Pulse Microwave Six-Port Reflectometer," *IEEE Trans. on Instrument and Measurement*, No.1. February 1990.

[33] Tatu, S. O., E. Moldovan, K. Wu, and R. G. Bosisio, "A New Direct Millimeter-Wave Six-Port Receiver," *IEEE Trans. Microwave Theory & Tech.*, Vol. 49, No.12, pp. 2517–2524, December 2001.

[34] Engen, G. F., "The Six-Port Reflectometer: an Alternative Network Analyzer," *IEEE Trans. Microwave Theory Tech.*, Vol. MTT-25, pp. 1075–1080, December 1977.

[35] Engen, G. F., "An Improved Circuit for Implementing the Six-Port Technique of Microwave Measurements," *IEEE* Trans. *Microwave Theory Tech.,* Vol. MTI-25, pp. 1080–1083, December 1977.

[36] Cronson, H. M., "A Six-Port Automatic Network Analyzer," *IEEE Trans. Microwave Theory Tech.,* Vol. MTT-25, pp. 1086–1091, December 1977.

[37] Kamarei, M., "Vector Voltmeter Applications for Microwave Imaging," *Microwave Journal*, Vol. 34, pp. 102–114, November 1991.

[38] Hodgetts, T. E., and E. J. Griffin, "A Unified Treatment of the Theory of Six-Port Reflectometer Using the Minimum of Standards," *Tech. Report 83003, Royal Signals and Radar Establishment,* Malvern, U.K., 1983.

[39] Laurin, J-J., R. G. Bosisio, F. M. Ghannouchi, "Calibration of a Monitoring System for Antenna Arrays Based on Six-port Junctions," *1992 IEEE Antennas and Propagation International Symposium,* Chicago, IL, pp. 458–461, 1992.

[40] Cassivi, Y., F. M. Ghannouchi, and R. G. Bosisio, "Six-Port Junctions in a Phased Array Antenna for Accurate Beam Steering," 1992 *IEEE Antennas and Propagation International Symposium,* Chicago, IL, pp. 462–466, 1992.

[41] Ghannouchi, F. M., A. B. Kouki, and A. Khebir, "On the Experimental Characterization of Electromagnetic Emissions from Printed Circuit Board," *1993 IEEE AP-S International Symposium*, Ann Arbor, MI, pp. 1490–1493, 1993.

Chapter 8

Six-Port Microwave Applications

The six-port architecture has found many applications in microwave systems. These applications include reflectometer, directional finder, radar, antenna measurement, and material characterization. Moreover, there have recently been some applications using the six-port architecture in optical systems. In this chapter, we present the theoretical issues and implementation techniques for using the six-port in different microwave systems.

8.1 SIX-PORT MICROWAVE REFLECTOMETER

The six-port junction is commonly used as a reflectometer. Moreover, it can be used in very high power microwave applications by the use of a hybrid directional coupler.

8.1.1 Six-Port Reflectometer

The schematic of a six-port reflectometer for measuring the complex reflection coefficient of a load (DUT) is shown in Figure 8.1. The setup is comprised of a fixed frequency sinusoidal source, the passive six-port junction, and four power meters. As discussed in previous chapters, the six-port theory establishes that the complex reflection coefficient of the load, at frequency f_0, can be precisely determined, after calibration, from the four readings of the power meters.

In addition, if measurement in a certain frequency range is needed, the frequency of the source would have to be changed. For any linear passive six-port junction, as in Figure 8.1, the incident waves on the four power meters can be calculated as [1]

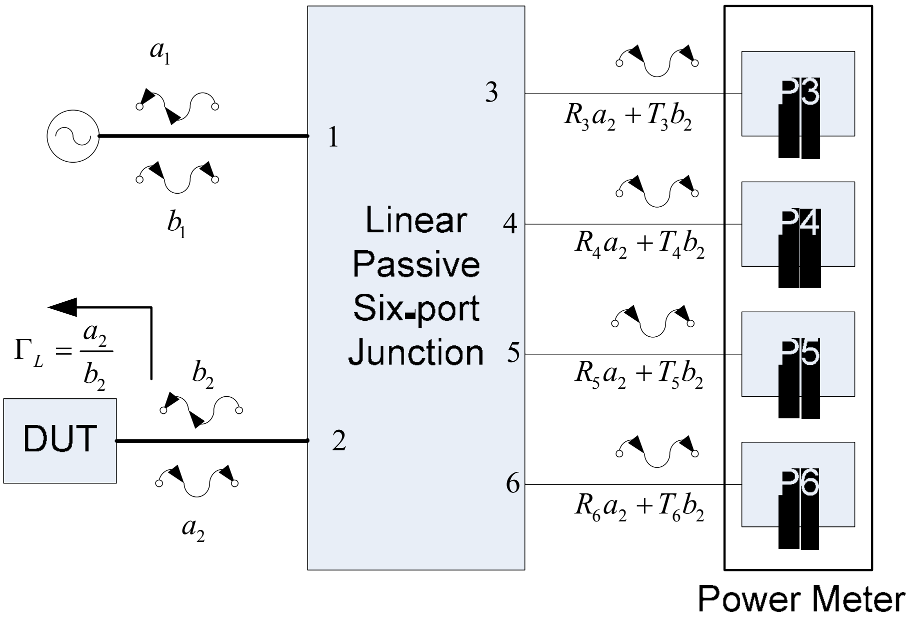

Figure 8.1 Six-port reflectometer for complex reflection coefficient measurement.

$$b_i = R_i a_2 + T_i b_2 \qquad i = 3,4,5,6 \tag{8.1}$$

where R_i and T_i are complex constants that only depend on the six-port junction and the reflection coefficients of the power. Thus, the input to any of the power meters is a linear combination of the incident b_2 and reflected a_2 wave on the DUT with relative amplitude and phase given by the complex ratio

$$q_i = -\frac{R_i}{T_i} \qquad i = 3,4,5,6 \tag{8.2}$$

The power meter readings can then be calculated as

$$\begin{aligned} P_i &= (1-|\Gamma_i|^2)|b_i|^2 \\ P_i &= |b_2|^2 |K_i||1-q_i\Gamma_L|^2 \qquad i = 3,4,5,6 \end{aligned} \tag{8.3}$$

where Γ_i are the reflection coefficients of the power meters and K_i are real constants defined as $|K_i| = (1-|\Gamma_i|^2)|T_i|^2$. Normalizing power (8.3) with respect to the power of the reference port (e.g., P_3, we come up with the three power ratio equations)

$$\frac{P_4}{P_3} = \left|\frac{K_4}{K_3}\right| \frac{\left|1 - q_4\Gamma_L\right|^2}{\left|1 - q_3\Gamma_L\right|^2} \tag{8.4a}$$

$$\frac{P_5}{P_3} = \left|\frac{K_5}{K_3}\right| \frac{\left|1 - q_5\Gamma_L\right|^2}{\left|1 - q_3\Gamma_L\right|^2} \tag{8.4b}$$

$$\frac{P_6}{P_3} = \left|\frac{K_6}{K_3}\right| \frac{\left|1 - q_6\Gamma_L\right|^2}{\left|1 - q_3\Gamma_L\right|^2} \tag{8.4c}$$

which are used to calculate the reflection coefficient of the load Γ_L. In these equations, there are four complex constants (q_3, q_4, q_5, and q_6) and three real constants (the ratios $\left|\frac{K_4}{K_3}\right|, \left|\frac{K_5}{K_3}\right|, \left|\frac{K_6}{K_3}\right|$), which depend on the six-port junction and the reflection coefficient of the power meters but not on the load. These constants are determined by calibration, that is, by measuring a certain number of known loads (calibration standards).

As discussed in Chapter 5, there are procedures to calibrate the six-port by means of a two-step procedure consisting of (1) a six-to-four port reduction, which requires a certain number of different loads whose values do not need to be exactly known, and (2) a classical one-port calibration that usually requires three well-known standards (for example, load–short–open). However, any other set of known loads can be used to calibrate the six-port.

Equation (8.4) defines three circles in the complex plane whose intersection is the reflection coefficient of the load Γ_L. The design criterion of the six-port junction aims at making these equations as robust as possible. The port 3 may be used as a reference of the DUT's incident power (choosing $R_3 = 0 \to q_3 = 0$) and one may set the remaining measurement ports q_4, q_5, and q_6 in a symmetrical arrangement and located at 120 degree over a circumference of a radius equal to 1.5 [2].

Notice that with these design values, (8.4) represents three circles with fixed centers, whose radii are directly proportional to the square root of the normalized power measurements. In this case, the six-port operation is especially simple and geometrically interpretable.

8.2.1 High Power Microwave Reflectometer

In high power microwave radiation, the load characteristics may change with time as its temperature increases. This change may result in an unmatched loading condition between the power generator and the energy applicator. Moreover, in practical microwave power applications such as microwave drying, it is often desirable to monitor the power absorbed by the load.

A high power reflectometer is shown in Figure 8.2. It is composed mainly of a low power microstrip six-port junction, a directional coupler, and a rectangular waveguide section [2]. The key component of the high power reflectometer is the hybrid waveguide to coaxial directional coupler used to reduce the power exchange level and feed the lowpower six-port junction.

The measurement results of a given load for different input power are presented in Table 8.1. As may be seen, the load reflection coefficient changes as the input power varies. This technique can be efficiently used in thermo-dielectric measurement applications [2].

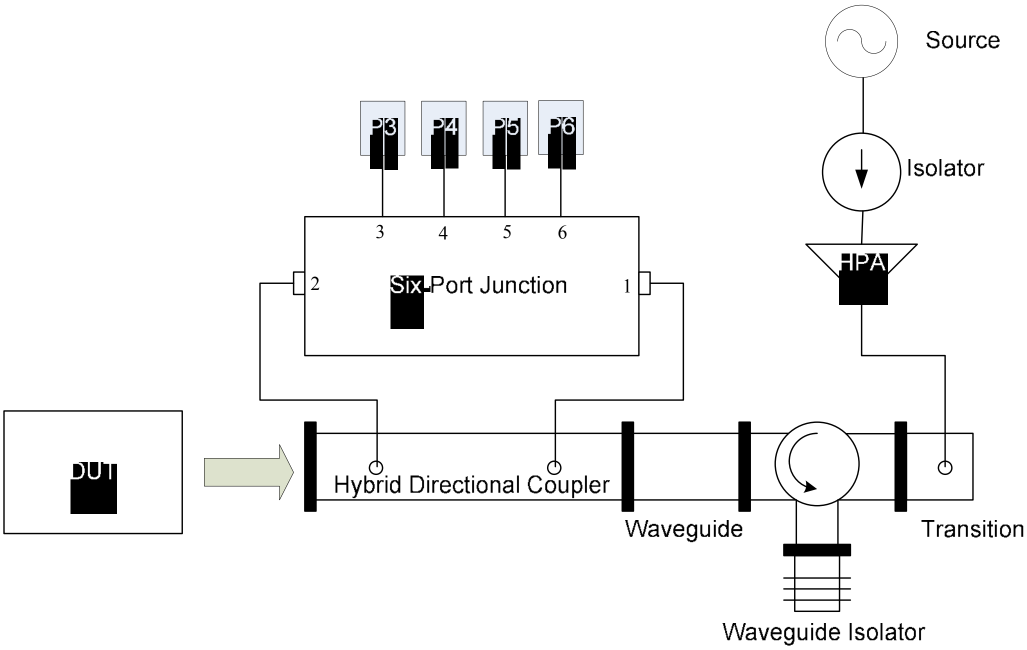

Figure 8.2 Setup of a high power six-port reflectometer. (© 1995 IEEE [2].)

Table 8.1

Measurement Results of a Given Load for Different Input Power

Input Power (watt)	*Reflection Coefficient (Γ)*
200	$0.234\angle 129.07^0$
50	$0.237\angle 128.50^0$
12.5	$0.239\angle 129.13^0$
3.13	$0.245\angle 131.27^0$

8.2 SIX-PORT WAVE-CORRELATOR

8.2.1 General Concept

The schematic of a two-channel wave receiver using a six-port junction is shown in Figure 8.3. The vector relation of two microwave signals a_1 and a_2, applied at ports P1 and P2, is obtained by measuring the power levels at the four remaining ports. The signal at port 1 usually comes from the reference generator and the one at port 2 is unknown. The waves at the power detectors can be written as a linear combination of the incident signals

$$b_i = A_i a_1 + B_i a_2 \qquad i = 3,4,5,6 \tag{8.5}$$

The power measured by the detectors can be expressed as the following values:

$$P_i = |b_i|^2 = |A_i|^2 |a_1|^2 |1 + t_i W|^2 \tag{8.6}$$

where $t_i = \frac{B_i}{A_i}$ and W is the complex correlation ratio of the two incident waves a_1 and a_2, that is, $W = \frac{a_2}{a_1}$. We denote an arbitrary side arm port by subscript h and one of the other three by I; then the power ratio can be expressed as

$$P_{i,h} = \frac{P_i}{P_h} = T_{i,h} \left| \frac{1 + t_i W}{1 + t_h W} \right|^2 \qquad i,h = 3,4,5,6;\ i \neq h \tag{8.7}$$

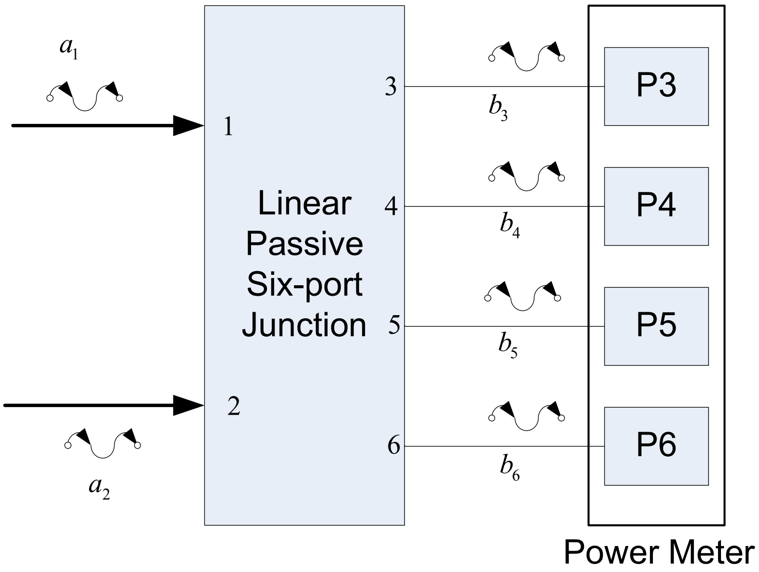

Figure 8.3 Block diagram of a six-port two-channel wave receiver.

where $T_{i,h} = \left|\frac{A_i}{A_h}\right|^2$ and $T_{i,h}$, t_i, and t_h are calibration parameters of the six-port junction, which should be determined in advance.

8.2.2 Calibration System

A calibration procedure using only one phase shifter is presented in Figure 8.4. The incoming signal from the source is split into two parts using a two-way power divider. One of them directly feeds port P1 of the six-port junction, while the other feeds port P2 through a sliding phase shifter. We denote the wave correlation ratio as $W^c e^{-j\theta}$ where θ is the phase angle corresponding to the position of the slidingphase shifter. We used superscript *c* to represent the calibration procedure. Referring to Figure 8.4, the observed port power ratio as a function of the variable θ may be written as

$$P^c{}_{i,h}(\theta) = T_{i,h}\left|\frac{1+t_i W^c e^{-j\theta}}{1+t_h W^c e^{-j\theta}}\right|^2 \tag{8.8}$$

Obviously, $P^c{}_{i,h}(\theta)$ is a periodic function with period *2π*. Hence, it can be represented by the Fourier series

$$P^c{}_{i,h}(\theta) = \sum_{n=-\infty}^{\infty} C^c_{n,i,h} e^{-jn\theta} \tag{8.9}$$

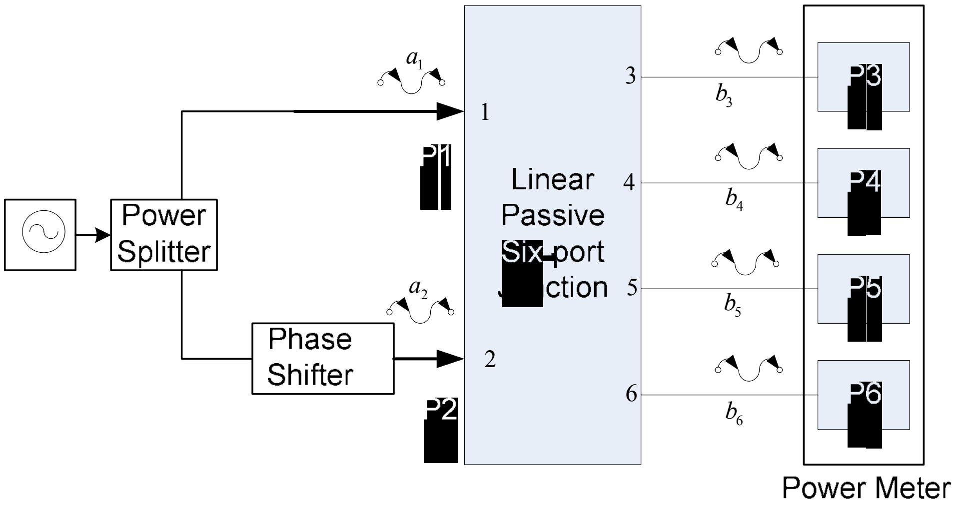

Figure 8.4 Six-port based wave-correlator and the calibration system. (© 2001 IEEE [3].)

where

$$C^c_{n,i,h} = \frac{1}{2\pi}\int_0^{2\pi} P^c{}_{i,h}(\theta)e^{jn\theta}d\theta \tag{8.10}$$

is the complex Fourier coefficient of the n^{th} harmonic. Furthermore, the right-hand side of (8.8) can be expanded into a series by employing the Maclaurin expansion. Then, one can derive the relations between the complex Fourier coefficients and the system calibration parameters as

$$T_{i,h} = C^c_{0,i,h}\frac{1-\left|t^c_h\right|^2}{1+\left|t^c_i\right|^2 - 2\operatorname{Re}(t^c_i t^c_h{}^*)} \tag{8.11}$$

$$t_h = \frac{t^c_h}{W^c} \qquad i,h = 3,4,5,6, i \neq h \tag{8.12}$$

and

$$t^c_h = -\frac{C^c_{2,i,h}}{C^c_{1,i,h}} = -\frac{C^c_{4,i,h}}{C^c_{3,i,h}} = \cdots \tag{8.13}$$

Finally, in order to determine the calibration parameters, we must extract the unknown W^c. For the six-port based wave-correlator, this can be done easily by moving out the phase shifter and determining W^c uniquely as the radical center using a procedure similar to that in [4]. It is important to note that although there exist 12 ratios of $T_{i,h}$, only three ratios are independent of each other. Consequently, the calibration parameters are three independent real ratios, for example, $T_{3,4}$, $T_{3,5}$, $T_{3,6}$, and four complex ratios t_i, for $i = 3, 4, 5$, and 6.

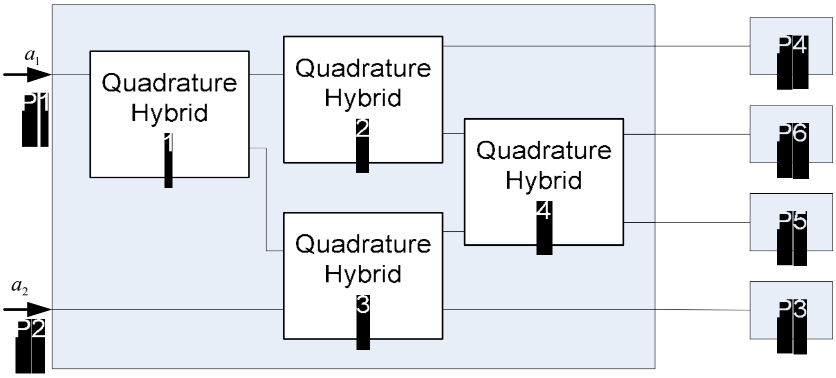

Figure 8.5 Six-port circuit components.

After these 11 real calibration parameters are determined during the above calibration procedure, the six-port based wave-correlator can be operated as a two-channel receiver and can determine the wave-correlation ratio W using (8.7).

8.2.3 Architecture of a Wave-Correlator

A typical architecture for the six-port wave-correlator is shown in Figure 8.5. The six-port can be fabricated using four quadrature hybrids. In this wave-correlator structure, two incident waves are fully utilized for measuring the powers at the remaining four ports. In the calibration process, the position of the sliding phase shifter is adjusted. One of the main features of this calibration method is that only one phase shifter is required, enabling the method to be applied over a broad frequency band.

8.2.4 Beam Direction Finder Using a Six-Port Wave-Correlator

The six-port wave correlator may be efficiently used in the beam direction finding applications. The beam direction finder is shown in Figure 8.6. We assume that two receiving antennas are in the far-field region of the transmitting radiator. In a far-field case, $d >> 2D^2 f/c$ where d is the distance between transmitting radiator and receiving antennas, c is the light velocity, and D is the maximum linear dimension of the receiving antennas. Suppose L is the distance between receiving antennas, and Φ is the estimated direction angle of the received beam. Assuming a two-dimensional case with plane wave incidence, the phase of the wave complex field ratio at two antenna locations separated by a distance L is simply extracted as [5]

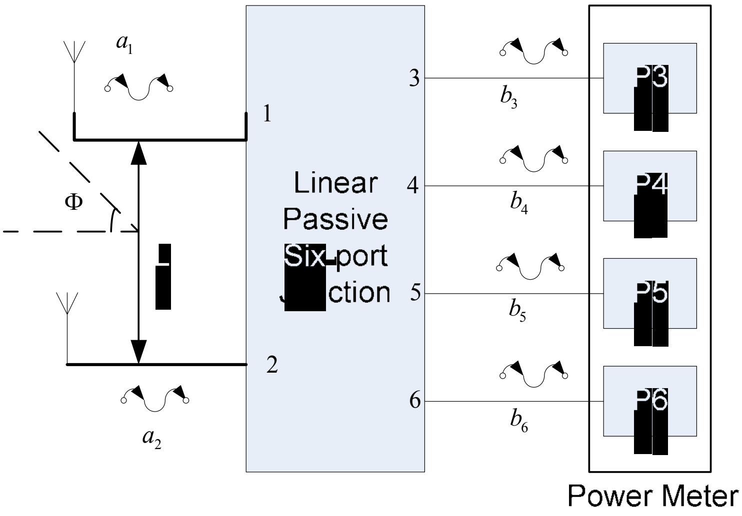

Figure 8.6 Block diagram for the beam direction finder using a wave-correlator.

$$\arg(W) = \frac{2\pi}{\lambda} L \sin\Phi \tag{8.14}$$

where $\arg(W)$ is the phase of the wave ratio [3]. Thus, it can be easily deduced that the beam direction angle Φ is calculated as

$$\Phi = \sin^{-1}\left\{ c \frac{\arg(W)}{2\pi f L} \right\} \tag{8.15}$$

8.2.5 Doppler Estimation Using a Six-Port Wave-Correlator

A system based on the six-port wave-correlator is described in this section to measure the Doppler frequency of a moving target [3]. As seen, a six-port wave-correlator determines the vector relation between the two input signals directly by measuring the power levels. To measure the Doppler frequency of a moving object and then inferring its velocity, one may use a wave-correlator to evaluate the relative velocity from the rate of phase variation between the transmitted and received signals. After the relation between the input and output ports of the six-port wave-correlator becomes known, the vector relation (amplitude and phase) between the two input signals is determined by measuring the power levels at the four output ports. The relation between the input and output ports can be described

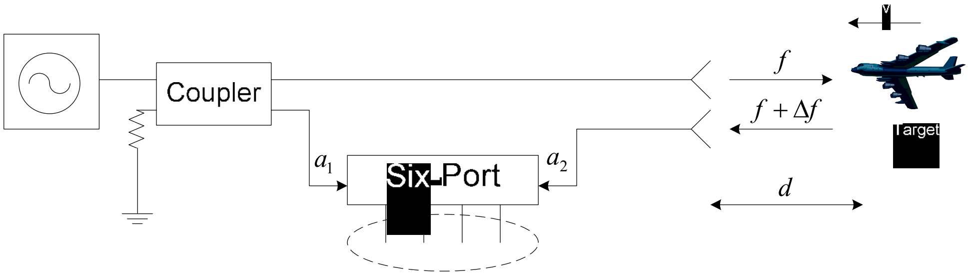

Figure 8.7 Block diagram of a Doppler radar system implemented with a six-port wave-correlator from [3].

by the calibration parameters (8.11) and (8.12). The calibration procedure is shown in Figure 8.4 [6].

The concept of the Doppler radar system based on the six-port wave-correlator is shown in Figure 8.7.

The transmitted signal of frequency f is radiated by the transmitting antenna. If the target is in motion with respect to the radar system, the received echo signal back at the receiving antenna is shifted in frequency (i.e., the Doppler frequency shift, Δf). This shift in frequency is dependent on the target velocity with respect to the radar system and can be easily determined from

$$\Delta f = \frac{2v}{c - v} f \tag{8.16}$$

where c is the speed of light and v is the velocity of the target. The plus value of v applies for a target approaching the measurement system, while the minus value applies for a receding target. The two input waves of the six-port wave-correlator a_1 and a_2 are the transmitted and received waves, respectively, and the equations that represent these two input waves are

$$a_1 = \alpha_1 e^{j(2\pi f t + \Phi_1)} \tag{8.17}$$

$$a_2 = \alpha_2 e^{j(2\pi(f+\Delta)t + \Phi_2)} \tag{8.18}$$

where Φ_1 and Φ_2 represent the phase constants of the transmitted wave and the reflected Doppler shifted wave, respectively.

The W in Figure 8.6 represents the complex wave ratio of the two input waves, which can be expressed as

$$W = \frac{a_2}{a_1} = \left|\frac{a_2}{a_1}\right| e^{j(\Delta\omega t + \Delta\Phi)} \tag{8.19}$$

where $\Delta\omega = 2\pi\Delta f$ and $\Delta\Phi = \Phi_2 - \Phi_1$. Obviously, if we denote the phase of the wave ratio as $\arg(W)$, then

$$\Delta\omega = \frac{d(\arg W)}{dt} \tag{8.20}$$

One may extract the velocity from (8.16) and (8.20) as

$$\frac{v}{c-v} = \frac{1}{4\pi f}\frac{d(\arg W)}{dt} \tag{8.21}$$

For $c>>v$, we have

$$v = \frac{c}{4\pi f}\frac{d(\arg W)}{dt} \tag{8.22}$$

From this equation, it is clear that the target's relative velocity can be determined by measuring the phase difference between the transmitted and received signals.

8.3 SIX-PORT APPLICATIONS IN DIRECTION FINDERS

In order to obtain the beam direction, the phase difference between the RF input signals can be measured using the output in-phase and quadrature baseband signals. It is shown that these signal values will be directly related to the angle of arrival [7]. A two-dimensional approach to direction of arrival estimation is presented in this section. Figure 8.8 shows a schematic view of the geometrical model. The receiving antennas are separated by a distance *L*. Owing to the angle of arrival θ, a path difference (Δx) between the two propagation paths will appear. Consequently, the RF input signals will be phase shifted with respect to each other by an angle $\Delta\varphi$. As mentioned before, the phase difference between the RF input signals is directly related to the path difference. The path difference can be expressed as

$$\Delta x = c\Delta t \tag{8.23a}$$

or similarly,

$$\Delta x = \lambda\frac{\Delta\varphi}{2\pi} \tag{8.23b}$$

Therefore, the angle of arrival θ can be obtained as follows

$$\sin\theta = \frac{\Delta x}{L} = \frac{\lambda}{L}\frac{\Delta\varphi}{2\pi} \tag{8.24}$$

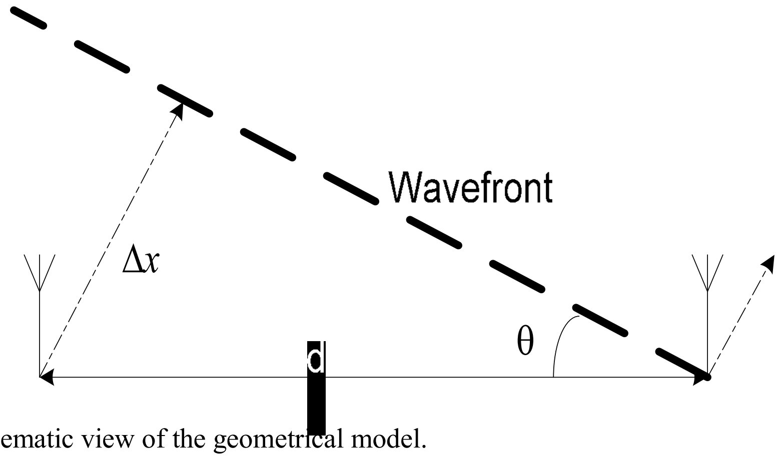

Figure 8.8 Schematic view of the geometrical model.

From (8.23), it can be concluded that the two waves will arrive in phase if the path difference is zero or an integer number of wavelengths. Furthermore, to avoid any ambiguity, the distance between the two antennas is chosen to be equal to half the wavelength at the operating frequency.

Figure 8.9 shows the block diagram of the six-port circuit composed of four 90 degree hybrid couplers [8]. The power reading at each output port (i=1, 2, 3, 4) can be expressed as

$$P_i = \left|\{S_{5i}.|a_5|\exp(j\varphi_5) + S_{6i}.|a_6|\exp(j\varphi_6)\}\right|^2 \tag{8.25}$$

where a_5 and a_6 represent the normalized input voltages of the six-port circuit corresponding to the local oscillator (LO) and RF signals, respectively. In addition, S_{5i} and S_{6i} are the six-port transmission scattering parameters between the LO, the respective RF input ports, and the four SP output ports. For the same amplitude of the RF input signals, (a_5=a_6=a), the output signal powers become

$$P_i = K_i|a|^2\left|\exp[j(\frac{\pi}{4} + \varphi_6 - \varphi_5)] - \zeta_i\right|^2 \tag{8.26}$$

where K_i is a constant and

$$\zeta_i = \exp\{j[\frac{\pi}{4} + (i-1)\frac{\pi}{2}]\} \tag{8.27}$$

represents the solutions of equation $P_i = 0$ in the complex plane.

The dc output voltage of an ideal power detector is proportional to the power of the RF signal magnitude. For the six-port detection circuit presented in Figure 8.9, the corresponding dc output voltages are proportional to the signal power.

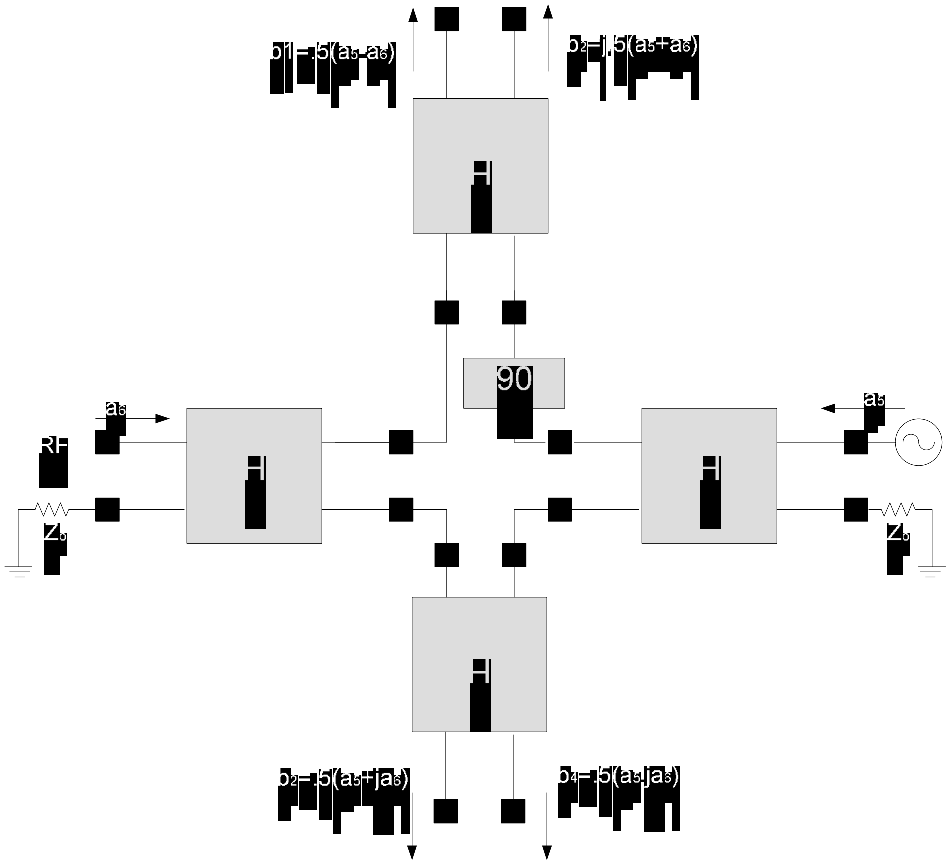

Figure 8.9 Block diagram a typical six-port junction. (© 2004 IEEE [8].)

Supposing that four identical detectors K_i=K are used, the theoretical dc output voltages are a function of the phase difference between the RF input signals ($\Delta\varphi = \varphi_6 - \varphi_5$).

$$U_i = K\left|a\right|^2 \left|\sin(\frac{\Delta\varphi}{2} - (i-1)\frac{\pi}{4})\right|^2 \tag{8.28}$$

Each dc output voltage is periodical with 2π and shifted in phase with π/2 multiples compared to other dc output signals [8]. Accordingly, in a six-port architecture, in-phase (I) and quadrature (Q) signals are obtained as

$$I = U_3 - U_1 = K.a^2 \cos(\Delta\varphi) \tag{8.29a}$$

$$Q = U_4 - U_2 = K.a^2 \sin(\Delta\varphi) \tag{8.29b}$$

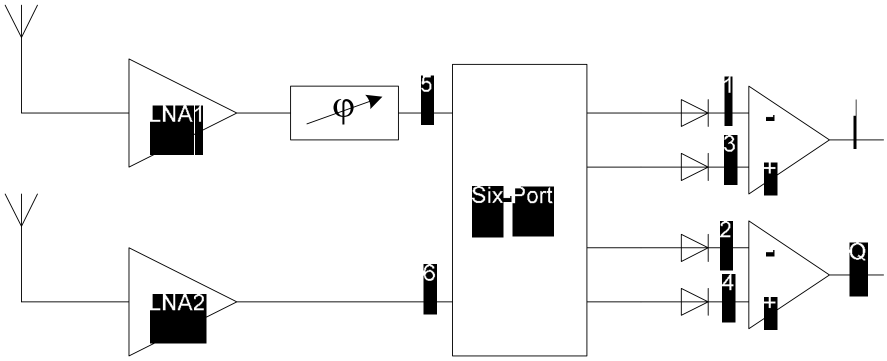

Figure 8.10 Block diagram of the directional finding circuit.(© 2006 IET [11].)

In these equations, U_i are four six-port detected output voltages, a is the magnitude of the input normalized wave at one port ($a_5=a_6=a$), $\Delta\Phi$ is the phase difference between the input normalized waves, and K is a constant that depends on the power detector characteristics and on the baseband circuit gain.

Using I/Q signals, a baseband vector can be defined in the complex plane by the following equation

$$\Gamma = I + jQ = K.a^2.\exp(j\Delta\Phi) \tag{8.30}$$

This equation shows that the phase of the Γ vector is equal to the phase difference between RF input signals ($\Delta\Phi$). Therefore, this RF phase difference can be directly measured using both I and Q signals.

By using (8.22) and (8.25), the angle of arrival is presented as

$$\sin\theta = \frac{\Delta\Phi}{\pi} = \frac{1}{\pi}\arg(\Gamma) \tag{8.31}$$

A block diagram for the beam-direction-finding circuit, according to this geometrical model, is presented in Figure 8.10 [9]. Two antennas, which feed the low-noise amplifiers, are connected to the six-port RF inputs. Then the six-port output signals are detected, amplified, and processed according to (8.25), and consequently the baseband complex signal (Γ) is obtained. In order to perform initial direction of arrival estimations, the Γ vector can be directly visualized on an oscilloscope screen (in XY format). According to (8.31), the position of the point on the screen is related to the angle of arrival θ. In addition, one can deduce from (8.30) that if the imaginary part of Γ is equal to zero, the RF input signals are in phase. Due to an internal phase difference between two transmission paths, an initial phase adjustment must be performed. After this adjustment, if the antenna system is rotated in the horizontal plane, the imaginary part of Γ becomes equal to zero when $\theta=0^\circ$. As a further step, the angle of arrival θ can be calculated using (8.31).

8.4 SIX-PORT APPLICATIONS IN RADAR

A six-port radar is working based on the concept of wavecorrelation. By measuring the complex relation of the transmitted and received signals, one may use this radar to extract the speed and range information of a moving target. The architecture of a basic six-port radar is shown in Figure 8.11. The signal at port 1 comes from LO and the one at port 2 is unknown. The objective is to obtain a power reading proportional to the reference signal thus not influenced by the received signal. This permits correcting the power instability of the signal source by normalizing the power measurements at the other detectors. Considering Figure 8.4, detector 3 will be used for this purpose, so $R_3 = 0 \rightarrow q_3 = 0$. Then, (8.4) may be rewritten as

$$P_{43} = \frac{P_4}{P_3} = \left|\frac{K_4}{K_3}\right| \left|1 - q_4 \Gamma_L\right|^2 \tag{8.32a}$$

$$P_{53} = \frac{P_5}{P_3} = \left|\frac{K_5}{K_3}\right| \left|1 - q_5 \Gamma_L\right|^2 \tag{8.32b}$$

$$P_{63} = \frac{P_6}{P_3} = \left|\frac{K_6}{K_3}\right| \left|1 - q_6 \Gamma_L\right|^2 \tag{8.32c}$$

These are the equations of three circles centered on q_i, whose radius is $\sqrt{P_{i3}}$. $\Gamma = a_2 / a_1$ is determined by the intersection of the three circles. Constants K_i and q_i are found with a previous calibration.

8.4.1 Six-Port Doppler Sensor

The relations in (8.32) can be used to design a Doppler sensor [10, 11]. Suppose a signal a_1, transmitted by a radar and reflected by a target at a distance *d,* is received at the radar after a propagation time $T=2d/c$, where c is the speed of light. If the target has a relative speed v to the radar, the propagation time will be

$$T = 2\frac{d - vt}{c} \tag{8.33}$$

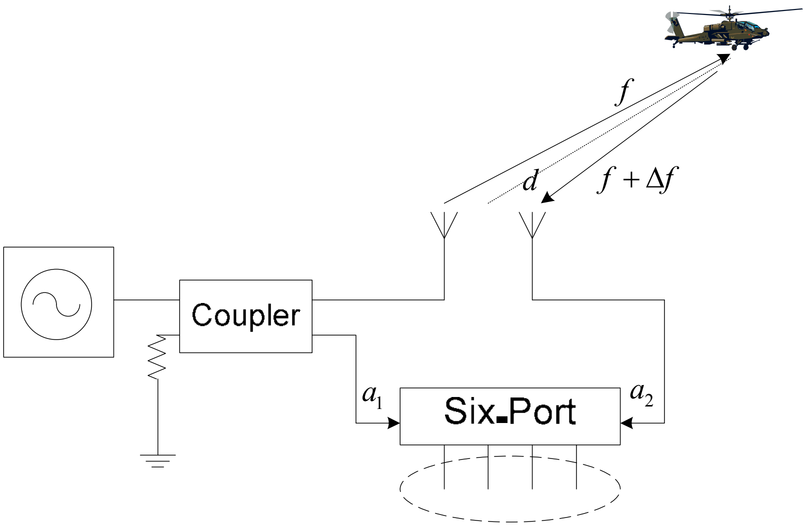

Figure 8.11 Block diagram of a Doppler radar system.

As seen in Section 8.2.5, if the transmit signal can be written as

$$a_1 = |a_1| e^{j\omega t} \tag{8.34}$$

where ω is the carrier frequency, then the received signal will be

$$a_2 = |a_2| e^{j\omega(t-T)} = |a_2| e^{j[(\omega+\Delta\omega)t-\varphi]} \tag{8.35}$$

where $\omega_D = \Delta\omega = 2\omega.v / c$, and $\varphi = 2\omega.d / c$. The complex relation of the transmitted and received signals is

$$\Gamma = \frac{a_2}{a_1} = \frac{|a_2|}{|a_1|}.e^{j(2\pi f_D t-\varphi)} \tag{8.36}$$

where Γ is a vector that turns at a Doppler frequency, $f_D = \omega_D / 2\pi$, and its phase is proportional to the range. Measuring this rotation, we can determine the Doppler frequency. Its sign, which indicates whether the target is approaching or moving away, can be derived by the sense of rotation.

8.4.2 Six-Port Range Sensor

Range information contained in the phase of Γ is somewhat hidden. The distances measured are much bigger than the wavelengths at the used frequencies, so the measure will be ambiguous as follows from the expression of (8.35), where n is unknown

$$\varphi + 2\pi n = 2\frac{\omega . d}{c} \tag{8.37}$$

To avoid this ambiguity, a second signal can be used [10], and the range can be obtained measuring the phase shift between the Γ coefficients at two frequencies f_1 and f_2

$$\varphi_1 - \varphi_2 = 2\frac{(\omega_1 - \omega_2).d}{c} \tag{8.38}$$

$(f_1 - f_2)/2$ sets the maximum unambiguous range. For example, a range of 100m requires a frequency shift of 1.5 MHz. This distance measurement procedure allows determining distance easily, even if the target speed is null. To obtain a better accuracy in short distances without introducing ambiguity for the long ranges, three frequencies can be used. When the target becomes closer than a certain range, the system changes one of the transmitted frequencies so the frequency difference between them is now larger (e.g., 15 MHz), which gives a maximum range of 10m.

8.4.3 Radar Structure

Figure 8.12 shows the block diagram of the radar [10]. The microwave oscillator is frequency modulated by a square signal, which gives the two different frequencies needed for the range measurement. The modulator and the VCO may be substituted by noncontrolled oscillators and a fast switch, as only three different frequencies are needed. A portion of the emitted signal is coupled to the six-port, which plays the role of a mixer.

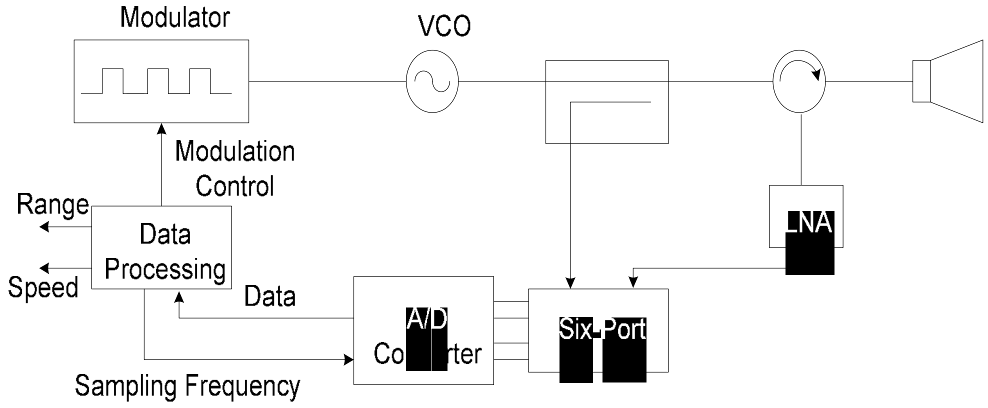

Figure 8.12 Block diagram of a six-port radar. (© 2000 IEEE [10].)

The received signal is injected to the port 2 of the circuit after amplification, and power detectors are placed at outputs 3–6. The frequency of the four signals that go into the analog to digital (A/D) converter is the Doppler frequency of the target. These signals have different phases as they come from different linear combinations of the signal at port 1 and 2. The signal processing unit finds and determines the frequency and the range as described before. This unit also commands the modulation in order to change the frequency shift as the target becomes closer.

8.4.4 Radar Calibration

It is necessary to find the values of K_i and q_i in (8.32) before using the six-port network. In this section, a straightforward algorithm is proposed [12]. The method requires a minimum of five loads with a constant absolute value of the reflection coefficient and unknown but well-distributed phases, followed by three known loads. As mentioned in previous sections, speed and range are obtained from the phase of Γ, so its magnitude is not used; hence, it is not necessary to calibrate it. Even more, they are obtained from phase differences. Doppler frequency, therefore speed, is derived from the phase difference of two points at the same frequency, and distance is found with (8.38) from the phase difference of two points, one at each frequency. Thus, calibration of the absolute phase of is not required. In this case, the three known loads are now reduced to one, plus two other loads with unknown magnitude and phase but with a known phase difference between them.

8.5 ANTENNA MEASUREMENT USING SIX-PORT

8.5.1 Near-Field Antenna Measurement

As seen, the complex signal ratios (including magnitude and phase information) can be determined using six-port network analyzers. Moreover, they can easily be designed to operate in a dynamic range of 50 dB. Hence, they are an attractive choice for near-field measurements [13]. A typical planar near-field antenna measurement setup system is shown in Figure 8.13. It consists of a scanning frame housed in an anechoic chamber, a receiver for detection of vector signals, and a control and process unit. The test antenna radiation pattern can be directly related to the forward transmission coefficient between the test antenna and a probe antenna. An ideal six-port receiver would measure the transmission coefficient directly. Furthermore, since near-field measurement techniques are approximate in nature [14,15], the six-port network analyzer needs only measure transmission coefficients with greater accuracy than the errors.

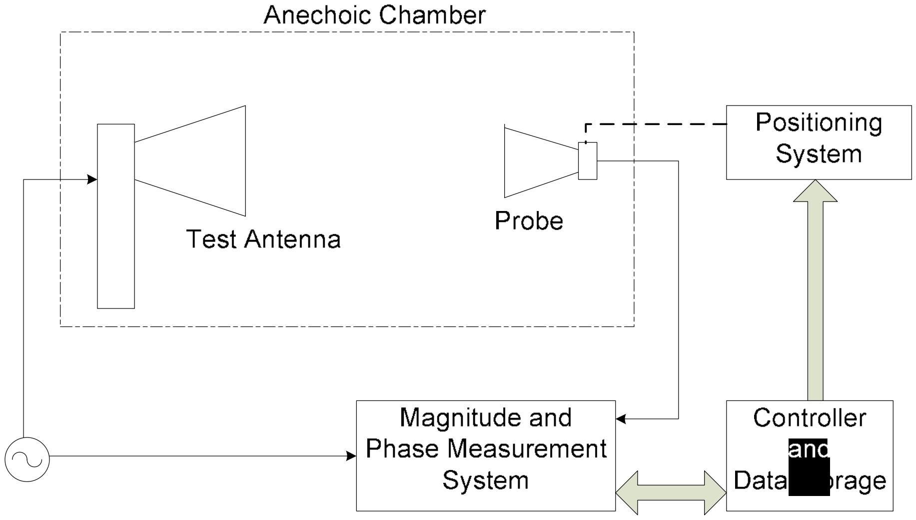

Figure 8.13 Near-field antenna measurement systems.

To determine the far-field radiation pattern of an antenna under test, two sets of measurements are required: the far-field radiation pattern of the probe, and, the responses of the probe to the near-field radiated from the test antenna at preselected points on a plane. These two sets of data are then sufficient to calculate the test antenna's far-field radiation pattern [14, 15]. From the point of view of the measurements, the near-field antenna setup can be regarded as a two-port network.

The two ports can be defined as being the planes at which the antennas are connected to the measurement network. The two-port network is described by a two-port scattering matrix S_{ik} as:

$$b_1 = S_{11}.a_1 + S_{12}.A_2 \tag{8.39a}$$

$$B_2 = S_{21}.a_1 + S_{22}.A_2 \tag{8.39b}$$

The signals a_1, A_2, $b_{1,}$ and B_2 are as shown in Figure 8.14. The near-field measurement technique introduces some constraints on the scattering parameters S_{ik}. The theory relies on the fact that the free-space radiation pattern of the test and probe antennas are unaffected by mutual coupling. This assumption is equivalent to the condition that the parameters S_{11} and S_{22} in (8.39) are constants and do not change for different probe positions [14].

Furthermore, for this assumption to be true, the two antennas should not be strongly coupled, and therefore the product of the forward and backward transmission coefficients $S_{21}S_{12}$ has to be small. In practice this is achieved by positioning the probe and test antennas a reasonable distance apart. The small dimensions of the probe antenna and proper spacing of the two antennas ensures the ratio (a_1/A_2), the ratio of the signal entering the probe antenna to the signal entering the test antenna from the receiver, is small. This is assuming that there is negligible leakage of the signal A_2 through the receiver to the probe port and the probe is not badly mismatched. Finally, under reciprocal conditions ($S_{21} = S_{12}$), the variable S_{21} is the only scattering parameter changing during near-field measurements. The principles of designing a receiver to measure this parameter are described in [13].

8.5.2 Polarization Measurement

A six-port polarimetric measurement system with the use of two dual-polarization antennas can be realized to measure the polarization states of incoming waves [16]. A six-port junction used for polarization measurement is shown in Figure 8.15. As can be seen, the two output ports of a dual-polarization receiving antenna are connected to a six-port network.

Suppose the polarization state of an incoming wave as

$$\mathbf{b}'' = b_V''\mathbf{v} + b_H''\mathbf{h} \tag{8.40}$$

where $\mathbf{v}$ and $\mathbf{h}$ are vertical and horizontal unit vectors.

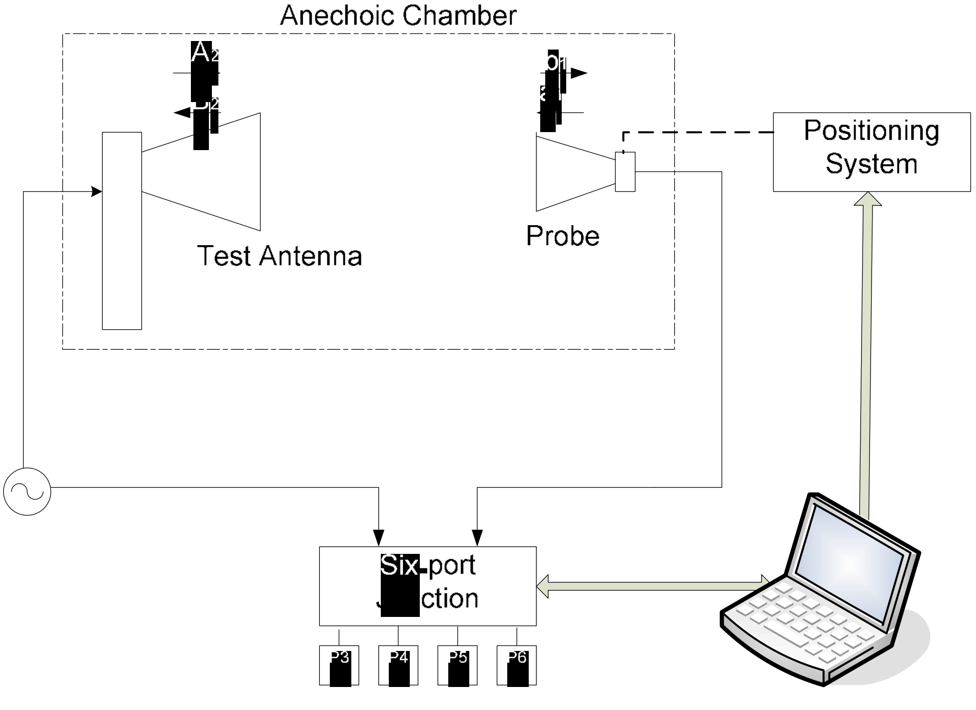

Figure 8.14 A block of a six-port near-field antenna measurement system. (© 1987 IET [13] .)

The polarization of the incoming wave can be determined by its polarization ratio as,

$$r = b''_V / b''_H \tag{8.41}$$

The received signals b'_V and b'_H from the antenna vertical and horizontal channels are related to the incoming wave $\mathbf{b}''$ using

$$\begin{bmatrix} b'_V \\ b'_H \end{bmatrix} = \begin{bmatrix} R_{VV} & M_{VH} \\ R_{HV} & R_{HH} \end{bmatrix} \begin{bmatrix} b''_V \\ b''_H \end{bmatrix} \tag{8.42}$$

or

$$\mathbf{b}' = \mathbf{R}\mathbf{b}'' \tag{8.43}$$

where $\mathbf{R}$ is the transfer matrix of the receiving dual-polarization antenna and accounts for the imbalance and coupling between its horizontal and vertical polarization channels. By using six-port theory and according to (8.5), the signals of the power detectors, $b_i (i = 3,4,5,6)$, can be expressed as a linear combination of two variables b'_V and b'_H . Accordingly, b_3 and b_4 become

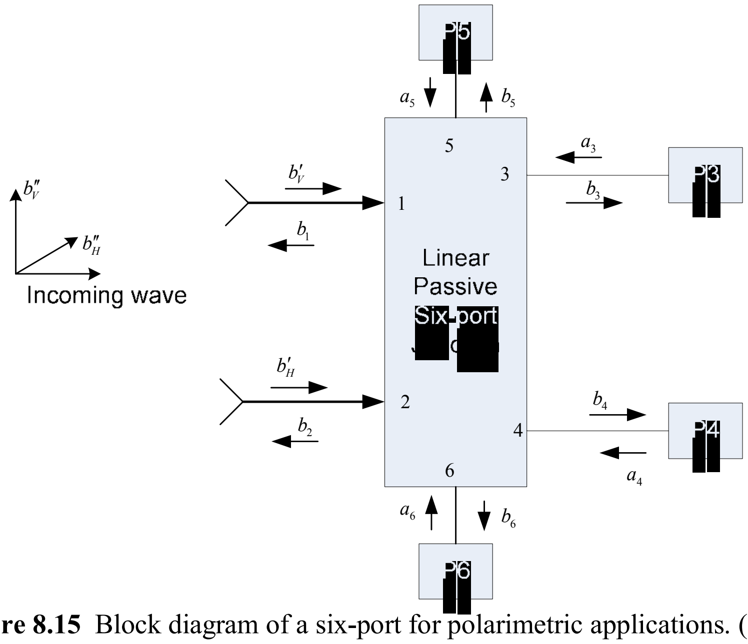

Figure 8.15 Block diagram of a six-port for polarimetric applications. (©1997 IEEE [16] .)

$$\begin{bmatrix} b_3 \\ b_4 \end{bmatrix} = \begin{bmatrix} M_{11} & M_{12} \\ M_{21} & M_{22} \end{bmatrix} \begin{bmatrix} b'_V \\ b'_H \end{bmatrix} \tag{8.44}$$

or

$$\mathbf{b} = \mathbf{M}\mathbf{b}' \tag{8.45}$$

where $\mathbf{b}$ and $\mathbf{b}'$ are the input and output signals of a six-port network. $\mathbf{M}$ is a matrix dependent on the six-port network configuration and must be determined in the calibration process.

By using (8.43) in (8.45), $\mathbf{b}$ and $\mathbf{b}''$ are related as

$$\mathbf{b} = \mathbf{M}\mathbf{R}\mathbf{b}'' \tag{8.46}$$

where $\mathbf{R}' = \mathbf{M}\mathbf{R}$ is the receiving transfer matrix. The incoming wave can then be determined from (8.46) as

$$\mathbf{b}'' = \mathbf{R}'^{-1}\mathbf{b} \tag{8.47}$$

The calibration procedures to determine the polarization state of an incoming wave are discussed in [16, 17].

8.6 MATERIAL CHARACTERIZATION USING SIX-PORT

The six-port technique can be used to perform nondestructive permittivity measurements. The measured permittivity is related to the reflection coefficient by means of an effective transmission-line model.

This method is suitable for measuring relatively high-loss dielectric liquids.

8.6.1 Measurement System

Figure 8.16 shows a microwave permittivity measurement system. It consists of a six-port microwave junction and a number of standard microwave laboratory instruments (power meters, counters, sweepers, and so forth) controlled via a bus interface. The device under test (DUT) is an open-ended coaxial test probe immersed in the test liquid kept at a constant temperature [18].

8.6.2 Probe Model Analysis

An open-ended coaxial probe is used in this measurement system. Figure 8.17 shows the equivalent electrical model of the probe immersed into a test medium with a relative complex permittivity ε_d. An effective transmission line is used to model the fringing electric field in the test medium at the extremity of the probe [19]. Assuming a quasi-TEM propagating mode, the complex admittance at plane AA' is given by

$$Y_L = Y_d \frac{Y_E + jY_d \tan(\beta_d L)}{Y_d + jY_E \tan(\beta_d L)} \tag{8.48}$$

where YL is the admittance at the input of the effective transmission line, Yd is the characteristic admittance of the effective transmission line, YE is the terminating admittance at the end of the effective transmission line, βd is propagation constant in the test medium, and L is the effective transmission line length.

For physical (radial dimensions of the probe versus wavelength) and practical (resolution on the measurement of the complex reflection coefficient is ± 0.5 degree and ± 0.5 percent in phase and amplitude values, respectively) considerations, the radiation loss can be neglected [20]. In such a situation, the terminating impedance is fully reflected impedance (open circuit) and the admittance YE vanishes. Equation (8.48) becomes

$$Y_L = jY_d \tan(\beta_d L) \tag{8.49}$$

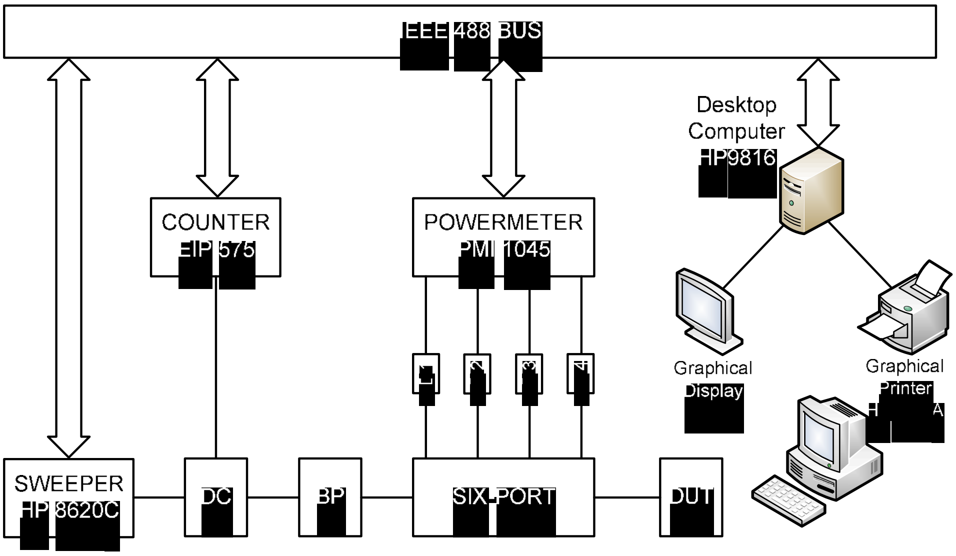

Figure 8.16 Experimental block diagram of the six-port reflectometer. DC: directional coupler; BP: bandpass filter; D1, D2, D3, D4: Schottky diode detectors. (© 1989 IEEE [18].)

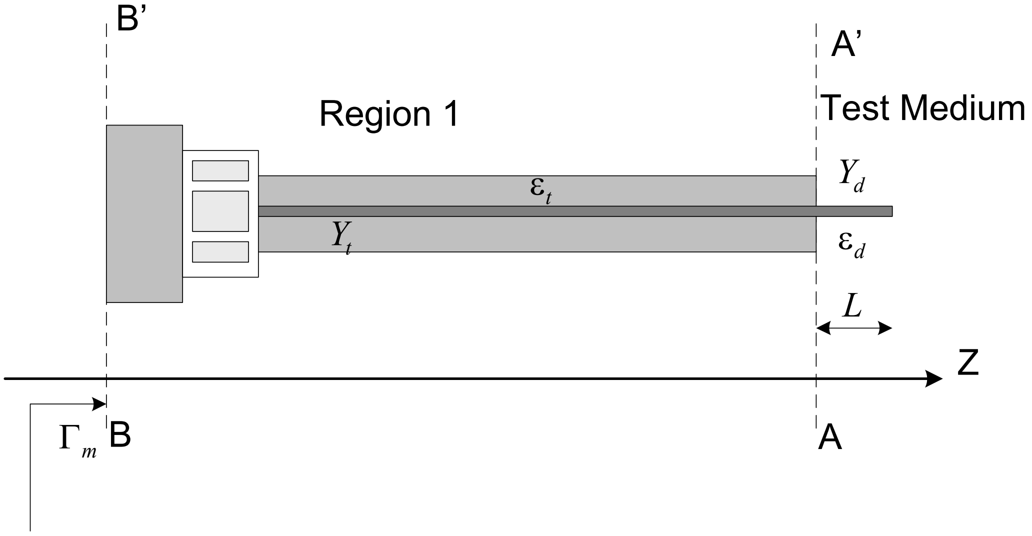

Figure 8.17 An open-ended coaxial line homogeneous medium.(©1989 IEEE [18].)

Y_d can be expressed as a function of physical parameters of the effective transmission line as follows:

$$Y_d = \frac{\sqrt{\varepsilon_d}}{60\ln(b/a)} \tag{8.50}$$

where a and b are the inner and the outer diameters of the coaxial probe, respectively. Furthermore, the admittance Y_L can be related to the characteristic admittance of probe Y_t and the measured reflection coefficient reported at plane AA' as follows [18]:

$$Y_L = \left[\frac{1-\Gamma_m e^{j2\beta_t D}}{1+\Gamma_m e^{j2\beta_t D}}\right] Y_t \tag{8.51}$$

where $Y_t = \dfrac{\sqrt{\varepsilon_t}}{60\ln(b/a)}$, ε_t is dielectric constant of dielectric material inside the **a** coaxial line (subscript t for Teflon, ε_t = 2.03-j.004), D is the physical length of the probe, β_t is the propagation constant in coaxial probe, and Γ_m is the complex reflection coefficient at plane BB' given by the six-port reflectometer. Substituting (8.49) in (8.51) and using expression Y_d as given by (8.50), one can get

$$\varepsilon_d = \frac{-jc\sqrt{\varepsilon_t}}{2\pi fL}\left[\frac{1-\Gamma_m e^{j2\beta_t D}}{1+\Gamma_m e^{j2\beta_t D}}\right] X \cot g(X) \tag{8.52}$$

where $X = \frac{2\pi fL\sqrt{\varepsilon_d}}{c}$, ε_d is the complex permittivity of the dielectric under test, D is the physical length of the probe, L is the effective line length, c is the wave velocity in free space, and f is the measuring frequency. This equation is used to compute the permittivity from the measured reflection coefficient.

8.6.3 Probe Calibration

In order to evaluate the relative dielectric constant and loss factor of the test medium, we need to know the probe parameters D and L at each measuring frequency. The determination of D and L is based on the use of two standard dielectric mediums [18]. Substituting (8.49) in (8.51), one can obtain

$$\Gamma_m e^{j2\beta_t D} = \frac{\rho + \Gamma_m e^{-j2\beta_d L}}{1+\rho e^{-j2\beta_d L}} \tag{8.53}$$

where

$$\rho = \frac{\sqrt{\varepsilon_t} - \sqrt{\varepsilon_d}}{\sqrt{\varepsilon_t} + \sqrt{\varepsilon_d}} \tag{8.54}$$

The two calibration parameters L and D can then be evaluated by using (8.51) and (8.53) with an iterative computation procedure. This method is also successfully applied to determine the permittivity of moisture textile [21] and the measurement of complex dielectric constant of ferroelectrics [22].

8.7 OPTICAL MEASUREMENT USING SIX-PORT

The six-port technique has received some attention from the optical community after successful application of the six-port technique at microwave frequencies [23, 24]. The early investigation on using six-port in optics was reported, in which a six-port optical reflectometer was constructed, using free-space propagation, and was used to measure optical complex reflection coefficients. The reasons for using six-port technique in optical applications are probably related to the following facts. First, the phase measurement of optical devices has been recently required for many optical measurements. Second, the six-port measurement technique is an optical domain continuous-wave (CW) interferrometric approach that requires a narrow line width and wavelength-stable source. These measurement instruments are currently available at an affordable cost.

8.7.1 Optical Six-Port Junction Design

The three power ratio equations for a six-port reflectometer are obtained in Section 8.1 as

$$\frac{P_4}{P_3} = \left|\frac{K_4}{K_3}\right| \frac{|1 - q_4\Gamma_L|^2}{|1 - q_3\Gamma_L|^2} \tag{8.55a}$$

$$\frac{P_5}{P_3} = \left|\frac{K_5}{K_3}\right| \frac{|1 - q_5\Gamma_L|^2}{|1 - q_3\Gamma_L|^2} \tag{8.55b}$$

$$\frac{P_6}{P_3} = \left|\frac{K_6}{K_3}\right| \frac{|1 - q_6\Gamma_L|^2}{|1 - q_3\Gamma_L|^2} \tag{8.55c}$$

The design criteria of the six-port junction aims at making these equations as robust as possible by using one-port as a reference of the DUT's incident power and setting the remaining measurement ports in a symmetrical arrangement with ports q_4, q_5, and q_6 located at 120° over a circumference of radius approximately equal to 1.5. Therefore, the objective is to get a six-port junction with

$$R_3 = 0 \leftrightarrow q_3 = 0 \tag{8.56a}$$

$$q_4 = \frac{3}{2}\exp(j(\theta + \pi/3)) \tag{8.56b}$$

$$q_5 = \frac{3}{2}\exp(j(\theta + \pi)) \tag{8.56c}$$

$$q_6 = \frac{3}{2}\exp(j(\theta - \pi/3)) \tag{8.56d}$$

where θ is an arbitrary angle. From an optical point of view, it must be noticed that the six-port technique shares many similarities with other coherent optical-frequency-domain (C-OFD) techniques. Each of the power meters (photodetectors) receives a combination, with different phases, of the two monochromatic waves to be compared (incident and reflected waves at the DUT) so that each received signal (photocurrent) contains an optical interference term that is proportional to the cosine of the phase difference; in fact, the six-port technique could be properly defined, in optical parlance, as being a *C-OFD technique with phase diversity* [24].

An architecture to implement the optimum six-port junction, as defined by (8.56), is proposed in [24]. This junction uses multimode interference (MMI) couplers.

These couplers can be easily constructed in planar lightwave circuit (PLC) technology. MMI couplers are the basic building blocks of today's photonic integrated circuits because of their compactness, low loss, polarization insensitivity, large bandwidth, high fabrication tolerance, and cascadability, which allow interconnections to construct more complex structures [25].

The six-port optical architecture is shown in Figure 8.18. It is basically composed of three MMI: two identical 2×2 couplers (M_1 and M_2) whose phase responses are unimportant and one 2×3 120° coupler (M_3). The same architecture contains two interconnecting waveguides: W_D is the waveguide (of length L_D) between the reference measurement plane and port 1 of M_2, and W_C is a waveguide (of length L_C) used to balance the design, as shown next. For the theoretical analysis presented in this section, the remainder of the connections between MMIs is considered to be direct (i.e., zero length of interconnecting waveguides).

The first MMI (M_1) acts as a power divider (a nonreflective load has been added to its port 2) and is used to get a sample of the power incident on the DUT into the measurement port P_3 (so that R_3=0). The second MMI (M_2) is used as a directional coupler, i.e., to separate the incident and reflected waves in the DUT that is, at ports 2 and 3.

As signals have traveled different optical paths, and hence suffered different phase shifts, a length of waveguide W_C is included, as shown in Figure 8.18. To balance the design, the 2×3 MMI (M_3) has been designed so that at any output port the two input signals are present with equal amplitudes and relative phases of 120°. This is the key component of the six-port junction as it is mainly responsible for placing the q_4, q_5, and q_6 constants on a circle with a 120° phase difference.

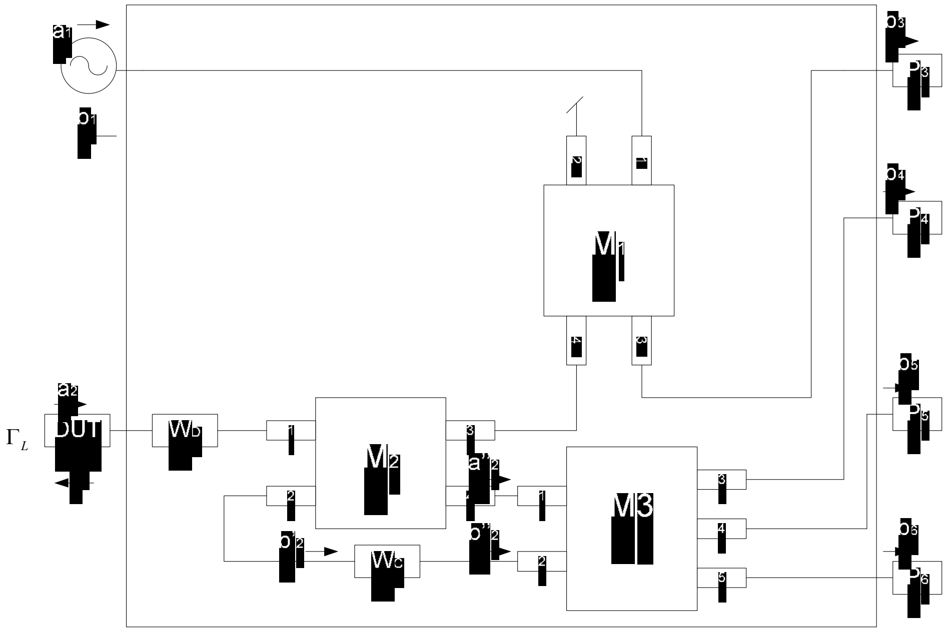

Figure 8.18 An optical six-port architecture. (© 2005 IEEE [24].)

8.7.2 Optical Six-Port Analysis

The S-parameters of the different components of the circuit, shown in Figure 8.18, are obtained as

$$W_D : S_{21} = \exp(j\xi_D) \tag{8.57a}$$

$$W_C : S_{21} = \exp(j\xi_C) \tag{8.57b}$$

$$M_1, M_2 : \begin{cases} S_{31} = S_{42} = \dfrac{\exp(j\varphi)}{\sqrt{2}} \\ S_{41} = S_{32} = \dfrac{\exp(j(\varphi - \pi/2))}{\sqrt{2}} \end{cases} \tag{8.57c}$$

$$M_3 : \begin{cases} S_{31} = S_{52} = \dfrac{\exp(j\psi)}{\sqrt{3}} \\ S_{41} = S_{42} = \dfrac{\exp(j(\psi - \pi))}{\sqrt{3}} \\ S_{51} = S_{32} = \dfrac{\exp(j(\psi - 2\pi/3))}{\sqrt{3}} \end{cases} \tag{8.57d}$$

where phase shifts ξ_C and ξ_D are related to the optical length ($l_C = L_C n_{eff}$ and $l_D = L_D n_{eff}$) of the corresponding waveguides by

$$\xi_{C,D} = \frac{l_{C,D}}{c}\omega \tag{8.58}$$

Both φ and ψ take arbitrary values given approximately, near the design frequency ω_0, by the first-order Taylor expansion, as

$$\varphi = \varphi_o + \frac{l_{M_2}}{c}(\omega - \omega_o) \tag{8.59}$$

$$\psi = \psi_o + \frac{l_{M_3}}{c}(\omega - \omega_o) \tag{8.60}$$

where $l_{M_2} = L_{M_2} n_{eff}$ and $l_{M_3} = L_{M_3} n_{eff}$ are the optical lengths of M_2 and M_3 respectively. For the remaining parameters, the relation $S_{ij} = S_{ji}$ between scattering parameters linking any two ports is valid by reciprocity theorem, and we also suppose, for the theoretical analysis, infinite directivity and perfect matching conditions. Simple analysis of Figure 8.18 yields

$$b_3 = \frac{S_{31}^{M_1}}{S_{21}^{W_C} S_{23}^{M_2} S_{41}^{M_1}} b_2'' \tag{8.61a}$$

$$b_4 = S_{31}^{M_3} a_2'' + S_{32}^{M_3} b_2'' \tag{8.61b}$$

$$b_5 = S_{41}^{M_3} a_2'' + S_{42}^{M_3} b_2'' \tag{8.61c}$$

and

$$b_6 = S_{51}^{M_3} a_2'' + S_{52}^{M_3} b_2'' \tag{8.61d}$$

In addition, from Figure 8.18 and taking into account (8.57) we get

$$\left.\begin{aligned} a_2'' &= S_{21}^{W_D} S_{41}^{M_2} a_2 \\ b_2'' &= \frac{S_{21}^{W_C} S_{23}^{M_2}}{S_{12}^{W_D} S_{13}^{M_2}} b_2 \end{aligned}\right\} \Rightarrow \frac{a_2''}{b_2''} = \frac{\exp(-j(\xi_C - 2\xi_D - \varphi))}{\sqrt{2}} \Gamma_L \tag{8.62}$$

Finally, introducing (8.62) into (8.61) and taking into account (8.57), one finally obtains the following expressions for the power at the four measurement ports [24]:

$$P_3 = |b_3|^2 = 2|b_2|^2 \tag{8.63a}$$

$$P_4 = |b_4|^2 = \frac{1}{6}|b_2|^2 \left|\Gamma_L - \sqrt{2}\exp(j(\xi_C - 2\xi_D - \varphi + \pi/3))\right|^2 \tag{8.63b}$$

$$P_5 = |b_5|^2 = \frac{1}{6}|b_2|^2 \left|\Gamma_L - \sqrt{2}\exp(j(\xi_C - 2\xi_D - \varphi + \pi))\right|^2 \tag{8.63c}$$

and

$$P_6 = |b_6|^2 = \frac{1}{6}|b_2|^2 \left|\Gamma_L - \sqrt{2}\exp(j(\xi_C - 2\xi_D - \varphi - \pi/3))\right|^2 \tag{8.63d}$$

with

$$\theta = \xi_C - 2\xi_D - \varphi \tag{8.63e}$$

Thus, the proposed topology fulfills the design goals given by (8.56) with the center point parameters q_i located at 120° on a circumference of radius 1.41, and with an arbitrary angle θ.

References

[1] Engen, G. F., "The Six-Port Reflectometer: An Alternative Network Analyzer," *IEEE Trans. Microw. Theory Tech.*, Vol. 25, No. 12, pp. 1075–1080, December 1977.

[2] Caron, M., A. Akyel, and F. M. Ghannouchi, "A Versatile Easy to Do Six-Port Based High Power Reflectometer," *Journal of Microwave Power and Electromagnetic Energy,* Vol. 30, No. 4, pp. 231–239, 1995.

[3] Yakabe, T., F. Xiao, K. Iwamoto, F. M. Ghannouchi, K. Fujii, and H. Yabe*, "*Six-Port Based Wave-Correlator with Application to Beam Direction Finding," *IEEE Trans. on Instrumentation and Measurements,* Vol. 50, No. 2, pp. 377–380, April 2001.

[4] Yakabe, T., M. Kinoshita, and H. Yabe, “Complete Calibration of a Six-Port Reflectometer with One Sliding Load and one Short,” *IEEE Trans. Microwave Theory Tech.*, Vol. 42, pp. 2035–2039, November 1994.

[5] Xiao, F., Ghannouchi, F. M., and T. Yakabe, “Application of a Six-Port Wave-Correlator for a Very Low Velocity Measurement Using the Doppler Effect,” *IEEE Trans. on Instrumentation and measurement*, Vol. 52, No. 2, April 2003.

[6] Hnyart, B., J. Laurin, R. G. Bosisio. and D. Roscoe, “A Direction-Finding Antenna SystemUsing an Integrated Six-Port Circuit,” *IEEE Trans. on Antennas and Propagation,* Vol. 43, No. 12, pp.1508–1512, December 1995.

[7] Tatu, S. O., K. Wu, and T. A. Denidni, “Direction-of-Arrival Estimation Method Based on Six-Port Technology,” *IEE Proc.-Microw. Antennas Propag.*, Vol. 153, No. 3, June 2006.

[8] Miguelez, C. G., B. Huyart, E. Bergeault, and L. P. Jallet, “A New Automobile Radar Based on the Six-Port Phase/Frequency Discriminator,” *IEEE Trans. Veh. Technol.*, Vol. 49, No. 4, pp. 1416–1423, July 2000.

[9] Wiedmann, F., “New Structure for a Six-Port Reflectometer in Monolithic Microwave Integrated-Circuit Technology,” *IEEE Trans. Instrum. Meas.*, Vol. 46, pp. 527–530, April 1997.

[10] Moldovan, E., S. O. Tatu, T. Gaman, K. Wu, and R.G. Bosisio, “A New 94GHz Six-Port Collision Avoidance Radar Sensor,” *IEEE Trans. Microw. Theory Tech*., Vol. 52, No. 3, pp. 751–759, 2004.

[11] Tatu, S. O., K. Wu, and T. A. Denidni, “Direction-of-Arrival Estimation Method Based on Six-port Technology,” *IEE Proc.-Microw. Antennas Propag*., Vol. 153, No. 3, pp. 263–269, June 2006.

[12] Zhang, H., L. Li, and K. Wu, “Software-Defined Six-Port Radar Technique for Precision Range Measurements,” *IEEE Sensor Journal*, Vol. 8, No. 10, pp. 1745–1751, October 2008.

[13] Bialkowski, M. E., and G. S.Woods, “Design and Analysis of a Six-Port Receiver for Use in Near-Field Antenna Measurements, *IEE Proceedings,* Vol. 134, Pt. H, No. 6, pp. 515-520, December 1987.

[14] Joy, E. B., W. M. Leach, and D. T. Paris, “Applications of Probe Compensated Near-Field Measurements,” *IEEE Trans. on Antennas and Propagation*, Vol. 26, No. 3, pp. 379–389, 1978.

[15] Pereira, J. F. R., A. P. Anderson, and J.C, Bennett, “New Procedure for Near-Field Measurements of Microwave Antennas Without Anechoic Environments,” *Proc. IEE,* 131, Vol. 6, pp. 351–358, 1984.

[16] Chen T. J., and T. H. Chu, “Calibration and Measurement of a Wideband Six-Port Polarimetric Measurement System,” *IEEE Trans. on Antennas & Propagation,* Vol. 45, No. 7, pp.1080–1085, July 1997.

[17] Ghannouchi, F. M., R. G. Bosisio, and R. Hajji, “Polarization Measurements of Microwave/Millimeter Wave Antennas Using Six Port Techniques,” *International Conference on Electromagnetics in Aerospace Applications,* Turin, Italy, pp. 283–286, 1989.

[18] Ghannouchi, F. M., and R. G. Bosisio, “Measurement of Microwave Permittivity Using a Six-Port Reflectometer with an Open-Ended Coaxial Line,” *IEEE Trans. Instrum. Meas.,* Vol. 38, No. 2, pp. 505–508, April 1989.

[19] Cole, R. H., “Evaluation of Dielectric Behavior by Time-Domain Spectroscopy, Part 11: Complex Permittivity,” *J. Phys. Chem.,* Vol. 79, No. 14, pp. 1469–1474, 1975.

[20] Stuchly, M. A., “Equivalent Circuit of an Open-Ended Coaxial Line in Lossy Dielectric,” *IEEE Trans. Instrum. Meas.,* vol. IM-31, June 1982.

[21] Pourova, M., R. Zajicek, L. Oppl, and J. Vrba, "Measurement of Dielectric Properties of Moisture Textile," *14th Conference on* COMITE 2008, pp. 1–4, April 2008.

[22] Ivanov, M., J. Banys, S. Rudys, and R. Grigalaitis, "Measurements of Complex Dielectric Constant of Ferroelectrics with Six-port Reflectometer in 80-120 GHz Frequency Range," *Ferroelectrics*, Vol. 367, pp. 229–233, No. 1, 2008.

[23] Zhang, Y., G. Colef, Y. Li, and G. Eichmann, "Six Port Optical Reflectometer," *IEEE Trans. Instrum. Meas.*, Vol. 40, No. 5, pp. 869–871, October 1991.

[24] Fernández, I. M., J. G. Wangüemert-Pérez, A. O. Moñux, R. G. Bosisio, and K. Wu, "Planar Lightwave Circuit Six-Port Technique for Optical Measurements and Characterizations," *IEEE Journal of Lightwave Technology*, Vol. 23, No. 6, pp. 2148–2157, June 2005.

[25] Shibata, Y., S. Oku, M. Yamamoto, and M. Naganuma, "Reflection Characteristics and Cascadability of a Multimode Interference 3 dB Coupler," *Proc. Inst. Elect. Eng., Optoelectronics*,Vol. 149, pp. 217–221, 2002.

About the Authors

Fadhel M. Ghannouchi, a senior Canada research chair in intelligent RF radio technology, iCORE professor, founder, and director of iRadio Laboratory, University of Calgary is regarded as one of the foremost authorities in the fields of RF electronics and radio technology. His current research interests are in their applications in broadband wireless, satellite, and biomedical sciences.

Other recognitions received by Prof. Ghannouchi include: The Alberta Professional Engineers Geologists and Geophysicist (APEGGA) Alberta Ingenuity Fund Research Excellence Award, The Research Excellence Award of Schulich School of Engineering, University of Calgary, and being elected distinguished lecturer of the IEEE Microwave Theory and Technique.

For his scientific and technical accomplishments, Dr. Ghannouchi's peers have elected him to fellow in The Canadian Academy of Engineering, fellow of The Engineering Institute of Canada, fellow of The Institution of Engineering and Technology (IET formally IEE), and fellow of Institute of Electrical and Electronics Engineers (IEEE).

Prof. Ghannouchi held several invited positions at several academic and research institutions in Europe, North America, and Japan. He has provided consulting services to a number of microwave and wireless communications companies worldwide. His research interests are in the areas of microwave instrumentation and measurements, nonlinear modeling of microwave devices and communications systems, design of power and spectrum efficient microwave amplification systems, design of intelligent RF transceivers for wireless and satellite communications, and software defined and cognitive radio systems.

Prof. Ghannouchi has published extensively. He has authored two books, was awarded 7 patents, published more that 400 peer-reviewed articles, given over 50 invited/keynote/plenary conference presentations, trained over 60 master and Ph.D. graduates, and founded three spin-off companies.

Abbas Mohammadi is currently a professor at the Electrical Engineering Department of Amirkabir University of Technology and director of Microwave/Millimeter-Wave and Wireless Communications Research Lab. He held an invited position at the University of Calgary. His research interests are in the areas of microwave and wireless communications, six-port techniques, software defined radio, adaptive transceivers, and MIMO systems. His research activities led to over 120 publications, 3 U.S. patents, and one Canadian patent. He is a senior member of the IEEE.

Index